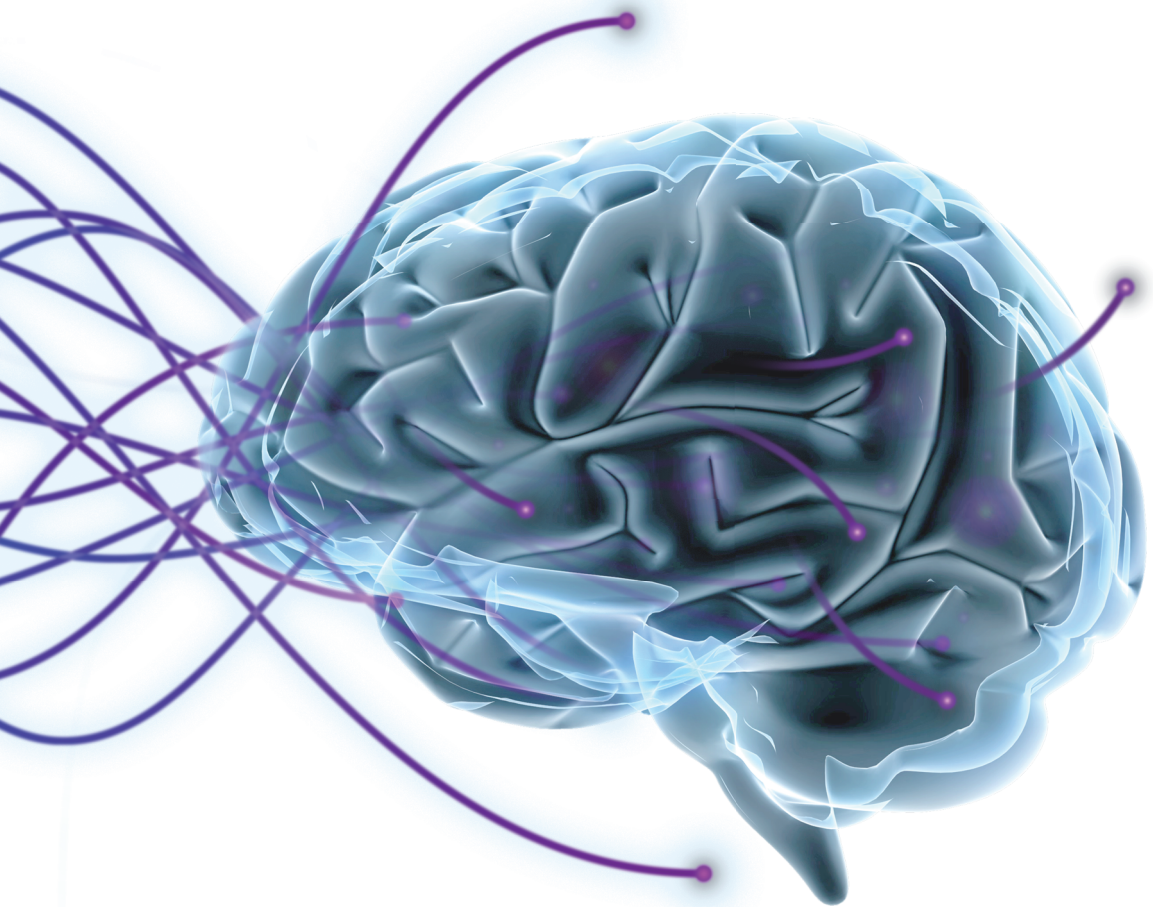


Quantitative MRI of physiological brain tissue deformation in humans



Jacob Jan Sloots

Quantitative MRI of physiological brain tissue deformation in humans

Jacob Jan Sloots

ISBN 978-90-393-7412-2

© 2021 Jacob Jan Sloots

All rights reserved. No part of this publication may be reproduced or transmitted in any form or by any means without the prior permission of the author. The rights of the published chapters have been transferred to the publishers of the respective journals.

Lay-out and printed by Optima Grafische Communicatie (www.ogc.nl)

Quantitative MRI of physiological brain tissue deformation in humans

*Kwantitatieve MRI van fysiologische hersenweefselvorming
bij mensen*

(met een samenvatting in het Nederlands)

Proefschrift

ter verkrijging van de graad van doctor aan de Universiteit Utrecht
op gezag van de rector magnificus, prof.dr. H.R.B.M. Kummeling,
ingevolge het besluit van het college voor promoties in het openbaar te verdedigen
op dinsdag 26 oktober 2021 des middags te 2.15 uur

door
Jacob Jan Sloots
geboren op 2 juni 1989
te Zeist

Promotoren: Prof. dr. G.J. Biessels
Prof. dr. P.R. Luijten

Copromotor: Dr. ir. J.J.M. Zwanenburg

Financial support by the Dutch Heart Foundation for the publication of this thesis is gratefully acknowledged.

Financial support by Alzheimer Nederland for the publication of this thesis is gratefully acknowledged.

Financial support by ChipSoft for the publication of this thesis is gratefully acknowledged.

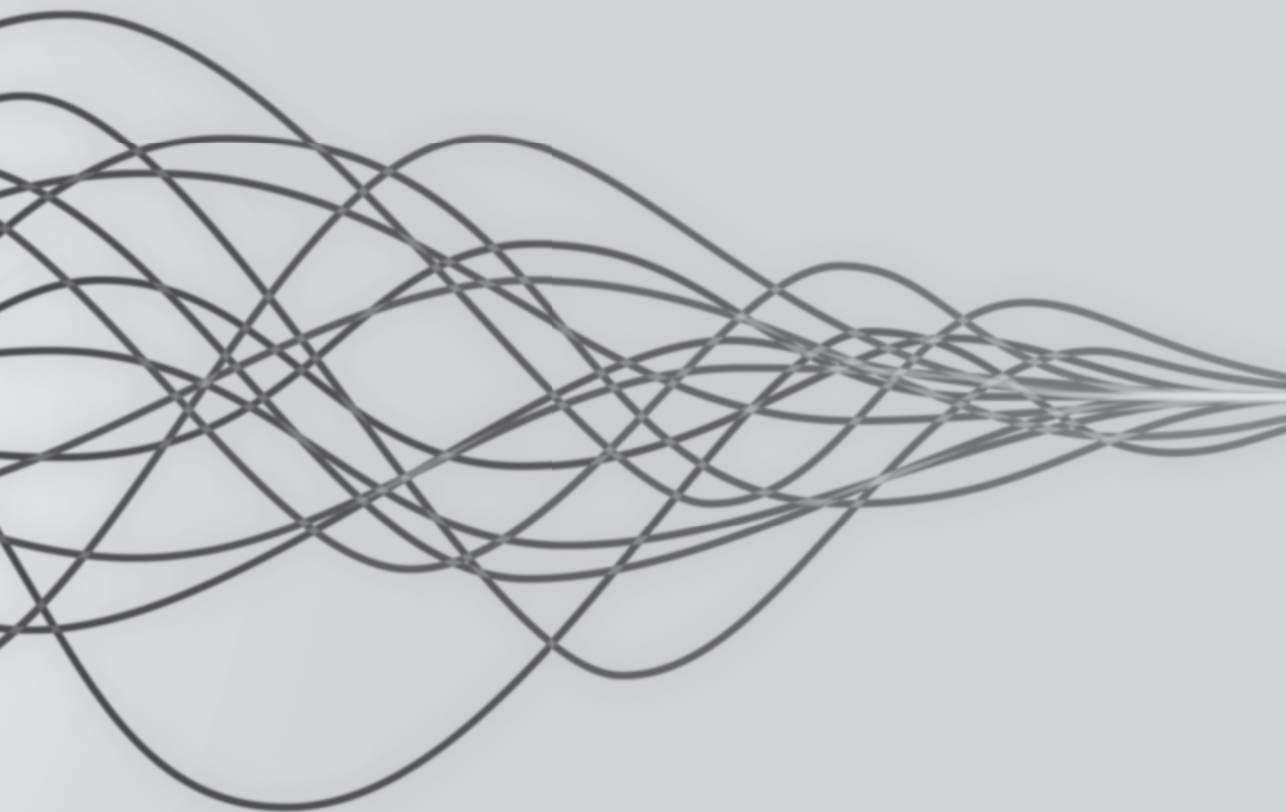
CONTENTS

Chapter 1	General introduction	7
Chapter 2	Comparing PC-MRI with DENSE for accurate brain tissue strain measurements	25
Chapter 3	Cardiac and respiration-induced brain deformations in humans quantified with high-field MRI.	43
Chapter 4	Strain Tensor Imaging: Cardiac-induced brain tissue deformation in humans quantified with high-field MRI	65
Chapter 5	Strain Tensor Imaging: abnormalities in cardiac-induced brain tissue deformation detected on an individual subject level	99
Chapter 6	Dynamic brain ADC variations over the cardiac cycle and its relation to tissue strain assessed with DENSE at high-field MRI.	107
Chapter 7	Summary and general discussion	133
Chapter 8	Summary in Dutch (Nederlandse samenvatting)	149
Appendices	List of publications	161
	Acknowledgements (Dankwoord)	163
	References	167
	Curriculum Vitae	179



1

General introduction



GENERAL INTRODUCTION

The cardiac cycle induces variations in blood pressure that drive tissue deformation in the brain. As the pulsatile blood pressure waves are transmitted through the vascular tree all the way to the level of the brain's microvasculature, it causes the surrounding tissue to swell and stretch elastically, resulting in a pulsating brain. Due to the rise of the intravascular blood volume during systole, the cerebral tissue expands and cerebral spinal fluid (CSF) is squeezed out of the brain to compensate for the additional blood volume. As the blood leaves the brain during diastole, the vessels relax and CSF returns. It is important to note that brain tissue in the context of this thesis includes the microvasculature embedded in the tissue.

These pulsatile tissue deformations in the brain are of interest as they carry information on both blood supply and vessels that drive the pulsations and on the surrounding tissue that deforms in response to the vascular pulse. For example, it is known that tissue expansions from diastole to systole are smaller in white matter than in grey matter [1; 2; 137]. Differences in tissue expansion may be due to an overall lower blood flow to the white matter compared to the grey matter, but may also reflect differences in tissue stiffness, tissue integrity and vessel wall stiffness. For instance, *ex-vivo* studies have shown that white matter could be stiffer than grey matter, which could lead to reduced tissue expansion for a given blood flow [80]. On the other hand, blood vessel condition and tissue integrity are generally affected in disease. Indeed, studies have shown that brain tissue becomes less stiff with age, which probably reflects change in the tissues microstructures [132]. Diseases such as cerebral small vessel disease (cSVD) are associated with stiffening of the arterial walls. cSVD is a major cause of stroke and dementia that can currently only be detected when macroscopic, mostly irreversible, tissue lesions have been developed [121; 166; 168]. Assessment of changes in the microvascular- and tissue properties prior to the development of such damage might yield insight in the underlying disease processes. Quantifying brain tissue deformation could be an important piece of the puzzle to assess microvascular and tissue properties directly.

Apart from the fact that tissue deformations reflect tissue condition and properties, these deformations may also be of interest for their potential role in physiological processes. The mechanical deformation of brain tissue and its pulsatile nature evoke mechanotransductive responses in endothelial cells, which constitute the blood-brain barrier [33; 35; 37]. Endothelial cells exposed to regular mechanical pulsations constitute better organized cellular structures than cells that do not [35]. In addition, the pulsations drive CSF around the brain that plays an important role in the drainage of cerebral waste [101; 141]. Tissue deformation can therefore be considered an important factor to waste clearance in the brain.

Brain tissue deformation is very subtle and involves relative changes in tissue length of typically less than 1%. Moreover, brain tissue is shielded by the skull, which poses a challenge from a measurement point of view. Magnetic resonance imaging (MRI) is a powerful, non-invasive technique that can be used to measure these deformations. This thesis addresses the major objective to non-invasively measure brain tissue deformation with MRI to pave the way to non-invasive *in-vivo* assessment of the impact of disease and physiological stressors (such as hypertension and ageing) on the properties of the brain tissue and vasculature.

HISTORY OF MEASURING BRAIN PULSATIONS

At the end of the 19th century, Angelo Mosso (1846-1910) studied the pulsating brain (or in his words the *cerebral pulse*) with a device he developed for graphical recordings of the *in vivo* cerebral blood flow. He performed his experiments in patients with skull openings. In his latest of four major articles on the link between blood flow and neural activity, he presented the interesting case of a 37-year-old farmer named Michele Bertino [178]. In his report entitled *Sulla circolazione del sangue nel cervello dell'uomo* (On the circulation of blood in the human brain) Mosso writes about Bertino [107; 124]:

“On July 30, 1877, as he stood below the bell tower of his village, a brick that had slipped from the hands of a mason working near the roof fell on his head. Under the impact of this 3-kg mass dropped from a height of 14 m, Bertino fell on the ground unconscious.”

Bertino survived and all that remained was a crushed laceration, shaped like an irregular triangle of 7cm long and 4cm wide. The fractured bones were removed, revealing a bone breach in the skull of approximately 20 mm in diameter. Bertino did not suffer from apparent brain damage; memory and language remained unimpaired. Dr. De Paoli, who at the time had been Bertino's attending physician, invited Mosso almost 3 months after the incident to collaborate on the experiments Mosso describes in his report. He writes [107; 124]:

“I believe it would have been difficult to produce intentionally in animals a cranial defect more profitably designed for this, because when the skull is trephined⁽¹⁾, as Mr. Salathé⁽²⁾ correctly pointed out, one often encounters an insurmountable obstacle to the recording of the cerebral movements.”

The obstacle Mosso refers to is the fact that the recordings of the pulsating brain fail when the brain swells during the experiment and obstructs the cranial opening through which the mea-

1 Trephine: to perform a surgical intervention in which a hole is drilled in the skull

2 Salathé: *Recherches sur les mouvements du cerveau*. Paris, 1877, p. 74

surements are obtained. Such an obstruction could not happen for Bertino's breach, since his brain had an indentation of 5cm^3 underneath the skull defect, allowing for additional brain swelling. Mosso could therefore record the pulsations of Bertino's brain through a device connecting the air within the cerebral indentation to a recording barrel (see Figure 1-1b). Simultaneously, Mosso recorded the blood pulsation in the forearm by immersing the arm in a glass cylinder filled with water. Figure 1-1c presents a selection of paired traces Mosso obtained during the experiment. Of each pair, the upper trace represents the variations of blood volume recorded as a reference by immersing the forearm in a glass cylinder filled with water. The bottom trace shows the brain's blood volume pulsations obtained through the skull breach. Mosso recorded the brain's blood pulsations (i) in rest and (ii, iii) during cognitive stimuli. For instance, trace (ii) shows the response of brain volume change when the pendulum clock in the room struck 12, and was accompanied by the sound of the bell of the neighboring church. He wrote [107; 124]:

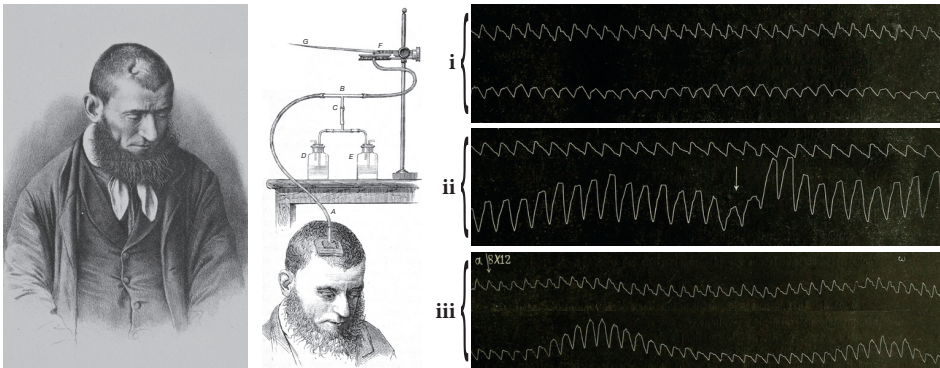


Figure 1-1 The experimental setup and results of the cerebral blood flow as measured by Angelo Mosso. The device of Angelo Mosso (b) was connected to the skull breach of Michele Bertino (a). Pairs of traces were recorded (c) in (i) resting state, (ii) when Michele Bertino was asked to multiply 8 times 12 and (iii) when the clock in the room struck noon. The bottom trace of each pair represents the brain pulsations and the upper trace shows the blood volume changes in the forearm for reference. This reference trace was obtained through the 'hydrophygmograph' that recorded the blood volume changes in the forearm by positioning the arm in a glass cylinder filled with water. The figure is reproduced with permission from Raichle et al. (2014) [124].

"If I had reproduced in the present figure the direct continuation of trace 2⁽³⁾, one would notice such an increase in the inflow of blood to the brain that the 20th pulsation of line C indicated by the symbol ↓ (which corresponds to the first peal of the clock striking noon) went so far beyond the upper line A of the forearm pulsations that I was forced to open the release valve (clarinet) in order to prevent excessive tension of the tambour membrane."

Mosso later continued with a mental task where he asked Bertino to multiply 8×12 . At the time denoted by α in trace (iii), the task was posed on Bertino and at ω he provided the response. Besides an increase in cerebral volume, Mosso also observed a larger amplitude of the pulsations during both mental stimuli. From these observations, it is evident that the brain pulsates over the cardiac cycle, which is of interest to assess. Mosso's methods, however, require a lot of effort to be put in before hemodynamics in the brain can be measured. The approach also relies on the availability of patients to connect to the device called the *hydrophygmograph* (see Figure 1-1b). It makes Mosso's method intrinsically invasive, which poses a challenge for interpretation of the findings, since the observations are performed with different boundary conditions compared to healthy subjects.

MAGNETIC RESONANCE IMAGING OF BRAIN PULSATIONS

In the past 150 years, the rise of imaging modalities have played a crucial role for improved investigation of the brain's hemodynamics [50]. MRI is a powerful, non-invasive technique which signal is acquired as a distribution of spatial frequencies, represented in k -space. The acquired k -space relates to the MRI image data by the mathematical operation 'Fourier transform'. The image data is described by both magnitude and direction (called *phase*), implying that the signal is similar to a vector. Both magnitude and phase can be harnessed to track tissue motion. The most widely used motion tracking MRI techniques are myocardial tagging and phase-contrast MRI (PC-MRI) [75]. Tagging sequences modulate the magnitude signal by vector fields that induce signal voids. The tag lines in the acquired signal provide information from which tissue strains can be inferred by using post-processing methods. These methods track adjacent tag-line intersection points to calculate the strain. Although the technique is capable to track sub-voxel motion, its sensitivity is low [177]. Because signal voids need to be identified over neighboring voxels, the sensitivity of tagging methods reduces even more for lower spatial resolutions. This poses a challenge to assess more subtle tissue motion in the brain with this technique [59]. Instead, phase-contrast methods for MRI are often used. These methods manipulate the phase-signal such that it becomes proportional to motion which facilitates increased sensitivity and accuracy of the motion field maps compared to tagging sequences. Unlike for tagging methods, the sensitivity of phase-based methods does not depend on voxel-size directly. Lower resolution in this case only implies lower spatial resolution to identify anatomical structures in the obtained motion field maps.

Principle of cine MRI

Cine MRI refers to MRI sequences designed to capture motion, for which the reconstructed images resemble a movie when played consecutively. For the heart, each movie frame is also referred to as a *cardiac phase*. Furthermore, the temporal resolution indicates how many cardiac

phases constitute the cardiac interval; the more cardiac phases are acquired, the higher the temporal resolution.

Cardiac phases are obtained by synchronizing the MRI acquisition with the ECG of the subject. The data acquisition is then performed during several heartbeats. In each heartbeat – also referred to as R-R interval – multiple radiofrequency (RF) excitations are performed that each provide a line of k -space data at different time-points along the R-R interval. To acquire all cardiac phases in a reasonable amount of R-R intervals, in general sequences are required to have a very short echo time (TE) and repetition time (TR). These short times (1-2ms) permit multiple consecutive acquired lines of k -space to be combined within a single cardiac phase [102].

Alternatively, sequences suitable for cine MRI utilize acceleration techniques such as echo-planar imaging (EPI) [131; 145]. The main principle of EPI is that for each RF-excitation, multiple lines of k -space can be acquired (see Figure 1-2) [123]. For very small datasets (e.g. low resolution 2D image), only one excitation may be enough to fill the complete k -space. Such acquisitions are referred to as single-shot EPI acquisitions and resemble a *snapshot* image. For larger datasets, however, multiple excitations may still be required. These acquisitions are referred to as multi-shot EPI and often involve 3D and/or high resolution data. Although EPI offers some major advantages, it may introduce geometric distortions in the final image that need to be compensated for by using a correction method [53; 79].

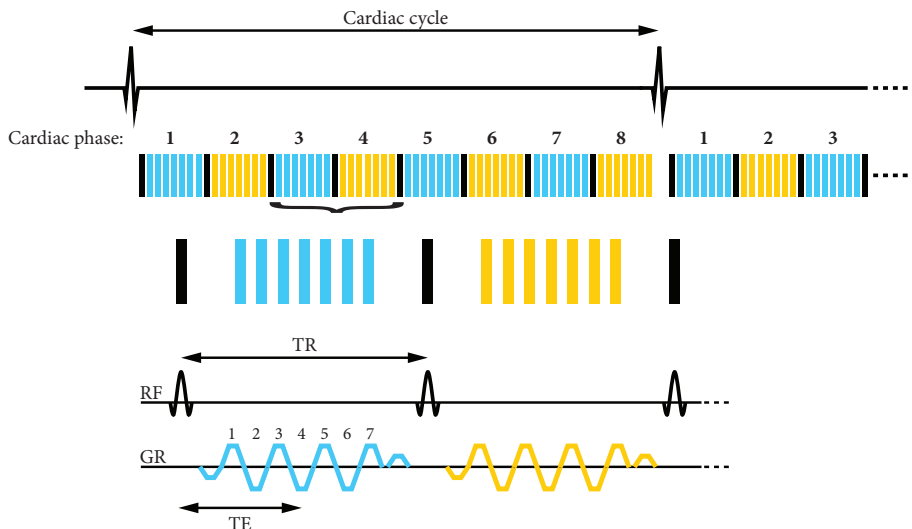


Figure 1-2 Cine MRI routine for gradient-echo multi-shot EPI MRI sequence. In this example, 8 cardiac phases are acquired and the EPI factor is set to 7. The EPI acceleration technique is used to acquire all cardiac phases in a reasonable amount of R-R intervals. The total number of cardiac intervals required to acquire the full k -space is typically 10 – 40+ cardiac intervals, but varies per application and depends, among other things, on resolution and FOV.

Principle of motion encoding

The MRI signal can be represented as the net magnetization of *isochromats*⁴. The magnitude of the net magnetization is normally represented on a voxel-by-voxel basis in a MR image. The principle of motion encoding involves manipulating the relative frequency of isochromats and is depicted in Figure 1-3. In this figure, the top row represents a collection of isochromats all precessing at the initial (Larmor) frequency. An additional magnetic gradient (indicated by the read bar) now ensures that isochromats on the right side precess with a slightly higher frequency compared to isochromats on the left. As the magnetic gradient is stopped, isochromats precess in the Larmor frequency again, yet are no longer spinning *in-phase*. Instead, isochromats on the right (that preceded at a higher frequency when the gradient was applied) are front runners compared to isochromats on the left, as indicated by the arrows. To get the isochromats back in-phase, an equal but opposite gradient is required. Isochromats on the left (that previously experienced a lower field) will now precede at a higher frequency so that they ‘catch up’ with the front runners on the right, as shown in the bottom row.

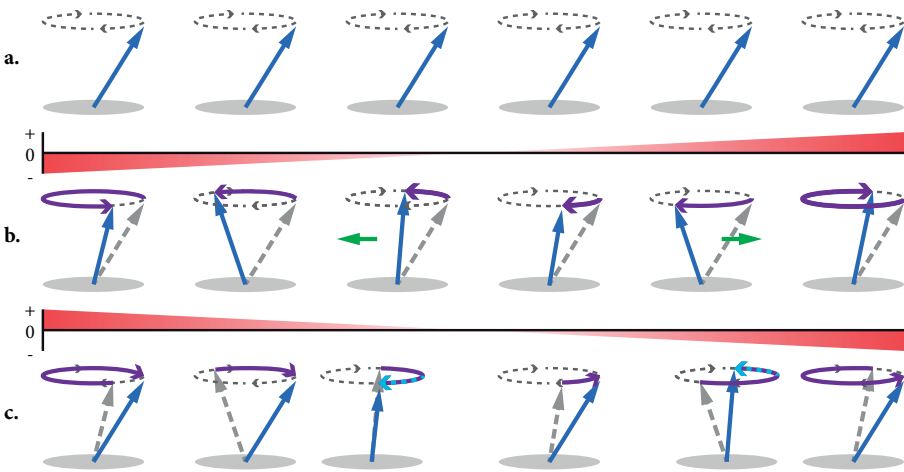


Figure 1-3 Schematic representation of motion encoding principle. (a) Isochromats are represented as tiny gyroscopes that initially precess in-phase with the Larmor frequency. (b) For a given duration δ of an applied gradient, normally in the order of a few milliseconds, spins on the right have obtained a positive phase shift and can be regarded ‘front runners’ whereas spins on the left have obtained a relative negative phase shift and, thus, are fallen behind. (c) Applying an equal but opposite magnetic gradient field ensures that isochromats will return in-phase, provided no motion has occurred in the meantime. In-phase is visualized by the vector of the isochromat returning to its initial position. Isochromats 3 and 5 show how displacement results in accumulated phase depending on the displacement’s magnitude and direction. The arrow indicating the vector of the isochromat does not return to its initial position, but instead accumulates a phase-shift indicated by the dotted light-blue arrow.

4 Isochromat: microscopic collection of spins, all resonating at the same frequency.

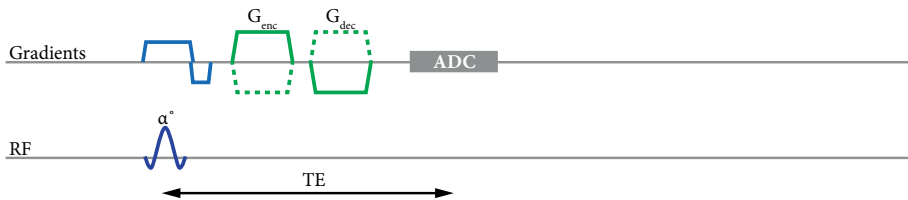
Isochromats will obtain a phase-shift when they have moved in the time between the two applied gradients. For instance, after the first gradient, isochromat 3 moved to the left and will consequently experience a stronger second gradient field than necessary to catch up with the spins on the right. As a result, isochromat 3 will 'run too fast' and become a front runner compared to the stationary spins when the second magnetic gradient field is stopped. Meanwhile, isochromat 5 moved to the right, experiencing a lower field than necessary to catch up with spins on the right. Consequently, isochromat 5 will 'run too slow' to make up for the phase difference, and therefore remain a rear runner compared to isochromats that did not move. In this particular case, isochromats that moved to the left obtain a positive phase-shift, while isochromats moving to the right yield a negative shift. Apart from the displacement of isochromats, the phase shift also depends on the applied gradients. The stronger the gradients or the longer its duration, the larger the obtained phase shift for a given displacement of isochromats. Note that the size of the final phase shift is not related to the initial or final position of the isochromats.

Phase shifts may be confounded by many factors, including, but not limited to, inhomogeneity of the static magnetic field and RF phase. In practice, motion field maps are therefore computed from two motion encoded images with opposite encoding direction. This implies that isochromats moving to the right, for instance first accumulate a motion-induced positive phase shift in the first image and an equal but negative phase shift in the second image, while confounding phase contributions remain unchanged for both images. By subtracting the second phase image from the first and dividing the result by 2, a motion encoded map is then obtained where static confounding phase factors have vanished. Only an eddy current component remains, because this confounding factor follows the polarity of the motion sensitizing gradient. This component becomes more pronounced as the motion sensitizing gradients increase in strength [93]. Especially for increased motion sensitivity, it may therefore be necessary to remove these effects, for which several approaches exist [96]. One approach is, for example, to subtract the first acquired cardiac phase image from all images, thereby setting the first cardiac phase to 0 and subtracting the eddy current component from the remaining cardiac images.

PC-MRI

Phase contrast MRI (PC-MRI) is probably the MRI sequence most widely used to obtain motion field maps [104; 105]. In general, the sequence consists of an excitation RF pulse followed by two motion sensitizing gradients, as shown in Figure 1-4a. Since the time between the gradients is short and varies between sequences, it is more convenient to normalize for these effects and express the resulting maps in terms of velocity. This way, the sequence provides velocity maps of, for example, blood flow in larger vessels or CSF stroke volumes in the neck and spinal canal. The sequence is particularly suited for flows of 1cm/s or higher. Lower velocities require larger gradients that result in technical limitations, but are also associated with longer echo times (TE), which is an important limiting factor for PC-MRI as the signal decays with T2*.

a. PC-MRI



b. DENSE

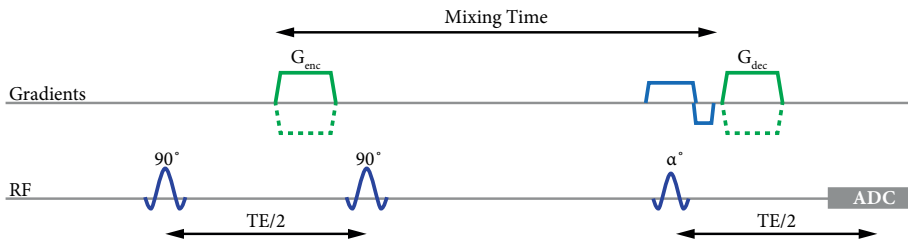


Figure 1-4 Comparison between the motion encoding sequences (a) PC-MRI and (b) DENSE. The main advantage of DENSE compared to PC-MRI is that the signal loss is predominantly proportional with T_1 . The time between the encoding gradient (G_{enc}) and decoding gradient (G_{dec}) can therefore be prolonged without much signal loss. Furthermore, for DENSE, the signal decays with T_2 as function of TE as compared with the much faster T_2^* for PC-MRI. Hence, DENSE is better suited for measuring very subtle motions that develop over relatively long time scales, like tissue displacement in the human brain during heartbeat and respiration.

In the early 1990s, Greitz et al. already used PC-MRI to capture the brain pulsations [15; 58]. These early observations showed a resultant movement in a funnel-shaped fashion, directed towards the foramen magnum. Transverse slices encoded in the Head-to-Foot direction are reproduced in Figure 1-5. At the time, gradient performance was less and combined with increased motion sensitivity resulted in TEs ranging between 35 and 47 ms. Therefore, they used PC-MRI in combination with a spin-echo acquisition, to ensure that the signal decayed with T_2 instead of T_2^* . Calibrated encoding sensitivities were found to be equivalent to VENCs ranging between 7.7 and 10.5 mm/s.

DENSE

Displacement Encoding with Stimulated Echoes (DENSE) was initially proposed by Aletras et al. in 1999 to obtain motion field maps in the heart and combines principles of both cardiac tagging and PC-MRI [5; 83]. The main advantage of DENSE compared to cardiac tagging is that the sequence can be optimized independently of voxel-size. This way, DENSE provides motion field maps with increased sensitivity without the need for high spatial resolution. Compared with PC-MRI, the main advantage of DENSE is its stimulated echo acquisition mode (STEAM), which facilitates longer times between encoding and decoding (indicated by *mixing time*) because STEAM ensures that the signal loss during the mixing time is predominantly proportional to

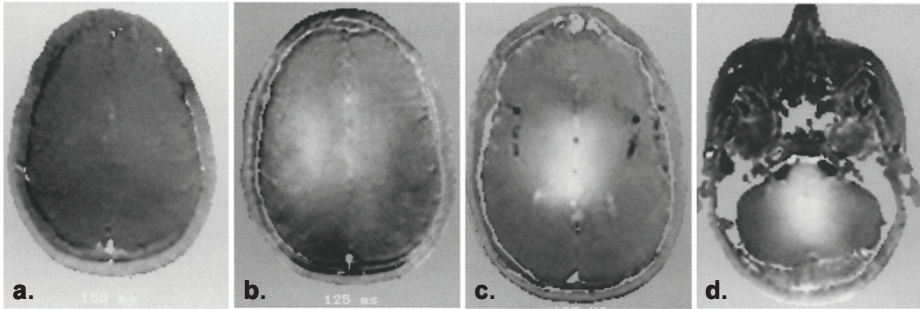


Figure 1-5 Transverse phase-images demonstrate motion in the Head-to-Foot direction (brighter areas move in Feet direction) of the central and caudal parts of the brain in systole (delay time after R-top is 125-150 ms). The most pronounced movement is at the level of corpus callosum. The figure is reproduced with permission from Greitz et al. (1992) [58].

T1, and decays with T2 as a function of TE (see Figure 1-4b) [49]. The extended delay between the bipolar gradients provides more time for tissue to displace, and hence, has increased motion sensitivity. In addition, the DENSE sequence allows for non-selective motion encoding. Combined with selective decoding, this approach requires a lower gradient duty cycle and thus has fewer technical constraints.

The STEAM approach in DENSE produces three signals (see Figure 1-6). The motion encoding gradient produces a stimulated echo (STE) signal and stimulated anti-echo (STAE) signal, of which the stimulated echo contains the displacement information of interest [83]. As a result, STEAM intrinsically distributes the available magnetization over the two stimulated echoes, thereby reduced the MRI magnitude signal by a factor of 2. The third signal consists of a free induction decay (FID) peak that accumulates during the mixing time. It is important to acquire the stimulated echo that contains the displacement information, without being corrupted by the other echoes. Here, two factors play a role. First, larger encoding sensitivities increase the separation between the STE and FID signal. Second, increased spatial resolution is reflected by a larger FOV in k -space, which increases the risk of the FID peak contaminating the acquisition. Brain tissue motions are very subtle, which requires large encoding sensitivities that naturally separate the STE signal from the FID peak. This illustrates that it depends on the study objective which MRI sequence is optimal to obtain motion field maps.

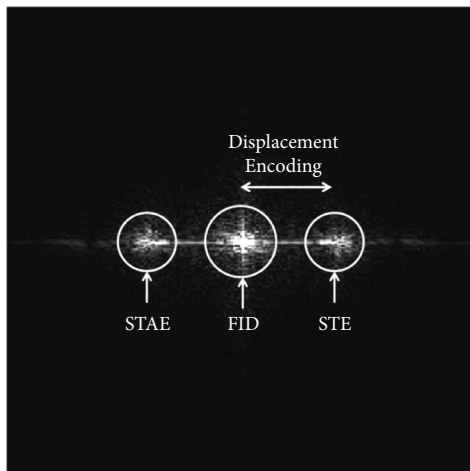


Figure 1-6 The k-space representation of the three signals generated in DENSE: stimulated echo (STE), stimulated anti-echo (STAE) and free induction decay (FID) signal. The STE signal contains the displacement information of interest, while other signals are to be suppressed. The larger the displacement encoding sensitivity, the larger the separation between the STE signal and the FID peak. Especially for brain motion field maps, encoding sensitivities are generally high, which results in displacement-encoded image not corrupted by other signals. Figure is adapted with permission from Ibrahim et al. (2011) [75].

ANALYSIS OF MECHANICAL DEFORMATION AND STRAIN

The mathematical description of brain tissue deformation can be derived by considering the brain as a *continuum*. A continuum is an ideal material object, for which the neighborhood of a material point is dense and fully occupied with other material points. Modeling objects this way ignores the fact that matter is made of atoms, but still yields highly accurate results on length scales much larger than inter-atomic distances [86]. In the following example, we derive the definitions required to describe deformation. Here, we use the term *object* for generalization purposes, but this refers to the brain tissue in the context of this thesis. Furthermore, brain tissue includes the microvasculature embedded in the tissue. This way, brain tissue deformation provides an indirect window into blood volume pulsations, which do not include the larger vessels surrounding the brain tissue.

Deformation

Consider the object as represented in Figure 1-7, in which a material point P moves from position \mathbf{X} at time $t = 0$ to position \mathbf{x} at time $t = t$. The coordinate \mathbf{x} relates to \mathbf{X} as follows: $\mathbf{x}(\mathbf{X}, t) = \mathbf{X} + \mathbf{u}(\mathbf{X}, t)$, where \mathbf{u} is the displacement field, that includes rigid-body rotations and translations of the complete object.

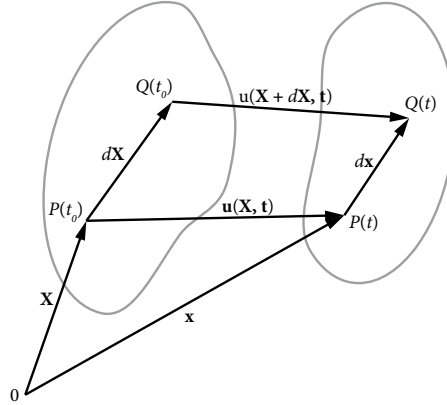


Figure 1-7 Deformation of a continuum body object. At time $t=t_0$ the object is in the undeformed state. For every material point P , the displacement field describes the new location after deformation.

Now consider Q in the neighborhood of P and at position $\mathbf{X} + d\mathbf{X}$. Our concern is what the relative position of Q and P is in the current (deformed) position of the object. To obtain this relative position, we determine the position where P and Q will arrive, that is at \mathbf{x} and $\mathbf{x} + d\mathbf{x}$, respectively:

$$\mathbf{x} = \mathbf{X} + \mathbf{u}(\mathbf{X}, t) \tag{1-1a}$$

$$\mathbf{x} + d\mathbf{x} = \mathbf{X} + d\mathbf{X} + \mathbf{u}(\mathbf{X} + d\mathbf{X}, t) \tag{1-1b}$$

Substituting Eq. 1-1a in Eq. 1-1b yields the relative position of P and Q in the current configuration

$$\begin{aligned} d\mathbf{x} &= d\mathbf{X} + \nabla \mathbf{u} d\mathbf{X} \\ &= (\mathbf{J} + \mathbf{I})d\mathbf{X} = \mathbf{F} d\mathbf{X} \text{ and } \mathbf{J} = \nabla \mathbf{u} \end{aligned} \tag{1-2}$$

where \mathbf{I} is the identity matrix, \mathbf{J} is the *displacement gradient tensor* and \mathbf{F} is the *deformation gradient tensor* that relates the line element $d\mathbf{X}$ in the undeformed state to its deformed counterpart $d\mathbf{x}$. Although \mathbf{F} is independent of rigid-body translations, it still depends on rigid-body rotations ($d\mathbf{X}$ and $d\mathbf{x}$ typically can point in different directions): $\mathbf{F} = \mathbf{R} \cdot \mathbf{U}$, where \mathbf{R} is the rotation vector and \mathbf{U} is the *stretch tensor*. These tensors have the following properties:

$$\begin{aligned} \mathbf{R}: & \quad \text{Proper orthogonal: } \mathbf{R}^{-1} = \mathbf{R}^T \text{ and } \det(\mathbf{R}) = 1 \\ \mathbf{U}: & \quad \text{Symmetric: } \mathbf{U} = \mathbf{U}^T \end{aligned} \tag{1-3}$$

Stretch and strain

The fact that \mathbf{F} depends on rigid-body rotations makes it less suitable for purposes of brain physiology. While it is conceivable that the physiology is different for a subject in lying or upright position, characterizing the pulsations should also not depend on the angle from which the observation is obtained. A rotation of the coordinate system in which the analysis is performed,

directly influences the appearance of \mathbf{F} . To circumvent this limiting factor, ds (the length of $d\mathbf{x}$) and dS (the length of $d\mathbf{X}$) are considered instead. These quantities define stretch and strain, which are normalized measures of deformation that characterize the change of distances and angles between particles:

$$\begin{aligned} \text{Stretch: } \quad \lambda &= \frac{L'}{L} = \frac{ds}{dS} & 0 < \lambda < \infty \\ \text{Strain: } \quad \varepsilon &= \frac{L' - L}{L} = \frac{\Delta L}{L} = \frac{ds - dS}{dS} = \lambda - 1 & -1 < \varepsilon < \infty \end{aligned} \quad (1-4)$$

To find the relationship between dS and ds , we derive

$$ds^2 = d\mathbf{x} \cdot d\mathbf{x} = Fd\mathbf{X} \cdot Fd\mathbf{X} = d\mathbf{X} (\mathbf{F}^T \mathbf{F}) d\mathbf{X} \quad (1-5)$$

and

$$\begin{aligned} ds^2 - dS^2 &= d\mathbf{X} \mathbf{F}^T \mathbf{F} d\mathbf{X} - d\mathbf{X} \mathbf{I} d\mathbf{X} \\ &= d\mathbf{X} (\mathbf{F}^T \mathbf{F} - \mathbf{I}) d\mathbf{X} \stackrel{\text{def}}{=} 2d\mathbf{X} \mathbf{E} d\mathbf{X} \end{aligned} \quad (1-6)$$

from where we obtain the *Green-Lagrangian strain tensor* \mathbf{E}

$$\mathbf{E} = \frac{1}{2} (\mathbf{F}^T \mathbf{F} - \mathbf{I}) \quad (1-7)$$

\mathbf{E} is a symmetric tensor and independent of rigid body motion. Writing the stretch and strain in terms of the Green-Lagrangian strain tensor results in

$$\lambda = \sqrt{1 + 2\mathbf{T} \mathbf{E} \mathbf{T}} \quad \text{and} \quad \varepsilon = \sqrt{1 + 2\mathbf{T} \mathbf{E} \mathbf{T}} - 1 \quad (1-8)$$

where \mathbf{T} is the unit vector in the direction of $d\mathbf{X}$, such that $d\mathbf{X} = \mathbf{T}dS$.

Infinitesimal strain theory

The infinitesimal strain theory is a mathematical approach that relies on the assumption that the displacements of the material particles of a body are much smaller compared to the body's size. In other words, the geometry of the body is assumed unchanged during the deformation process. Although this may be perceived as inconsistent, brain tissue deformations are very subtle and as such are considered not to change the macroscopic geometry of the brain. This assumption considerably simplifies the equations of continuum mechanics as described in the previous section. The initial and current coordinates of the body can now be assumed to coincide, that is $\mathbf{x} = \mathbf{X} + \mathbf{u} \approx \mathbf{X}$, yielding a simplified expression of the Green-Lagrangian strain tensor, called the *infinitesimal strain tensor*:

$$\begin{aligned}
\mathbf{E} &= \frac{1}{2}(\mathbf{F}^T\mathbf{F} - \mathbf{I}) = \frac{1}{2}((\mathbf{I} + \mathbf{J})^T(\mathbf{I} + \mathbf{J}) - \mathbf{I}) = \frac{1}{2}(\mathbf{J} + \mathbf{J}^T + \mathbf{J}^T\mathbf{J}) \\
&\approx \frac{1}{2}(\mathbf{J} + \mathbf{J}^T) = \boldsymbol{\varepsilon} = \frac{1}{2}(\mathbf{F} + \mathbf{F}^T) - \mathbf{I}
\end{aligned}$$

$$\boldsymbol{\varepsilon} = \begin{pmatrix} \varepsilon_{xx} & \varepsilon_{xy} & \varepsilon_{xz} \\ \varepsilon_{yx} & \varepsilon_{yy} & \varepsilon_{yz} \\ \varepsilon_{zx} & \varepsilon_{xy} & \varepsilon_{zz} \end{pmatrix} \quad (1-9)$$

Here, $\boldsymbol{\varepsilon}$ is the infinitesimal strain tensor, also known as *Cauchy's strain tensor*, that – like \mathbf{E} – is a symmetric tensor. Furthermore, the expressions for stretch and strain can be simplified in the following way

$$\begin{aligned}
\text{Stretch:} \quad \lambda &= \sqrt{1 + 2\mathbf{T}\mathbf{E}\mathbf{T}} \approx 1 + \mathbf{T} \cdot \boldsymbol{\varepsilon} \cdot \mathbf{T} & 0 < \lambda < \infty \\
\text{Strain:} \quad \varepsilon &= \sqrt{1 + 2\mathbf{T}\mathbf{E}\mathbf{T}} - 1 \approx \mathbf{T} \cdot \boldsymbol{\varepsilon} \cdot \mathbf{T} & -1 < \varepsilon < \infty
\end{aligned} \quad (1-10)$$

The assumption of small strains makes it possible to simplify the stretch tensor \mathbf{U}

$$\begin{aligned}
\mathbf{u} &= \sqrt{\mathbf{F}^T\mathbf{F}} = \sqrt{(\mathbf{I} + \mathbf{J})^T(\mathbf{I} + \mathbf{J})} = \sqrt{\mathbf{I} + \mathbf{J} + \mathbf{J}^T + \mathbf{J}^T\mathbf{J}} \\
&\approx \sqrt{\mathbf{I} + \mathbf{J} + \mathbf{J}^T} \approx \mathbf{I} + \frac{1}{2}(\mathbf{J} + \mathbf{J}^T) = \mathbf{I} + \boldsymbol{\varepsilon}
\end{aligned} \quad (1-11)$$

Strain invariants

Certain scalar quantities derived from the strain tensor give the same result regardless of the orthonormal coordinate system used to represent the strain tensor. These scalar quantities are called *strain invariants*, of which several exist. Yet, not all of these quantities have a straightforward physiological interpretation. Here, we introduce two invariants. The most commonly used strain invariant is the *volumetric strain* ε_v (see Figure 1-8a). For the infinitesimal strain approximation, the volumetric strain is the trace of $\boldsymbol{\varepsilon}$:

$$\varepsilon_v = \text{tr}(\boldsymbol{\varepsilon}) = \varepsilon_{xx} + \varepsilon_{yy} + \varepsilon_{zz} \quad (1-12)$$

The volumetric strain can be regarded as a direct measure for blood volume pulsations. As blood flows into the brain, the net volume increase due to the rise in microvascular blood is represented by an increase in volumetric strain (see Figure 1-8a). However, it may also happen that a voxel deforms while its net volume remains unchanged. To quantify the behavior of volume preserving deformation, we use the octahedral shear strain ε_{oss} (see Figure 1-8b) [98]

$$\varepsilon_S = \frac{2}{3} \sqrt{(\varepsilon_{xx} - \varepsilon_{yy})^2 + (\varepsilon_{xx} - \varepsilon_{zz})^2 + (\varepsilon_{yy} - \varepsilon_{zz})^2 + 6(\varepsilon_{xy}^2 + \varepsilon_{xz}^2 + \varepsilon_{yz}^2)} \quad (1-13)$$

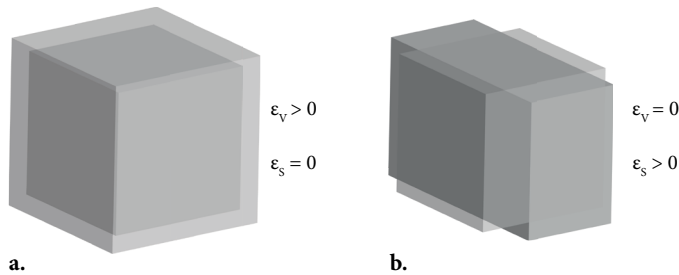


Figure 1-8 Example demonstrating the concepts of volumetric strain and shear strain. Isotropic swelling (a) results in increased volumetric strain without inducing shear strain. Isovolumic deformation (b, preserving its volume) yields non-zero octahedral shear strain.

AIM AND OUTLINE OF THE STUDY

The aim of this study is to introduce non-invasive *in-vivo* MRI methods that quantitatively map brain tissue pulsations from physiological animators such as heartbeat and respiration. Such MRI methods will allow clinical investigations to assess the impact of disease and physiological processes on the properties of the brain tissue and vasculature.

PC-MRI and DENSE have both been used in the past to measure brain tissue motion [58; 70; 140]. Strain measurements can be inferred from these motion field maps, yet this involves the use of spatial derivatives which amplifies the noise present in these maps. Even at 7T, strain measurements remain corrupted by noise, which requires averaging over large ROIs [1; 70]. The aim of **Chapter 2** was to investigate which motion encoding method yields the highest signal to noise ratio (SNR) in the motion field maps. To this end, we described the SNR behavior of PC-MRI and DENSE and compared their performance using computer simulations. For DENSE, the simulated SNR behavior was validated with phantom measurements.

It is currently unclear whether brain tissue deformation is dominated by cardiac or respiratory cycles. **Chapter 3** aims to unravel cardiac- and respiration-induced brain tissue deformations by introducing a single-shot DENSE sequence and a linear model that uses the physiological information regarding heartbeat and respiration. By using this dedicated linear model, initial entangled cardiac and respiratory contributions to the motion encoded in the snapshot images are unraveled.

Chapter 4 uses the results of Chapter 2 and Chapter 3 to build an SNR-optimized sequence that can capture the cardiac-induced strain tensor on a voxel-wise level. The 2D single-shot DENSE sequence from Chapter 3 is extended to be compatible with a simultaneous multi-slice acquisition approach, that can acquire data with full brain coverage. By acquiring multiple DENSE

series with different acquisition orientations and encoding directions, the 3D strain tensor is reconstructed.

Chapter 5 represents the Mosso experiment in modern days, where brain pulsations are measured in a patient with a partially removed cranial vault. Unlike the Mosso experiment, we did not pose any task upon the patient. Yet, we present a first ever case study showing that our method as developed in Chapter 4 is capable to detect abnormalities in cardiac-induced brain tissue deformation on an individual level.

Thus far the focus has been on brain tissue deformation as such. Yet, brain tissue deformation is considered to propel CSF around the brain [101; 141]. In **Chapter 6** we take a first step to assess the relation between tissue deformation and interstitial fluid flow. To this end, we illustrate how DENSE can be harnessed to simultaneously measure brain tissue strain and the apparent diffusion coefficient (ADC) variation over the cardiac cycle, which shows that DENSE can also be regarded as a diffusion sequence. The DENSE magnitude data provides the information on ADC, which we correct for artificial ADC variations arising from tissue deformation. Given that the artificial ADC variation is relatively small compared to the measured ADC variation, this chapter suggests that strain indeed is related to accelerated mixing of interstitial fluids.

Finally, **Chapter 7** provides the summary, general discussion and conclusion.



2

Comparing PC-MRI with DENSE for accurate brain tissue strain measurements

J.J. Sloots
J.J.M. Zwanenburg

*Based on
Proc. Intl. Soc. Mag. Reson. Med. 27, 2019*

ABSTRACT

Magnetic Resonance Imaging (MRI) is a powerful, non-invasive technique that provides motion encoding techniques to obtain tissue motion field maps. Brain tissue deformations as induced by physiological animators are very subtle and involve strains of typically less than 1%. Therefore, accurate measurements of motion field maps are crucial, especially as the required spatial derivatives amplify the noise present in these maps. Yet, in this regime of very small motion, the performance and sensitivity of the motion encoding techniques provided by MRI are unknown. In this work, we consider two MRI motion encoding techniques: PC-MRI and DENSE. For both techniques, we optimize the signal to noise ratio (SNR) in the motion field maps by using simulations. In optimizing the SNR, we use the assumption of small strains to solve phase aliasing that arises from increased motion sensitivity. Simulations showed that DENSE holds the best potential to study brain tissue strains in the brain. We therefore performed SNR simulations for repeated DENSE measurements and substantiated these simulations with measurements obtained in a phantom. We also tested the optimized settings in one volunteer and found a factor of 1.6 SNR increase compared to previously reported experiments. The optimized DENSE sequence thereby shows its potential for voxel-wise assessment of brain tissue strains in humans.

INTRODUCTION

Variations in blood pressure and blood volume induce pulsatile brain tissue deformations. These blood volume variations are mainly induced by cardiac and respiratory cycles, of which the cardiac cycle recurs with the highest frequency. Vasomotion is another recently proposed potential driver of blood volume variation in the brain [162]. Vasomotion refers to spontaneous arterial diameter fluctuations initiated by vascular smooth muscle cells that occurs at a frequency of approximately 0.1 Hz, which is even lower than respiration frequencies. Brain tissue deformations reflect the interplay of local blood volume change in the microvasculature and tissue properties such as stiffness. Moreover, these tissue deformations are considered one of the main drivers for the drainage of cerebral waste [101]. Brain tissue deformation is therefore an important physiological process to assess.

Despite these important implications, a large proportion of studies investigating brain clearance is performed in rodents. Limited non-invasive methods are available to study brain dynamics in humans. Tissue deformation, however, can be obtained from motion field maps by computing the spatial derivatives. Magnetic resonance imaging (MRI) is a powerful and non-invasive technique, that provides methods to obtain these motion field maps. Here we consider two methods: Phase-Contrast MRI (PC-MRI) [104; 143; 144] and Displacement Encoding with Stimulated Echoes (DENSE) [5]. Both techniques use motion sensitizing gradients that manipulate the MRI phase signal such that it becomes proportional to motion.

PC-MRI is commonly used to measure flows of blood and CSF [28]. The sequence employs two consecutive motion sensitizing gradients, thereby recording the motion over small time intervals resulting in velocity measurements. Soon after its introduction, Greitz et al. used PC-MRI to obtain early observations of the tissue pulsations in the brain [58]. In their study, Greitz et al. implemented PC-MRI using a spin-echo acquisition approach to reduce geometric distortions from field inhomogeneities. The spin-echo acquisition also ensured that the signal would decay with T_2 instead of T_2^* . Since then, many MRI hardware improvements have been developed, which lead to increased gradient performance that significantly reduced the echo time. Therefore, PC-MRI is now normally used in conjunction with a gradient echo acquisition instead of spin-echo [7; 36].

DENSE was initially proposed by Aletras et al. in 1999 to obtain motion field maps in the heart [5]. The sequence combines principles of both PC-MRI and cardiac tagging. Tagging sequences modulate the longitudinal magnetization with a cosine (or higher order periodic function), which induces signal voids, visible as stripes in successive MRI magnitude images. magnitude signal by vector fields that induce signal voids. These signal voids are visual as stripes in the acquired signal and move with the tissue as it deforms. By using dedicated post-processing methods, the tissue

deformation can be inferred from these stripes. However, although the technique is capable to track sub-voxel motion, its sensitivity is relatively low and reduces even further for lower spatial resolutions [177]. Instead, the main advantage of DENSE is that the motion sensitivity of the sequence is independent of voxel-size. Compared to PC-MRI, DENSE uses a stimulated echo acquisition mode (STEAM), which enables to separate the motion sensitizing gradients in time during which tissue motion can accumulate. DENSE was already used with a multi-shot 3D acquisition approach to obtain displacement field maps and strain measurements in the human brain [1; 140]. However, the 3D approach sometimes suffered from increasing artifact levels, especially towards the end of the cardiac cycle due to inter-shot phase inconsistencies (see Figure 2-1). These artifacts were especially seen in the Feet-to-Head (FH) direction. To reduce the severity of these artifacts, data was obtained by using sub-optimal (lower) encoding sensitivities. Even then, these artifacts could still be substantial, especially in patients [179].

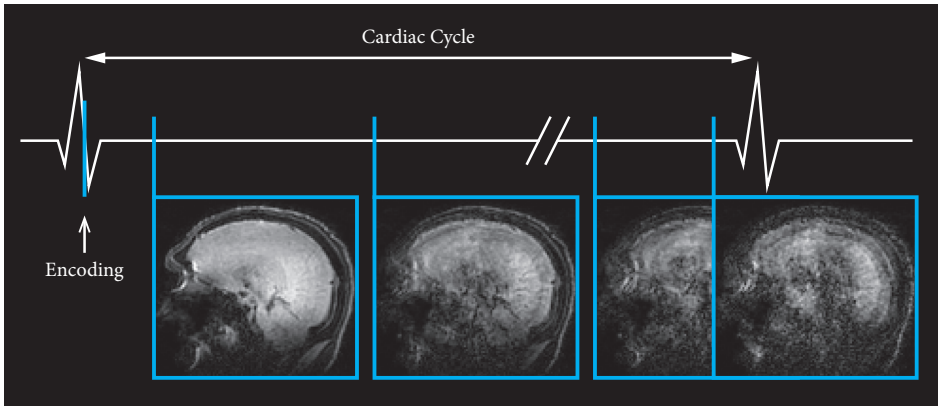


Figure 2-1 DENSE artifact for multi-shot acquisition approaches that arise from phase-inconsistencies across the shots, especially visible at the end of the cardiac cycle. The figure represents the magnitude DENSE images from a DENSE acquisition with encoding in the FH direction, which is the motion encoding direction most prone to show these artefacts. These artefacts are commonly seen in elderly subjects and patients. They are currently mitigated by using reduced motion encoding sensitivity, which obviously is not sufficient, apart from the fact that it reduces the maximally obtainable SNR in the motion maps.

In this work, we propose a single-shot 2D acquisition approach to circumvent phase inconsistencies, avoiding artifacts from increased motion sensitivity. This enables us to optimize for motion sensitivity, without the risk of increased artifacts. The aim of this study was twofold. First, we simulated signal to noise ratio (SNR) of the motion field maps obtained through PC-MRI and DENSE as function of motion sensitivity, to compare the performance of both sequences. We performed these simulations for both a clinical and a pre-clinical setting to investigate the translational capabilities of the methods. Second, we optimized and validated the SNR of the motion field maps obtained through DENSE, which was specifically designed to target contributions from respirations. We chose DENSE to validate in a phantom as the simulations showed

that DENSE holds the best potential to study brain tissue strains in the human brain. Besides, PC-MRI is a well-studied and established technique for which there is a vendor-supplied implementation available, which is used in daily clinical practice. In performing the DENSE simulations, we included effects from the motion encoding sensitivity as well as the signal loss due to diffusion effects from the motion sensitizing gradients. Furthermore, we assumed small tissue strains to solve phase aliasing that arises from increased motion sensitivity. For the DENSE sequence designed to include respiration effects, we also included the optimization of the variable flip angle scheme that was required to obtain multiple measurements from the same 2D slice. Furthermore, we also tested the optimized DENSE sensitivity in one volunteer versus the previously used encoding sensitivity [1; 140].

THEORY

SNR behavior

The SNR of the phase of the MRI signal is related to the SNR of the magnitude by

$$SNR_{\varphi} = \varphi \cdot SNR_M \quad (2-1)$$

where SNR_M is the SNR of the magnitude of the MRI signal and φ denotes the phase (in radians). For a given SNR_M , Eq. 2-1 shows that SNR_{φ} is proportional to φ . For simplicity, we now disregard confounding phase contributions such as from field inhomogeneities and RF phase. (These confounders do not affect the SNR behavior as function of motion sensitivity, and are easily resolved by obtaining acquisitions with motion encoding with opposite polarities and a subsequent subtraction of these two acquisitions.) The phase observed in a PC-MRI motion encoded image depends on the velocity encoding sensitivity (VENC, in meters per second) as well as on the observed velocity v :

$$\varphi = \frac{v}{VENC} \pi \quad (2-2)$$

The observed velocity depends on physiology and cannot be controlled. Therefore, the velocity encoding sensitivity therefore determines the observed SNR in the velocity maps, which is then proportional to

$$SNR_v \propto \frac{1}{VENC} SNR_M \quad (2-3)$$

where SNR_v is the SNR of the velocity map. Increased motion sensitivity yields smaller VENC and requires larger gradients, thereby increasing SNR_v . Yet, at the same time, these larger gradients make the acquisition sensitive to diffusion effects that reduce the SNR of the magnitude image. Consequently, an optimal VENC exists, which depends on the diffusion coefficient of the tissue.

DENSE can be regarded as a PC-MRI sequence, for which the time between the motion encoding gradients have been extended (see Figure 1-4). The motion sensitivity of the DENSE sequences

are characterized by a *displacement* encoding (DENC in meters), which approximately relates the VENC by:

$$\text{DENC} \approx \text{VENC} \cdot \text{TM} \quad (2-4)$$

To obtain the exact VENC of the sequence, the first order moment has to be computed over the motion sensitizing gradients. The first order moment is related to the VENC by [20; 112]

$$\text{VENC} = \frac{1}{2 \cdot \gamma \cdot M_1} \quad (2-5)$$

where γ is the gyromagnetic ratio, which depends on the nucleus for imaging (for hydrogen nuclei: $42.58 \text{ MHz} \cdot \text{T}^{-1}$). The first order gradient moment M_1 is obtained by the time-integral over the motion sensitizing gradients

$$M_1 = \int G(t) \cdot t \, dt \quad (2-6)$$

where G is the gradient strength at each time t .

In general, the SNR in the magnitude of the MRI signal depends on the relaxation of the longitudinal magnetization between excitations (T1 relaxation) as well as the echo time (TE). The stimulated echo acquisition mode (STEAM) employed by DENSE ensures that signal loss during the time between the motion sensitizing gradients (mixing time, TM) is predominantly proportional to T1, and decays with T2 as function of the TE [49]. For a gradient echo PC-MRI sequence the signal decays with T2*, which is much faster. However, the STEAM intrinsically distributes the available magnetization over the stimulated echo and stimulated anti-echo. Because only the a single echo can be acquired at a time, the MRI magnitude signal of this echo is reduced by a factor of 2. In this work, we consider the simple case where the excitation angle for both PC-MRI and DENSE is 90 degrees, so that all magnetization is utilized to acquire the single-shot image. Consequently, the magnetization is zero after each acquisition time and recovers over the repetition time (TR). Then, the SNR in the magnitude image of PC-MRI and DENSE can be described as follows:

$$\text{PC-MRI: } \text{SNR}_M = \left(1 - \exp\left(-\frac{\text{TR}}{\text{T1}}\right) \right) \cdot \exp\left(-\frac{\text{TE}}{\text{T2}^*}\right) \cdot \exp(-b \cdot D) \quad (2-7)$$

$$\text{DENSE: } \text{SNR}_M = \frac{1}{2} \cdot \left(1 - \exp\left(-\frac{\text{TR}}{\text{T1}}\right) \right) \cdot \exp\left(-\frac{\text{TE}}{\text{T2}^*}\right) \cdot \exp(-b \cdot D) \cdot \exp\left(-\frac{\text{TM}}{\text{T1}}\right) \quad (2-8)$$

Here, D is the tissue-specific diffusion coefficient and TM is the mixing time of the DENSE sequence. The diffusion weighting induced by the motion sensitizing gradients is described by b (in s/mm^2). For ordinary trapezoid shaped gradients, the diffusion weighting of the motion sensitizing gradients is described by [146]

$$b = \gamma^2 G^2 \left[\delta^2 \left(\Delta - \frac{\delta}{3} \right) + \frac{\xi^3}{30} - \frac{\delta \xi^2}{6} \right] \quad (2-9)$$

where δ is the effective duration of the gradient (in ms), ξ is the rise time (in ms) and Δ is the diffusion time (i.e. time between the motion sensitizing gradients). For DENSE, Δ is equal to the

TM. A full visualization of the timing parameters of the motion-sensitizing gradients is provided in Chapter 6, Figure 6-1.

Sequence optimization and strain measurements

Deformation of tissue can be assessed by the relative displacement of neighboring voxels, which results in strain. Local stretch is signified by positive strain, while shortening of tissue results in negative strain. The one-dimensional (1D) strain ε is simply the change in length of a line segment L and defined to give the relative change in length of the line segment during deformation

$$\varepsilon = \frac{L' - L}{L} = \frac{\Delta L}{L} \quad (2-10)$$

where L is the original length of the line segment and L' is the length of the line segment after deformation. The strain is calculated from motion field maps by applying spatial derivatives. Given Δx , the voxel size along x , we can define the 1D strain in that direction as

$$\varepsilon_{xx}(n) \stackrel{\text{def}}{=} \frac{m_x(n+1) - m_x(n-1)}{2\Delta x} \quad (2-11)$$

Accurate measurements of the motion field maps are crucial, since the computation of spatial derivatives amplifies noise present in these maps. Larger encoding gradients yield an increased motion sensitivity (smaller VENC), yet, at the same time increase the number of phase wraps present in the images. Fortunately, strain computations allow for straightforward unwrapping under the assumption of small strains, as any phase wrap in the original image yields unlikely high strain values (see Figure 2-2). A phase wrap causes a large numeric derivative $\Delta\phi$, which can be resolved by adding or subtracting 2π to $\Delta\phi$ to bring it closer to zero if

$$|\Delta\phi| > 1.5\pi = \Delta\phi_{max} \quad (2-12)$$

For DENSE, the maximum tolerated numeric derivative $\Delta\phi$ relates to the maximum tolerated strain by

$$\varepsilon_{max} = \frac{\Delta\phi_{max}}{2\Delta x} \frac{D_{enc}}{\pi} = 0.75 \frac{D_{enc}}{\Delta x} \quad (2-13)$$

where ε_{max} is the maximum tolerated strain. A similar relation holds for PC-MRI, where the maximum tolerated numeric derivative $\Delta\phi_{max}$ is related to the maximum strain *rate* εr_{max} by VENC:

$$\varepsilon r_{max} = 0.75 \frac{VENC}{\Delta x} \quad (2-14)$$

Either way, as long as the expected strains in the brain do not exceed ε_{max} or εr_{max} , there are no additional constraints for the encoding sensitivity.

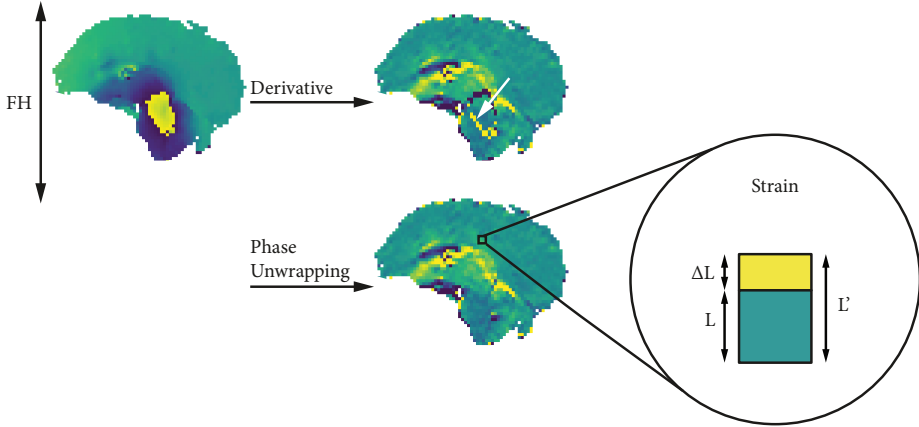


Figure 2-2 Principle of strain unwrapping illustrated with an example 2D slice with sagittal orientation. On the left, a displacement map is shown obtained through DENSE with FH displacement encoding. Taking the straightforward derivative of the displacement map in the FH direction yields the one-dimensional FH strain map, shown in the top-right corner. In this map, phase wraps are visible (indicated by the white arrow). These phase wraps can be resolved by assuming small strains (Eq. 2-12). All strain values which absolute value is larger than ϵ_{\max} are then solved by adding or subtracting 2π to $\Delta\phi$ to bring the strains closer to zero, which results in a smooth map shown in the bottom-left corner. For $DENC = 0.12$ mm and $\Delta x = 3$ mm, ϵ_{\max} is 3%, well over the expected strains in the brain.

Repeated DENSE measurements

In Section *SNR behavior* we assumed an excitation angle of 90° , so that all encoded magnetization was used to create the image. In the current situation, we encode the relaxed magnetization with DENSE and then create multiple images from a single encoding. Figure 2-3 shows a specific example, where each repeated scan consist of two cardiac cycles. Encoding is performed at the beginning of the first cardiac cycle, after which the 2D slice is decoded 3 times in the second cardiac cycle, resulting in 2D images of 3 cardiac phases. In order to obtain a stable signal across all acquired images, a variable flip angle sweep is employed [45]. Once the final flip angle of the sweep has been determined, all other flip angles can be calculated as well. We incorporate the choice for the final flip angle in our optimization. The optimal final flip angle depends on the T1 of the tissue. A larger final flip angle increases the excited signal, but prevents regrowth of magnetization for the next scan. For the optimization, we separate the part of the longitudinal magnetization containing the encoded information, Q_E (which forms the stimulated echo), from the part of the longitudinal magnetization that has relaxed after the application of the encoding, Q_R (see Figure 2-3). The encoded component of the longitudinal magnetization just before the RF excitation pulse of the k^{th} heart phase image was derived by Fischer et al. as [45]

$$Q_{E_k} = M_{ss} \text{ENC}(x,y) \exp\left(-\frac{t_k}{T_1}\right) \exp(-b_k \cdot D) \prod_{j=0}^{k-1} \cos(\alpha_j) \quad (2-15)$$

which we adapted to include the diffusion factor. The relaxed magnetization can be recursively written as

$$Q_{R_k} = (Q_{R_{k-1}} = \cos(\alpha_{k-1}) - M_0) \exp\left(-\frac{(t_k - t_{k-1})}{T_1}\right) + M_0 \quad (2-16)$$

In these equations, M_{ss} is the steady state magnetization just prior to tagging, ENC is the encoding function, t_k is the time of the k^{th} heart phase after encoding, α_j is the flip angle for heart phase

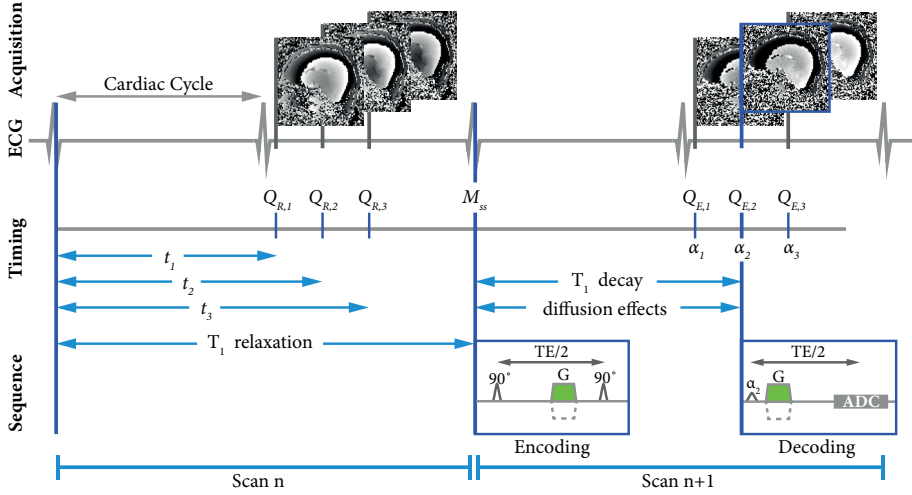


Figure 2-3 Schematic representation of the DENSE sequence, covering two repeated scans and four cardiac cycles. The longitudinal magnetization consists of two parts, which we indicate here selectively to show their relationship. The first part contains relaxed magnetization after tagging, Q_R (indicated in scan n), which is available for tagging in the next scan. The second part contains tagging information, Q_E (indicated in scan $n+1$), which forms the stimulated echo. In each scan, the cardiac phases are acquired during the second cardiac cycle to increase respiration induced motion. Decoding gradients are applied before each readout (green gradients). Inverting G was inverted between scans (dashed lines), to allow distinguishing phase errors from motion.

j (α_0 is 0), b_k the effective diffusion weighting at t_k , and T_1 and D are the relaxation time and diffusion coefficient of the tissue under consideration, respectively.

METHODS

Simulation of PC-MRI and DENSE

Both the clinical and pre-clinical setting were considered at a field strength of 7T. Tissue constants of $T_1 = 1200$ ms and $D = 0.8 \cdot 10^{-3}$ mm²/s were used, equal to white matter properties of the human brain at 7T [66; 130]. The T_1 and diffusion coefficient of white matter was chosen as this has a shorter T_1 than gray matter and, thus, faster decay of the encoded magnetization. There-

fore, the main difference between the clinical and pre-clinical setting was only the difference in physiology of a human and a rodent, as well as scanner performance. For a human, a typical RR interval of 1000 ms (60 bpm) was taken, whereas the RR interval of the rodent was considered to be 200 ms (300 bpm, which is representative for rats). The gradient performance for the clinical setting was set equal to the 7T MRI scanner (Philips, Best, The Netherlands) of our institution: gradient strength and slew rate of 40 mT/m and 200 T/m/s, respectively. For the pre-clinical scanner, the performance was set to 660 mT/m and 9200 T/m/s, respectively, which corresponds to the pre-clinical 7T MRI scanner in the Dijkhuizen lab. For both settings, the TE was set as the time required by the motion sensitizing gradients plus 5 ms to reach the central echo (k0) of the EPI readout. SNR in the motion field maps for both PC-MRI and DENSE were simulated as function of motion encoding sensitivity. To this end, Eq. 2-7 and 2-8 were each substituted in Eq. 2-3 to obtain a direct expression for the SNR in the motion field maps, while the respective b-values for the various motion encoding sensitivities were computed from Eq. 2-9, always using the maximally available gradient strength.

A main difference of DENSE compared to PC-MRI is that DENSE applies a non-selective encoding preparation, which prevented regrowth of magnetization. The repetition time of the sequence was therefore extended with an additional cardiac interval. In Chapter 4, we used this DENSE approach to acquire motion field maps with full brain coverage, where we used different mixing times for slices to cover the complete cardiac cycle. We separated the slices in two packages, each acquired during a separate cardiac cycle. As a result, relaxation per slice was limited to one RR interval. Because PC-MRI encodes tissue directly after a single slice-selective excitation pulse,

	Clinical setting	Pre-clinical setting
RR interval (ms)	1000	200
T1 (ms)	1200	1200
D ($10^{-3} \text{ mm}^2/\text{s}$)	0.8	0.8
TM 1 (ms)	250	50
TM 2 (ms)	750	150
Grad. strength (mT/m)	40	660
Grad. slew rate (T/m/s)	200	9200

Table 2-1 Complete overview of scan parameters for the clinical and pre-clinical setting, used for simulation of a single slice acquisition. Main difference between clinical and pre-clinical setting is reflected in physiological properties (e.g. RR interval and mixing times) and scanner gradient performance (e.g. gradient strength and slew rate). Tissue constants and relaxation times were constant for both settings. Relaxation times were set to 2000 ms and 1000 ms for PC-MRI and DENSE, respectively, to account for the differences which are realistic for use with an acquisition scheme with whole brain coverage (see Chapter 4).

relaxation starts immediately and is not affected thereafter. Here, we set T_{relax} to 2 s and 1 s for PC-MRI and DENSE, respectively, to reflect this main difference in relaxation between excitations. Furthermore, we evaluated the effect of the mixing time by simulating TMs of both 25% and 75% of the cardiac interval length. A complete overview of the parameters for simulation is provided in Table 2-1.

Simulation and validation of repeated DENSE measurements

Simulations of the repeated DENSE measurements were performed by implementing the formula's from Eq. 2-13 and 2-14 in MATLAB R2018b. All combinations of DENC factors (range: 0.05-0.35 mm) and α_{max} (range: 5-90 degrees) were simulated for a spherical phantom filled with 2% agar gel ($T_1 = 1700$ ms, $D = 1.9 \cdot 10^{-3}$ mm²/s). Simulations were verified in the phantom for which we used a multi-shot 3D EPI imaging protocol with imaging parameters: EPI factor: 19; SENSE factor: 2.6×2.5 (AP \times RL); resolution: $3 \times 3 \times 3$ mm³; FOV: $150 \times 150 \times 150$ mm³; TR: 2000 ms; and TE/2: 15 ms. Two phantom measurement series were performed: one for a static DENC = 0.45 mm and varying α_{max} and the other for static $\alpha_{max} = 45^\circ$ and varying DENC. The 3D multi-shot EPI acquisition was performed to obtain a larger volume to compare SNR behavior with the simulations. This was possible because the phantom did not move and therefore showed no phase inconsistencies. In comparing the actual measurements to the simulations, we scaled the measurements by a single scaling factor for the unknown noise level in the measurements, which depend, amongst others, on the receive coil sensitivity.

Additional validation was performed in one volunteer (male, age 27 years). Here, the cardiac triggered, 2D single-shot DENSE sequence as previously described (Figure 2-3), was applied. A key feature included mixing times extended with one cardiac cycle to make the sequence more sensitive for respiration induced motion contributions. Simulations showed optimal settings of DENC = 0.15 mm and $\alpha_{max} = 50^\circ$ (white matter: $T_1 = 1200$ ms, $D = 0.8 \cdot 10^{-3}$ mm²/s at 7T [66; 130]). Written informed consent was obtained in accordance with the Ethical Review Board of our institution. Two datasets were obtained: one with a displacement sensitivity DENC of 0.35 mm as was previously used in multi-shot approaches for the FH encoding direction [1; 140], and one with the theoretically optimal DENC of 0.15 mm. Other scan parameters of the single-shot acquisition were: EPI factor: 33; SENSE factor: 2.5 (AP); resolution: $3 \times 3 \times 3$ mm³; FOV 250×250 mm²; TR: 2 RR intervals; TE/2: 12 ms and EPI band width in the readout/phase encoding direction; 3.7 kHz/pixel; 62 Hz/pixel.

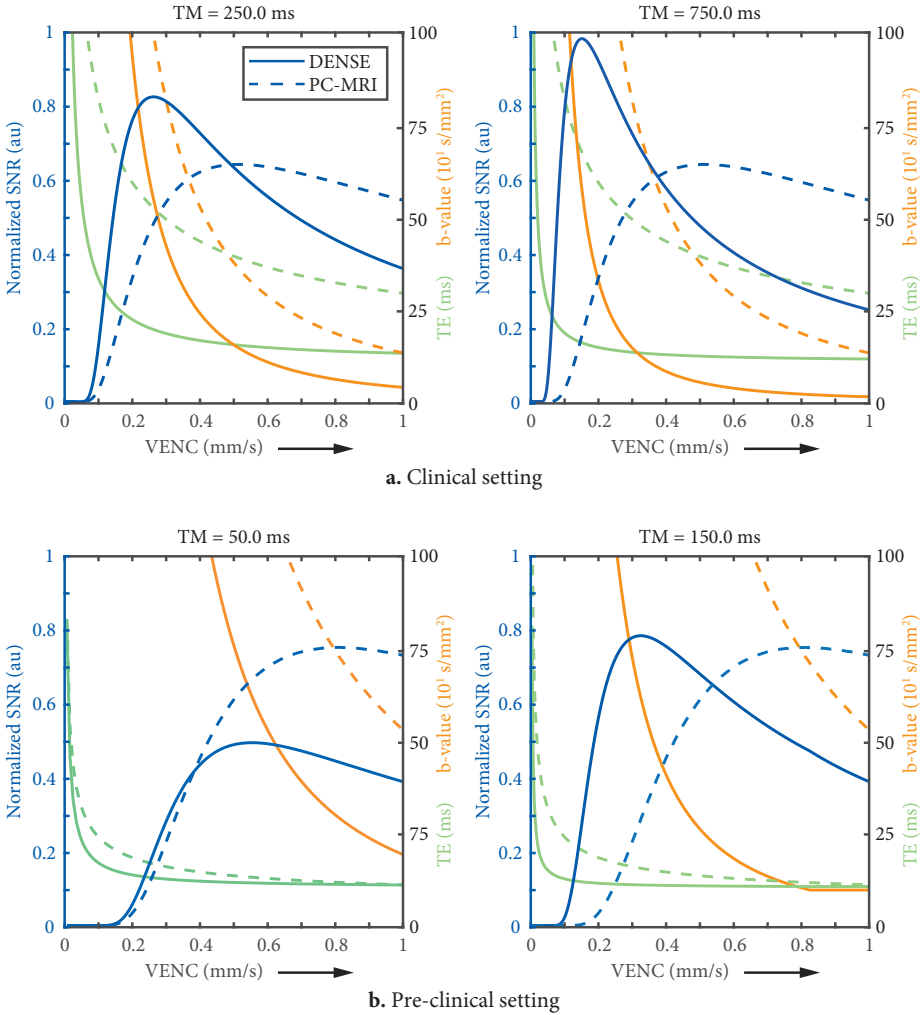


Figure 2-4 Simulation results for SNR in motion field maps for clinical and pre-clinical setting. SNR curves (blue) are normalized to range between 0 and 1 and can be compared between the clinical and pre-clinical setting. Echo times (TEs, green) and diffusion weighting (b-values, orange) are provided as well, with scaling along the y-axis provided at the right hand side of each graph. Scaling ranges between 0 and 100 ms for TEs and 0 and 1000 s/mm² for b-values. Motion encoding sensitivities between PC-MRI and DENSE are harmonized using VENC values. These VENC values can be multiplied with TM to obtain an approximation for the equivalent DENC values (see Eq. 2-4). Figure 2-4a (top row) represents the clinical setting, with simulated mixing times (TM) for the DENSE sequence of 250 ms and 750 ms, representative for peak systole and mid diastole of the human heartbeat, respectively. Figure 2-4b (bottom row) shows the results for the pre-clinical setting, with DENSE TM of 50 ms and 150 ms, representative for peak systole and mid diastole of the heartbeat of a rat, respectively. For the clinical setting, DENSE shows a clear advantage compared to PC-MRI. Especially for longer TM, DENSE has increased SNR. This advantage, however, evaporates when TM becomes very short, as is the case for the pre-clinical setting. Here, PC-MRI and DENSE perform comparably, with an advantage for PC-MRI at TM = 50 ms.

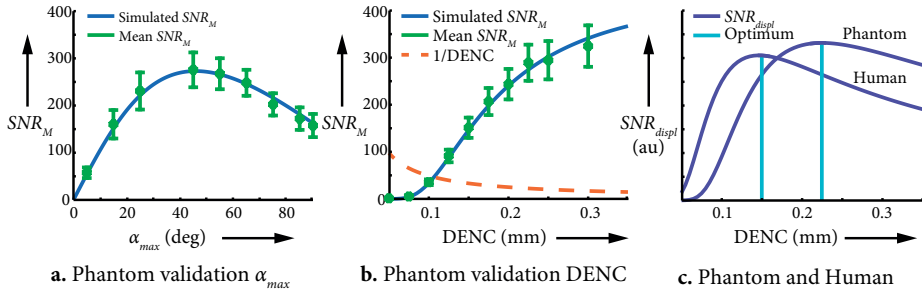


Figure 2-5 Signal to noise ratio of the magnitude image (SNR_M) and displacement map (SNR_{disp}) with error bars indicating the standard deviation. Figure 2-5a and 2-5b present simulated SNR_M with the SNR_M observed in the phantom. The simulated SNR line was linearly scaled to match the measured SNR_M in the phantom. The results show that the course of the line matches the measured SNR behavior. Figure 2-5c shows the simulated SNR_M divided by the displacement encoding (DENC), which yields the SNR in the displacement map. The optimum is shown for both the phantom and white matter in humans at 7T. The figure is adapted from Chapter 3.

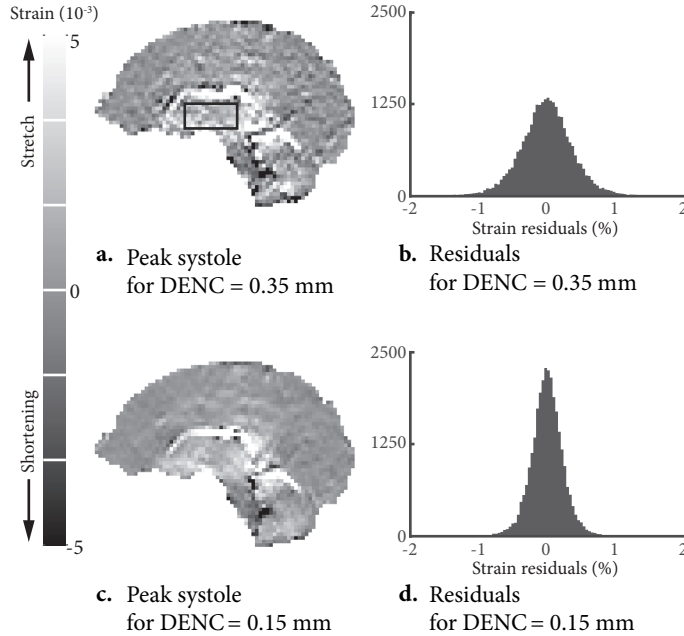


Figure 2-6 Strain maps in the Feet-to-Head direction acquired in the volunteer together with the residuals obtained after subtraction of the mean. The area as indicated in Figure 2-5a represents the region for which the mean strain and residuals were analyzed. Displacement encoding was DENC = 0.35 mm (top row) and DENC = 0.15 mm (bottom row), for which the cardiac related strain was $2.2 \pm 1.46\%$ and $2.1 \pm 1.03\%$, respectively. The distribution of the residuals for DENC = 0.35 mm and DENC = 0.15 mm had a standard deviation of $\sigma = 4.01 \cdot 10^{-3}$ and $\sigma = 2.42 \cdot 10^{-3}$, respectively. From the standard deviations, an SNR increase of 1.66 can be inferred.

RESULTS

Comparing PC-MRI and DENSE simulations

The results from computer simulations on the SNR in the motion field maps obtained through PC-MRI and DENSE are presented in Figure 2-4. Echo times (TE) of the sequences are indicated as well. The clinical setting (Figure 2-4a) shows that DENSE outperforms PC-MRI, especially when TM increases, which yields larger first order moments for DENSE. For the pre-clinical setting (Figure 2-4b), PC-MRI outperforms DENSE, however, the difference becomes less apparent as TM increases. Furthermore, PC-MRI shows some increase in performance for the pre-clinical setting, with its optimum shifting towards a larger VENC.

Simulation and validation of repeated DENSE measurements

Phantom validation

We found SNR_M to be consistent with computer simulations for both a variable final flip angle α_{max} and encoding sensitivity DENC (see Figure 2-5a and 2-5b, respectively). The simulated SNR in the displacement fields (SNR_{displ}) for both the phantom and white matter is shown in Figure 2-5c as a function of displacement encoding. All sequence dependent SNR behavior not related to DENC or α_{max} (e.g. coil array sensitivity, B1 effects etc.) is represented in a linear scaling parameter to match the simulated SNR_M curve with the measured SNR_M with the SNR_M from the phantom.

In-vivo validation

Imaging was successful in our volunteer; 59 of the 60 repeated scans could be used for analysis in both experiments. One scan was omitted due to false ECG triggering. Consistent cardiac-induced strain maps were obtained for both encoding sensitivities, which are presented in Figure 2-6. Residuals from averaging were obtained from the region of interest (ROI) indicated in Figure 2-6a. The distribution of the residuals are presented in Figure 2-6b and 2-6d, and show a reduced standard deviation for DENC = 0.15 mm compared to DENC = 0.35 mm ($\sigma = 2.4 \cdot 10^{-3}$ and $\sigma = 4 \cdot 10^{-3}$, respectively). This implies an SNR increase of 1.66.

DISCUSSION

In this work, we simulated the behavior of SNR in motion field maps obtained through PC-MRI and DENSE. We found that DENSE outperforms PC-MRI in a clinical setting, especially when mixing times increase. Furthermore, we validated simulations of repeated DENSE measurements in a phantom. We used these validated simulations to optimize the DENSE settings and tested these settings in a healthy volunteer. We found a factor of 1.66 SNR increase compared to the

motion encoding sensitivity as reported in previous experiments [1; 140]. The optimized DENSE sequence thereby shows its potential for voxel-wise assessment of brain tissue strains in humans.

The single-shot approach was a key feature to optimize the motion sensitivity for strain measurements, as it abolishes the risk for artifacts as are observed with multi-shot approaches [1; 140]. We think that the single-shot approach is especially an advantage for the DENSE sequence, as DENSE generally has longer times between the motion sensitizing gradients compared to PC-MRI, which provides more time for phase inconsistencies to accumulate. Since time between the motion sensitizing gradients in PC-MRI is generally much shorter, future studies should investigate whether a combination of PC-MRI with a multi-shot acquisition holds potential for brain tissue strain measurements. Similar 3D multi-shot PC-MRI studies have already been performed, yet these studies use the minimum VENC of 1 cm/s made available by the vendor [48; 56]. Lower VENC may be limited due to hardware constraints. Here it should be mentioned that we did not take into account limitations from the gradient duty cycle. If multiple acquisitions are obtained consecutively, gradient duty cycles may limit temporal resolution or motion sensitivities because PC-MRI applies two motion sensitizing gradients for each excitation pulse. This is in contrast to DENSE, which applies a non-selective encoding gradient, after which only one gradient is applied for each excitation pulse.

A second important aspect of the successful optimization of the DENSE method was to take into account the diffusion effects. These effects cause the SNR to degrade when the motion sensitivity increases (lower VENC). For the pre-clinical setting, gradient performance increased, which resulted in increased maximum SNR for the PC-MRI sequence due to a shorter TE. Yet, at the same time, the SNR degraded faster at lower VENC compared to the clinical setting. The results showed that this was caused by enhanced diffusion effects. Let us assess the relationship between the first order moment and the diffusion weighting by considering two gradients for different gradient performance,. Here, we start from Eq. 2-5 and substitute the different gradient performances that relates as $G_{max,1} = a \cdot G_{max,2}$. The boundary condition is to obtain equal M_1 (i.e. equal VENC) for both gradients in the shortest time possible. For simplicity, we consider these gradients to be of rectangular shape. We then obtain the relation:

$$\begin{aligned} G_{max,1} \cdot \delta_1^2 &= G_{max,2} \cdot \delta_2^2 \\ \delta_1 &= \frac{1}{\sqrt{a}} \cdot \delta_2 \end{aligned} \quad (2-17)$$

where δ (in ms) is the duration of each gradient. To determine the diffusion weighting (b-value) we have from Eq. 2-8:

$$b \propto G^2 \cdot \delta^3 \quad (2-18)$$

and substituting 2-17 in 2-18 we obtain

$$b_1 = (G_{max,1})^2 \cdot \delta_1^3 = a^2 \cdot (G_{max,2})^2 \cdot \frac{\delta_2^3}{\alpha \sqrt{\alpha}} = \sqrt{\alpha} \cdot b_2 \quad (2-19)$$

From Eq. 2-19 it can be inferred that for an increased gradient performance of factor α , the associated b-value for a given VENC at shortest TE increases with factor $\sqrt{\alpha}$. Although the derivation of the relationship between gradient performance, M_I and diffusion is simplistic, it illustrates that there exists an optimum where increasing gradient performance will not reduce TE sufficiently to compensate for the loss in SNR due to a higher b-value. The tradeoff between TE and gradient performance needs to be considered especially in pre-clinical settings, where gradient performance is generally higher. Furthermore, the relation between M_I and diffusion weighting shows that one can in principle obtain any diffusion weighting for a given VENC, provided the availability of unlimited gradient performance. This shows why DENSE is so successful at increased TM, which actually reduces diffusion weighting for constant M_I . Furthermore, the results suggest that using lower G_{max} (but maximum slew rate) might allow for further optimization. This is expressed by Eq. 2-9, which shows that the diffusion weighting is proportional to G^2 and decreases with δ^3 (for constant Δ). Consequently, reduced gradient performance (G reduces, δ increases) for constant TM might increase SNR, as long as longer TE does negate these effects.

The simulations presented in this work are representative for constant strain rates only. Particularly PC-MRI relies on this assumption. While results from DENSE can be interpreted as net displacements accumulated between the motion sensitizing gradients, regardless of trajectory, PC-MRI requires multiple acquisitions to capture the entire trajectory, and needs subsequent integration to obtain the net result. This might lead to cumulative errors, especially as the lowest temporal resolution of PC-MRI is worse than that for DENSE, given that each PC-MRI acquisition requires two gradients, while DENSE only requires one decoding gradient. Moreover, large gradients are accompanied by increased eddy currents, which induce confounding phase errors. These errors add to a cumulative offset and need therefore to be addressed in dedicated post-processing software. We did not consider how noise in the phase signal propagates in estimating net motions over longer durations, and the resulting effects on the accuracy of strain (rate) measurements. These errors will contribute less to strain (rate) errors as TM increases.

In the assessment of the simulations, it is important to note that we used tissue property values from white matter in humans at 7T, also to simulate SNR behavior in rodents. Furthermore, it remains an open question whether brain tissue strains are similar as observed in humans. This is important, because the SNR in the strain maps are affected by the magnitude of the strains itself. Although the validated repeated DENSE measurements provide confidence in the correctness of the simulations, it is a limitation of this study that we did not validate the comparison between PC-MRI and DENSE by the use of phantom measurements. When motion field maps are desired to compute the tissue strain in a pre-clinical setting, these validation measurements should be obtained to investigate the validity of the simulations. The validation should also determine whether the SNR in motion field maps (whether obtained with PC-MRI or DENSE) is sufficient to acquire these with the high resolution that is common and desired in pre-clinical

MRI research. These preliminary results can help to assess the feasibility to acquire brain tissue strain maps in rodents. In the meantime, DENSE outperforms PC-MRI for the clinical setting, even with favorable conditions used for PC-MRI (such as longer repetition times), which favors the use of the DENSE sequence in humans.

In conclusion, the choice for PC-MRI or DENSE to provide tissue motion field maps for strain computations depends on the setting in which the research is conducted. Although additional validation in phantoms is required, PC-MRI seems to have better performance compared to DENSE in a pre-clinical setting. For a clinical setting, however, DENSE outperforms PC-MRI. We validated the simulations for repeated DENSE measurements and tested the results in a healthy volunteer. The results indicate that the optimized DENSE sequence has potential for voxel-wise assessment of brain tissue strains in humans.



3

Cardiac and respiration-induced brain deformations in humans quantified with high-field MRI.

J.J. Sloots
G.J. Biessels
J.J.M. Zwanenburg

NeuroImage 210, 2020

ABSTRACT

Microvascular blood volume pulsations due to the cardiac and respiratory cycles induce brain tissue deformation and, as such, are considered to drive the brain's waste clearance system. We have developed a high-field magnetic resonance imaging (MRI) technique to quantify both cardiac and respiration-induced tissue deformations, which could not be assessed noninvasively before. The technique acquires motion encoded snapshot images in which various forms of motion and confounders are entangled. First, we optimized the motion sensitivity for application in the human brain. Next, we isolated the heartbeat and respiration-related deformations, by introducing a linear model that fits the snapshot series to the recorded physiological information. As a result, we obtained maps of the physiological tissue deformation with 3mm isotropic spatial resolution. Heartbeat- and respiration induced volumetric strain were significantly different from zero in the basal ganglia (median (25-75% interquartile range): $0.85 \cdot 10^{-3}$ ($0.39 \cdot 10^{-3} - 1.05 \cdot 10^{-3}$), $p = 0.0008$ and $-0.28 \cdot 10^{-3}$ ($-0.41 \cdot 10^{-3} - 0.06 \cdot 10^{-3}$), $p = 0.047$, respectively). Smaller volumetric strains were observed in the white matter of the centrum semi ovale ($0.28 \cdot 10^{-3}$ ($0 - 0.59 \cdot 10^{-3}$) and $-0.06 \cdot 10^{-3}$ ($-0.17 \cdot 10^{-3} - 0.20 \cdot 10^{-3}$)), which was only significant for the heart beat ($p = 0.02$ and $p=0.7$, respectively). Furthermore, heartbeat induced volumetric strain was about three times larger than respiration induced volumetric strain. This technique opens a window on the driving forces of the human brain clearance system.

INTRODUCTION

Cardiac and respiratory cycles induce blood volume changes resulting in subtle brain tissue deformations. These deformations are known to propel the cerebral spinal fluid (CSF) flow which fulfills an important role in the drainage of cerebral waste [101; 141]. Therefore, brain tissue deformation is considered an important driver of the clearance system of the brain [153]. Furthermore, brain tissue deformation affects cellular function. *In-vitro* studies have shown that the arterial waveform is crucial to regulate the formation and function of endothelial cells which constitute the blood-brain barrier [35]. Brain tissue and vessel stiffness naturally change with age [133; 158], which not only plays a role in age-related processes but may also have profound effects on tissue deformation of the brain and, thus, brain homeostasis. Unlike the larger arteries of the brain, the small cerebral vessels themselves are difficult to study *in vivo* with current neuroimaging techniques. This is an important knowledge gap. We hypothesize that the brain tissue deformation is dominated by the microvascular bed embedded in the tissue, and, thus provides a window to the small vessel function. We have developed a method to quantify brain tissue deformation that may form a valuable source of information on small vessel function as driving force in waste clearance, and may also allow for future assessment of the brain's biomechanics during both healthy and diseased state [57].

The dynamic relationship between intracranial blood volume changes, tissue deformation and CSF flow is complex [90]. As the brain's vessels are exposed to blood pressure waves, they swell and stretch elastically, displacing the surrounding tissue. Due to the rise of the intravascular blood volume during systole, the cerebral tissue expands inwards towards the ventricles [43; 58; 143]. Given the fixed intracranial volume as stated by the Monro-Kellie doctrine, the CSF is squeezed out of the brain into the CSF spaces towards the spinal canal to compensate for the additional blood volume [90; 103]. As the blood leaves the brain during diastole, the vessels relax and CSF returns. Similarly, the respiration cycles induce variations in thoracic pressure that cause variations in venous blood volume, which induces tissue deformation and CSF flow as well.

Despite the important role of the cardiac- and respiration-induced brain tissue deformation in the intracranial dynamics, no methods are available to directly assess these deformations. Instead, most studies have focused on CSF and blood flow to assess the intracranial volume dynamics [7; 36]. For instance, Dreha-Kulaczewski et al. used Magnetic Resonance Imaging (MRI) with phase contrast velocity encoding to study CSF flow and found upward CSF flow through the spinal canal during inspiration [39; 40], which they relate to an enhanced venous outflow. Furthermore, T2* weighted blood oxygen level dependent (BOLD) MRI signal fluctuations in the brain have been studied in relation with physiological signals like heartbeat and respiration [21; 81; 122]. These T2* weighted signals, however, are not specific and depend on blood oxygenation levels (spontaneous neuronal activity), inflow of blood and CSF into the slice, and tissue motion. As a

result, $T2^*$ weighted signal variations in the brain are hard to interpret, and only weakly correlate with physiological cycles like heartbeat and respiration [21]. Quantitative measurements of $T2^*$ variation induced by the cardiac cycle have also been reported, either with or without injection of a blood pool contrast agent [129; 163]. These quantitative $T2^*$ measurements are much more specific for blood volume pulsations compared to BOLD MRI, but still did not assess the changes due to respiration. The overall deformation of brain tissue is subtle and involves submillimeter displacements that can be tracked by an MRI technique that is called Displacement Encoding with Stimulated Echoes (DENSE) [5; 45; 126]. The cardiac-gated DENSE method was shown to be capable of capturing the displacement field maps over the cardiac cycle [1; 119; 140]. However, these data were acquired over several minutes, which prohibits to study the respiration-induced tissue motion and deformation.

In the present study, we propose a newly developed DENSE sequence at 7 tesla MRI, dedicated and optimized to disentangle and quantify cardiac and respiratory contributions to brain tissue deformation in humans (Figure 3-1). A key feature is its single-shot approach, which not only is required for unraveling the cardiac and respiratory contributions, but also allows for an optimization of the sequence without introducing additional data artifacts. The main advantage of our sequence is the separate assessment of both cardiac and respiratory tissue strain contributions with high sensitivity, which provides insight into the physiological brain tissue deformations in relatively small regions of interest (ROIs).

MATERIALS AND METHODS

Displacement images are required to derive the tissue deformation and can be provided by the DENSE MRI sequence [1; 5; 45; 138; 140]. DENSE, analogous to phase contrast velocity encoding, manipulates the phase information such that it becomes proportional to the displacement of brain tissue with respect to the point of encoding. The single-shot approach of our sequence captures the momentary physiological ‘state’ of tissue motion. We assume that this physiological ‘state’ of the tissue is an independent, linear combination of the cardiac and respiratory contributions. By repeating the measurements multiple times, we acquired different combinations of states. Next, we use a linear model, together with the associated physiological information, such as cardiac interval position and respiration trace, to disentangle the cardiac and respiratory contributions (Figure 3-1).

DENSE sequence

A cardiac triggered DENSE sequence was designed to measure heart beat and respiration related brain tissue motion (Figure 3-2) [1; 5; 45; 138; 140]. Key features included its 2D single-shot EPI approach to capture the momentary physiological ‘state’ (heart- and respiration induced motion)

and secondly, an additional time-delay of one cardiac cycle between encoding and decoding to make the sequence more sensitive for respiration induced motion contributions.

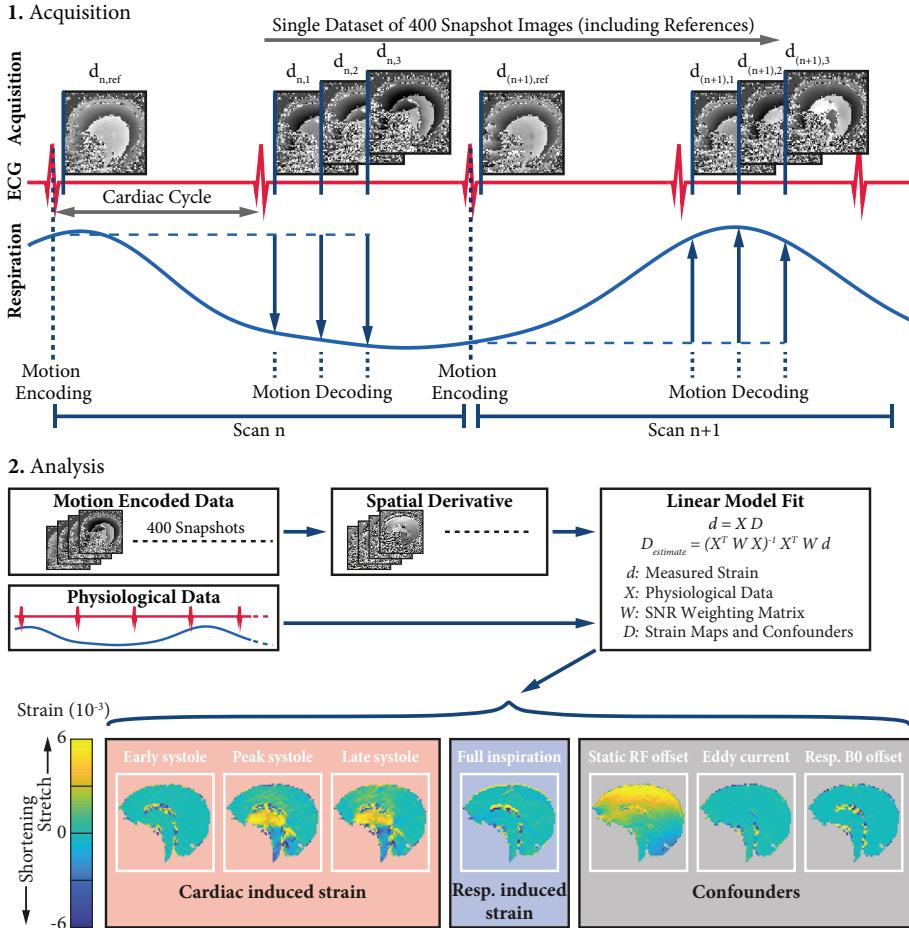


Figure 3-1 Example for data acquisition and analysis of one of the volunteers. The DENSE MRI sequence was used to encode motion into the phase of the MRI signal.

(1) Data was recorded over 100 dynamics (one slice, Feet-to-Head motion encoding direction) with alternating encoding direction sign to distinguish between phase contributions due to motion and motion independent phase confounders. Per dynamic scan, three snapshot DENSE images were acquired at different moments in the cardiac cycle together with the associated physiological data (see example traces). Also, a reference image was acquired directly after encoding to allow for corrections of potential eddy current effects.

(2) Time-series of displacement-encoded phase images were used to derive the strain maps by computing the spatial derivative along the encoding direction. Together with the associated physiological data, these strain maps were used in a linear model to isolate the components of cardiac and respiration induced strain. Including the confounders, the linear model produced seven maps.

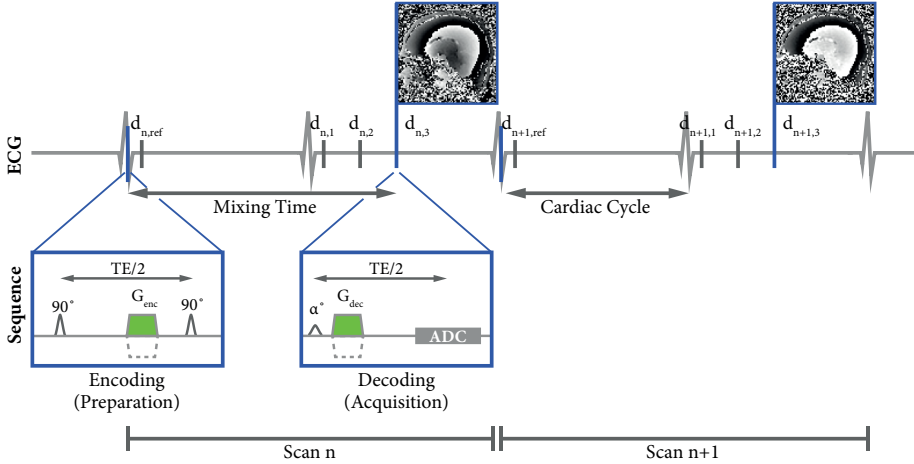


Figure 3-2 Schematic representation of the developed 2D single-shot DENSE sequence, covering two dynamic scans (n and $n+1$) that each comprise two cardiac cycles. The tissue's initial position is encoded in the longitudinal magnetization at the beginning of the dynamic scan, by the encoding gradient G_{enc} in the preparation part of the sequence. The prepared magnetization is decoded in the next cardiac cycle by the acquisition part of the sequence, which uses another RF pulse for signal excitation, followed by a decoding gradient (G_{dec}) that is equal to G_{enc} . Any tissue displacement along the direction of these gradients that occurs between G_{enc} and G_{dec} (during the so-called 'mixing time') leads to a corresponding phase shift in the resulting phase image. The DENSE images are acquired during the next cardiac cycle to increase the sensitivity to respiratory motion together with a reference phase directly after encoding to allow for potential eddy current corrections. Both encoding and decoding gradients G were inverted every two dynamics (dashed lines), to distinguish phase contributions due to motion from phase contributions due to confounding factors.

The DENSE sequence [5] consists of a motion encoding and -decoding part. The encoding part encodes the tissue's current position in the longitudinal magnetization by using two RF pulses with an encoding gradient (G_{enc}) in between. After a given mixing time, the decoding part reads out the prepared longitudinal magnetization by using another RF pulse followed by a decoding gradient (G_{dec}) that is equal to G_{enc} . Any tissue displacement along the direction of these gradients that occurred between G_{enc} and G_{dec} leads to a corresponding phase shift in the resulting phase image. The encoding- and decoding gradient alternated in sign every other dynamic to distinguish between phase contributions due to motion and confounding phase contributions from other sources (static RF phase, phase induced by off-resonance effects, and dynamic phase variation induced by respiration related B_0 fluctuations [55]). The signal from fat tissue was avoided through the use of low bandwidth (500 Hz) RF pulses during encoding, yielding water-selective tagging. Thus, we avoided artifacts from high fat signal close to the receiver elements of the head coil.

Data Acquisition

The Ethical Review Board (ERB) of the University Medical Center Utrecht approved the use of healthy volunteers for MRI protocol development. Nine healthy volunteers (6 males, 3 females, age 29 ± 3 years) were included and written informed consent was obtained in accordance with

the ERB approval. The volunteers were scanned at 7T (Philips Healthcare, Best, The Netherlands) using a 32-channel head coil (Nova Medical). A single DENSE dataset consisted of 100 dynamic scans with 4 motion decoding snapshots per dynamic, resulting in 400 snapshots over time, and a scan-duration of 2.5-5 min, depending on the heart rate (80-40 bpm). Other acquisition parameters were: EPI factor: 33; SENSE factor: 2.5 (AP or RL); resolution: $3 \times 3 \times 3 \text{ mm}^3$; FOV: $250 \times 250 \text{ mm}^2$; TE/2: 12 ms and BW: 61.9 Hz/pixel. A sagittal and perpendicular coronal slice were planned, and displacement images were separately acquired with two in-plane encoding directions. As a result, four 1D motion-encoded datasets were recorded: two datasets from a sagittal slice with 1D motion encodings in the Feet-to-Head and Anterior-to-Posterior direction respectively, and two datasets from a coronal slice with 1D motion encodings in the Feet-to-Head and Right-to-Left direction, respectively. The sagittal slice was planned 10 mm from the interhemispheric fissure of the brain and aligned with the brain stem (Figure 3-3 for planning details). The volunteers were asked for a calm abdominal breath during the experiment. Physiological data was simultaneously recorded by using a vector cardiogram (VCG) for triggering and a respiration belt to trace abdominal breathing. Additionally, a pulse oximeter was placed on the left index or middle finger as additional input in the analysis to cope with missed VCG triggers.

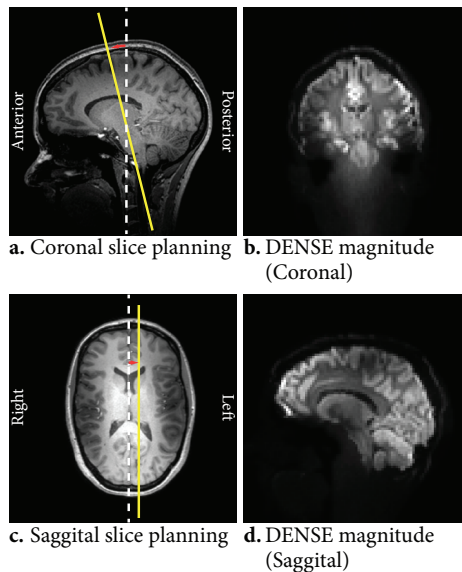


Figure 3-3 Slice planning of the 2D DENSE scans with respect to the whole-brain 3D T1-weighted TFE planning scan. The yellow lines indicate the planned slices with respect to the interhemispheric fissure, which is indicated by the white dotted line. (a) The coronal slice was planned through the brain stem as indicated in the figure (parallel to the brain stem; subject dependent RL angulation of 12-14 degrees). (c) The sagittal slice was planned perpendicular to the coronal slice, 10mm from the interhemispheric fissure towards the left. (b,d) The DENSE magnitude image as acquired, averaged over all acquisitions.

After encoding of the signal, three frames were acquired in the next cardiac cycle at respectively 0, 25 and 50% of the average cardiac interval. To allow for corrections of potential eddy current effects, an additional reference frame was acquired directly after encoding. Although the signal intensities of the successive frames are affected differently by T1 relaxation and diffusion-related signal attenuation, this does not affect the displacement information. Yet, the SNR present in the displacement images relates to the SNR in the magnitude images. To obtain a stable SNR over the acquired frames, a variable excitation flip angle scheme was recursively calculated [139], starting from the final flip angle α_{max} . Furthermore, the tag spacing T_{enc} (in units mm/π) summarizes the sensitivity for the spatial displacement encoding. Large encoding gradients yield an increased displacement sensitivity (smaller T_{enc}), yet, they reduce the SNR of the magnitude image due to their large b-values (diffusion sensitivity) [16].

Sequence optimization for strain estimates

The tissue deformation is physically described as strain, which signifies local stretch (positive strain) and shortening (negative strain) of tissue. The one-dimensional (1D) strain ε is simply the change in length of a line segment L and defined to give the relative change in length of the line segment during deformation

$$\varepsilon = \frac{L' - L}{L} = \frac{\Delta L}{L} \quad (3-1)$$

where L is the original length of the line segment and L' is the length of the line segment after deformation. The strain is obtained from displacement images by calculating spatial derivatives. Given Δx , the voxel size along x , we can define the 1D strain in that direction as

$$\varepsilon_{xx}(n) \stackrel{\text{def}}{=} \frac{D_x(n+1) - D_x(n)}{2\Delta x} \quad (3-2)$$

Accurate measurements are crucial, since the computation of spatial derivatives amplifies noise present in the displacement images. Larger encoding gradients yield an increased displacement sensitivity (smaller T_{enc}), yet, increase the number of phase wraps present in the displacement maps. Fortunately, strain computations allow for straightforward unwrapping under the assumption of small strains, as any phase wrap in the original image yields unlikely high strain values. A phase wrap causes a large numeric derivative $\Delta\phi$, which was resolved by adding or subtracting 2π to $\Delta\phi$ to bring it closer to zero if

$$|\Delta\phi| > 1.5\pi = \Delta\phi_{max} \quad (3-3)$$

The maximum tolerated numeric derivative $\Delta\phi$ relates to the maximum tolerated strain by

$$\varepsilon_{max} = \frac{\Delta\phi_{max}}{2\Delta x} \frac{T_{enc}}{\pi} = 0.75 \frac{T_{enc}}{\Delta x} \quad (3-4)$$

Thus, as long as the expected strains in the brain do not exceed α_{max} , there are no additional constraints for the encoding sensitivity. However, although larger encoding gradients yield an increased displacement sensitivity, they reduce the SNR of the magnitude image due to their larger diffusion sensitivity (expressed by its b-values). Similarly, a larger final flip angle increases the excited signal, but prevents regrowth of magnetization for the next encoding. Consequently, an optimal T_{enc} and final flip angle exists for a given apparent diffusion coefficient (ADC) and longitudinal relaxation time constant (T1) of the tissue.

We simulated the DENSE sequence for different settings of T_{enc} and α_{max} and found optimal DENSE sequence settings of $T_{enc} = 0.15 \text{ mm}/\pi$ and $\alpha_{max} = 50^\circ$ (white matter: T1 = 1200 ms and ADC = $0.8 \cdot 10^{-3} \text{ mm}^2/\text{s}$ at 7T [66; 130]) for acquiring strain images [139]. The T1 and apparent diffusion coefficient (ADC) of white matter was chosen as this has a shorter T1 than gray matter and, thus, faster decay of the tagged magnetization. We verified our simulations in a phantom [139] for which we used a multi-shot 3D EPI imaging protocol with imaging parameters: EPI factor: 19; SENSE factor: 2.6×2.5 (AP \times RL); resolution: $3 \times 3 \times 3 \text{ mm}^3$; FOV: $150 \times 150 \times 150 \text{ mm}^3$; and TE/2: 15 ms.

Linear Model

The linear model will be described starting from the two example images outlined in Figure 3-2. These two images represent the phase of the DENSE images acquired at 50% of the cardiac interval. Due to an alternating encoding direction, the second acquired image has an opposite phase contribution due to motion compared to the first image. This way, we can distinguish between phase contributions due to motion and static phase confounders. The phase image is converted to a displacement image by multiplying the phase image with T_{enc}/π . The cardiac related displacement map can be separated from the confounding background by modelling each of the two example images as a linear combination of the cardiac related displacement map ($D_{c,3}$) and the static displacement confounder (D_0):

$$d_{n,3} = x_0 D_0 + x_{c,3} D_{c,3} \quad (3-5)$$

The above equation represents the apparent total tissue displacement $d_{n,i}$ of snapshot i acquired in dynamic scan n (for the current example, $d_{n,3}$ represents the apparent motion in the only snapshot in dynamic n as shown in Figure 3-2). D_0 is the apparent displacement due to static RF phase errors and $D_{c,3}$ is the cardiac related displacement at the third time point in the cardiac cycle (which corresponds to 50% of the cardiac interval). The associated coefficients x are known, and required to estimate the displacement maps from the measured data. The coefficient x_0 is 1 for both images, whereas $x_{c,3}$ alternates in sign depending on the sign of the motion encoding gradient. The matrix formulation of the model for the two example images then yields

$$\begin{bmatrix} d_{n,3} \\ d_{n+1,3} \end{bmatrix} = \begin{bmatrix} 1 & 1 \\ 1 & -1 \end{bmatrix} \begin{bmatrix} D_0 \\ D_{c3} \end{bmatrix} \quad (3-6)$$

The equation in this example is easily solved by simple inversion. However, we will acquire many more measurements than unknowns, which will result in the descriptive matrix not being square. Therefore, we solve this equation for D_0 and D_{c3} using the Least-Squares estimation method if more than two dynamic scans are performed. The method thereby provides the displacement at 50% of the cardiac cycle (D_{c3}) together with the apparent displacement induced by static phase errors (D_0).

The model easily expands to incorporate the additional displacement images at 0 and 25% of the cardiac cycle. In addition to the displacement induced by the cardiac cycle, we incorporate displacement induced by respiration. We assume that the respiration related displacement depends linearly on the difference in respiration trace between encoding and decoding of the signal and is independent of the cardiac related displacement. We base this assumption on preliminary results where we analyzed the residuals of a model without respiration adaptation and found that the residual tissue displacements showed a linear dependence on the difference in respiration trace (between encoding and decoding). The term D_{resp} represents this linear respiration contribution. Furthermore, we include two additional correction terms. Firstly, an eddy-current offset term D_{eddy} to account for phase errors induced by the high decoding gradient and secondly, a respiration induced B0 offset term $D_{0,resp}$ [55]. The complete model then yields

$$d_{n,s}(c,r) = D_0 + x_{eddy}D_{eddy} + \sum_{i=1}^3 x_{c,i}D_{c,i} + x_{resp}D_{resp} + x_{0,resp}D_{0,resp} \quad (3-7)$$

The physiological data and sequence design provide the values of the weighting factors x . The weighting factors x_{eddy} , $x_{c,i}$ and x_{resp} have alternating signs related to the alternating sign of the motion encoding gradients. If coefficient ξ represents this sign, then $x_{c,i}=\xi$ for i is 1, 2 or 3, for a frame acquired at 0, 25 or 50% of the associated actual cardiac interval, respectively. Still, due to a varying heart rate during acquisition, frames can fall between these intervals. In that case, cardiac weighting factors are linearly interpolated such that

$$\begin{aligned} 0 &\leq |x_{c,i}| \leq 1 \\ \sum_{i=1}^3 |x_{c,i}| &= 1 \end{aligned} \quad (3-8)$$

The respiration weighting factors are described by $x_{resp}=\xi\Delta r$ (which accounts for respiration induced motion, with alternating sign ξ) and $x_{0,resp}=\Delta r$ (which accounts for respiration induces resonance shifts [55]), where Δr is the normalized difference in abdominal respiration position

between encoding and decoding. For clarity, we provide the matrix formulation for the extended linear model representing the 8 motion-encoded snapshot images in Figure 3-1.1. This extended model is used to unravel cardiac and respiratory contributions to the displacement of brain tissue.

$$\begin{bmatrix} d_{n,ref} \\ d_{n,1} \\ d_{n,2} \\ d_{n,3} \\ d_{n+1,ref} \\ d_{n+1,1} \\ d_{n+1,2} \\ d_{n+1,3} \end{bmatrix} = \begin{bmatrix} 1 & 1 & 0 & 0 & 0 & 0 & 0 \\ 1 & 1 & 1 & 0 & 0 & -0.75 & -0.75 \\ 1 & 1 & 0.02 & 0.98 & 0 & -0.80 & -0.80 \\ 1 & 1 & 0 & 0.05 & 0.95 & -0.85 & -0.85 \\ 1 & -1 & 0 & 0 & 0 & 0 & 0 \\ 1 & -1 & -1 & 0 & 0 & -0.10 & 0.10 \\ 1 & -1 & 0 & -0.94 & -0.06 & -0.85 & 0.85 \\ 1 & -1 & 0 & 0 & -1 & -0.65 & 0.65 \end{bmatrix} \begin{bmatrix} D_0 \\ D_{eddy} \\ D_{c,1} \\ D_{c,2} \\ D_{c,3} \\ D_{resp} \\ D_{0,resp} \end{bmatrix} \quad (3-9)$$

Analysis

The acquired time series were analyzed offline with custom MATLAB R2018b software (The MathWorks, Inc., Natick, MA, USA). The VCG and POx trigger moments as recognized by the scanner software were used to deduce the positions of the snapshot images relative to the cardiac interval. VCG triggering sometimes failed due to magneto hemodynamic effects. The associated images were retrospectively discarded by using only the images for which the related VCG triggers were accompanied by a POx trigger occurring within 200ms and 400ms after the VCG trigger. The respiration change between encoding and decoding was deduced from the recorded respiration trace, which was filtered with a band-pass filter with cut-off frequencies at 0.1 and 1 Hz. Furthermore, the respiration was normalized by using the interval between the minimum and maximum observed value of the respiration trace, after discarding the lowest and highest 2.5% of its values. The remaining interval is referred to as the 95% range of the respiration trace, which served as normalization. Thus, the respiration related coefficients in design matrix X had values ranging from just under -1 to just over 1. The estimated D_{resp} map, thus, represents the induced motion for a – by definition – ‘full’ inspiration (change of respiration coefficient from 0 to 1). Similarly, the effect of expiration can be found by multiplying the estimated D_{resp} map by -1 (change of respiration coefficient from 0 to -1).

The dynamic scans of DENSE images were registered with a rigid in-plane whole-voxel transformation using elastix [82]. All sagittal slices were registered to the last sagittal dynamic scan, whereas all coronal slices were registered to the first coronal dynamic scan, which was acquired subsequently to the last sagittal dynamic scan. No corrections for geometric EPI-distortion were performed, as we analysed only small ROIs in regions with very low B0 inhomogeneity. Strain images were obtained by computing the spatial derivative from the displacement images along the encoding direction, where derivatives larger than $0.75 \cdot T_{enc} / \Delta x$ were unwrapped. From the unwrapped strain images, the various motion contributions and confounders were unraveled voxelwise by computing the pseudoinverse (least-squares) of X that contained the physiological information at each measurement.

$$D_{estimate} = (X^T W X)^{-1} X^T W d \quad (3-10)$$

Here, d is the measured data (either (apparent) displacement or strain images) and W represents the weighting matrix accounting for the variable SNR in the different snapshots in each voxel. The values in the weighting matrix W consisted of the normalized SNR (proportional to the magnitude signal squared) in each voxel associated with the measurement for the displacement data. For the strain data, these values corresponded to the mean SNR of the two voxels that were used to compute the derivative. This way, W corrects for SNR differences caused by, among others, the spatial variation in flip angle due to the dielectric effects present at 7T. The model was solved voxel-wise which resulted in seven maps: 4 maps of displacement or strain (depending on the input data) and 3 maps of confounders as illustrated in Figure 3-1. An inter-subject comparison was then performed in two ROIs; one in the centrum semi ovale (CSO) and one in the basal ganglia (BG). To reduce the effect from noise in the strain maps, the median in each ROI was used for the analysis. Furthermore, the dependence of the strain in the Feet-to-Head direction on the ROI selection was tested by evaluating the FH strain along the entire intersection line of the sagittal and coronal slice.

RESULTS

The linear model: example for displacement maps

For illustrative purposes, the linear model was applied to the motion-encoded snapshot images, following the procedure of Figure 3-1 without computing any derivatives. An important constraint for correctly fitting the displacement maps is that the motion-encoded snapshot images are correctly unwrapped. To this end, the images were acquired with lower encoding sensitivity ($T_{enc} = 0.25 \text{ mm}/\pi$) than optimal for strain (optimal for strain: $T_{enc} = 0.15 \text{ mm}/\pi$) to avoid phase wraps.

The linear fit resulted in four smooth displacement maps (cardiac- and respiration-induced) and three confounding factors: a static RF phase offset, phase induced by off-resonance effects and a respiration-induced B_0 offset fluctuation ranging typically between 0 and 10 Hz from the base of the brain to the top of the brain (Figure 3-4). In the displacement map associated with a full inspiration, we observed a translation of the complete head in the Feet direction together with a slight rotation, where the back of the head moves in de Head direction and the front of the head moves in the Feet direction. However, mere translations and rotations of the head are not considered to drive any brain clearance. Therefore, tissue deformation will be considered for the remainder of this study.

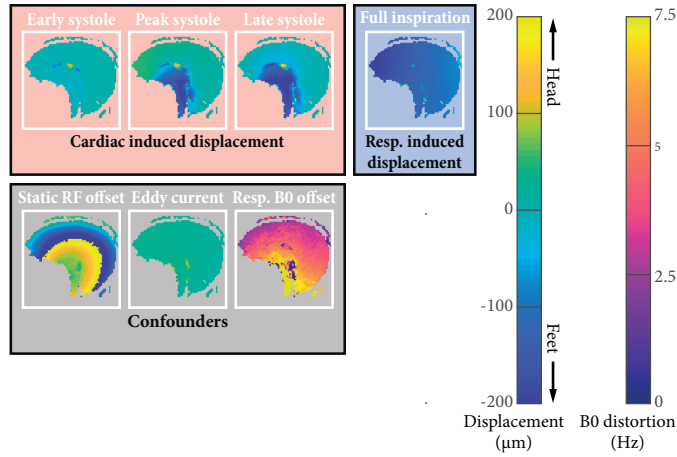


Figure 3-4 Feet-to-Head motion maps of subject 1, produced with a dataset that had lower encoding sensitivity (tag spacing: $0.25 \text{ mm}/\pi$) than optimal for strain (optimal for strain: $0.15 \text{ mm}/\pi$) to avoid phase wraps. The images are from the same subject as in Figure 3-1. For the current figure, the spatial derivative was not performed before fitting the linear model, in order to obtain motion maps rather than strain maps. The top row shows the cardiac and respiratory motion, respectively, whereas the bottom row represents the phase confounders. The dynamic B0 offset fluctuations due to respiration are scaled in Hz, for comparison with literature [55].

Validation of DENSE optimization

We found SNR_M to be consistent with computer simulations for both a variable final flip angle α_{max} and encoding sensitivity T_{enc} (Figure 3-5a and 5b, respectively). The simulated SNR_{displ} for both the phantom and white matter is shown in Figure 3-5c as a function of the tag spacing. All sequence-dependent SNR behavior not related to T_{enc} or α_{max} is represented in a linear scaling parameter that matches the measured SNR_M with the SNR_M observed in the phantom.

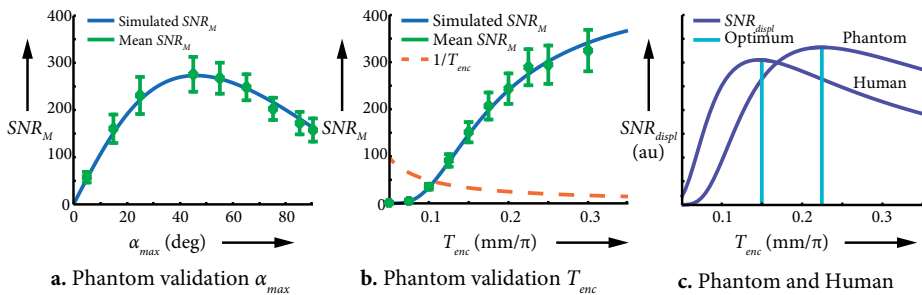


Figure 3-5 Signal to noise ratio of the magnitude image (SNR_M) and displacement map (SNR_{displ}) with error bars indicating the standard deviation. (a,b) Simulated SNR_M with the SNR_M observed in the phantom. The simulated SNR_M line was linearly scaled to match the measured SNR_M in the phantom. The results show that the course of the line matches the measured SNR behavior. (c) Simulated SNR_M divided by the tag spacing, which matches the SNR in the displacement map. The optimum is shown for both the phantom and white matter in humans at 7T.

Strain anisotropy

Cardiac related strain was largest at peak systole (25% of the cardiac interval) and was compared with strain induced by a full inspiration (95% range of the respiration trace). Figure 3-6 represents the resulting strain maps at peak systole for volunteer 1, two of which are in the sagittal plane and the other two in the coronal plane. The ROIs for inter-subject comparison are indicated as well. To capture the physiological 3D anisotropic tissue deformations, we combined the results in these ROIs along the intersection line from two orthogonal slices with different encodings.

Figure 3-7a-b shows the strain in the three orthogonal directions separately. The dependence of FH strain on the ROI on the ROI selection was tested by evaluating the FH strain along the entire intersection line of the sagittal and coronal slice. The results showed a smooth curve and narrow interquartile ranges in regions where no CSF was present (see Supplementary Figure 3-S1). In the selected ROIs, the cardiac-induced tissue deformation at peak systole (Figure 3-7a) shows anisotropic strain with expansion in the Feet-to-Head direction and minor compression in the other two directions. This observation is also known as the Poisson effect, where axial expansion of an object in the direction of the expansion load is accompanied by transverse compression. Although much smaller, we observed a similar but opposite trend for the respiration-induced strain (Figure 3-7b). For a full inspiration, the tissue contracts in the Feet-to-Head direction and expands in the other two directions. By design of the model, a full expiration would invert this trend. The tissue strains induced by the cardiac cycle are much larger compared to the strains induced by respiratory cycle.

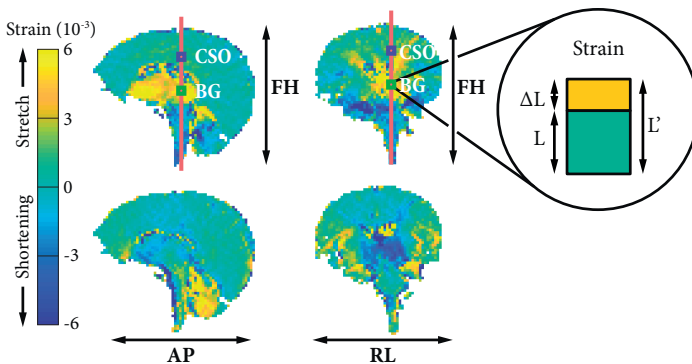


Figure 3-6 Four fitted 1D strain maps of one volunteer in three motion encoding directions for sagittal (left column) and coronal (right column) slice at peak systole. Two ROIs, one in the centrum semi ovale (CSO) and one in the basal ganglia (BG) (top-row), were manually selected per subject and used for further strain analysis. Each map represents the 1D strain calculated as the spatial derivative along the associated motion encoding direction, which is indicated by the black arrows. The one-dimensional strain is illustrated in the circled area and represents the change in length, ΔL , of a line segment L . The strain ϵ is defined as the relative change in length of the line segment during deformation:

$$\epsilon = \frac{L' - L}{L} = \frac{\Delta L}{L}$$

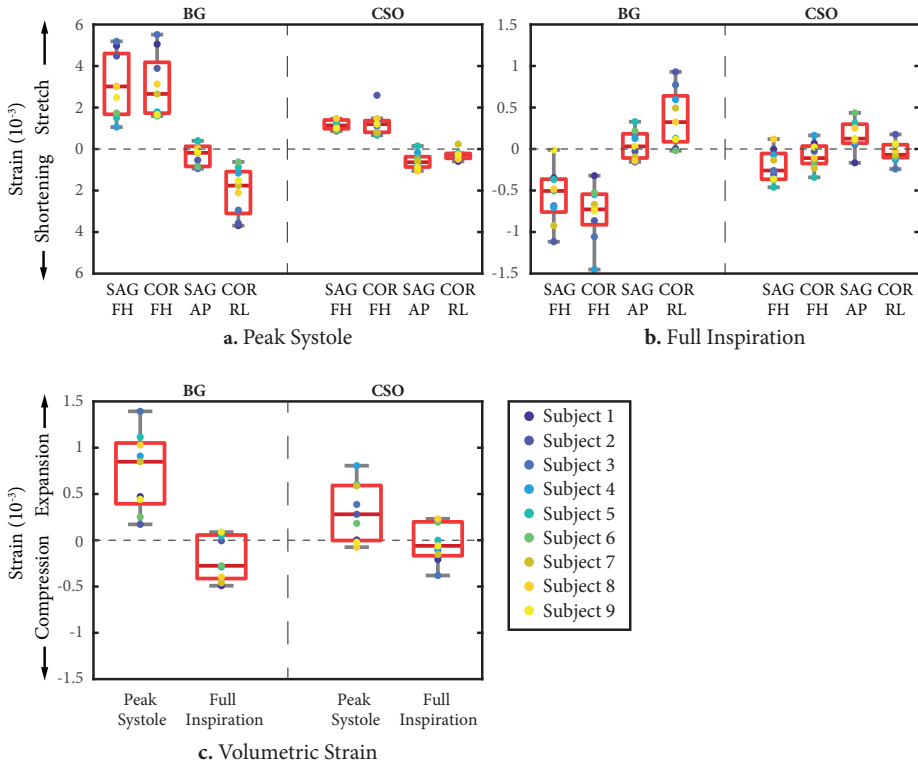


Figure 3-7 Strain measurements results at peak systole and for a full inspiration. The model was designed such that a full expiration would contribute the same as minus a full inspiration.

(a-b) 1D strains (ROI medians) shown for the three perpendicular motion encoding directions in the BG and CSO. The FH direction was measured twice, once in the sagittal oriented slice (SAG), and once in the coronal oriented slice (COR). The similar results for both FH acquisitions indicate good reproducibility of the measurements. The different colors represent different subjects. Figure 3-a and b show the cardiac and respiration contributions, respectively. Please note the difference in scale along the y-axis. For cardiac induced strain, the Feet-to-Head direction shows relatively large expansion, whereas the other two directions show some compression (this is known as the Poisson effect). The effect is most pronounced in the BG, yet is of the same trend in the CSO. Interestingly, the respiration induced strain shows a similar but opposite trend, consistent with outflow of (venous) blood with inspiration, due to lower thoracic pressure.

(c) Volumetric strain analysis for nine subjects. The volumetric strain was obtained by summing over the 1D strains from all 3 encoding directions. For each 1D strain direction, the median over the associated ROI indicated in Figure 3-6 was used. (For the Feet-to-Head direction, the median of the combined ROIs of both the coronal and sagittal slice was used). The left two boxes represent the results in the BG (green ROI in Figure 3-6), whereas the right two boxes represent the results in the CSO (purple ROI in Figure 3-6). In each region, both the cardiac and respiratory related contributions are represented.

Volumetric Strain

The volumetric strain is obtained by summing the observed strains over the three orthogonal directions. Figure 3-7c shows the volumetric strains, which are largest in the deep brain (basal ganglia). Here, we observed cardiac induced tissue expansion with median volumetric strain of

$0.85 \cdot 10^{-3}$ (IQR: $0.39 \cdot 10^{-3}$ to $1.05 \cdot 10^{-3}$). For inspiration, a slight compression was observed with a median strain of $-0.28 \cdot 10^{-3}$ (IQR: $-0.41 \cdot 10^{-3}$ to $0.06 \cdot 10^{-3}$). A one-sided t-test revealed that both these observations were significantly different from zero ($p = 0.0008$ and $p = 0.047$, respectively). Although less pronounced, similar trends were observed in the CSO with cardiac induced volumetric tissue expansion (median strain $0.28 \cdot 10^{-3}$ (IQR: 0 to $0.59 \cdot 10^{-3}$) and respiration-induced volumetric tissue compression (median strain $-0.06 \cdot 10^{-3}$ (IQR: $-0.17 \cdot 10^{-3}$ to $0.20 \cdot 10^{-3}$)). Only the cardiac-induced volumetric tissue expansion was significantly different from zero in this region ($p = 0.02$ and $p = 0.7$, respectively).

DISCUSSION

We developed a non-invasive method to measure brain tissue deformations resulting from cardiac and respiratory pulsations in the microvasculature that likely drive the brain's waste clearance system. The single-shot approach not only enabled us to unravel cardiac and respiratory contributions, but also allowed for an optimization of the tag-spacing for strain measurements without introducing additional artifacts as are observed with multi-shot approaches [1; 140]. This optimization made analysis possible in small ROIs, despite the amplified noise resulting from the use of spatial derivatives. For the CSO, we measured strain values comparable with values reported by Hirsch et al [70]. We found larger strain values in the BG, which may reflect regional heterogeneity in tissue volumetric strain (and blood volume). We observed that the cardiac induced strain in the microvasculature is larger than the respiration induced strain, both for the volumetric strain as well as the 1D strain components in the three directions separately. B_0 offset fluctuations related to respiration decreased from the base of the brain to the top of the brain, and ranged typically between 0 and 10 Hz (Figure 3-4), which compares well to the literature [55]. This finding substantiates the credibility of the proposed model.

The observed systolic cardiac-induced tissue expansion is induced by the blood volume pulsations of the microvascular bed embedded in the tissue. Rivera et al. reported average relative volume pulsations of $0.3 \cdot 10^{-3}$ for gray matter and $0.1 \cdot 10^{-3}$ for white matter, respectively [129]. These values are somewhat lower than our measurements, which is probably related to differences in methodology. We measured in small ROIs, while the 1D strain maps suggest considerable spatial variation in strain. Besides, we measured the tissue deformation directly, while Rivera et al. needed additional modeling to translate a measured T2* change induced by the injected contrast agent into a blood volume change via an estimated change in magnetic susceptibility. Mestre et al. reported a radius increase over the cardiac cycle of $\sim 1\%$ for arterioles (approximately $60 \mu\text{m}$ in diameter) in mice [100]. The volumetric tissue strain ϵ associated with expansion of the microvascular bed is related to the relative cerebral blood volume (rCBV) by

$$\varepsilon = \frac{V_{blood}}{V_{tissue}} \delta \quad (3-11)$$

where V_{blood}/V_{tissue} is the rCBV and δ is the relative change in blood volume. Assuming that the diameter change of 1% in arterioles is representative for the entire microvascular bed, and that the blood volume expansion is only due to the diameter increase of the blood vessels (i.e. elongation is negligible), the related relative blood volume change is $\sim 2\%$. Together with a rCBV of approximately 4% in gray matter and 2.5% in white matter [30], the resulting volumetric tissue strains for gray and white matter are $0.8 \cdot 10^{-3}$ and $0.5 \cdot 10^{-3}$, respectively. Given the difference in species and the rather coarse estimation, these values estimated from observations in mice compare remarkably well with the volumetric strain we observed in humans, in the ROIs in BG (gray matter) and CSO (white matter), respectively.

In the interpretation of the observed volumetric strain values, it is important to note that these reflect in fact the net effect of both blood volume increase (microvascular expansion) and potential simultaneous compression of the interstitial space. The volumetric strain can be regarded as a lower bound estimation of the underlying blood volume pulsations, as any simultaneous compression of the interstitial space would reduce the amount of observable volumetric tissue strain. Comprehensive computer models that take the interaction between blood, CSF and tissue as porous medium (cells and interstitial fluid) into account could help to gain further insight into this effect [91; 92].

The respiratory effect found in this study implies loss of tissue volume due to venous outflow and is in accordance with the upward CSF flow through the spinal canal observed by Dreha-Kulaczewski et al. The observed tissue deformation due to respiration can only explain a small portion of the CSF flow found by Dreha-Kulaczewski [40]. However, in literature quite different results exist of the relative contributions of heartbeat and respiration cycles to CSF flow; some studies report dominant cardiac-related CSF flow [36; 148; 175], while others identify respiration as the main driver of CSF flow [39; 172], especially in the spinal canal [40]. Moreover, one should note that the CSF flow does not only occur because of loss of tissue volume, but probably also due to compression of the larger veins that are embedded in the CSF (e.g. cortical veins and cavernous sinus) [58]. Venous compression seems to occur even during the cardiac cycle because the cortical veins behave as a Starling resistor, which facilitates backpropagation of the increased CSF pressure along the veins, thus preventing excessive pressure gradients across the capillary bed inside the brain tissue [135]. Previous flow studies of respiration related CSF flows, nor the current study assessed the volume of the larger veins. Future work should verify whether deflation of larger veins indeed dominate (upward) CSF flow during inspiration. Nevertheless, the current method helps to distinguish between the larger and smaller veins by providing a window to the microvasculature embedded in the tissue.

The proposed method allows for local assessment of tissue deformation and, thus, shows strong potential for studying mechanobiological processes of the brain. The results reveal interesting details of the deformation experienced by the brain's tissue including anisotropic strain that is consistent with the Poisson effect, which could be observed in a local ROI of only 3×3 pixels. Given that the brain is a porous medium [57], we speculate that large tissue deformation could locally 'choke' the tissue by systolic compression of the (venous) microvasculature [171]. If such a choke-mechanism exists, it is conceivable that this may contribute to the appearance of white matter hyper intensities (WMH) as observed in patients with cerebral small vessel disease [166; 167]. These WMH tend to form at the corners of the brain's ventricles, exactly at the location where we observe large tissue deformations in the coronal slice (see Figure 3-6), and where intravascular pressures are relatively low, at the end of the vascular tree [26]. It is less speculative to state that the observed deformations play an important role in cellular gene expression and, thus, in maintaining brain tissue and vascular integrity [35; 57; 154]. Moreover, the brain tissue deformations are one of the drivers of the clearance system, as the deformation of the interstitial space contributes to the mixing and flow of the interstitial fluid and CSF [10; 12; 100; 153]. Brain clearance is currently mainly studied in animals. Mestre et al. found in mice that the relative contribution of the cardiac cycle to the flow velocity of the perivascular fluid was approximately a factor of five larger than the contribution of the respiration cycle [100]. We found a compatible difference in the contribution to the tissue volumetric strain between cardiac and respiratory cycles. Although further research is needed to justify direct comparison between tissue deformation and perivascular fluid flows, these results suggest that our method has potential to reduce the gap between invasive preclinical research and non-invasive observations in humans.

At the same time, it must be acknowledged that the driving forces of clearance are still under debate. The wavelength of the cardiac related pulsations appears to be too long to induce significant spatial gradients that are needed for transport [4]. Vasomotion (spontaneous arterial diameter fluctuations initiated by vascular smooth muscle cells) occurs at a much lower frequency of approx. 0.1 Hz and with much shorter wavelengths. Indeed, recent animal work has shown that vasomotion is an important driver in clearance [162]. Still, vascular pulsations may contribute to the clearance process through dispersion, which is a combined effect of mixing and diffusion [10]. It is unclear whether vasomotion is sufficiently spatially coherent to lead to measureable tissue strains, and whether our method would be sensitive enough to detect those low frequencies. The duration between motion encoding and decoding is limited by the T1 tissue relaxation time, which is less than 2 seconds in the human brain at 7T. Still, we were also able to detect respiration related effects, which have a frequency of approx. 0.25 Hz, not too far from the vasomotion frequency. Targeting potential vasomotion effects with our method would be an interesting topic for future investigations.

The results showed different tissue deformation between gray matter (ROI in BG) and white matter (ROI in CSO) in healthy volunteers. The fact that the technique is sensitive enough to see normal regional differences in physiology in healthy people indicates that it also has potential for detecting abnormalities in tissue deformation in disease. As such, the technique may help in advancing our understanding of diseases like cerebral small vessel disease and the vascular contributions to neurodegenerative diseases. Currently, it is a limitation of this study that we could not assess the tissue strain in a 2D slice and perform a volumetric strain analysis along a single line only. We therefore cannot infer respiration-related strains of the complete brain, as were recently performed for cardiac-induced strains [2]. The sequence, however, holds the potential to extend the current 2D approach to a multi-slice acquisition, where the time between the cardiac phases is used to acquire additional slices at different locations in the brain. Such an approach would enable the acquisition of a 3D volume, without sacrificing any SNR and preserving the single-shot approach. It should also be investigated whether the proposed method – possibly extended to a multi-slice acquisition approach – can tolerate a 3/7 factor reduction in SNR, so that it can be implemented on 3T clinical scanners. A further limitation of this study is that no additional geometric EPI distortion corrections were performed, apart from 2nd order image based shimming. Although the analysis was performed in homogenous regions of the brain, geometric EPI distortion corrections would be necessary for regions with significant B0 inhomogeneities (e.g. near the nasal cavities) through the use of an acquired B0-field map.

In conclusion, the developed single-shot 2D DENSE method is capable to consistently disentangle cardiac related brain deformations from respiration-induced brain tissue deformations. We have successfully measured the separate contributions in small ROIs, despite the amplified noise induced by the use of spatial derivatives and found results that are consistent with physiological blood volume changes. This novel method provides a tool to directly study tissue dynamics that reflect fundamental aspects of the microvascular function and that holds potential to serve as a physiological marker of the waste clearance system of the brain.

SUPPLEMENTARY MATERIAL

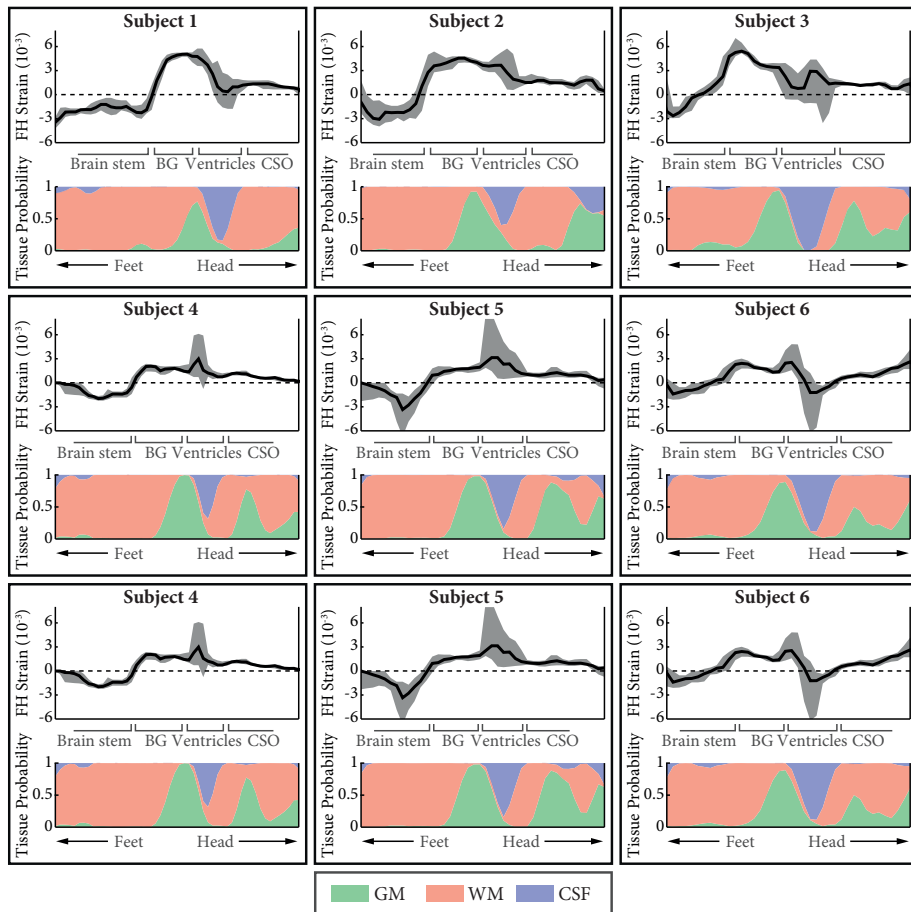


Figure 3-S1 Dependence of strain results on location of region of interest. Upper panels) FH strain along the Feet to Head intersection line between the acquired coronal and sagittal slices, represented for each volunteer separately. The black line indicates the median in a 3x3 pixel area for both the coronal and sagittal slice together. The gray area indicates the 25%-75% interquartile range in the associated area. Lower panels) Relative tissue probabilities in the area for which the FH strain was computed, which was obtained from the segmentation of the T1 scan (mean probability in ROI). As expected, strains have a higher variance in regions where CSF is dominant over tissue, due to flow effects.



4

Strain Tensor Imaging: Cardiac-induced brain tissue deformation in humans quantified with high-field MRI

J.J. Sloots
G.J. Biessels
A. de Luca
J.J.M. Zwanenburg

NeuroImage 236, 2021

ABSTRACT

The cardiac cycle induces blood volume pulsations in the cerebral microvasculature that cause subtle deformation of the surrounding tissue. These tissue deformations are highly relevant as a potential source of information on the brain's microvasculature as well as of tissue condition. Besides, cyclic brain tissue deformations may be a driving force in clearance of brain waste products. We have developed a high-field magnetic resonance imaging (MRI) technique to capture these tissue deformations with full brain coverage and sufficient signal-to-noise to derive the cardiac-induced strain tensor on a voxel by voxel basis, that could not be assessed non-invasively before. We acquired the strain tensor with 3mm isotropic resolution in 9 subjects with repeated measurements for 8 subjects. The strain tensor yielded both positive and negative eigenvalues (principle strains), reflecting the Poisson effect in tissue. The principle strain associated with expansion followed the known funnel shaped brain motion pattern pointing towards the foramen magnum. Furthermore, we evaluate two scalar quantities from the strain tensor: the volumetric strain and octahedral shear strain. These quantities showed consistent patterns between subjects, and yielded repeatable results: the peak systolic volumetric strain (relative to end-diastolic strain) was $4.19 \cdot 10^{-4} \pm 0.78 \cdot 10^{-4}$ and $3.98 \cdot 10^{-4} \pm 0.44 \cdot 10^{-4}$ (mean \pm standard deviation for first and second measurement, respectively), and the peak octahedral shear strain was $2.16 \cdot 10^{-3} \pm 0.31 \cdot 10^{-3}$ and $2.31 \cdot 10^{-3} \pm 0.38 \cdot 10^{-3}$, for the first and second measurement, respectively. The volumetric strain was typically highest in the cortex and lowest in the periventricular white matter, while anisotropy was highest in the subcortical white matter and basal ganglia. This technique thus reveals new, regional information on the brain's cardiac-induced deformation characteristics, and has the potential to advance our understanding of the role of microvascular pulsations in health and disease.

INTRODUCTION

Blood flow into the brain is pulsatile, driven by variation in blood pressure over the cardiac cycle. The pulsatile pressure waves, generated by the heart, are transmitted through the arterial tree all the way to the level of the microvasculature [64; 134]. As the arterial pressure wave reaches the microvascular bed, these microvessels swell and stretch elastically causing the surrounding tissue to be displaced [126; 140; 180]. These ensuing subtle tissue deformations show regional variation, depending on the amount of blood that is delivered locally, but also on tissue properties and the tissue's position relative to, for example, the ventricles.

Measuring brain pulsatility is of interest, as it carries information of both the blood vessels that drive these pulsations, and of the surrounding tissue that deforms in response to the vascular pulse. Indeed, it has been shown that brain tissue stiffness can be derived by performing magnetic resonance elastography (MRE) reconstructions on measured heartbeat-related tissue motions [169; 181]. Conventional MRE has shown that the brain tissue softens (becomes less stiff) with age, which probably reflects change in the tissues microstructure [132]. Also, one can compute the volumetric strain accompanying the brain tissue displacement, which is defined as the relative change in volume of an elementary piece of tissue [1; 2; 70; 137]. Regional variation in this volumetric strain most likely reflects (at least partially) regional variation in the arterial blood fraction of the tissue [1]. This notion is corroborated by observed white matter tissue swelling during systole, which is much smaller than the gray matter tissue swelling [1; 2; 137]. It is conceivable that combining dedicated computer models with precise measurements of the brain tissue deformation would yield insight in mechanical properties of both the vasculature (such as local blood volume and its compliance) and the tissue (such as the bulk- and shear modulus) [91; 92].

Apart from offering a window to microvascular and tissue microstructural features, brain tissue pulsations are also of interest for their potential role in essential physiological processes. Flow-induced shear stress and its pulsatility evoke mechanotransductive responses in endothelial cells, which constitute the blood-brain barrier [33; 35; 37]. Moreover, tissue deformations propel cerebral spinal fluid (CSF) around the brain. As CSF fulfills an important role in the drainage of cerebral waste, tissue deformation is considered to contribute to waste clearance in the brain [101; 141]. Although the exact mechanism of brain waste clearance are still controversial, it is likely that tissue deformations contribute this process by mixing of the interstitial and para-arterial fluids [10; 12]. Non-invasive assessment of brain tissue pulsations may therefore be of value for studying brain physiology, and could also be relevant for brain disease. For instance, stiffening of the vascular walls is known to be associated with increased risk of stroke and the development of cerebral small vessel disease (cSVD). cSVD is a major cause of stroke and dementia that can currently only be detected when macroscopic, mostly irreversible, tissue lesions have

been developed [121; 167]. Assessment of changes in the microvascular- and tissue properties prior to the development of such damage might yield insight in the underlying disease processes.

Despite the apparent relevance of cardiac-induced brain tissue deformations, there are currently limited methods to study these deformations in a non-invasive way in humans. The phenomenon of physiological brain tissue deformation is subtle, with typically maximal stretch along a single direction in the order of 0.3% [119; 137]. Volumetric strains are even more subtle, typically less than approx. 0.1% [1; 2; 137]. These deformations can be derived from motion field maps through the use of spatial derivatives. MRI techniques that in principle can provide these motion field maps include amplified MRI (aMRI) [73; 156] and phase-contrast MRI (PC-MRI) [43; 143]. Yet, aMRI is designed for standard anatomical cine images, which are not optimized to capture the subtle brain motion. Besides, the aMRI algorithms do not provide deformation fields directly, meaning that additional registration algorithms have to be used that only add to uncertainty. On the other hand, PC-MRI requires velocity sensitivities (VENCs) in the order of 1mm/s, which require bipolar gradients that are too large to be practically feasible with reasonable TRs and TEs (practically feasible VENCs are in the order of 1cm/s) [2]. Therefore, we use Displacement Encoding with Stimulated Echoes (DENSE) [5] to quantify these motion field maps [126; 140; 180]. However, the computation of spatial derivatives amplifies the noise present in these motion field maps. As a result, the signal to noise ratio (SNR) in the strain measurements are typically low. Even at 7T, current strain measurements as obtained with a time-resolved multi-shot 3D approach, require an increase in SNR by approximately a factor of 10, in order to perform a voxel-wise analysis of the tissues volumetric strain [1]. The lack in SNR in the multi-shot 3D approach mainly originated from the use of suboptimal encoding sensitivities of the DENSE sequence. In these studies, less-than optimal motion encoding sensitivity already induced considerably ghosting artifacts due to phase inconsistencies between the shots, which were due to involuntary subject motion resulting from, among other things, respiration [1; 140]. This sensitivity to involuntary motion prohibited the use of the theoretically optimal motion encoding sensitivity. The recently proposed DENSE sequence [137] circumvents these phase inconsistencies by using a single-shot approach, thereby enabling to increase the motion sensitivity that yields higher SNR in the motion field maps [139]. Moreover, as this approach is less sensitive to subject motion it may be more advantageous to use in patients. Yet, this technique was limited in brain coverage by the 2D acquisitions.

In this work, we present a comprehensive single-shot DENSE sequence with optimized sensitivity that combines the benefit of high SNR for a voxel-wise strain analysis, and a simultaneous multi-slice (SMS) acquisition approach for whole-brain coverage. We use the technique to derive the cardiac-induced tissue deformations and characterize this deformation across the brain. Specifically, we derive the full strain tensor and map it for the entire brain. Besides, we present two scalar maps derived from the tensor: volumetric strain and octahedral shear strain. First,

a brief background on the derivation of the strain tensor is provided, which summarizes the established relevant theory. The heart of this work, however, is the acquisition of deformation gradient fields with sufficient SNR that make the strain tensor reconstruction feasible, without suffering from excessive noise. We acquire the strain tensor in multiple subjects to investigate its inter-subject consistency and also include repeated measurements to assess its repeatability. By combining the data from 9 subjects to MNI space, we aim to quantitatively describe the typical pattern of cardiac-induced brain tissue deformation.

MATERIALS AND METHODS

DENSE sequence

The DENSE sequence [5] consists of a motion encoding and decoding part (see Figure 4-1). The encoding part consists of a gradient between two 90 degrees RF pulses, which imposes a sinusoid on the longitudinal magnetization of which the local phase encodes the current position of the tissue. After a given time, the decoding part reads out the prepared longitudinal magnetization. Any tissue displacement along the direction of the encoding gradient leads to a corresponding phase shift in the resulting phase image. This way, DENSE – analogue to velocity encoding – manipulates the phase information such that it becomes proportional to the displacement of brain tissue that occurred between encoding and decoding.

Tissue displacement maps (u_x , u_y , u_z) can be derived from motion-sensitive phase images acquired through DENSE by

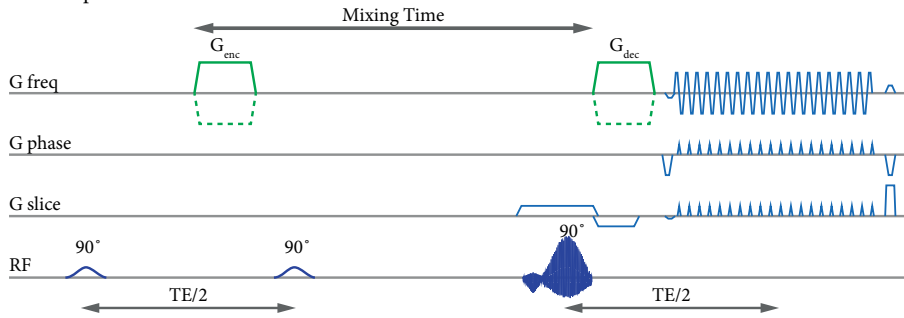
$$u_x = \frac{DENC}{\pi} \phi_x \quad (4-1)$$

where ϕ_x is the phase of the DENSE MRI signal acquired after motion encoding in the x-direction and DENC is the displacement encoding value in units of meters (similar to the VENC parameter used in phase-contrast MRI, which has units of meters/second). At this point, the MRI phase signal contains both phase contributions due to cardiac-induced motion, subject motion and phase confounders from respiration and the RF coils, which are later regressed out after computing the deformation gradients.

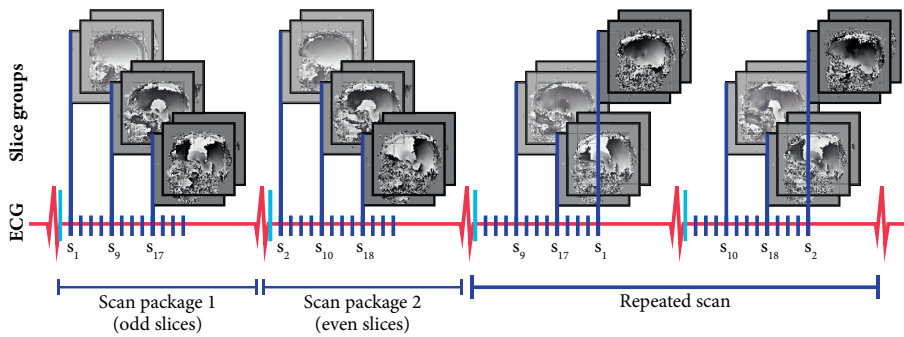
Simultaneous multi-slice DENSE

Our previous developed cardiac triggered, single-shot DENSE sequence [137] was modified to be compatible with a simultaneous multi-slice (SMS) acquisition approach to obtain time- and SNR-efficient whole brain DENSE acquisitions [17]. While the encoding part of the DENSE sequence (first two RF pulses) remained unchanged and non-selective, the third RF pulse for slice selective excitation needed modification to be compatible with a multiband SENSE acquisition

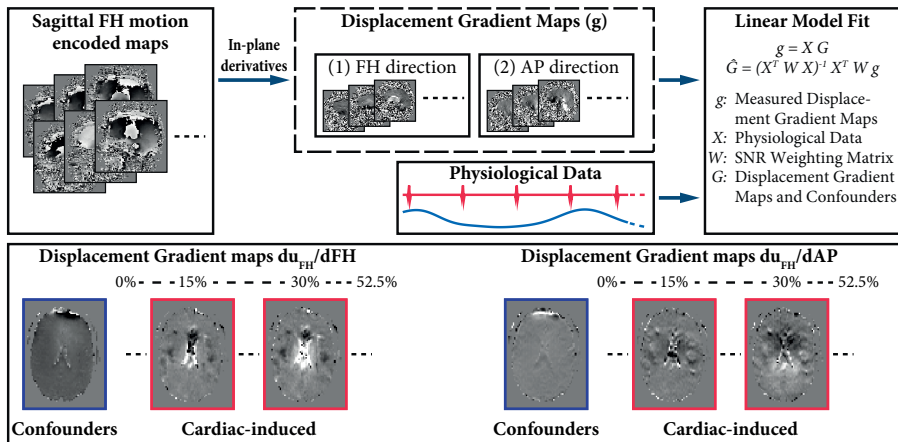
1. Principle SMS DENSE



2. Data acquisition



3. Analysis



← **Figure 4-1** Simultaneous multi-slice (SMS) DENSE acquisition principle, combined with an example for data acquisition and analysis of one DENSE series. In the current example, motion encoding was in the Feet-to-Head direction with a sagittal acquisition orientation. Repeating the DENSE MRI sequence for additional in-plane encoding directions with sagittal, coronal and transverse orientation, resulted in 6 datasets.

(1) SMS DENSE consists of 2 non-selective 90° RF pulses to encode the tissue. After a given mixing-time, a selective 90° multi-band RF pulse is employed to excite and acquire (in the current method) a slice group of 3 2D slices.

(2) Data was recorded over 24 repeated acquisitions with alternating encoding direction sign to distinguish between phase contributions due to motion and a motion independent phase confounders. Each repeated acquisition consisted of 12 excitations in each package with a multi-band factor of 3, which equals to 72 slices. Odd slices (associated with excitations s1, s3 ... s23) were acquired in the first package whereas the even slices (associated with excitations s2, s4 ... s24) were acquired in the second package. Slice order was permuted over the repeated acquisitions to obtain each slice at different moments in the cardiac cycle.

(3) Time-series of displacement-encoded phase images (d) were used to derive displacement gradient maps (g, two maps for each encoding direction). The current sagittal example yields the $\frac{\delta u_{FH}}{\delta FH}$ and $\frac{\delta u_{FH}}{\delta AP}$ displacement gradients, which are shown here in transverse orientation to illustrate the full brain coverage with isotropic voxels. Using the physiological data, these gradient maps were fitted in a linear model to obtain the displacement maps and confounders (G) in 8 interpolated cardiac phases across the 0 - 52.5% of the cardiac cycle.

approach [17]. We achieved this by replacing the standard excitation pulse with a SMS excitation pulse as implemented by the vendor on the scanner for other sequences. This SMS excitation pulse combines a standard two-lobe sinc pulse with two frequency offsets to obtain a user defined spacing (72 mm in our case) between the slices. The duration of the multiband RF pulses was longer compared to the standard RF-pulse (3.39 ms vs 1.13 ms). The simultaneously acquired volumes were reconstructed by the standard reconstruction platform of the MRI scanner. A full evaluation of the SMS method for the proposed DENSE sequence is provided in the supplementary file (Figures 4-S1 and 4-S2).

Data acquisition

The Ethical Review Board (ERB) of the University Medical Center Utrecht approved the use of healthy volunteers for MRI protocol development. Nine healthy volunteers (6 males, 3 females, age 30 ± 4 years) were included and written informed consent was obtained in accordance with the ERB approval. The volunteers were scanned at 7T (Philips Healthcare, Best, The Netherlands) using a 32-channel receive head coil within an 8 channel transmit/receive head coil (Nova Medical) operated in quadrature mode. In each volunteer, 6 DENSE series with in-plane motion-encoding in the Right-to-Left (RL), Anterior-to-Posterior (AP) and Feet-to-Head (FH) direction were obtained. The series were acquired with different orientations: 2 sagittal series (in-plane FH and AP encoding), 2 coronal series (in-plane FH and RL encoding) and 2 transverse series (in-plane AP and RL encoding). The purpose of each of these DENSE series was to provide two components of the deformation gradient tensor (see Eq. 4-5), by taking the in-plane spatial derivatives from the motion encoded data (see Table 4-S1 in the supplementary files for complete overview). Each DENSE series consisted of 72 slices and had the following imaging parameters (see Figure 4-1): acquired resolution: $3 \times 3 \times 3 \text{ mm}^3$; FOV: $250 \times 250 \times 216 \text{ mm}^3$ (72 slices);

multi-band factor: 3 (24 excitations); slice gap: 0 mm; displacement encoding (DENC): 80 μm ; 2 packages (12 excitations per package; odd slices in first package and even slices in the second); single-shot EPI readout (EPI factor: 33); SENSE factor: 2.6 (AP or RL, depending on acquisition orientation); TE/2: 20 ms and EPI band width in the readout/phase encoding direction; 2.7 kHz/pixel; 47 Hz/pixel. Furthermore, each DENSE series consisted of 24 repeated scans, in which 12 slice order permutations were applied together with 2 opposite encoding directions (to distinguish between motion-induced phase and phase confounders). Saturation effects from neighboring slices were remedied by acquiring odd and even slices in two separate packages. Slice order permutations for each repeated scan ensured that each slice was acquired at different time-locations into the cardiac cycle. Physiological data were simultaneously recorded by using a vector cardiogram (VCG) and a pulse oximeter (POx) for backup. Acquisition of each DENSE series had a duration of 48 heartbeats: 2 slice packages (odd vs. even slices; each package covering one cardiac interval) \times 12 permutations over the cardiac cycle \times 2 encoding polarities, resulting in a scan time of 48 s for 60 beats per minute (bpm) and 4:48 min total scan time to produce a complete set. Each slice package consisted of 12 slice groups, which, together with a MB factor of 3, resulting in 36 slices per cardiac interval. The temporal slice spacing depended on the heartrate of the volunteer and was chosen such that the 11 intervals between the 12 slices covered at least 50% of the cardiac cycle (which implies a temporal slice spacing of 45 ms for 60 bpm). The minimum temporal slice spacing required to perform the EPI acquisition was 42 ms, regardless of the heartrate. Furthermore, the time required between encoding and decoding the first slice was 30 ms, regardless of heart rate.

Time-resolved 2D CSF flow measurements were acquired using retrospectively-gated phase-contrast MRI (PC-MRI) to compare the CSF stroke volume with the brain volumetric strain as an independent means for validation of the DENSE measurements. The 2D slice was planned at the C2-C3 level of the spinal canal. Motion-encoding was in the FH direction towards the spinal canal. Two different encoding sensitivities of 5 and 10 cm/s were acquired to obtain accurate measurements while avoiding phase wraps. Other imaging parameters included: acquired resolution $0.45 \times 0.45 \times 3 \text{ mm}^3$; FOV: $424 \times 408 \text{ mm}^2$; SENSE: 2 (RL) and 30 reconstructed cardiac phases over the cardiac interval. The scan duration of the PC-MRI was 1:43 min for a heart rate of 60 bpm.

Two additional scans were acquired for data processing purposes. First, a T1-weighted (T1w) turbo field echo (TFE) scan (acquired resolution $1.00 \times 1.00 \times 1.00 \text{ mm}^3$; FOV $250 \times 250 \times 190 \text{ mm}^3$; TFE factor 600; inversion delay 1292 ms, SENSE 2 (AP direction); FA 5° ; TR 4.2 ms; TE 1.97 ms; acquisition time 2 min) was acquired as anatomical reference. Second, two B0 field maps were obtained: the first was acquired at the beginning of the scanning session, and was used to perform second order image-based B0 shimming; the second was acquired after shimming to allow us to correct for remaining geometric distortions in the acquired DENSE images. A single B0

field map was reconstructed from the phase difference of two successive gradient echo scans with fixed TR, and different TE, as available from the vendor (acquired resolution $3.50 \times 3.50 \times 3.50$ mm³; FOV $224 \times 224 \times 224$ mm³; FA 8°; TR 3.9 ms; TE 1.57 ms and 2.57; scan duration: 25 s).

Strain tensor reconstruction

From DENSE series to displacement gradient fields

The acquired DENSE series were analyzed offline with custom software written in MATLAB R2018b (The MathWorks, Inc., Natick, MA, USA). The positive and negative encoded slices in one DENSE series were registered using Elastix with a rigid transformation [82]. Linear interpolation on the complex data was performed to transform the data. Since slices were acquired at different time-locations into the cardiac cycle, only in-plane translations and rotations were allowed during registration, preventing interpolation between adjacent slices that were not acquired at the same time location. The shimmed B0-map was then registered to the DENSE series and used for EPI distortion correction [79]. Registration and distortion corrections were applied to the real and imaginary components of the complex data of the DENSE series. After these initial corrections to the data, apparent displacement field maps were obtained from the phase signal for the positive and negative polarities of the encoding gradient (see Eq. 4-1). These fields still included confounding factors from non-motion related phase contributions such as the RF phase. Gradients were derived from these apparent displacement field maps by computing spatial derivatives along the two in-plane coordinate axes. Each DENSE series thereby produced two apparent displacement gradient fields (which still contained phase confounders). As a result, 12 apparent displacement gradient fields for the 6 DENSE series were produced (see Supplementary Table 4-S1). Phase wraps in the phase images caused a large numeric derivative $\Delta\phi$, which was resolved by adding or subtracting 2π to $\Delta\phi$ to bring it closer to zero if

$$|\Delta\phi| > \Delta\phi_{max} = 1.5\pi \quad (4-2)$$

which represents a maximum tolerated strain of

$$\varepsilon_{max} = \frac{\Delta\phi_{max}}{2\Delta x} \frac{DENC}{\pi} = \frac{3}{4} \frac{DENC}{\Delta x} \quad (4-3)$$

For a resolution of 3mm isotropic and an encoding sensitivity DENC of 80 μ m, this results in a maximum strain of 2%, which is well over the maximum expected tissue strains of 0.6%. The VCG and POx trigger data as recognized by the scanner software were used to deduce the positions of the acquired slices relative to the cardiac interval. Each apparent displacement gradient map was fitted voxel-wise to the physiological data in a linear model as described before [137]. To account for differences in heart rate between subjects, and between repeated scans, the linear model was defined for 8 cardiac phases at fixed relative positions in the cardiac cycle, in a way that is equivalent to linear interpolation between the 12 acquired heart phases. As a result, 8

displacement gradient maps were obtained, distributed over the over the cardiac cycle at 0, 7.5, 15, 22.5, 30, 37.5, 45 and 52.5% of the cardiac interval. The 8 displacement gradient maps over the cardiac cycle, show these displacement gradients with reference to end-diastole, which has by definition zero strain (and, thus, zero displacement gradients).

From displacement gradient fields to strain tensor

The displacement gradient fields were obtained from all 6 motion-encoded DENSE series that were acquired for each subject. Next, magnitude data of these DENSE series were used to register the displacement gradient fields by using Elastix in a group-wise rigid registration in combination with third order b-spline interpolation [82]. Each DENSE series provided two components of the displacement gradient tensor. For instance, the sagittal oriented dataset with FH encoding direction from Figure 4-1 provides the displacement gradient fields $\frac{\delta u_{FH}}{\delta FH}$ and $\frac{\delta u_{FH}}{\delta AP}$ (see Eq. 4-5). The diagonal elements of the displacement gradient tensor were obtained twice, each for a different acquisition orientation. We inspected the consistency between the pairs of diagonal elements and confirmed that they showed reasonable agreement and no systematic differences (see Figure 4-S3 in the supplementary files for consistency). Hence, we averaged the pairs of data before the strain tensor was obtained from Equation 4. In this work, we reconstructed the strain tensor of tissue relative to diastole (e.g. the R-top in the ECG signal). The strain tensor describes the stretch and compression behavior of an image-voxel along three orthogonal directions. In principle this can be any direction, yet, for three dimensions, the eigenvalue decomposition returns the three directions in which only pure stretch or compression occurs, without shear strains. The accompanying eigenvalues are the respective strains in these directions, and known as the principal strains. We will mainly focus on two of these directions: the first principle direction of dominant stretch and the third principle direction of dominant compression. The principle strains are visualized by using directionally encoded color (DEC), known from diffusion tensor imaging, enabling qualitative visual comparisons [120]. Figure 4-2 shows this principle, where the direction of the eigenvector in each voxel is depicted by the RGB color scheme, while the intensity represents the magnitude of associated principle strain.

Volumetric strain and octahedral shear strain

The Lagrangian strain tensor strain tensor \mathbf{E} can be written as follows [52]:

$$\begin{aligned} \mathbf{E} &= \frac{1}{2}(\mathbf{F}^T\mathbf{F} - \mathbf{I}) \\ &= \begin{pmatrix} \varepsilon_{xx} & \varepsilon_{xy} & \varepsilon_{xz} \\ \varepsilon_{yx} & \varepsilon_{yy} & \varepsilon_{yz} \\ \varepsilon_{zx} & \varepsilon_{zy} & \varepsilon_{zz} \end{pmatrix} \end{aligned} \quad (4-4)$$

\mathbf{E} is symmetric and independent of rigid body translation or rotation. It describes the tissue deformation, where the diagonal elements of \mathbf{E} (ε_{xx} , ε_{yy} and ε_{zz}) describe the local stretch (positive)

or shortening (negative) of the tissue in the associated direction, while the off-diagonal elements describe the shear components. The deformation gradient tensor \mathbf{F} is given by

$$\mathbf{F} = \nabla \mathbf{u} + \mathbf{I} \quad (4-5)$$

where \mathbf{I} is the identity matrix and u_x , u_y and u_z are the measured displacements in Right-to-Left, Anterior-to-Posterior and Feet-to-Head, respectively. From \mathbf{E} we derive two scalar quantities: the volumetric strain and octahedral shear strain. The volumetric strain reflects net expansion or compression of the voxel, relative to (in the present study) end-diastole. Under the assumption of very small deformations, the volumetric strain ε_V can be approximated by summing over all eigenvalues [1]:

$$\varepsilon_V = \frac{\Delta V}{V} \approx \varepsilon_{xx} + \varepsilon_{yy} + \varepsilon_{zz} \quad (4-6)$$

Octahedral shear strain signifies how much the voxel deforms and is independent of volumetric strain. The octahedral shear strain can be considered as a measure for the differences between of the three principal strains, indicating the deviation from isotropic swelling (three equal, positive principal strains) of a voxel during the heartbeat and is given by Eq. 4-7 below [98].

$$\varepsilon_S = \frac{2}{3} \sqrt{(\varepsilon_{xx} - \varepsilon_{yy})^2 + (\varepsilon_{xx} - \varepsilon_{zz})^2 + (\varepsilon_{yy} - \varepsilon_{zz})^2 + 6(\varepsilon_{xy}^2 + \varepsilon_{xz}^2 + \varepsilon_{yz}^2)} \quad (4-7)$$

While the octahedral shear strain is zero for isotropic swelling (or shrinkage), it is larger than zero for deformations (either isovolumic or non-isovolumic) with different principal strains (e.g. stretch in one direction and compression in a perpendicular direction). The octahedral shear strain is a positive number, while a value of 0 indicates isotropic deformation of the voxel (i.e. the same amount of stretch or compression in each orthogonal direction).

Repeatability

DENSE series were repeated with repositioning of the subject to assess the test-retest reliability of the measurements. The total scan session including both repeated measurements lasted less than 90 minutes. Comparing the original measurement with the repeated measurement was done by rigid registration of the T1w scan associated with the repeated measurement to the T1w scan associated to the original dataset. The resulting transformation was then performed on the displacement gradient fields belonging to the repeated measure using third order b-spline interpolation. Both T1w scans were segmented using Computational Anatomy Toolbox (CAT12, version 1615, Jena University Hospital, Departments of Psychiatriu and Neurology) for Statistical Parametric Mapping (SPM12, version 7771, Wellcome Trust Centre for Neuroimaging, University College London) and a combined brain mask was created out of the tissue probability maps, where voxels containing any CSF in the original or the repeated T1w scan were discarded. An additional city-block erosion step was included to assure that no partial volume effects from CSF

were present in the deformation gradient maps, as neighboring voxels would influence values in a given voxel via the derivative calculations. All remaining voxels were used to assess regional repeatability.

Per subject, repeatability analysis was performed on the eigenvalues, volumetric strain and octahedral shear strain measures deduced from the two strain tensor reconstructions. The analysis was separately performed for seven brain regions of interest (ROIs): cerebellum, brain stem, basal ganglia, temporal lobe, occipital lobe, parietal lobe and frontal lobe. MNI labels registered to the original T1w scan were used to distinguish between the different regions. The repeated measurements were evaluated using the voxel-wise SNR as the reciprocal of the coefficient of variation:

$$SNR = \frac{|\mu|}{\sigma} \quad (4-8)$$

where μ is the mean of the two measurements averaged over all voxels in the ROI and σ the standard deviation over the voxel-wise difference between the measurements.

External validation

Per subject, the volumetric strain measurements were validated against the CSF in/outflow in the foramen magnum. To this end, we compared the average volume change of brain tissue resulting from the volumetric strain to the change in CSF volume obtained at the C2-C3. This method was used previously to validate the multi-shot 3D DENSE method and an approximately linear relationship was reported between CSF flows and brain tissue volume pulsations over the cardiac cycle [2]. Here we use the same approach to validate the current single-shot SMS DENSE method.

The average volume change over the cardiac cycle can be obtained from the whole-brain average volumetric strain by solving Eq. 4-6 for ΔV . The absolute volume of white matter and gray matter was obtained through brain segmentation of the T1w scan (registered to the mean DENSE magnitude image resulting from the group-wise registration) using CAT12. From the tissue probability maps, a mask was created where all voxels containing any CSF in the original or the repeated T1w scan were discarded. An additional city-block erosion step was included to assure that no partial volume effects from CSF were present. This way, the analysis was exclusively due to the rise in volume of the tissue, as all CSF and large vessels embedded in the CSF, like the circle of Willis, were excluded by using such a stringent mask. The average volumetric strain was obtained over the same eroded, CSF free tissue mask, that was generated for assessing the regional repeatability. Multiplying the volume of grey and white matter with the average volumetric strain, resulted in the volume change over the cardiac phases.

The volume of CSF was calculated by integrating the CSF velocity maps over the cardiac cycle and multiplying the result by the area of the spinal canal. Furthermore, the volume curves were shifted in time to compensate for the encoding delay in the DENSE series. The encoding delay is defined as the time between an observed R-top trigger by the MRI system and the encoding gradient applied to encode the signal. The encoding delay was 20ms, resulting in a shift of 2-3%, depending on the heartrate. Both the tissue volume curve and CSF stroke volume curve were independently corrected so that they both would intersect the origin at point (0 , 0).

Average strain tensor

The overall behavior of the strain tensor was assessed by combining the results of the first measurement for all individual subjects in MNI space (ICBM 2009c Nonlinear Symmetric [46; 47]). Per subject, the reconstructed strain tensor was registered to MNI space using the associated T1w scan: First, the T1w scan was registered to the mean DENSE magnitude image resulting from the group-wise registration of the six DENSE series, after which it was registered to MNI space by using Elastix using an affine registration followed by a non-linear b-spline regularized registration [82]. The resulting transformation was then applied to the strain tensor with third order b-spline interpolation for the eigenvalues and nearest neighbor interpolation for the (unit) eigenvectors. Furthermore, the direction of the eigenvectors were corrected using the rotation component of the affine registration step [88]. The volumetric strain and octahedral shear strain were computed in native space before transforming the maps to MNI space. Third order b-spline interpolation was used when transforming these scalar maps to MNI space. The resulting maps were averaged over all subjects, resulting in average maps for the first eigenvector (most expansion), the third eigenvector (most compression), the volumetric strain and octahedral shear strain. SNR maps representing the voxel-wise SNR derived from the repeated measurements, were also included for the volumetric strain and octahedral shear strain (see Eq. 4-6 and 4-7).

RESULTS

Strain tensor

Figure 4-2 represents an example of the strain tensor map for subject 4 at peak systole (specifically 30% of the cardiac cycle for the current subject) in the native space of this subject. Only the first principal strain (maximum expansion, Figure 4-2b) and third principle strain (maximum compression, Figure 4-2c) are represented together with its associated eigenvalue. In rare occasions an eigenvector decomposition of a voxel resulted in either three positive (< 1% of the voxels) or three negative eigenvalues (< 0.3% of the voxels). In these cases respectively, the associated compression (third component) or expansion direction (first component) were set to 0. The first principle strain and third principle strain will be referred to as the positive strain and negative strain, respectively.

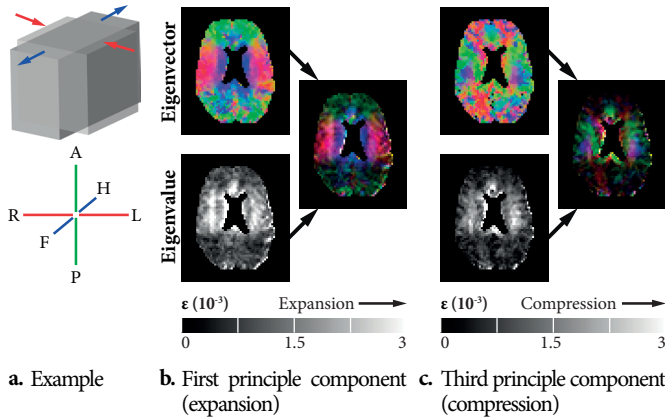


Figure 4-2 (a) Top figure: A deformed voxel at peak systole relative to end-diastole serves as an example to illustrate how a voxel stretches along a certain 1D direction (blue arrows), while at the same time it compresses along another orthogonal direction (red arrows). Bottom figure: The RGB color coding of directionality [120]. Red: Right-to-Left (RL); green: Anterior-to-Posterior (AP) and blue: Feet-to-Head (FH). Figure 4-b and c show the direction and magnitude of largest expansion (first principal strain) and largest compression (third principal strain) in each voxel for subject 4, respectively (unsmoothed data from measurement 1 in its native space). Top figure: the direction of the eigenvector in each voxel using the directionally encoded color scheme. Bottom figure: gray-scale maps representing the magnitude of the associated principle strain. For the third principle component, the absolute value of the eigenvalues was taken, resulting in a map with only positive values. Multiplying the eigenvectors with the eigenvalues results in an intensity color map.

Brain regions with large expansions (positive strain) were generally accompanied by large compressions (negative strain) in a direction perpendicular to the expansion direction. This observation, where axial expansion of an object in the direction of the expansion load is accompanied by transverse compression, is also known as the Poisson effect (See Figure 4-2).

Volumetric strain and octahedral shear strain

Peak systole, defined as the moment of largest mean volumetric strain, ranged between 30 – 37.5% of the cardiac interval, depending on the subject. Figure 4-3 shows the volumetric strain and octahedral shear strain at peak systole for subject 5 at different locations in the brain. Cortical regions show mostly isotropic expansion (low shear strain). Volumetric strain and shear strain did not substantially correlate (average $R^2 = 0.003$). On average, peak volumetric strain and peak shear strain were reached at the same time. However, in subject 5 the volumetric strain peak came after the peak in octahedral shear strain, at 37.5% and 22.5%, respectively. This observation was consistent between the first and repeated scan.

Per subject

The individual strain maps are provided in Figure 4-4 for all subjects. The results show similar trends for all subjects, where the positive principal strain direction follows the known brain

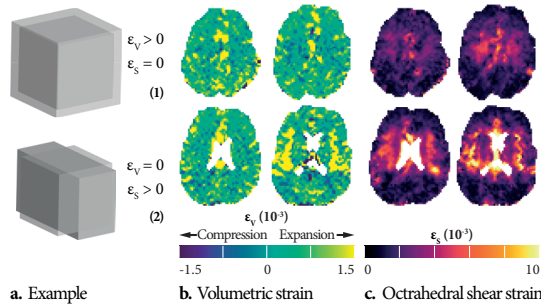


Figure 4-3 Volumetric strain and octahedral shear strain for subject 5 (unsmoothed data from measurement 1). (a) Example demonstrating the concepts of volumetric strain and shear strain. The first example (top) shows a voxel with isotropic swelling at peak systole. This voxel increases its volumetric strain without inducing shear strain. The second example (bottom) represents a voxel with isovolumetric deformation (preserving its volume), which yields non-zero octahedral shear strain [98]. (b) Peak volumetric strain (with respect to diastole) shows an increase at the cortical surface and near sulci. (c) Peak shear strain is most pronounced in regions near the ventricles. The volumetric strain and octahedral shear strain barely correlate ($R^2 < 0.0001$ for current subject), illustrating that they reflect different aspects of the deformation of the voxel.

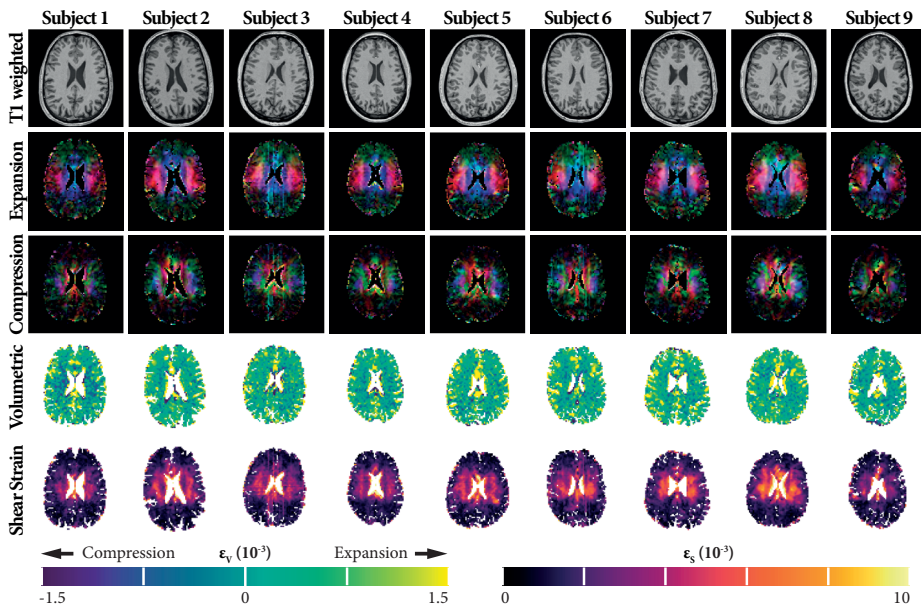


Figure 4-4 Transverse slice in the middle of the brain represented for each subject (columns) and the various outputs from the strain tensor analysis (rows). The color scaling of the principle strains is the same as illustrated in Figure 4-2. The T1-weighted image is shown as anatomical reference (top row). A similar trend in all subjects can be observed. The positive principal strain tensor (second top row, expansion) follows the known funnel shaped pattern pointed towards the foramen magnum [58]. The negative principal strain tensor (middle row, compression) is more heterogeneous across subjects, but is locally of the same magnitude as the positive principal strain, reflecting the Poisson effect. The volumetric strain (second bottom row) is larger towards the periphery of the brain compared to regions where white matter is present. Furthermore, the volumetric strain is weakly correlated to the octahedral shear strain (bottom row), which shows large shear strains in the white matter, around the ventricles.

motion pattern, which is funnel shaped and pointing towards the foramen magnum [58]. The negative principal strain direction is somewhat heterogeneous across subjects, but its magnitude correlates with the magnitude of the positive principal strain, reflecting the Poisson effect in all subjects. The volumetric strain is larger in regions where more gray matter is present. On the other hand, the octahedral shear strain is more pronounced in regions in the white matter, near the ventricles. Data quality was high in all subjects with some visible artifacts (stripes) in subject 3 and 6, presumably due to subject motion during scanning.

Repeatability

Repeated measurements were performed for all subjects, except subject 3, who opted out after the first scan as he felt uncomfortable. Subject 3 could therefore not be included in the repeatability study.

The comparison between the initial measurement and the repeated measurement is shown in Figure 4-5, which consists of a summarized Bland-Altman plot for each individual subject, for seven spatial brain regions. The mean of the two repeated scans is shown as a black dot, with surrounding error bars representing the non-parametric reproducibility coefficient ($\pm 1.45 \times$ interquartile range). The mean voxel-wise SNR (see Eq. 4-8) over all subjects per ROI is presented as well. The complete set of Bland-Altman plots for the volumetric strain and octahedral shear strain of one of the subjects, is shown in the supplementary files (see Figures 4-S4 and 4-S5).

Of the quantities that were assessed, the octahedral shear strain shows the best voxel-wise repeatability and also has the highest SNR in all regions compared to the other quantities. Volumetric strain has the lowest SNR and showed poor voxel-wise repeatability.

External validation

A good agreement was found between volumetric tissue strains and the changes in the CSF flow through the spinal canal over the cardiac cycle, between 0 and 52.5% (see Figure 4-6). Linear regression of volumetric tissue strain versus CSF yielded a mean slope of 0.78 ± 0.10 with R^2 of 0.91 ± 0.08 . The peak CSF stroke volume occurred at 43% of the cardiac interval and was on average 0.58 ± 0.09 mL. The peak in brain tissue volume increase was on average 0.46 ± 0.11 mL and occurred at 34% of the cardiac interval.

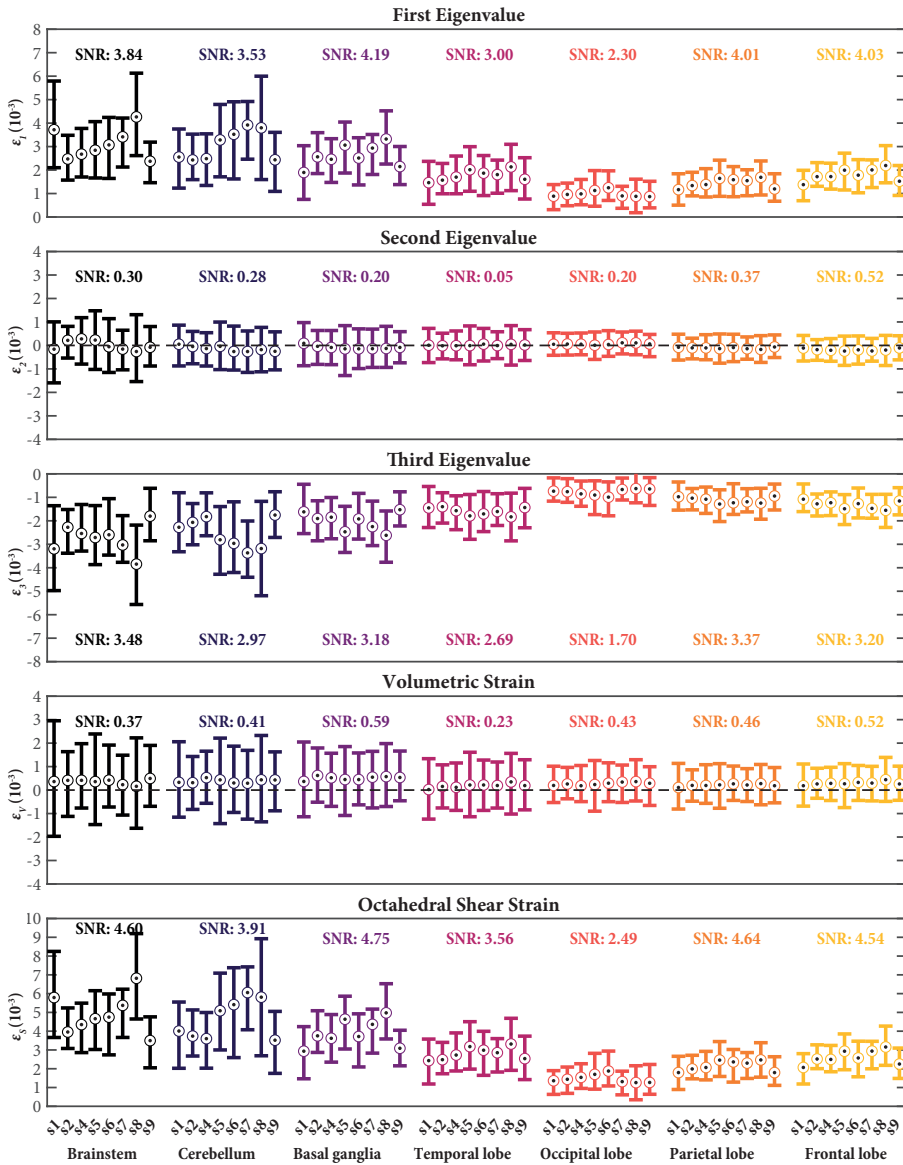


Figure 4-5 Representation of the voxel-wise analysis of the repeated measurements for seven separate brain regions. Each error bar in fact represents a summarized Bland-Altman plot of one subject for each brain region (see Figure 4-S4 and S5 for complete Bland-Altman plots). The mean of the two repeated scans is shown as a black dot. The reproducibility coefficient and systematic offset from the voxel-wise difference between the two scans in the indicated brain region are indicated as follows: the error bar represents the non-parametric reproducibility coefficient ($\pm 1.45 \cdot \text{IQR}$) and systematic offset is captured by a shift of the error bars with respect to the mean. As a result, repeated measurements without a systematic difference have a positive and negative error bar of equal length. The systematic offset between the two scans was at most $0.4 \cdot 10^{-3}$ for the octahedral shear strain and $0.2 \cdot 10^{-3}$ for the volumetric strain. The listed SNRs represent the SNR within each brain region derived from the voxel-wise difference between the repeated scans (see Eq. 4-8), averaged over all subjects.

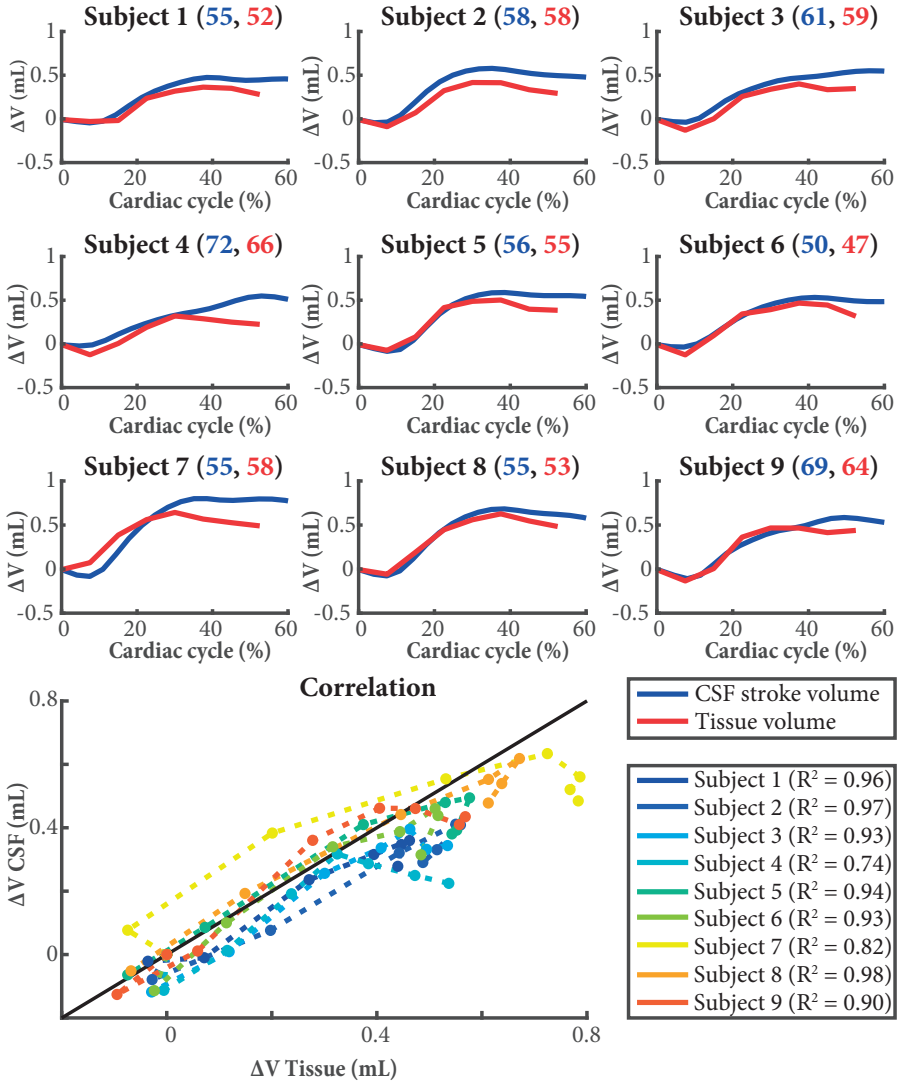
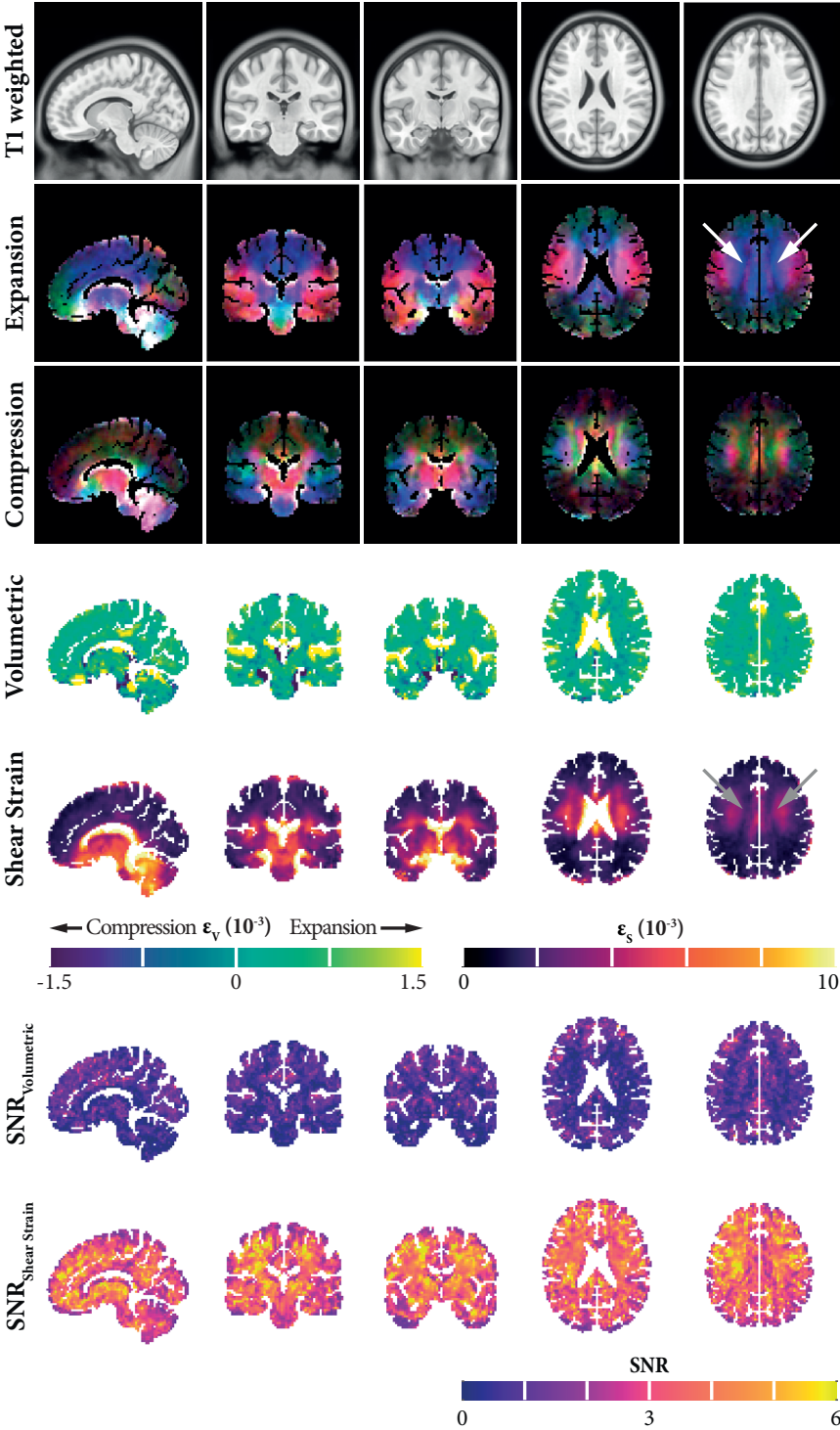


Figure 4-6 Per subject comparison of CSF volume expelled from the intracranium (measured at the C2-C3 level) with tissue volume change obtained from the volumetric strain measurements. The expelled CSF volume (in mL) is shown over the cardiac cycle interval running from 0 to 60%. Tissue volume measurements were obtained only for 0 to 52.5% of the cardiac interval. Numbers in the title of each graph represent the average heartrate of the subject for the associated measurements (CSF stroke volume in blue and tissue volume in red, in beats per minute). Additionally, we provide a correlation graph that shows the relation between expelled CSF volume and tissue volume change. Each subject is represented by a different colored line; the black line indicates the identity relation.

Average strain

The overall behavior of the strain tensor, volumetric strain and octahedral shear strain in MNI space, averaged across subjects, is shown in Figure 4-7. This Figure 4- clearly shows distinct strain patterns. These patterns are already discernable at the individual subject level in Figure 4-4, but can be better explored in relation to brain anatomy on the averaged data. While tissue expansion roughly follows the typical macroscopic, funnel-like direction towards the foramen magnum, some white matter bundles can be distinguished due to a different expansion direction compared to its surroundings. The location that might be the corona radiata [3], for example, has a different expansion direction compared to its surrounding white matter tissue (see Figure 4-7). The same fiber tract is also observed in the octahedral shear strain, where this bundle has reduced anisotropy compared to its surrounding. Furthermore, tracts like the cerebral peduncles and corpus callosum also show distinct expansion from surrounding tissue, which is accompanied by large shear strains. The rostral slices indicate increased shear strain in the deep white matter structures (i.e. centrum semiovale and cingulum) relative to the cortical gray matter.

Volumetric strain, on the other hand, is most pronounced at the cortical gray matter and basal ganglia. Here, it should be noted that the mask overlaying the results was derived from the CSF probability map, but did not include an additional erosion step to assure no partial volume effects from CSF. As a result, regions adjacent to CSF (e.g. ventricles or sulci) may suffer from artefacts due to free moving water. This is reflected by extreme values in these areas, especially visible in the volumetric strain map, and is shown in more detail in the supplementary files (Figure 4-S6). Voxel-wise SNR maps of the volumetric strain and octahedral shear strain are added to the figure in the bottom two rows, where the standard deviation was calculated over the nine subjects. The average SNR across voxels for the volumetric strain and shear strain in the brain's tissue was 0.82 and 3.4, respectively. Again, virtually no correlation between volumetric strain and octahedral shear strain was found ($R^2 = 0.0004$).



← **Figure 4-7** Voxel-wise average of the positive and negative strain in MNI space over all 9 subjects (taking measurement 1 only, without smoothing of the data).

A T1-weighted image is included for anatomical reference. The voxel-wise average of the volumetric strain and octahedral shear strain are shown as well, including an SNR map of the volumetric strain and shear strain, where the standard deviation per voxel was calculated over the nine subjects in MNI space. Color scaling for the positive and negative principle strain is different from Figure 4-2 and is limited to $2 \cdot 10^{-3}$ to better capture the anterior and posterior structures. Color scaling for the volumetric strain and shear strain is equal to the scaling presented in Figure 4-3. Please note that voxels adjacent to CSF may suffer from artefacts due to free moving water. Especially the extreme values in the volumetric strain maps are probably artefacts due to partial volume effects.

The figure shows how specific tracts and other anatomical structures clearly emerge from the strain maps, with distinct patterns for different adjacent structures. The bundle that looks like the corona radiata, for example, can be distinguished due to a different expansion direction compared to its surrounding white matter tissue and is indicated with white arrows (expansion map), and a lower octahedral shear strain, as indicated with gray arrows (anisotropy map).

DISCUSSION

In this work, we presented a comprehensive single-shot DENSE sequence that combines the benefit of sufficient SNR to perform a voxel-wise strain analysis, with a simultaneous multi-slice acquisition approach that enables whole-brain coverage within approximately 5 minutes of scan time. We used the developed sequence to reconstruct the strain tensor of brain tissue resulting from cardiac pulsations in the microvasculature and explored its behavior across the brain [1; 2; 140]. Additionally, we derived two scalar maps: volumetric strain and octahedral shear strain. We acquired the strain tensor in nine subjects, with repeated measurements in eight subjects to assess test-retest reliability. An external validation of the volumetric strain was performed by correlating the results to the CSF flow at the C2-C3 level. By combining the data from all subjects to MNI space, we documented the behavior of tissue deformation as for an average brain and investigated the inter-subject consistency of the observations. To the best of our knowledge, this is the first time that the full strain tensor from cardiac-induced deformation is measured in the human brain with full brain coverage.

The cardiac-induced 3D strain tensor was visually represented by the first principle strain (expansion) and third principle strain (compression). These deformation maps reflect neuroanatomical details of the brain's structure; parts of white matter bundles like the cerebral peduncles, corpus callosum and corona radiata in the centrum semiovale can be distinguished due to a different expansion direction compared to their surrounding tissue. Regions with large positive eigenvalues, often show large negative eigenvalues as well, reflecting the Poisson effect. Given the random orientation of the microvasculature, we initially expected a more isotropic deformation pattern (less shear strains) as a result of the non-oriented swelling of the microvascular bed. However, the first principle strain is predominantly directed both towards the ventricles and downwards towards the brain stem, which could reflect low resistance towards CSF spaces. We

found principle strains ranging from 0.09 – 0.43% (Figure 4-5), with largest strains in the brain stem (range: 0.23% – 0.43%) and lowest strains in the occipital lobe (range: 0.09% – 0.12%), indicating regional heterogeneity of tissue deformation. Pahlavian et al. mention 0.38% as maximum principle strain observed in the brain stem [119; 142], which compares well to our findings. Yet, they derived \mathbf{F} under the assumption of volume conservation, which relies on the false assumption of no volumetric strain fluctuations [1; 70; 138]. As a result, it is necessary to measure \mathbf{F} in all directions. Furthermore, it is not directly apparent to what extent regional microstructure affects the strain tensor's behavior. While tissue expansion roughly follows the typical directions of white matter fiber bundles pointing towards the foramen magnum, the corpus callosum, for example, mainly expands in directions perpendicular to the fiber bundles running from the left to right hemisphere [18; 106]. It should be noted that we implicitly assumed that the strain tensor would not change principal directions during the cardiac cycle, so we could limit our analysis to the strain tensor at peak systole. The exact time course of the strain tensor over the cardiac cycle and its relation to the microstructure of the brain remain topics for future research.

The different locations for which volumetric strain and shear strain are most pronounced, show that these quantities depict different aspects of the local mechanical behavior of the tissue. Especially shear strain showed good repeatability and relative high SNR. Volumetric strain, on the other hand, was most difficult to repeat on a voxel by voxel basis. This is due to the summation over all three eigenvalues, of which the first (positive) and the last (negative) eigenvalues largely cancel each other, while the noise increases by a factor of $\sqrt{3}$ from the summation. Yet, averaging over a small ROI already leads to enough noise reduction to detect regional physiological differences reflected by the volumetric strain. For instance, individual volumetric strain maps already show regional differences in subjects between the insula and white matter. Comparing the SNR to previous work shows that we gained at least a factor of 1.8 in SNR of the volumetric strain maps [1]: Adams et al. reported a voxel-wise standard deviation of the volumetric strain of $1.4 \cdot 10^{-3}$, while we measured an SNR for strain of 0.39 (mean over all regions), which corresponds to a standard deviation of $0.74 \cdot 10^{-3}$ (given an average volumetric strain of $2.9 \cdot 10^{-4}$). In comparing these numbers one should note that Adams' estimation was theoretically derived from SNR measurements of the magnitude images, while we obtained the noise estimate from voxel-wise comparison between repeated scans after repositioning. Our noise estimation, thus, includes contributions from physiological noise and imperfections in the registration. Most importantly, the 3D approach used by Adams et al. often suffered from increasing artifact levels towards the end of the cardiac cycle due to inter-shot phase inconsistencies, which we avoided by the single-shot approach. These artifacts cannot easily be quantified and prohibits in depth comparison of the gain in SNR and image quality. Nevertheless, we obtained the gain in SNR in less than half of the scan time (4.8 min vs 13.5 min), albeit at the cost of an increased voxel size (3 mm versus 2.2 mm isotropic resolution).

The rise in blood volume that enters the cranium from the heart during systole, is compensated by an outflow of CSF into the spinal canal. We measured the cerebral tissue expansion with DENSE and assessed the outflow of CSF at the C2-C3 level. Given the incompressibility of CSF, this approach is justified under the Monro-Kellie doctrine, which implies a fixed intracranial volume [58]. We analyzed the 0-50% cardiac interval and found an approximate linear relationship between CSF and volumetric strain over the cardiac cycle, which is consistent with current concepts of intracranial volume change [2]. Since the phase difference between the two curves is known to be minimal, no additional challenges were posed on this analysis [2]. Yet, the method does not take into account contributions from both larger arteries and veins embedded in the intracranial CSF. The C2-C3 location is often used to measure CSF outflow, since the narrow spaces ensure higher and more homogeneous flows, mainly directed Feet-to-Head, which can be measured more reliably [6; 15; 58]. The choice of this location by us and in previous literature, implicitly assumes that CSF volume buffering between the foramen magnum and this level is negligible compared to the volume buffered by the rest of the spinal sac below the C2-C3 level, which seems reasonable given the relative proximity to the foramen magnum. The internal validation of our method with CSF stroke volumes confirms the correct implementation and scaling of the strain measurements obtained through DENSE. The effect on volumetric strain due to partial volume effects was addressed by including a stringent mask to calculate the volumetric strain. Still, it remains a limitation of this method that we could assess the DENSE series only with a rather coarse resolution of 3mm isotropic. The effective resolution of the derived strains is further reduced by the spatial derivative operation, which uses the displacement information from two neighboring voxels to compute the strain. These artifacts are particularly seen at CSF-tissue boundaries as shown in Figure 4-S6, and also visible around the ventricles of other work (e.g. Figure 4-2 in reference [119]). We mitigated these effects as much as possible by using a stringent mask. Computing the derivative on the complex signal through the Fourier transform could possibly avoid smoothing through the spatial derivative, albeit at even higher noise amplification than the spatial derivative operation [89]. Nevertheless, we are hampered in our analysis by partial volume effects, especially in regions near free moving water like sulci, and in structures that fall below the current resolution, like the cerebral cortex. Cortical regions tend to contribute more to the average volumetric strain compared to the deep white matter structures. Excluding these voxels from the analysis by the stringent masking, probably led to a slight underestimation of the tissue volume compared to the CSF. Although the ability to study the swelling of the microvasculature bed with DENSE remains advantageous over ‘mass-balance’ approaches that study blood- and CSF flows at the spinal canal [15; 165], the proposed method has currently limited capabilities to avoid partial volume effects with medium- to large-sized vessels at the cortex, which may hamper accurate assessment of cortical gray matter volumetric strains. In the meantime, the rather good correlation between CSF flows and total brain tissue volumetric strain shows the potential of 2D CSF measurements at the spinal canal as a straightforward approach to assess the average pulsation of the brain’s blood volume. Since CSF measurements are easily done

and have less SNR constraints, it may be attractive to perform these measurements at 1.5 or 3T [13]. One caveat, however, is the open question whether it will faithfully reflect cerebral blood volume pulsations in disease, as the relative contribution from the vessels embedded in the brain tissue and the larger vessels in the CSF might be different in disease.

The DENSE method has some intrinsic properties that are important to consider when comparing DENSE with other methods (e.g. PC-MRI) or for different field strengths. The stimulated echo acquisition employed by DENSE ensures that signal loss during the time between encoding and decoding is predominantly proportional to T1, and decays with T2 as function of the TE [49]. As a result, the time between encoding and decoding can be extended significantly with DENSE compared to PC-MRI, resulting in increased motion sensitivity [169]. Besides, tissue T1 time-constants are considerably longer at higher field strengths, yielding a better performance of this sequence at high-field for longer encoding-decoding delays. When optimizing the DENSE motion sensitivity for assessing strain like we did in the current paper, the largest source of signal loss is due to diffusion effects arising from the large b-values induced by the large encoding gradients combined with long decoding times, which does not change with field strength. In studies that used DENSE for tissue displacement only, diffusion effects did not play a key role since the encoding sensitivity (and thus the associated b-value of the encoding gradients) was limited to avoid phase wraps [140; 180]. In this study, the high sensitivity of the DENSE sequence resulted in raw displacement images corrupted with many phase wraps, which prohibits the reconstruction of displacement images. Furthermore, the high sensitivity of the sequence prohibits the use of a multi-shot approach to potentially increase the resolution. Phase inconsistencies between shots from involuntary subject motion may then lead to artifacts. While we mitigated this effect by using a single-shot approach, we are limited in the spatial resolution. Furthermore, we do not think the proposed method can tolerate a 3/7 factor reduction in SNR resulting from a translation to 3T clinical scanners without compensating this SNR loss by, for example, further increasing the voxel size.

Volumetric strain reflects both blood volume increase (microvascular expansion) and tissue stiffness. For instance, white matter could be stiffer [80] and has reduced blood-volume to tissue ratio compared to gray matter [9; 30; 164]. These combined properties result in volumetric strain increase being dominant in the cortical gray matter compared to white matter regions. Extensive elastography reconstructions could help to unravel blood volume change from tissue elasticity [150], providing a window to tissue integrity as well as perfusion pressure [68]. Yet, it is important to note that, besides microvascular expansion and tissue stiffness, the volumetric strain also reflects potential simultaneous compression of the interstitial space and draining veins that act as Starling resistors [135]. Comprehensive computer models that take into account the interaction between blood and CSF, while correcting for tissue stiffness, could help to gain further insight into these effects [91; 92; 133]. In the meantime, the observed volumetric tissue strain can be regarded as a lower bound estimation of the underlying blood volume pulsations

and may help in advancing our understanding of diseases like cerebral small vessel disease and vascular contributions to neurodegenerative diseases [137].

The mean spatial pattern of high octahedral shear strain roughly follows the distribution of deep medullary veins as reported previously [85]. The presence of these medullary veins may reduce the apparent shear stiffness of these regions. The deep medullary veins support the venous drainage of the brain and have shown abnormalities in the context of different cerebrovascular diseases [60; 108; 174]. Although the current young population is not a representative group to study these types of diseases, these results show that the technique is sensitive enough to detect regional normal differences in tissue deformation that can be compared with other structural brain maps. This indicates that the technique has potential for studying abnormal tissue deformation in disease.

The technique proposed in this study is prone to EPI distortion. To mitigate the effects, we used 2nd order image-based B0 shimming. To address remaining geometric distortions, we used a shimmed B0 field map to correct these. Registration to a reference volume or blip-up blip-down acquisition are alternative methods that aim to solve EPI distortion corrections, and are in principle suited to implement as an alternative [8]. Since the spatial derivative used to obtain strain maps depends on an accurate distance between adjacent voxels, it is important to correct for EPI distortions before the strain is computed from the displacement fields. Moreover, the different acquisition orientations also require correct EPI distortion correction, especially as they do not all share the same phase encoding direction. Here, it must be acknowledged that the correction and registration steps used in this method are prone to error propagation due to multiple interpolation steps. Although we tried to mitigate these effects by linear interpolation on the complex data and limited degrees of deformation freedom in the groupwise registration, especially the MNI registration may have induced additional noise. Furthermore, it should be mentioned that the proposed technique relied on single-shot 2D acquisitions, that are prone to blurring in the slice direction due to thickened slices as a result of imperfect slice profiles.

In conclusion, the developed single-shot SMS DENSE method is capable of consistently assessing the brain tissue strain tensor on a voxel-wise level, despite the amplified noise introduced by the use of spatial derivatives. Through a principle component analysis, we successfully derived the principal strain directions, and illustrated the Poisson effect *in vivo* in brain tissue. Besides, we derived the volumetric strain and octahedral shear strain. Volumetric strain measurements were consistent with physiological blood volume change and CSF flow through the spinal canal. Shear strain can be interpreted as a metric of inequality of the three principal strains, indicating to what extent an induced volumetric strain is achieved by equal expansion of the tissue element in all directions. This novel method provides a tool to visualize and study tissue dynamics that

reflect fundamental aspects of both the microvascular function as well as mechanical properties of tissue and holds potential to serve for detecting abnormalities in tissue deformation in disease.

SUPPLEMENTARY MATERIAL

Simultaneous Multi-Slice validation

We validated the slice profile of the simultaneous multi-slice acquisition approach in Subject 1 using a standard multi-shot gradient echo sequence with in-plane resolution of $0.3 \times 0.3 \text{ mm}^2$ and FOV $250 \times 250 \text{ mm}^2$. The slice thickness was set to 3 mm. Two datasets were acquired: one with the SMS excitation pulse and one with the conventional 2D excitation pulse for validation. For the SMS excitation, the gap between the slices was set to 69mm (equal as for the DENSE sequence). Further imaging parameters included: coronal acquisition orientation; EPI factor: 5; SENSE factor: 1; flip angle 90 degrees; TR: 4 s; TE: 16 ms. Readout gradients were placed on the slice selection axis to obtain slice profiles (see Figure 4-S1 top-left for example). Slice profiles were obtained by analyzing the intensity projection along the RL direction and are provided in Figure 4-S1. The results show well defined slice profiles without significant sidebands that could lead to cross-talk.

Additional validation was performed by comparing DENSE datasets acquired with conventional multi-slice and simultaneous multi-slice acquisitions. We obtained DENSE datasets with these sequences for Subject 1 and Subject 2 with sagittal orientation and in-plane encoding (AP and FH) according to the protocol described in the paper. Acquisition of the conventional multi-slice DENSE series took 3 times longer compared to the simultaneous multi-slice approach (48 s versus 2:24 min for 60 bpm). From the motion encoded DENSE series, we computed displacement gradient fields and interpolated the data to obtain 8 cardiac phases between 0 and 52.5% of the cardiac interval as described in the Methods section. We compared the values voxel wise at peak systole (37.5% of cardiac interval for both subjects). The results are provided in Figure 4-S2 and consist of 4 Bland-Altman plots per subject (one Bland-Altman plot for each obtained displacement gradient field at peak systole).

The obtained reproducibility coefficients are smaller than the ones obtained from comparing the same parameter as obtained from DENSE series with different acquisition orientations (see Figure 4-S3), illustrating that the SMS implementation works well and contributes negligible additional uncertainty to the measurements.

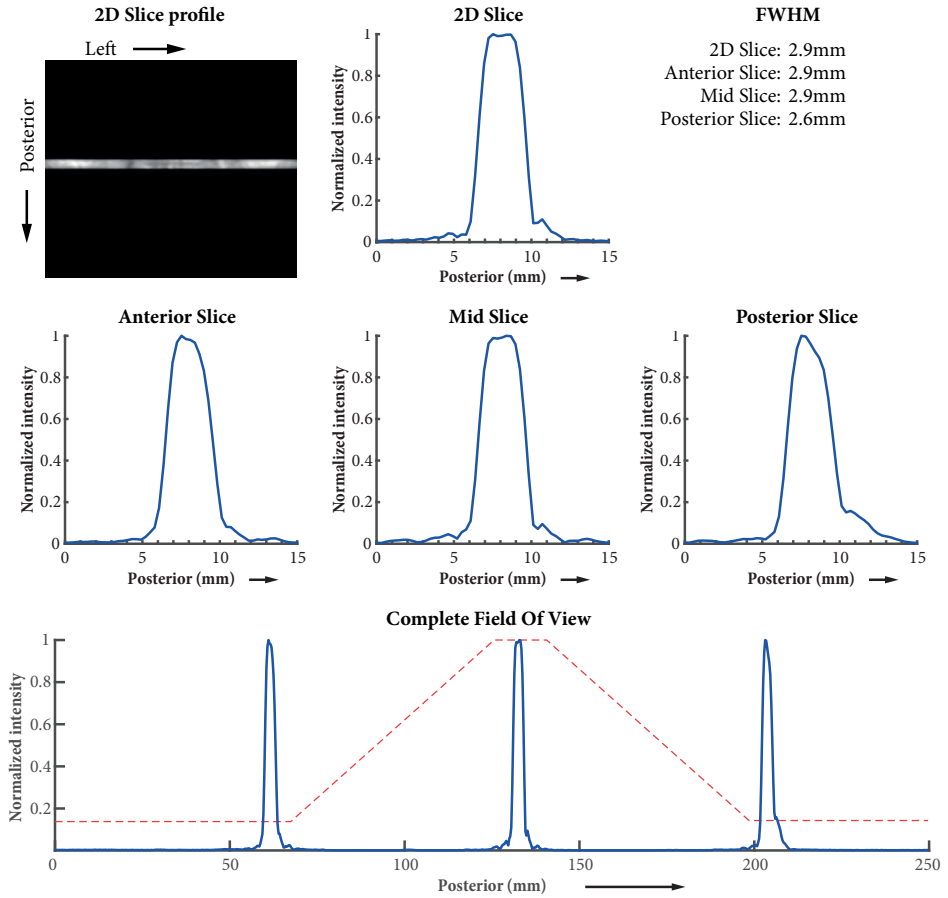
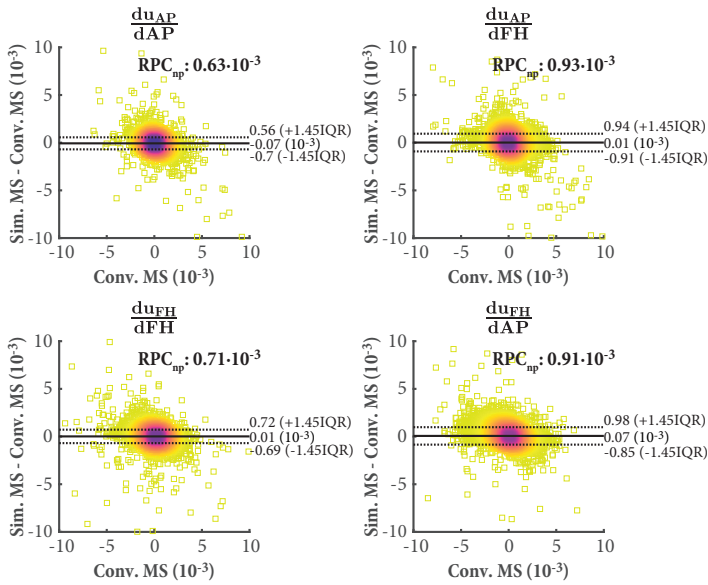
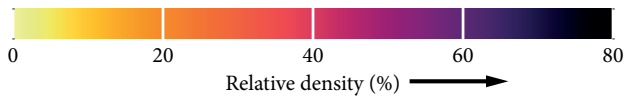
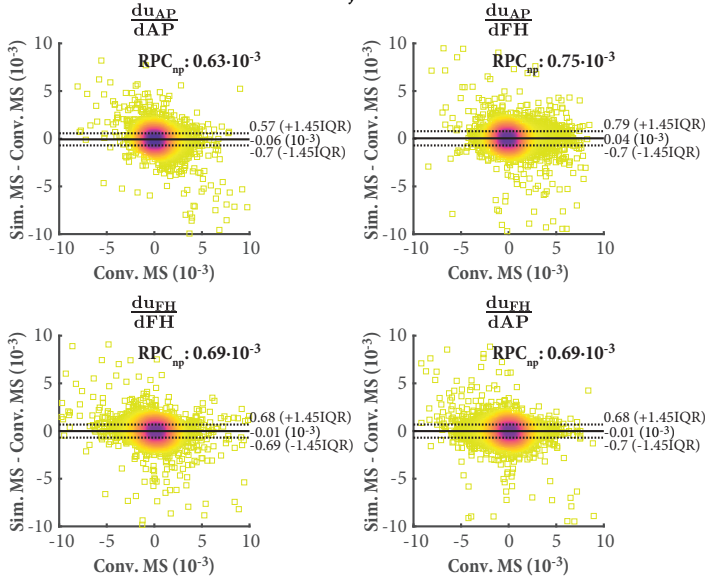


Figure 4-S1 Slice profiles for a conventional 2D acquisition (top row) and simultaneous multi-slice acquisition with factor 3 (middle row), together with the complete FOV for the simultaneous multi-slice acquisition (bottom row). For illustration purposes, we show the acquired image that was used to obtain the slice profile for the 2D acquisition in the top-left corner. Slice profiles were obtained by projecting the intensity along the RL direction. The intensity for each slice was normalized. This normalization varied over the FOV depending on the magnitude intensity of the slice. The relative normalization denominator is indicated by the dotted red line (bottom row). Especially the Anterior and Posterior slice had low intensity, since these slices were only just inside the head, where B1+ (flip angle) is relatively low. Full width at half maximum (FWHM) for each slice profile are provided in the top right corner of the figure.

Subject 1



Subject 2



← **Figure 4-S2** Bland-Altman plots for data obtained with conventional multi-slice (Conv. MS) and simultaneous multi-slice (Sim. MS) in Subject 1 and Subject 2. Measurements obtained with conventional multi-slice are considered the ‘ground truth’. The dotted lines intersecting the y-axis indicate the non-parametric reproducibility coefficient (RPC_{np}). The RPC_{np} is defined as $1.45 \cdot IQR$, which is $\sim RPC$ if the distribution of differences is normally distributed. Any systematic offset between conventional multi-slice and simultaneous multi-slice is defined as the median of the difference between the datasets and indicated by the solid line intersecting the y-axis. Since these methods should yield similar results, a systematic offset of 0 is to be expected. The colors in the scatter plot indicate the density of points relative to the total number of points, determined by using Gaussian moving average with $\sigma = 1 \cdot 10^{-3}$ as weighting kernel.

Remaining supplementary figures and tables

Acq. Orientation	Motion encoding direction	Displacement gradient
TRA	AP	$\delta u_{AP} / \delta AP$
		$\delta u_{AP} / \delta RL$
	RL	$\delta u_{RL} / \delta RL$
		$\delta u_{RL} / \delta AP$
SAG	FH	$\delta u_{FH} / \delta FH$
		$\delta u_{FH} / \delta AP$
	AP	$\delta u_{AP} / \delta AP$
		$\delta u_{AP} / \delta FH$
COR	RL	$\delta u_{RL} / \delta RL$
		$\delta u_{RL} / \delta FH$
	FH	$\delta u_{FH} / \delta FH$
		$\delta u_{FH} / \delta RL$

Table 4-S1 Overview of the displacement gradient field components obtained from the different DENSE series to fill the full displacement gradient tensor $\nabla \vec{u}$ from which the deformation gradient tensor \mathbf{F} is obtained (see Eq. 4-5). The components on the diagonal are obtained twice in this scheme, for different acquisition orientations. These double components were averaged before further analysis.

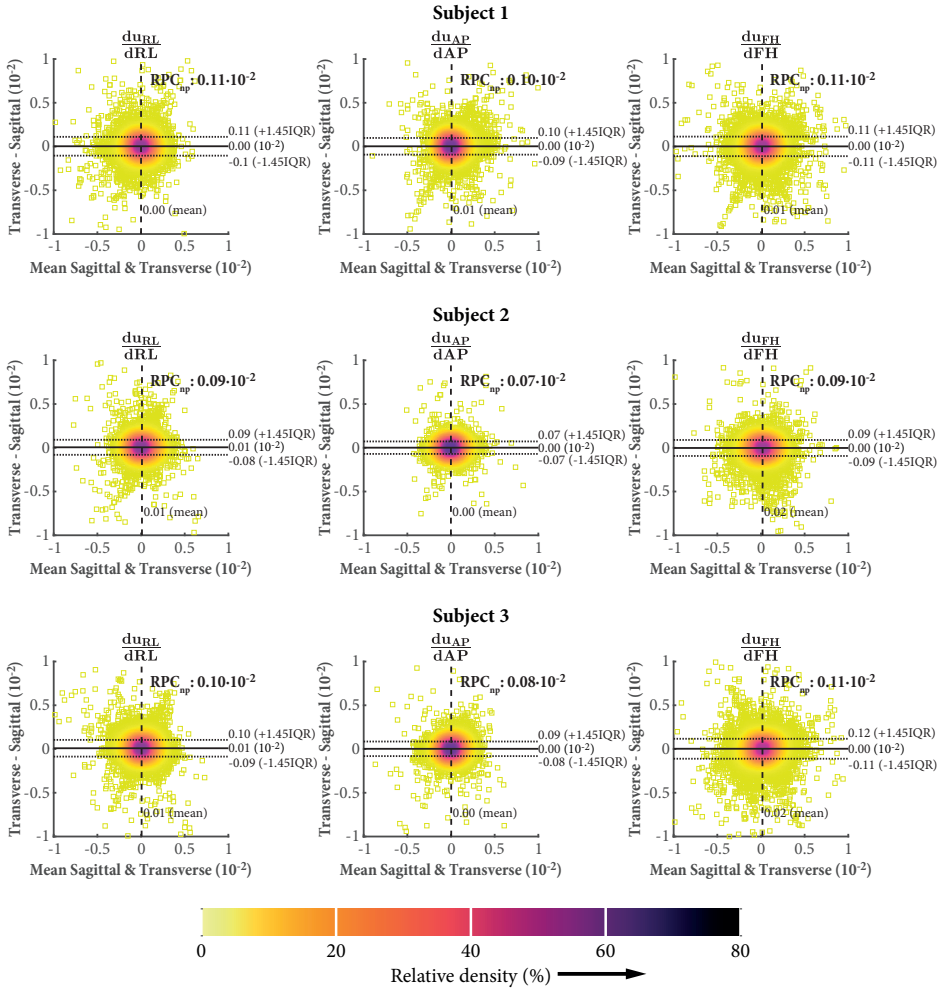


Figure 4-S3 Bland-Altman plots for the diagonal elements of the deformation gradient tensor (see Eq. 4-2), which were obtained twice, as a result of the acquisition scheme (see Table 4-S1). The Bland-Altman plots are given for Subject 1-3, and show the consistency between deformation measurements using different slice orientations during acquisition. The non-parametric reproducibility coefficient (RPC_{np}) is defined as 1.45-IQR (which is $\sim RPC$ if the distribution of differences is normally distributed). Although the $\frac{\delta u_{AP}}{\delta AP}$ deformation gradient field was obtained with phase-encoding direction in the AP direction for both the transverse and sagittal slice orientation, the consistency of $\frac{\delta u_{AP}}{\delta AP}$ is similar to that of $\frac{\delta u_{RL}}{\delta RL}$ and $\frac{\delta u_{FH}}{\delta FH}$, where the phase encoding directions were different between the respective slice orientations (the phase-encoding direction for coronal slices is RL). This indicates that the different phase-encoding direction (and related water-fat shift or deformation) is not the main source of variability between different orientations. The colors in the scatter plots indicate the density of points relative to the total number of points, determined by using Gaussian moving average with $\sigma = 1 \cdot 10^{-3}$ as weighting kernel.

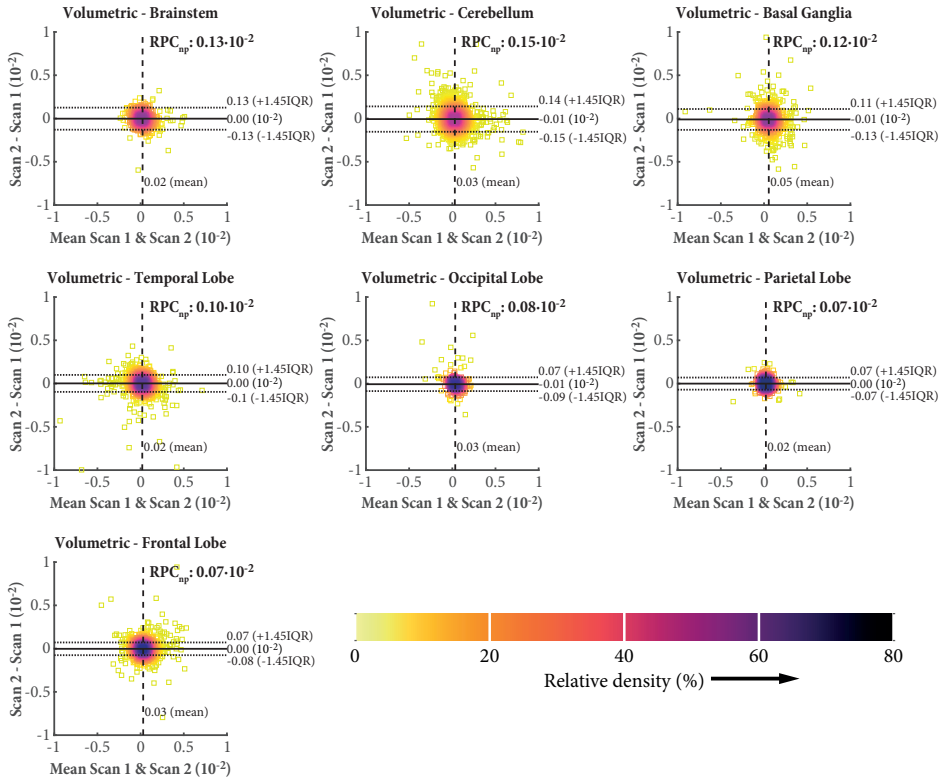


Figure 4-S4 Full Bland-Altman plots for the volumetric strain of Subject 7 serve as an example for how Figure 4-5 was constructed. The mean of Scan 1 and Scan 2 is indicated with the dashed line intersecting with the x-axis and is used as the middle of the error bar plotted in Figure 4-5. The dotted lines intersecting with the y-axis indicate the non-parametric interval of agreement, which is indicated as error bars in Figure 4-5. The non-parametric reproducibility coefficient (RPC_{np}) is defined as $1.45 \cdot IQR$ (which is $\sim RPC$ if the distribution of differences is normally distributed). Any systematic offset is defined as the median of the difference between Scan 1 and Scan 2, indicated by the solid line intersecting the y-axis. Since the methods between Scan 1 and Scan 2 do not differ, a systematic offset of 0 is to be expected. Nevertheless, Figure 4-5 in the main text represents potential systematic offsets by a shift of the error bars relative the mean of Scan 1 and Scan 2. The colors in the scatter plots indicate the density of points relative to the total number of points, determined by using Gaussian moving average with $\sigma = 1 \cdot 10^{-3}$ as weighting kernel.

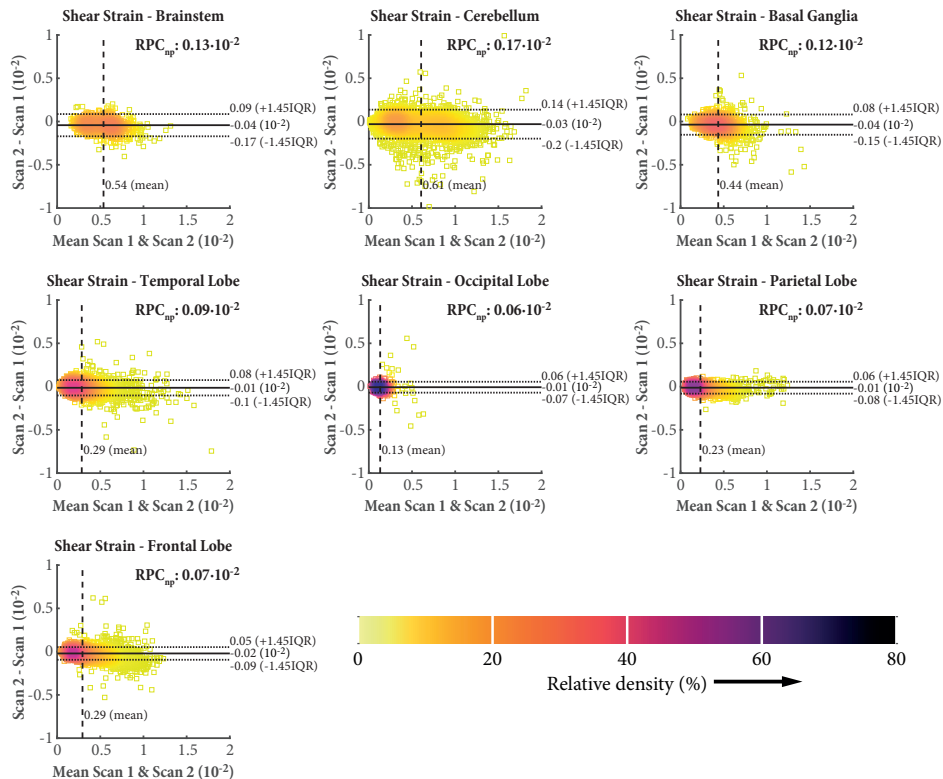


Figure 4-S5 Full Bland-Altman plots for the octahedral shear strain of Subject 7 serves as an example of how Figure 4-5 was constructed. The colors in the scatter plots indicate the density of points relative to the total number of points, determined by using Gaussian moving average with $\sigma = 1 \cdot 10^{-3}$ as weighting kernel. See for full explanation legend of Figure 4-S4.

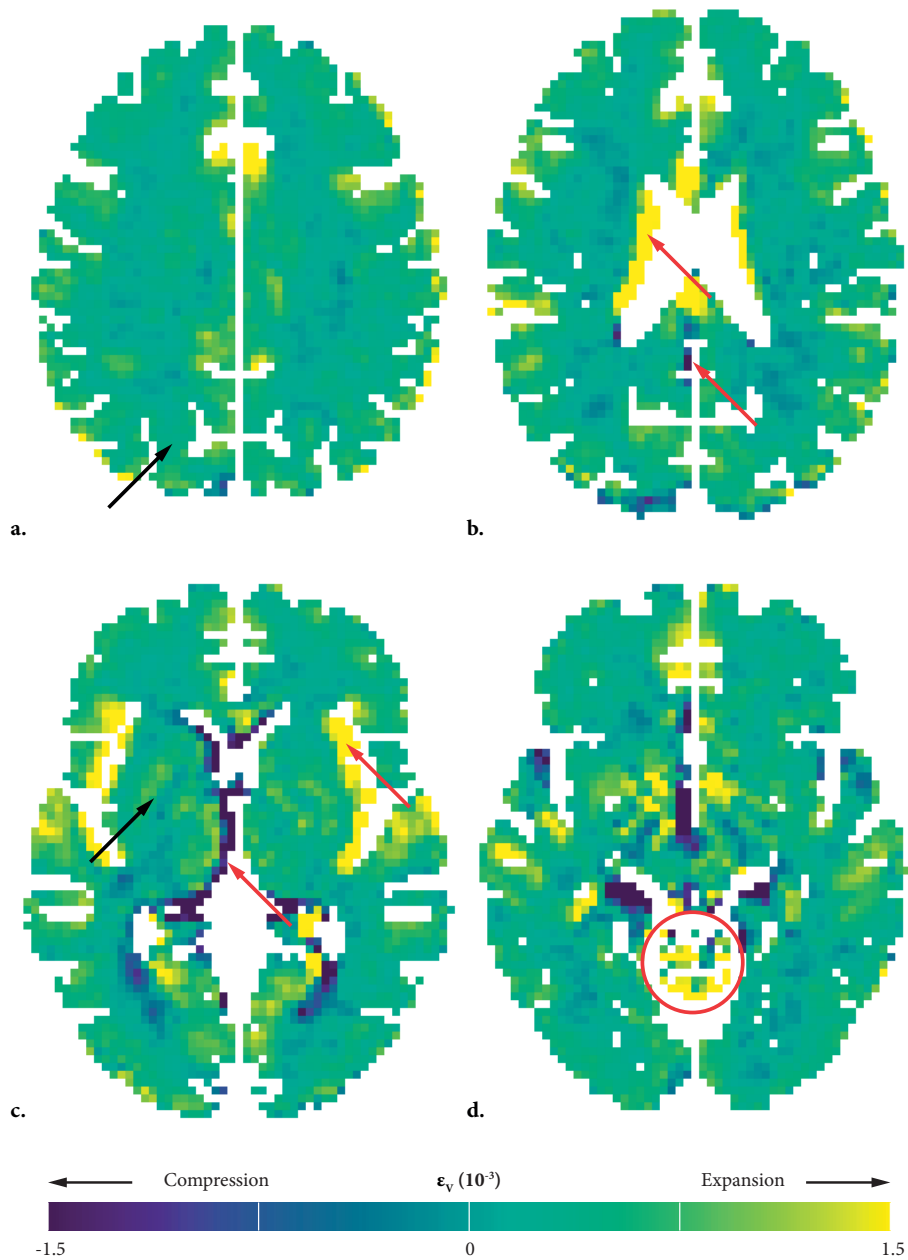


Figure 4-S6 Volumetric strain maps in MNI space. Note that strain values in regions close to CSF can be unreliable due to partial volume effects and registration imperfections. This is reflected by the extreme values as indicated by the red arrows and red circle. Regions with relatively high volumetric strain were observed in the cortical gray matter, compared to the underlying subcortical white matter (black arrow, Figure 4-S6a). The basal ganglia are another area with relatively high volumetric strain (black arrow, Figure 4-S6c).



5

Strain Tensor Imaging: abnormalities in cardiac-induced brain tissue deformation detected on an individual subject level

J.J. Sloots
G.J. Biessels
G.J. Amelink
J.J.M. Zwanenburg

In preparation

ABSTRACT

We present a first ever case study showing abnormal cardiac-induced brain tissue deformations after a craniectomy using a novel 3D strain tensor imaging method at 7T MRI.

INTRODUCTION

Variations in blood pressure and blood volume over the cardiac cycle induce pulsatile brain tissue deformations reflecting the interplay between local blood volume change, tissue properties and tissue position relative to, for example, the ventricles [1; 58]. This causes brain tissue to expand inwards towards the ventricles, thereby showing a funnel-shaped pattern directed towards the foramen magnum [58].

Recently, we developed a magnetic resonance imaging (MRI) method that enables quantification of these tissue deformation patterns [136]. Here we show that the technique is sensitive enough to detect abnormal patterns of cardiac-induced tissue deformations on an individual subject level in a patient who had undergone a craniectomy after severe head injury.

MATERIALS AND METHODS

Patient

An 18-year-old man had suffered a traumatic brain injury from a serious motor cycle accident. He was diagnosed with an acute left-sided subdural hematoma and was treated with a craniectomy. A cranial opening was created with a maximal diameter of 12 cm to reduce cranial pressure. At the time of MRI, one year after the accident, the patient had fully recovered and was about to get an operative skull reconstruction.

Data Acquisition

Written informed consent was obtained from the patient, according to a protocol approved by our Institutional Review Board. Data was acquired at 7T (Philips Healthcare, Best, The Netherlands) using a 32-channel receive head coil within an 8 channel transmit/receive head coil (Nova Medical), operating in quadrature mode.

Strain tensor imaging (STI) was employed with 3mm isotropic resolution to capture cardiac-induced brain tissue deformations. Additional time-resolved 2D flow measurements were acquired at the C2-C3 level using retrospectively-gated phase-contrast MRI (PC-MRI) to compare CSF volume with whole brain tissue volume change. Scan protocols were employed as previously described [136]. However, for the patient, two encoding sensitivities were used (80 μm and 90 μm) to account for possible larger strains. Furthermore, additional data was acquired for which encoding started halfway of the cardiac cycle, enabling us to reconstruct the strain tensor over the complete cardiac cycle for this patient. Thereby, the scan time for the patient took 4 times 4:48 min, resulting in 19:12 min total (for a heartrate of 60 bpm).

Comparison data

We included reference data from our previous study introducing STI for comparison [136]. The reference data originated from STI measurements in nine healthy subjects (6 males, 3 females, age 30 ± 4 years) that was averaged in standard MNI space (ICBM 2009c Nonlinear Symmetric [46]). Out of these nine subjects, the data of the youngest male participant (age 26 years) was selected as single subject comparator.

RESULTS

Figure 5-1 shows the STI maps. Tissue deformation maps of the healthy control are in accordance with the group reference maps. In the patient, however, tissue deformation follows a fundamental different direction. Here, tissue shear strains are high at the frontal edge of the craniectomy, with pulsatile expansion of tissue in the frontal lobe towards the craniectomy. Moreover, the tissue that protrudes from the craniectomy expands parallel to the skin surface, similar to a bulging bicycle tire. Consequently, the other parts of the brain also show patterns that differ substantially from the reference.

Figure 5-2 shows overall volume variation of brain tissue (in red), resulting from cardiac-induced blood volume variations in the microvasculature that is normally compensated by outflow of CSF at the foramen magnum (in blue). In the patient, tissue volume variation remained comparable to the reference data. However, outflow of CSF no longer compensated for this volume variation because brain tissue could pulsate outward from the skull. This shows the invalidity of the Monro-Kellie doctrine in the patient [2; 58].

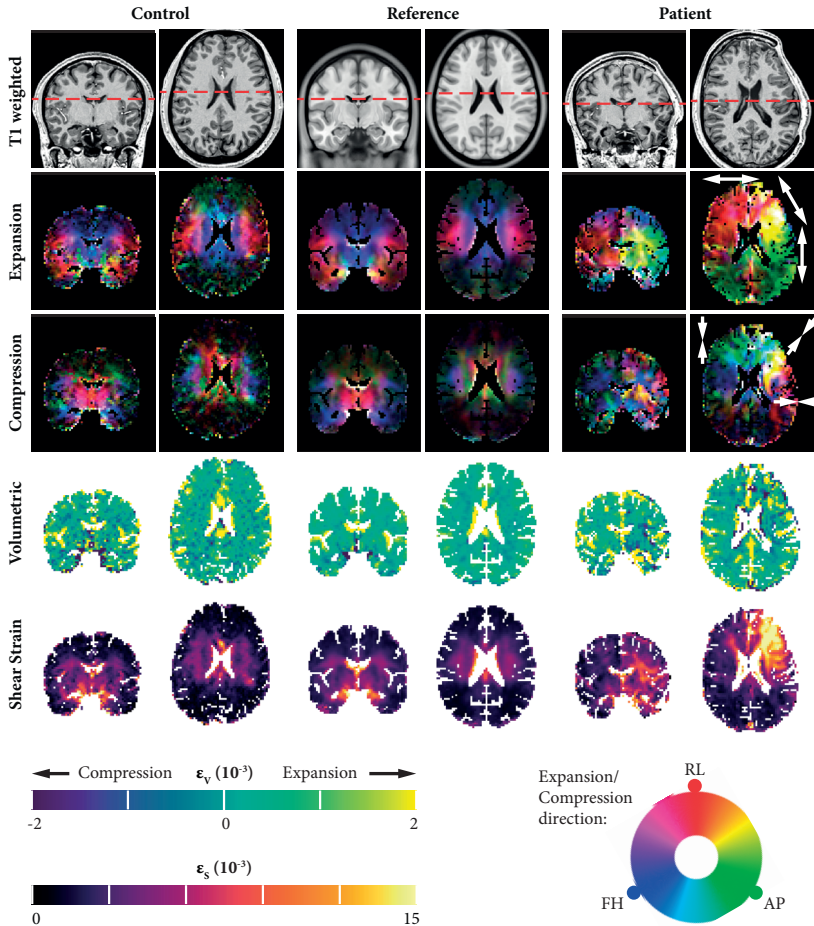


Figure 5-1 Transverse and coronal slice in the center of the brain. Maps of a single control subject (left), a reference set in standard space composed of the average of nine subjects (middle) and the patient (right). T1-weighted images are shown as anatomical reference (top row), where dotted red lines indicate slice intersections. The second row represents the vector of primary tissue expansion: the color denotes the direction of tissue expansion (Red: Right-to-Left, Green: Anterior-to-Posterior, Blue: Feet-to-Head) and the saturation indicates the magnitude of this expansion (increased saturation indicates larger expansion). The complementary tissue compression vector is represented in the middle row. This vector is (by definition) directed perpendicular to the stretch vector, reflecting the so-called Poisson effect. Volumetric strain and shear strain are indicated in the second bottom en bottom row, respectively. Volumetric strain reflects net expansion or compression of a voxel. Shear strain signifies how much a voxel deforms, i.e. the imbalance between expansion and compression, irrespective whether or not this deformation is accompanied by a change in volume. All maps represent peak-systole relative to end diastole.

The single control subject shows deformation maps that match the group reference. However, in the patient deformation patterns are very different. Much tissue expansion is observed around the surface of the craniectomy, directed parallel to the skull opening (indicated with white arrows). The increased inhomogeneous pattern of volumetric strain in the patient might reflect local tissue damage. A main contrast to the reference group are the abnormal shear strains, which are most pronounced on the left frontal part of the brain, at the edge of the craniectomy.

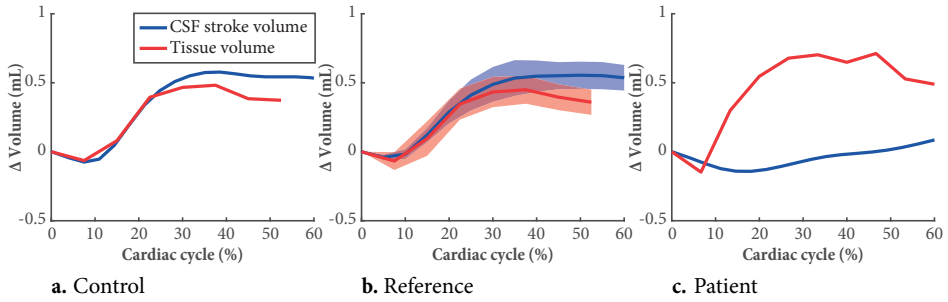


Figure 5-2 CSF volume (blue) pushed out of the skull at peak systole (measured at the C2-C3 level) is compared with whole brain tissue volume change (red) obtained from the volumetric strain measurements. As reference data was only available to 52.5% of the cardiac interval, the interval shown here reaches from 0 and 60% of the cardiac cycle. Data from an individual control subject (a) shows that tissue volume increase during systole is compensated by an outflow of CSF. The reference data (b) was obtained from nine subjects where the shaded area indicates 1 standard deviation over the subjects. (a) and (b) are in line with the Monro-Kellie doctrine, which implies a constant intracranial volume [58; 136]. This doctrine is no longer valid for the patient (c), as the cranial opening changes the boundary conditions. Tissue volume increase is now compensated by tissue swelling through the cranial opening, for which intracranial CSF volume no longer has to compensate.

DISCUSSION

The skull defect had a major impact on brain tissue deformation. As the rigid barrier of the skull was no longer present, tissue strains increased substantially, particular around the edge of the craniectomy. Furthermore, CSF outflow was no longer required to compensate for the pulsatile volume changes of brain tissue, as tissue could swell outward from the skull. The prolonged resulted in an increased SNR of factor $\sqrt{2}$ for the patient compared to the data from healthy subjects.

STI thus showed, for the first time, marked abnormalities in this single patient, but may have much wider potential applications in the evaluation of conditions with aberrant brain deformation or tissue compliance, such as hydrocephalus or brain tumors. Application of the method in these settings, that will likely involve more subtle abnormalities in tissue deformation, warrants further study.



6

Dynamic brain ADC variations over the cardiac cycle and its relation to tissue strain assessed with DENSE at high-field MRI.

J.J. Sloots
M. Froeling
G.J. Biessels
J.J.M. Zwanenburg

Submitted

ABSTRACT

The apparent diffusion coefficient (ADC) of brain tissue slightly varies over the cardiac cycle. Various physiological reasons have been proposed to explain this variation, including mixing or stirring of the interstitial fluid that is relevant for effective brain waste clearance. Yet, it is known from cardiac diffusion imaging that tissue deformation by itself affects the magnitude of the MRI signal, leading to artificial ADC variations that have no further physiological implication. This study investigates to what extent tissue deformation causes artificial ADC variations in the brain. We implemented a high-field magnetic resonance imaging (MRI) sequence with stimulated echo acquisition mode that simultaneously measures brain tissue deformation and ADC. Based on the measured tissue deformation, we simulated the artificial ADC variation and compared the results to the measured ADC variation. The artificial ADC variation was simulated by combining established theoretical frameworks on phase dispersion, tissue deformation, and the diffusion coefficient. We acquired data in 8 healthy volunteers with diffusion weighting $b=300$ and $b=1000$. ADC variation was largest in the Feet-to-Head direction and showed the largest deviation from the mean ADC at peak systole. Tissue deformation accounted for an estimated artificial ADC variation of $0.75 \cdot 10^{-5} \pm 0.29 \cdot 10^{-5} \text{ mm}^2/\text{s}$ in the FH direction. The measured ADC variation in the FH direction, however, was $2.55 \cdot 10^{-5} \pm 0.98 \cdot 10^{-5} \text{ mm}^2/\text{s}$, which was a factor of 3.4 ± 0.57 larger than the artificial diffusion variation from deformation-induced measurement errors. The measured diffusion variations in the RL and AP direction were a factor of 2.0 ± 0.91 and 2.5 ± 0.94 larger than the artificial diffusion variations, respectively. Consequently, ADC variations in the brain likely largely reflect physiology.

INTRODUCTION

The diffusion coefficient reflects the random motion of water molecules as induced by intrinsic thermal energy. It can be measured by applying a pulsed-gradient magnetic resonance imaging (MRI) sequence in a certain direction, providing the apparent diffusion coefficient (ADC) in the associated direction [146]. This way, diffusion weighted imaging (DWI) provides a well-defined diffusion measurement. The magnitude and anisotropy of multiple DWI measurements is used to study neuroanatomical microstructures in the human brain. Previous studies have found slight variations of ADC in brain tissue over the cardiac cycle [94; 111]. Various physiological reasons have been proposed to explain these variations, including variation in amounts of intra and extra cellular fluids and mixing or stirring of fluids in the interstitial space [173]. As interstitial fluids are considered to be involved in the drainage of cerebral waste, dispersion effects like mixing or stirring might contribute to the clearance [65; 125].

Yet, when the targeted tissue deforms during measurements, it has been demonstrated that the measured ADC can vary due to strain modulation of diffusion encoding [127; 128; 159]. Contraction of the tissue increases the spatial frequency of the longitudinal modulation as imposed by the motion encoding gradient, while stretch causes a decrease in this frequency. These changes in spatial frequency change the effective b-value experience by the tissue [127]. At the same time, tissue deformation leads to imperfect refocusing of the signal resulting in a lower magnitude signal than if there had been no tissue deformation [170]. Especially in cardiac diffusion imaging, these effects have become most apparent because of the considerably high tissue deformations in the beating *in-vivo* heart [159]. Thus, measured ADC variations depend on at least two factors: physiological factors reflecting differences in fluid properties of the tissue and “artificial” variations that arise from tissue deformation with no further physiological implication. It is yet unclear to what extent ADC variations in the brain can be explained by these “artificial” effects that tissue strains have on ADC measurements.

ADC variations in the *in-vivo* heart can be mitigated by imaging the diffusion tensor with a stimulated echo acquisition mode (STEAM) only in so-called “sweet spots” of myocardial strain at which the temporal mean of strain approaches zero [159]. Each cardiac interval has two such spots, but the temporal positions of these spots depend on the cardiac interval of the subject. Stoeck et al. proposed a method to correct for strain influences on diffusion measurements [147]. Especially at peak systole, mean diffusivity (MD) measurements increased on average from $0.90 \cdot 10^{-3} \text{mm}^2/\text{s}$ before correction to $0.103 \cdot 10^{-3} \text{mm}^2/\text{s}$ after correction, which is an increase of 14%. In the human brain, these ADC fluctuations are much more subtle. Nakamura et al. reported ADC's over the cardiac cycle ranging between 0.71 and $0.78 \cdot 10^{-3} \text{mm}^2/\text{s}$, which is still equivalent to a measured variation of almost 10%. Although the comparison between these studies is difficult, the difference in ADC variation between cardiac and brain can be explained – at

least partly – by differences in tissue strain. Maximum tissue strains in the heart are in the order of 20%, which is two orders of magnitude larger than observed in the brain [118; 147; 155]. Although brain tissue deformations are much smaller compared to the heart, previous studies reporting ADC variations in the brain did not account for the “artificial” effects [19; 42]. Instead, they attributed the observed variation to physiological effects only, which may not be justified. Moreover, some studies included low b-values [111; 114; 117], while it is known from the intra voxel incoherent motion (IVIM) model that these low b-values are sensitive to variations from blood flow pulsations [23; 24].

Strain correction of ADC variations require tissue strain maps. For cardiac diffusion imaging, strain maps are obtained from separately acquired data, typically using myocardial tagging [147]. In myocardial tagging, the magnitude of the longitudinal magnetization is modulated by a sinusoidal function, which induces dark ‘taglines’ in the tissue from which tissue displacements and strains can be inferred [11]. As the analysis relies on visible taglines in the magnitude images, the taglines need to be at least 2 voxels apart, which limits the motion sensitivity. For brain imaging, the sensitivity of such tagging sequences needs to be increased substantially. By encoding displacement information in the phase data rather than the magnitude data, arbitrary motion sensitivity can be obtained. Displacement Encoding with Stimulated Echoes (DENSE) is an MRI tagging sequence that encodes tissue displacements in the MRI phase signal [83]. At the same time, high motion sensitivity comes with high encoding gradients in the DENSE sequence, which induce considerable b-values and, thus, diffusion weighting in the magnitude images. Consequently, a DENSE sequence can simultaneously provide both strain data and diffusion data in the brain.

In this study, we investigate to what extent dynamic ADC variations over the cardiac cycle can be explained by artificial fluctuations in ADC induced by deformation of the tissue between the gradient pulses of the diffusion weighted sequence. To this end, we implemented a *slice-selective* DENSE sequence that simultaneously provides data to measure brain tissue strain and ADC measurements over the cardiac cycle. We acquire data with b-values 300 and 1000 s/mm², high enough to exclude perfusion effects from blood flow. Furthermore, we combine established theoretical frameworks on phase dispersion, tissue deformation, and their effects on the measured ADC [127; 170]. We use the theory to simulate the artificial ADC variation based on measured tissue deformation and compare these artificial fluctuations in ADC to the measured ADC variation over the cardiac cycle. We show that tissue deformation indeed induces artificial ADC variations, but that these only account for a small part of the actual measured ADC variation, which leaves room for discussion about the physiological origin of the additional ADC variation.

THEORY

Infinitesimal strain

Over time, an elementary piece of brain tissue moves from position \mathbf{X} at time $t = 0$ to position \mathbf{x} at time $t = t'$. The coordinate \mathbf{x} relates to \mathbf{X} as follows: $\mathbf{x} = \mathbf{X} + \mathbf{u}(\mathbf{X}, t)$, where \mathbf{u} is the tissue displacement that includes rigid body rotations and translations. Hereafter t is omitted for brevity.

The *deformation gradient tensor* \mathbf{F} relates a line element of tissue in the undeformed state to its deformed counterpart:

$$d\mathbf{x} = \mathbf{F} d\mathbf{X} \quad (6-1)$$

where \mathbf{F} is given by

$$\mathbf{F} = \mathbf{I} + \nabla \mathbf{u} = \mathbf{I} + \mathbf{J} \quad (6-2)$$

Here, \mathbf{I} is the identity matrix and \mathbf{J} the *displacement gradient tensor*. The elements of \mathbf{J} are the spatial derivatives of u_x , u_y , and u_z ; the measured incremental displacements in Right-to-Left (RL), Anterior-to-Posterior (AP) and Feet-to-Head (FH), respectively. Under the assumption of infinitesimal incremental strains, Cauchy's strain tensor can be derived from \mathbf{F} as

$$\begin{aligned} \boldsymbol{\varepsilon} &= \frac{1}{2}(\mathbf{F}^T + \mathbf{F}) - \mathbf{I} \\ &= \begin{pmatrix} \varepsilon_{xx} & \varepsilon_{xy} & \varepsilon_{xz} \\ \varepsilon_{yx} & \varepsilon_{yy} & \varepsilon_{yz} \\ \varepsilon_{zx} & \varepsilon_{zy} & \varepsilon_{zz} \end{pmatrix} \end{aligned} \quad (6-3)$$

where $\boldsymbol{\varepsilon}$ is symmetric and independent of rigid body translation or rotation [86]. The assumption of infinitesimal incremental strain implies that the displacements of brain tissue are small, such that the geometry of the brain is macroscopically unchanged during the deformation process. As a result, any given voxel in the deformed state at position \mathbf{x} can be assumed to coincide with its undeformed counterpart at position \mathbf{X} , such that $\mathbf{x} = \mathbf{X} + \mathbf{u} \approx \mathbf{X}$. Using this assumption, the stretch tensor \mathbf{U} can be expressed in terms of $\boldsymbol{\varepsilon}$:

$$\begin{aligned} \mathbf{U} &= \sqrt{\mathbf{F}^T \mathbf{F}} = \sqrt{(\mathbf{I} + \mathbf{J})^T (\mathbf{I} + \mathbf{J})} = \sqrt{\mathbf{I} + \mathbf{J} + \mathbf{J}^T + \mathbf{J}^T \cdot \mathbf{J}} \\ &\approx \sqrt{\mathbf{I} + \mathbf{J} + \mathbf{J}^T} \approx \mathbf{I} + \frac{1}{2}(\mathbf{J} + \mathbf{J}^T) = \mathbf{I} + \boldsymbol{\varepsilon} \end{aligned} \quad (6-4)$$

and similarly

$$\mathbf{U}^{-1} = \mathbf{I} - \boldsymbol{\varepsilon} \quad (6-5)$$

Spatial frequency modulation

Diffusion MRI encodes molecular diffusion effects in the NMR signal by using pulsed gradients (see Figure 6-1 for sequence design). However, tissue deformation that occurs during the time

between these pulsed gradients leads to measurement errors, because tissue deformation induces alterations in the magnitude of the MRI signal. Therefore, the measured diffusion coefficient is different from the diffusion coefficient had there not been tissue deformation between the pulsed gradients. Given the infinitesimal strain assumption, the effects of deformation on the measured diffusion can be analyzed by considering the signal of a given voxel, without considering the deformation of the remainder of the organ. Two factors play a role here. First, tissue deformation leads to imperfect refocusing of the signal and, thus, phase dispersion. Second, deformation results in a modified spatial frequency, which induces a different effective b-value at the tissue level and, thus, an observed (measured) diffusion coefficient \mathbf{D}^{obs} that is different from the actual diffusion coefficient \mathbf{D} . Consequently, the stimulated echo signal $M(\mathbf{r})$ over a given voxel is affected by these two factors. Under the assumption of a short gradient duration δ compared to the evolution time Δ after the second gradient lobe (see Figure 6-1), $M(\mathbf{r})$ yields

$$M(\mathbf{r}) = \frac{M_0}{2} \cdot \iiint_V \exp(i\mathbf{r} \cdot (\mathbf{k} - \mathbf{k}_0)) dV \cdot \exp(-\Delta \cdot \mathbf{k}^T \cdot \mathbf{D} \cdot \mathbf{k}) \quad (6-6)$$

where Δ is the time between the pulsed gradients. The spatial frequency that results from the applied gradient pulses is represented by κ_0 . It changes to κ as a result of tissue deformation as will be specified below. The phenomenon of phase dispersion and the effective b-value were already described by Wedeen et al. [170] and Reese et al [127], respectively. As the effect of these two factors on diffusion measurements are independent and central to the work described in this paper, we revisit these factors here separately. Eventually, both factors will be combined to simulate the artificial ADC variation in the brain given a constant diffusion tensor and varying incremental strain over the cardiac cycle.

Phase dispersion

Incremental tissue deformation that accumulates in the time between the pulsed gradients leads to imperfect refocusing of the MRI signal. This effect is known as phase dispersion and results in a reduction of the magnitude of the MRI signal [74]. The amount of phase dispersion not only depends on the incremental tissue deformation (represented by the deformation gradient tensor \mathbf{F}), but also on the spatial frequency modulation (represented by κ_0), leading to increased phase dispersion effects for a given tissue deformation as b-values increase. The initial spatial frequency modulation κ_0 of the longitudinal magnetization in a given voxel as induced by the pulsed gradients is given by $\mathbf{k}_0 = 2\pi\gamma G\delta\mathbf{n}$ (in mm^{-1} , where \mathbf{n} is the unit vector in the direction of encoding). The spatial frequency of the modulated magnetization changes as a result of the tissue deformation, yielding the following spatial frequency in the tissue just prior to the application of the second gradient pulse:

$$\mathbf{k} = (\mathbf{F}^{-1})^T \cdot \mathbf{k}_0 \quad (6-7)$$

If no deformation occurred in the time between the pulsed gradients, \mathbf{F} would yield the identity matrix \mathbf{I} .

Substituting $\mathbf{r} = x\mathbf{x} + y\mathbf{y} + z\mathbf{z}$ and $(\mathbf{k} - \mathbf{k}_0) = \Delta_{k_x}\mathbf{x} + \Delta_{k_y}\mathbf{y} + \Delta_{k_z}\mathbf{z}$ (\mathbf{x} , \mathbf{y} , and \mathbf{z} unit vectors) in Eq. 6-6, we rewrite the volume integral by using the linearity property

$$\begin{aligned} \iiint_V \exp(i\mathbf{r} \cdot (\mathbf{k} - \mathbf{k}_0)) dV &= \iiint_V \exp(ix\Delta k_x) \exp(iy\Delta k_y) \exp(iz\Delta k_z) dx dy dz \\ &= \int \exp(ix\Delta k_x) dx \int \exp(iy\Delta k_y) dy \int \exp(iz\Delta k_z) dz \end{aligned} \quad (6-8)$$

Each separate integral in Eq. 6-8 along the orthogonal directions x , y and z can be solved analogue to the integral along x

$$\begin{aligned} \int_{-d_x/2}^{d_x/2} \exp(ix\Delta k_x) dx &= \left[\frac{1}{i\Delta k_x} \exp(ix\Delta k_x) \right]_{-d_x/2}^{d_x/2} \\ &= \frac{2}{\Delta k_x} \left| \sin\left(\frac{d_x}{2} \Delta k_x\right) \right| \end{aligned} \quad (6-9)$$

where d_x is the length of the voxel in the x -direction.

From Eq. 6-7 it follows that for a given incremental tissue deformation, the difference in spatial frequency modulation ($\kappa - \kappa_0$) will increase when κ_0 increases. Consequently, larger κ_0 leads to more signal attenuation due to enhanced phase dispersion effects, yielding an increased ADC when computed from two datasets with different spatial modulation frequencies, but equal tissue deformation.

Modified effective b-value

Tissue deformation induces a different effective b-value due to a modified spatial frequency. Reese et al [127] already derived an expression for this phenomenon. Under the assumption of a short gradient duration δ compared to the evolution time Δ , the factor in Eq. 6-6 related to diffusion can be rewritten in terms of the initial spatial frequency modulation κ_0

$$\exp(-\Delta \cdot \mathbf{k}^T \cdot \mathbf{D} \cdot \mathbf{k}) = \exp(-\Delta \cdot \mathbf{k}_0^T \cdot \mathbf{D}^{\text{obs}} \cdot \mathbf{k}_0) \quad (6-10)$$

Ignoring the effect of the tissue deformation on the spatial modulation frequency of the longitudinal magnetization would lead to an observed diffusion coefficient \mathbf{D}^{obs} that is in general different from the actual diffusion coefficient \mathbf{D} . The observed diffusion coefficient \mathbf{D}^{obs} is related to the actual diffusion coefficient \mathbf{D} by

$$\mathbf{D}^{\text{obs}} = \frac{1}{\Delta} \int_0^{\Delta} \mathbf{U}^{-1}(t) \cdot \mathbf{D} \cdot \mathbf{U}^{-1}(t) dt \quad (6-11)$$

where \mathbf{U} is the stretch tensor (see Eq. 6-4) [127]. From Eq. 6-11 it follows that the strain history of the tissue is encoded in \mathbf{D}^{obs} . Even if the tissue deforms, but is again in its initial position during readout, \mathbf{D}^{obs} can differ from \mathbf{D} . The observed diffusion coefficient reduces for positive strain (lower effective b-values) and increases for negative strain (higher effective b-values).

METHODS

Slice-Selective DENSE

The DENSE sequence consists of a motion encoding and decoding part, which – analogue to velocity encoding – manipulate the phase of the MRI signal such that it becomes proportional with the displacement, relative to the point of encoding [5]. Here we introduce a slice-selective DENSE approach. The main difference compared to conventional DENSE is that the two encoding RF pulses become slice-selective the same way as the third RF pulse (see Figure 6-1). This approach ensures that, the repetition time and evolution time Δ are constant, and equal for each slice. At the same time, the slice-selective approach requires RF pulses with high bandwidth (BW) to ensure proper slice profiles. The approach is therefore not well compatible with water selective excitation using low bandwidths for fat suppression, as used previously [136; 137]. Instead, fat suppression is performed by using the gradient reversal approach, where the slice-selective gradient of the second RF pulse is reversed (see Figure 6-1) [110].

From the motion-encoded phase images acquired through DENSE, tissue displacement maps can be derived by

$$u_x = \frac{DENC}{\pi} \phi_x \quad (3-12)$$

Here, ϕ_x is the phase of the DENSE MRI signal acquired by motion-encoding in the x-direction. The displacement encoding value D_{enc} in units of meters describes the sensitivity of the encoding (lower D_{enc} requires larger gradients). By acquiring images with opposite gradient polarities, phase contributions due to cardiac-induced motion can be distinguished from phase confounders such as static RF phase.

At the same time, slice-selective DENSE can be regarded as a STEAM diffusion sequence [113]. The pulsed gradients induce a b-value, leading to decreased signal in the magnitude images as a result of diffusion effects. Changing the gradient strength yields diffusion weighted images with different b-values, according to [146]

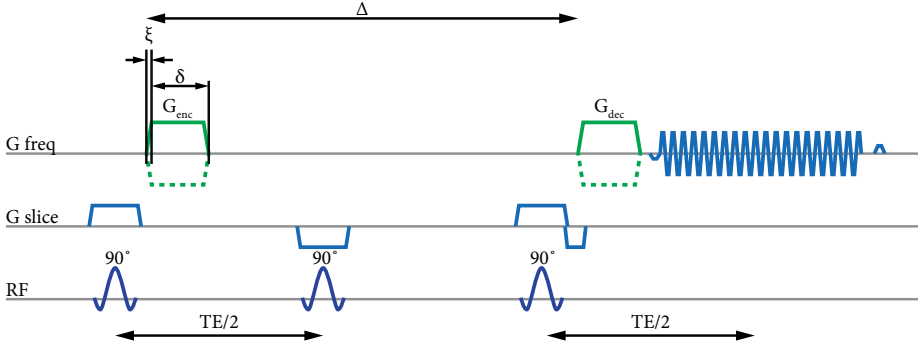


Figure 6-1 Schematic representation of the slice-selective single-shot DENSE sequence. The tissue's initial position is encoded in the longitudinal magnetization using G_{enc} . After an evolution time Δ of 100ms, the position of the tissue is decoded by applying G_{dec} (equal to G_{enc}), which yields a signal phase that is proportional with the tissue displacement during Δ . At the same time, this scheme can be regarded as a STEAM diffusion sequence. The pulsed gradients induce diffusion weighting which changes the signal magnitude. As a result, changing the gradient strength not only yields different displacement encoding sensitivity, but also a different diffusion weighting. For the brain, the unique situation arises where the pulsed gradients both meet the requirements for sufficient accuracy in the tissue-motion field maps for strain computations, while at the same time reasonable diffusion weighting is achieved.

$$b = \gamma^2 G^2 \left[\delta^2 \left(\Delta - \frac{\delta}{3} \right) + \frac{\xi^3}{30} - \frac{\delta \xi^2}{6} \right] \quad (3-13)$$

Here, δ is the effective duration of the gradient (in ms) and ξ is the rise time (in ms). When at least two b-values are acquired, these images can subsequently be used to derive the ADC. For two b-values ADC can directly be computed:

$$ADC = \frac{\ln(S_{b_1}) - \ln(S_{b_2})}{b_2 - b_1} \quad (3-14)$$

Data Acquisition

The Ethical Review Board (ERB) of the University Medical Center Utrecht approved the use of healthy volunteers for MRI protocol development. Eight healthy volunteers (4 females, age 25 ± 4 years) were included and written informed consent was obtained. The volunteers were scanned at 7T (Philips Healthcare) using an 8-channel transmit operating in quadrature mode and 32-channel receive head coil (Nova Medical). In each subject, 6 slice-selective DENSE series were acquired with only in-plane motion-encoding. To obtain motion encoding in the Right-to-Left (RL), Anterior-to-Posterior (AP), and Feet-to-Head (FH) direction, these series were acquired with different orientations: 2 sagittal series (in-plane FH and AP encoding), 2 coronal series (in-plane FH and RL encoding) and 2 transverse series (in-plane AP and RL encoding). Each DENSE series consisted of 52 non-triggered repeated scans, half of the scans (26 repeated scans) with $k_0 = 55\text{mm}^{-1}$ and the other half with $k_0 = 100\text{mm}^{-1}$ (diffusion and motion encoding equivalent: $b = 300/1000 \text{ s/mm}^2$ and $DENC = 56/31 \mu\text{m}$, respectively). The evolution time Δ

was set to 100ms to limit signal loss due to relaxation effects (predominantly determined by T1 instead of T2 in STEAM). Different k_0 , i.e. different b-values, were obtained by varying the gradient strength G while keeping the effective gradient time parameters constant ($\delta = 9.5$ ms, $\xi = 0.4$ ms). Each DENSE series provided two components of the deformation gradient tensor \mathbf{J} by taking the in-plane spatial derivatives from the motion encoded data (see Eq. 6-2 for the definition of \mathbf{J}). Alternating encoding polarities were applied to distinguish between motion-induced phase contributions and phase confounders. To ensure a fixed repetition time (TR) and constant diffusion effects with respect to Δ , no fixed encoding reference was present, unlike the triggered DENSE sequences reported before [1; 136; 140]. Instead, the volumes were continuously acquired, resulting in displacement gradient maps randomly distributed over the cardiac cycle. As these displacements concern only the displacement developed during the mixing time Δ (100 ms in our case), we refer to these displacements and strains as *incremental* displacements and *incremental* strains. Physiological data from a pulse-oximeter (POx) was simultaneously recorded to measure the cardiac interval position. Acquisition of a single DENSE series took 7 min regardless of heart rate. Further imaging parameters were: 72 slices; resolution: $3 \times 3 \times 3$ mm³; FOV: $240 \times 240 \times 216$ mm³; SENSE: 2.6 (AP or RL, depending on acquisition orientation); single-shot EPI (EPI factor: 35, EPI BW in the readout/phase encoding direction for sagittal and transverse orientation: 2.6 kHz/pixel and 47 Hz/pixel; for coronal orientation: 3.5kHz/pixel and 56 Hz/pixel); B1: 10 μ T; TR: 7.5 s and TE/2: 24 ms.

A single-shot multi-slice spin echo diffusion tensor imaging (DTI) dataset was acquired for each volunteer, which was required to simulate ADC variations over the cardiac cycle based on incremental strain measurements (see Eq. 6-11). DTI was obtained with 16 directions, b-values 300 and 1000 mm²/s, together with an additional b=0 image. Different b-values were obtained by varying the pulsed-gradient strength G, while keeping time deltas constant ($\Delta = 36.4$ ms, $\delta = 17$ ms, $\xi = 0.3$ ms). The dataset was acquired with transverse orientation and acquired resolution of $2 \times 2 \times 2$ mm³. Additional imaging parameters included: FOV: $224 \times 224 \times 150$ mm³; single-shot EPI readout (EPI factor: 47; EPI BW in the readout/phase encoding direction: 2.5 kHz/pixel and 35.9 Hz/pixel, respectively); SENSE factor: 2.4 (AP direction); TR: 8.4 s and TE: 75 ms. The acquisition time was 5 minutes.

Two additional scans were acquired for data processing purposes. First, a T1-weighted (T1w) turbo field echo (TFE) scan was acquired as anatomical reference (acquired resolution: $1.00 \times 1.00 \times 1.00$ mm³; FOV: $250 \times 250 \times 190$ mm³; TFE factor: 600; inversion delay: 1292 ms; SENSE: 2 (AP direction); FA: 5°; TR: 4.2 ms; TE: 1.97 ms; acquisition time: 2 min). Second, two B0 field maps were obtained: the first was acquired at the beginning of the scanning session to perform second-order image-based B0 shimming; the second was acquired after shimming to allow for remaining geometric distortion corrections in the acquired DENSE images. A single B0 field map was reconstructed online from the phase difference of two successive gradient echo

scans with fixed TR and different TE, as available from the vendor (acquired resolution: $3.50 \times 3.50 \times 3.50 \text{ mm}^3$; FOV: $224 \times 224 \times 224 \text{ mm}^3$; FA: 8° ; TR: 3.9 ms; TE: 1.57 ms and 2.57 ms; scan duration: 25 s).

Post-Processing

Each acquired DENSE series was processed independently offline by using custom software written in MATLAB R2018b (The MathWorks, Inc., Natick, MA, USA). Per DENSE series, magnitude data was used for rigid registration of each repeated scan to the first repeated scan by using Elastix [82] (see Figure 6-2 for analysis overview). Since adjacent slices were acquired at different positions in the cardiac cycle, only in-plane degrees of freedom were used for registration. Subsequently, the shimmed B0-map was registered to the DENSE series and used for EPI distortion correction [79]. Registration and distortion corrections were applied to the complex data using linear interpolation.

From the complex DENSE data, magnitude and phase data were obtained. Magnitude data (diffusion weighted) was log-transformed and the phase data were transformed to displacement fields, from which the in-plane spatial derivatives were computed. Each DENSE series thereby produced two apparent displacement gradient maps. Unwrapping was performed under the assumption of small incremental displacement gradients ($\epsilon_{xx} \ll DENC/\Delta x$), where Δx is the voxel size [137]. The limit of the incremental displacement gradients detectable over the evolution time Δ without phase wraps for $b=1000$ was approximately $5 \cdot 10^{-2}$, which is well over the expected incremental displacement gradient. At this point, the data still included static background contributions. Averaging the data from the opposite gradient polarities yielded this static background offset, which was subtracted from the data.

Retrospective binning

Per DENSE dataset, twenty cardiac phases of ADC and incremental displacement gradients were obtained. To this end, log-transformed magnitude data and incremental displacement gradient maps were ordered over the cardiac cycle by using the position of acquisition that followed from the recorded physiological trace. Subsequently, a moving average window with a width of 10% of the cardiac interval was applied to the data to generate 20 cardiac frames. Each DENSE dataset provided 52 frames of displacement gradient maps (both $k_0=55\text{mm}^{-1}$ and $k_0=100\text{mm}^{-1}$ data) distributed over the cardiac cycle for the moving average window. The log-magnitude data was processed separately per diffusion weighting, resulting in 26 frames per b-value for the moving average window. After the moving average window was applied to the individual b-values, these results were used to compute the ADC maps per cardiac phase. Sometimes, no data was available in the bin. In those cases, the values of the two neighboring data points on either side of the bin were averaged. This happened in $<5\%$ of cases for the diffusion weighted data and in $<1\%$ of cases for displacement gradient maps.

Incremental strain tensor maps

Per subject, the incremental displacement gradient maps and ADC data from all 6 slice-selective DENSE series were combined by using a group-wise rigid registration with Elastix and third-order b-spline interpolation [82]. Next, the incremental deformation gradient tensor was reconstructed from the displacement gradient maps. Each DENSE series provided two components. For instance, the sagittally oriented dataset with FH encoding direction from Figure 6-2 provided the incremental displacement gradient fields $\frac{\delta u_{FH}}{\delta FH}$ and $\frac{\delta u_{FH}}{\delta AP}$ (see Eq. 6-2). The diagonal ele-

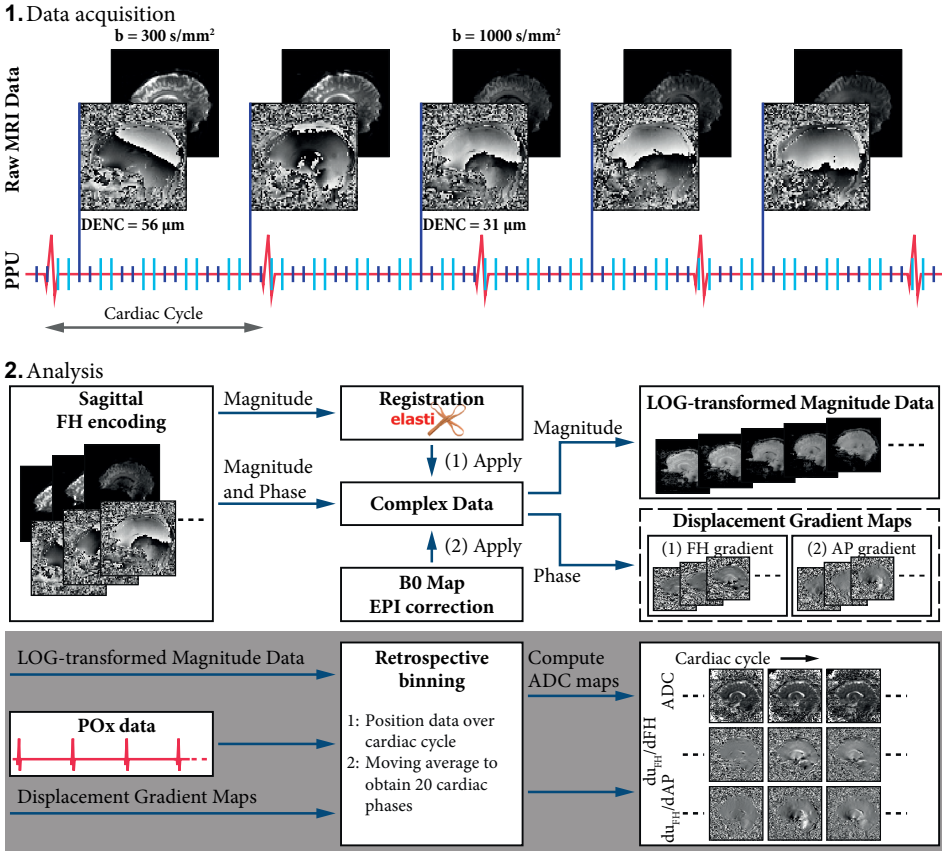


Figure 6-2 Schematic representation of DENSE data acquisition and analysis. (1) Slice-selective single-shot multi-slice DENSE images were acquired with 2 encoding sensitivities ($b=300$ and $b=1000 \text{ s/mm}^2$). Encoding (light blue) and decoding (dark blue) were interleaved per 2 slices to speed up acquisition. (2) Magnitude data was used for registration and the B0 map was used for EPI distortion correction. Derived parameters were applied to the complex data. From the complex data, magnitude and phase data were derived. The magnitude data was log-transformed and the phase data was transformed into displacement maps, from which displacement gradients maps were computed. Log-transformed data and incremental displacement gradient maps were repositioned over the cardiac cycle and twenty binned maps over the cardiac cycle were constructed for the log-transformed magnitude data and displacement gradient maps, using a moving average. Using the binned log-transformed magnitude data, ADC maps were computed for 20 cardiac phases following Eq. 6-14.

ments of the displacement gradient tensor were obtained twice, each for a different acquisition orientation. Each double obtained element was averaged.

Two scalar quantities were derived from the incremental strain tensor for comparison with the ADC variations: the incremental volumetric strain and the incremental octahedral shear strain [136]. The volumetric strain reflects the net incremental expansion or compression of the voxel [1]. Octahedral shear strain, on the other hand, signifies the differences between the three principal strains, which can be interpreted as the deviation from isotropic swelling or shrinkage [98]. To reduce the inter-subject variability of strain curves due to noise in the measurements, these curves were overlaid between subjects over the cardiac cycle as follows. Per subject, the mean incremental volumetric strain over the cardiac cycle was subtracted, resulting in volumetric strain curves oscillating around 0. Furthermore, the minimum incremental shear strain value over the cardiac cycle was subtracted from the shear strain curve, so that shear strain start and end at zero.

T1w data and diffusion tensor

Per subject, the T1w anatomical scan was registered to the DENSE data. The full diffusion tensor was reconstructed offline from the DTI data by using Explore DTI [87]. Only the DTI data associated with $b=300$ and $b=1000$ was used to obtain a representative comparison to the ADC measurements obtained through DENSE. To correct for EPI distortions, non-linear b-spline regularized registration with the registered T1w scan as reference was used.

Artificial ADC Variations

Artificial ADC variations, induced by tissue deformations, were calculated based on the theoretical framework (see Section *Spatial frequency modulation*). The acquired DTI data and measured incremental displacement gradient tensor from the DENSE data over the cardiac cycle were used to simulate these artificial variations. Since we measured ADC variations with DENSE in the RL, AP and FH direction, we only simulated the artificial ADC variations for these directions.

We calculated the artificial deformation-induced magnitude variations of the MRI signal (see Eq. 6-6) for both $b=300$ ($k_0=55\text{mm}^{-1}$) and $b=1000$ ($k_0=100\text{mm}^{-1}$) in the associated direction. Two components contribute to the variation: phase dispersion and the effective b-value. Calculating the phase dispersion effect is straight forward and can be done by expanding Eq. 6-9 to all three orthogonal directions (RL, AP and FH). The terms Δk that are required to express Eq. 6-8 in terms of the displacement gradient tensor \mathbf{J} were obtained by substituting Eq. 6-2 in Eq. 6-7

$$\mathbf{k} - \mathbf{k}_0 = ((\mathbf{I} + \mathbf{J})^{-1\text{T}} - \mathbf{I}) \cdot \mathbf{k}_0 \quad (6-15)$$

The effective b-value contribution, however, is more complex to derive and depends on the time-dependent inverse stretch $\mathbf{U}^{-1}(t)$. From the incremental displacement gradient tensor, we first computed the strain tensor following Eq. 6-3. By using Eq. 6-5, the stretch tensor \mathbf{U} was obtained.

In deriving the time-dependency of \mathbf{U} , we assumed a piece-wise constant strain rate over the evolution time Δ . From this assumption it follows that the incremental strain (that is, the strain at each time-point t over evolution time Δ) can be written as $\boldsymbol{\varepsilon}(t) = \frac{\boldsymbol{\varepsilon} \cdot t}{\Delta}$. The time-dependent inverse stretch tensor can then be written as

$$\mathbf{U}^{-1}(t) = \mathbf{I} - \boldsymbol{\varepsilon}(t) \quad (6-16)$$

With this, and by substituting Eq. 6-5 into Eq. 6-11 we obtain (using Einstein summation convention)

$$\begin{aligned} D_{ij}^{obs} &= \left[\frac{1}{\Delta} \int_0^{\Delta} \left(I_{ik} - \frac{\varepsilon_{ik} \cdot t}{\Delta} \right) \cdot \left(I_{lj} - \frac{\varepsilon_{lj} \cdot t}{\Delta} \right) dt \right] D_{kl} \\ &= \left[I_{ik} I_{lj} - \frac{\varepsilon_{lj}}{2} I_{ik} - \frac{\varepsilon_{ik}}{2} I_{lj} + \frac{\varepsilon_{ik} \varepsilon_{lj}}{3} \right] D_{kl} \end{aligned} \quad (6-17)$$

Here, ε_{ik} and ε_{lj} is the measured strain after the evolution time Δ , which varies for each cardiac phase. For a given, constant \mathbf{D} (measured through the ungated DTI) we obtain a prediction for \mathbf{D}^{obs} that varies over the cardiac cycle.

By combining both phase dispersion and effective b-value contributions, the magnitude of the MRI signal is described as

$$\begin{aligned} |M_d| &= \frac{M_0}{2} \cdot \frac{2}{\Delta k_x} \left| \sin \left(\frac{d_x}{2} \Delta k_x \right) \right| \cdot \frac{2}{\Delta k_y} \left| \sin \left(\frac{d_y}{2} \Delta k_y \right) \right| \\ &\quad \cdot \frac{2}{\Delta k_z} \left| \sin \left(\frac{d_z}{2} \Delta k_z \right) \right| \cdot \exp(-bD_{obs}) \end{aligned} \quad (6-18)$$

In predicting the ADC variation over the cardiac cycle, it is important to note that the ADC prediction depends on the log-transform of Eq. 6-18. Log-transforming Eq. 6-18 will result in a summation rather than a product, from which the predicted ADC variation can be derived by using Eq. 6-14. Consequently, the ADC variation does not depend on M_0 . The artificial (deformation-induced) component of the variations in ADC were computed voxel-wise for each of the three diffusion directions available from the DENSE magnitude images: RL, AP, and FH.

Procedure for analysis of ADC variations

For both measured and artificial ADC variations, ADC maps per cardiac phase (cp) were computed from the log-magnitude data with diffusion weighting of $b=300$ and $b=1000$, using the following equation:

$$\text{ADC}(cp) = \frac{M_{300}^{\ln}(cp) - M_{1000}^{\ln}(cp)}{1000 - 300} \quad (6-19)$$

Here, M_{300}^{\ln} and M_{1000}^{\ln} are the log-transformed magnitude data with diffusion weighting of $b=300$ and $b=1000$, respectively. The ADC deviation (dADC) from the mean ADC (ADC_{mean}) over the cardiac cycle was obtained by using:

$$dADC(cp) = ADC(cp) - ADC_{\text{mean}} \quad (6-20)$$

The time dependency (cp) of dADC will be omitted in further references for brevity.

For the inter-subject analysis, ADC variation curves were synchronized. To this end, peak incremental shear strains per subject were positioned at 30% of the cardiac interval and associated ADC curves were shifted accordingly. Furthermore, the maximum temporal ADC change over the cardiac cycle (ΔADC) was calculated for a region of interest (ROI):

$$\Delta ADC = ADC_{\text{max}} - ADC_{\text{min}} \quad (6-21)$$

where ADC_{max} and ADC_{min} indicate the maximum and minimum ADC average in the ROI over the cardiac cycle, respectively. A conservative white matter tissue mask was created as ROI to avoid partial volume effects from large vessels and CSF. The T1w data was first registered to the DENSE data and subsequently segmented by using the Computational Anatomy Toolbox (CAT12, version 1615, Jena University Hospital, Departments of Psychiatry and Neurology) for Statistical Parametric Mapping (SPM12, version 7771, Wellcome Trust Centre for Neuroimaging, University College London). The conservative white matter tissue mask was created from the intersection of two masks. The first mask consisted of a tissue mask where all voxels with CSF probability larger than 0 had been disregarded, followed by one additional city-block erosion step. The second mask consisted of a white matter tissue mask obtained by using a probability threshold of 90% for white matter.

RESULTS

Tissue deformation and ADC

Average ADC values over the cardiac cycle obtained through DENSE compared well with the MD values obtained with conventional DTI scanning. Overall, a slightly lower mean ADC (ADC_{mean}) was found compared with the mean diffusivity (MD) obtained with DTI: $6.97 \cdot 10^{-4} \pm 0.38 \cdot 10^{-4} \text{ mm}^2/\text{s}$ versus $8.02 \cdot 10^{-4} \pm 0.21 \cdot 10^{-4} \text{ mm}^2/\text{s}$. Figure 6-3 shows example maps for one of the subjects for data encoded in the FH direction. On the top left, T1w data is shown for anatomical reference. On the bottom left, MD and ADC maps are shown as obtained from the DTI and DENSE data, respectively. Since only in-plane encoding was employed, FH encoding implies that DENSE data was acquired with sagittal and coronal orientation.

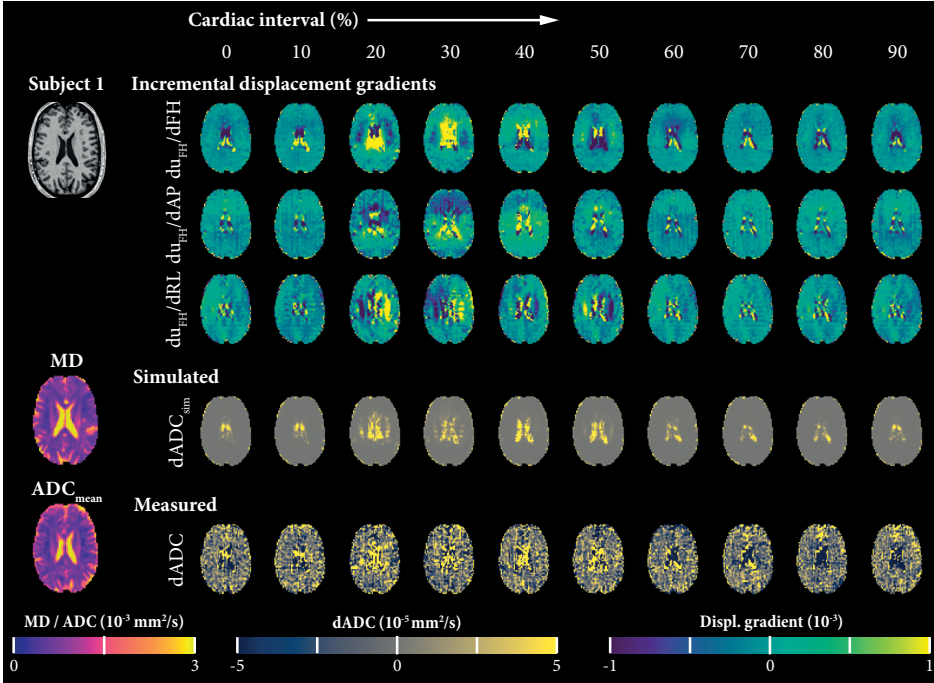


Figure 6-3 ADC deviations from the mean ($dADC$) and incremental displacement gradient maps over the cardiac cycle for Subject 1. Cardiac phases are represented with peak incremental shear strain at 30% of the cardiac cycle. Although twenty cardiac phases were obtained, ten are represented here. Slice-selective DENSE data was acquired with FH encoding, which implies sagittal and coronal orientation. Here, we present the data in a transverse orientation. On the left, the T1-weighted image is shown as an anatomical reference. Below, the measured mean diffusion in the FH direction is represented by the reconstructed MD and the mean ADC maps on the left, obtained through the DTI and DENSE data, respectively. On the right, the upper 3 rows represent the incremental displacement gradient fields observed over time Δ (100 ms). The $\frac{du_{FH}}{dFH}$ component was obtained with both sagittal and coronal orientation and averaged. The additional $\frac{du_{FH}}{dAP}$ and $\frac{du_{FH}}{dRL}$ components were obtained with sagittal and coronal acquisition orientation, respectively. The bottom two rows show the ADC deviation from the mean over the cardiac cycle, as simulated ($dADC_{sim}$) and measured $dADC$, respectively.

Three incremental displacement gradient maps (first 3 rows) over the cardiac cycle are shown that were obtained through the phase data. The strain-induced simulated artificial ADC deviations ($dADC_{sim}$) and the actual measured deviations $dADC$ over the cardiac cycle are represented in rows 4 and 5, respectively.

Simulated and measured ADC deviations

Simulated ADC variations consist of two components: phase dispersion effects and modulated effective b-value. Figure 6-4 represents the calculated artificial contribution of these components separately. The effect of phase dispersion on ADC variations is two orders of magnitude larger than the modulation of the effective b-value. Furthermore, phase dispersion is responsible for an

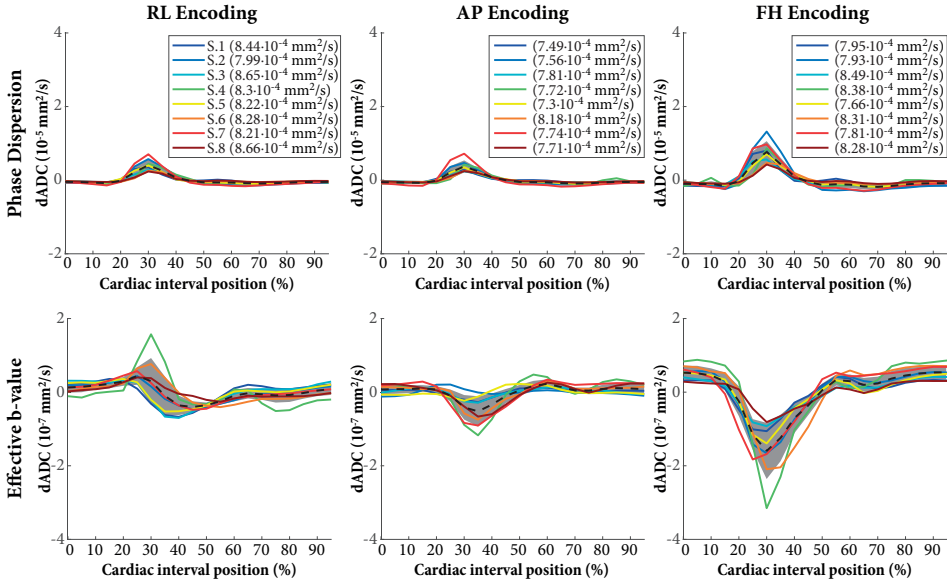


Figure 6-4 Simulated phase dispersion and effective b-value contributions that constitute the simulated ADC variation ($dADC_{sim}$) represented as the deviation from the MD over the cardiac cycle MD. Please note the difference in scaling along the y-axis. ADC variations were simulated voxel-wise and the results were averaged over the conservative white matter mask, avoiding blood and CSF signals. From the DTI data, MD values along the associated direction are indicated per subject, in the legend. The dotted black line represents the mean $dADC_{sim}$ over all subjects whereas the gray shaded area indicates the standard deviation. Largest variation was observed in the Feet-to-Head direction. Phase dispersion effects contributed to a $dADC_{sim}$ increase at peak systole whereas the effective b-value contributed to a slight decrease in simulated $dADC_{sim}$ at peak systole. Furthermore, phase dispersion effects were two orders of magnitude larger than the effective b-value contribution. Since $dADC$ is derived from the log-transformed magnitude data, multiplications become summations and the overall simulated $dADC_{sim}$ is obtained by summing $dADC_{sim}$ for phase dispersion with $dADC_{sim}$ for the effective b-value.

increase of the diffusion coefficient, whereas the effective b-value component results in a reduced diffusion coefficient at peak systole.

Measured ADC values deviated from the mean ADC value over the cardiac cycle for each of the three investigated orthogonal directions. Figure 6-5 shows $dADC$ for each encoding direction, where $dADC$ with the same encoding direction but different acquisition orientation were averaged (see Figure 6-S1 in supplementary files for $dADC$ curves per acquisition orientation). Mean ADC values over the cardiac cycle are indicated per subject in the legend. For the analysis, peak incremental shear strains were synchronized, which resulted in a relative shift between subjects of at most 2 cardiac phases (which is equal to 10% of the cardiac interval). The largest $dADC$ was observed at peak incremental shear strain (by definition at 30% of the cardiac interval) in the FH direction. The incremental shear strain curves computed from the incremental strain tensor are shown in Figure 6-6 together with the incremental volumetric strain. The maximum temporal ADC change (ΔADC) in the FH direction was $3.2 \cdot 10^{-5} \pm 1.0 \cdot 10^{-5} \text{ mm}^2/\text{s}$ (mean \pm SD

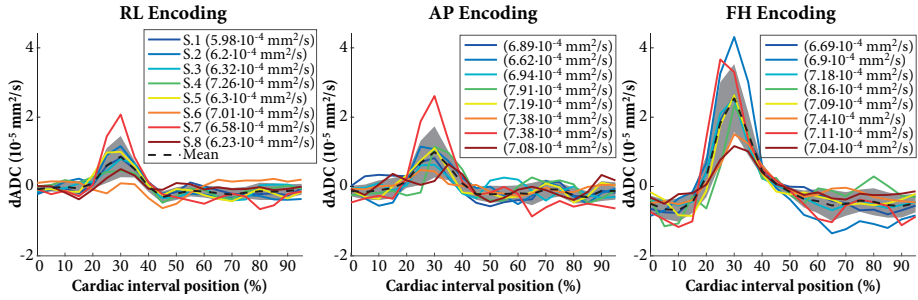


Figure 6-5 Measured ADC variation (dADC) represented as the deviation from the mean ADC over the cardiac cycle. Each orthogonal encoding direction was acquired two times, each with a different acquisition orientation for which the average is represented here (see Figure 6-S1 for separate results per acquisition orientation). Curves over the cardiac cycle were obtained by averaging over the conservative white matter mask, avoiding blood and CSF signals. Mean ADC values over the cardiac cycle per subject and along the associated direction are indicated in the legend. Curves between subjects were synchronized such that peak incremental shear strain occurred at 30% of the cardiac interval. The dotted black line represents the mean dADC over all subjects whereas the gray shaded area indicates the standard deviation. The largest dADC was observed in the Feet-to-Head direction.

across subjects). Maximum temporal ADC change in the RL and AP direction were slightly lower: $1.2 \cdot 10^{-5} \pm 0.62 \cdot 10^{-5}$ and $1.3 \cdot 10^{-5} \pm 0.76 \cdot 10^{-5}$ mm^2/s , respectively. Furthermore, inter-subject variability in dADC at peak systole (mainly observed in the FH direction) was mostly explained by peak incremental shear strain rather than mean ADC: the coefficients of determination (R^2) in the RL, AP and FH direction for peak shear strain were 0.69 ($p = 0.01$), 0.70 ($p = 0.009$) and 0.70 ($p = 0.01$) while for mean ADC these coefficients were 0.10 ($p = 0.45$), 0.02 ($p = 0.74$) and 0.10 ($p = 0.44$), respectively.

Correlation tissue strain and measured ADC deviation

Correlation plots for dADC with both volumetric strain and shear strain (see Figure 6-6) are presented in Figure 6-7. The coefficient of determination (R^2) per subject is indicated in the legend. The overall coefficient of determination was calculated by using the mean traces over the cardiac cycle for dADC, volumetric strain and shear strain (i.e. the dotted black lines indicated in Figure 6-7), rather than averaging the individual coefficients of determination. This coefficient of determination was highest in the FH direction for both volumetric strain and shear strain: 0.65 and 0.94, respectively. The ADC deviation correlated best with tissue shear strain increments in all three orthogonal directions, indicating that shear strain was the best predictor of the amount of ADC variation measured.

Corrected ADC deviation

Measured ADC deviations from the mean ADC were corrected for simulated ADC deviations by subtracting dADC_{sim} from the measured dADC. The simulated dADC resulted from the summation of both phase dispersion and effective b-value contributions (separately shown in Figure

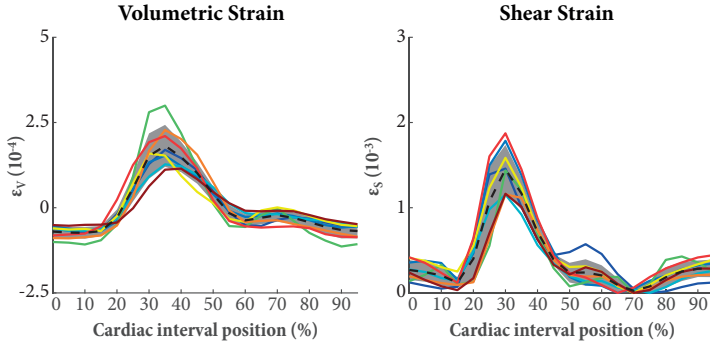


Figure 6-6 Incremental curves of volumetric strain and shear strain. Peak incremental shear strains per subject were placed at 30% of the cardiac interval. Shifts required to obtain this result were applied to all associated curves (e.g. volumetric strain and dADC). Furthermore, volumetric strain and shear strain were normalized over the cardiac cycle. To this end, the mean volumetric strain per subject was subtracted from the associated curve, so that volumetric strain curves oscillated around 0. For shear strain, the minimum incremental shear strain over the cardiac cycle was subtracted, resulting in shear strain curves touching to zero.

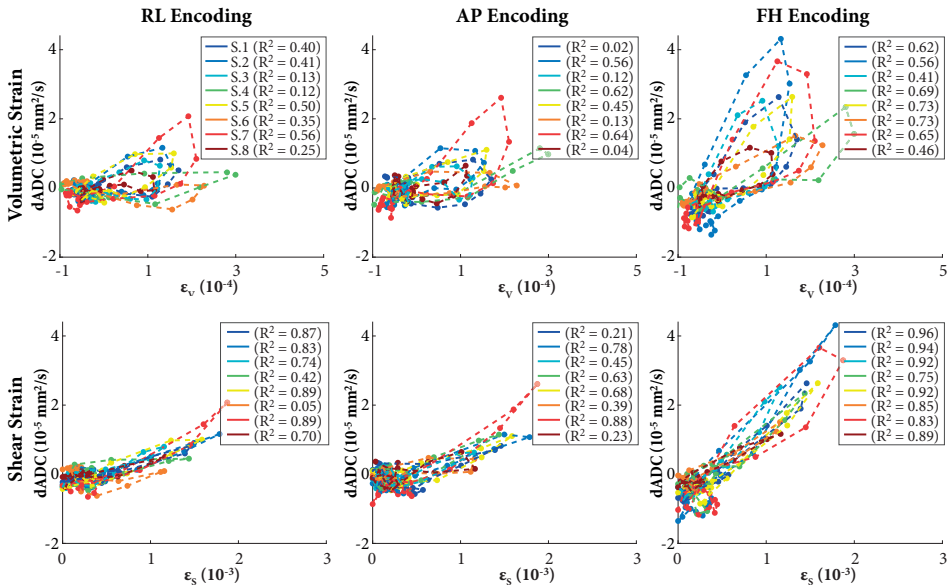


Figure 6-7 Correlation plots that show the relation between dADC and tissue strain. The first and second rows show the relation of dADC with volumetric strain and shear strain, respectively. Coefficients of determination are indicated per subject in the legend. Measured dADC correlated best with shear strain. The coefficient of determination for the shear strain on the mean traces (dotted black lines, see Figure 6-5) was 0.86, 0.87 and 0.94 in the RL, AP and FH direction, respectively. These coefficients were lower for the mean dADC versus volumetric strain: 0.34, 0.46 and 0.65, respectively.

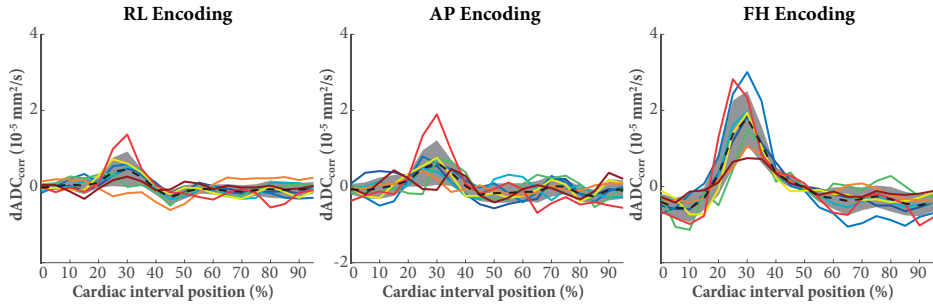


Figure 6-8 Corrected measured ADC deviations ($dADC_{corr}$) over the cardiac cycle. Results were obtained by subtracting simulated dADC induced by tissue deformation from measured dADC. Since measured dADC deviations were on average 2.6 ± 0.82 times larger than simulated deviations, $dADC_{corr}$ is still of the same order of magnitude as the measured dADCs (Figure 6-5). These corrected ADC deviations from the mean ADC cannot be explained by intrinsic artificial signal variations arising from tissue deformation.

6-4). The corrected dADC ($dADC_{corr}$) is presented in Figure 6-8 and shows similar behavior for individual subjects as already observed for the measured and simulated dADC. The ratio between dADC and $dADC_{sim}$ was on average 2.0 ± 0.91 , 2.5 ± 0.94 and 3.4 ± 0.57 in the RL, AP and FH direction, respectively.

DISCUSSION

We developed a comprehensive method to investigate to what extent ADC variations over the cardiac cycle in the brain can be explained by artificial variations induced by tissue deformation. We combined principles of DENSE and DTI in a single MRI sequence to simultaneously measure tissue strains and diffusion. This sequence could be regarded as either a slice-selective DENSE sequence or a STEAM diffusion sequence. The sequence took advantage of the unique situation that occurs in the brain where the pulsed gradients both meet the requirements for optimal accuracy in the tissue-motion field maps for strain computations, while at the same time reasonable diffusion weighting is achieved. This way, strain and ADC measurements could be obtained simultaneously from the phase and magnitude data, respectively. We measured ADC variation over the cardiac cycle in eight subjects, for three orthogonal directions (RL, AP and FH) and compared the results to artificial ADC variations based on the measured tissue strain tensor.

The temporal profile of the artificial dADC showed good similarities with the measured dADC, although the amplitude of the simulated effects was much lower. These similarities were especially observed for the FH direction, because of the relatively high amplitudes in that direction. Phase dispersion effects dominated the overall artificial ADC variation, its effect being two orders of magnitude larger as compared to the effective b-value contribution. We found systematically

larger MDs than ADCs obtained through DTI reconstructions and DENSE, respectively. The use of these slightly larger MDs in the simulations only affected the effective b-value contribution and resulted in a slight overestimation of this effect. Yet, because of the large difference between phase dispersion and effective b-value contributions, the effect on the outcome of the artificial ADC variation was negligible. It would have been sufficient to consider only the phase dispersion contribution and disregard the effective b-value altogether. As for the discrepancy between MDs and ADCs, this is most likely explained by differences in the time between the pulsed gradients, i.e. the diffusion time. The diffusion time was considerably longer for DENSE compared to DTI: 100 ms versus 36.4 ms, respectively. Mathematical models have shown that the effective diffusion coefficients decrease as evolution times increase [62].

Measured ADC variation was up to 3 times larger than the artificial ADC variation, depending on the encoding direction. The largest ADC variation was observed in the FH direction, which is consistent with larger strains associated for that direction [136; 137]. Measured ADC variations correlated best with incremental shear strains and showed a brief peak at peak systole. Inter-subject differences at peak systole in measured dADC were also largely explained by differences in incremental shear strains rather than differences in mean ADC values. The calculated phase dispersion effects showed that in the analysis of diffusion parameters, it is important to take shear strains into account. These effects might also be relevant for simultaneous DTI and MR Elastography (MRE) measurements, where additional shear strains are induced by an external actuator as is commonly used in conventional MRE [176]. Meanwhile, incremental volumetric strain correlated less with measured ADC variations. Volumetric strain curves were generally more stretched in time compared to incremental shear strain, which also indicates that volumetric strain variations are not the main cause of shear strain.

The measured ΔADC ranged between $1.2 \cdot 10^{-5} \pm 0.62 \cdot 10^{-5}$ and $3.2 \cdot 10^{-5} \pm 1.0 \cdot 10^{-5}$ mm^2/s . Largest ΔADC was observed in the FH direction, which was still one to two orders of magnitude smaller than ΔADC reported in literature [111; 114; 117]. Especially Ohno et al. and Osawa et al. have reported large ΔADC of approximately $0.24 \cdot 10^{-3}$ mm^2/s . Yet, in these studies the ΔADC was calculated on a voxel-by-voxel basis rather than on an ROI basis [114; 117]. Calculating ΔADC is sensitive to noise as it involves a difference between minimal and maximal values, and will tend to result in an overestimation. By using an ROI-based approach instead, the SNR will increase, yielding a ΔADC that is more reliable. Nakamura et al. used this approach and found a ΔADC of $0.07 \cdot 10^{-3}$ mm^2/s . While this finding is more in line with the results we obtained, the difference is still well over a factor of 3. The remaining difference is probably explained by the use of $b=0$ data in the referenced studies [111]. It is known from the intravoxel incoherent motion (IVIM) model that low b-values reflect signal variations from the blood pool and perfusion [22]. By using only $b=0$ and $b=1000$ data, obtained ADC variations will include blood flow pulsations reflected by an increased ADC at peak systole. Some studies specifically targeted the blood pool using the IVIM

model as a surrogate for microvascular pulsatility [19; 42]. In this work, however, we used high b-values (300 and 1000, equivalent to displacement encoding of 56 and 31 μm) to exclude any contributions from blood or perfusion in the reconstructed ADC signal, which did not allow for a further investigation of these effects. The findings reported by Federau et al., however, indicate that perfusion effects in the measured signal are already reduced to less than 2% at $b = 300$ [42]. Furthermore, since there is evidence that volumetric strain reflects blood volume pulsations [1; 70; 136], the rather poor correlation of the volumetric strain with measured ADC variations indicates that the measured ADC variations were not dominated by blood volume. Besides, it is a limitation of this study that the acquisition of a dataset with two b-values already took 7 minutes. Adding additional b-values would therefore result in infeasibly prolonged protocols. Moreover, the high bandwidths used for the RF pulses to prevent slices from bending, at the same time requires increased B1, particularly at high field strengths like 7T. Consequently, while scans were within normal specific absorption rate (SAR) limits, the accumulated specific energy dose (SED) at the end of the entire protocol was already nearing its limit. SED (in J/kg) specifies the total energy absorbed by the body during an MRI scan. Extending the protocol for additional data would run the protocol infeasible from a safety perspective. More advanced encoding routines could potentially reduce the acquisition time. For instance, chunk encoding may be a routine that could reduce acquisition times (and SED) [27], albeit at the cost of shorter TRs. This approach may therefore be used especially at lower field strengths, where T1s are generally shorter.

In this work, ADC and strain measurements were binned retrospectively over the cardiac cycle. This approach ensured a fixed TR for all slices independent of heartrate, yet resulted in data points being distributed randomly across the cardiac cycle. Consequently, data density and, thus, SNR in both strain and ADC measurements may differ for different cardiac phases, which was reduced by the use of the moving average window. Prospective cardiac triggering facilitates more direct control of SNR distribution over the cardiac cycle, because it enables fixed time delays with respect to the cardiac R-top [136; 137]. While this approach is frequently used in literature to assess ADC variation over the cardiac cycle, it makes the repetition time heartbeat dependent. Especially when repetition times are short (e.g. 2 R-R intervals [114; 117]) variations in the subject's heart rate lead to unwanted signal variations due to T1 relaxation. Federau et al. already noticed this dependency between heart rate and TR, and minimized the effect by applying a minimum TR of 5 seconds [42]. However, T1s are generally longer at higher field strengths and variations in TR just over 5 seconds still may yield signal variation. Moreover, we were also interested in fluid contributions from CSF and ISF, which have longer T1s compared to tissues like gray and white matter. Although the TR in this work is still not two times the T1 of CSF [130], it does not vary between measurements.

The ratio between artificial and measured ADC variations implies that there is room for a physiological component that can explain the difference. As measured ADC variation increased, larger

ratios were observed between measured dADC and artificial ADC variations. Correcting the measured ADC variation in the FH direction for these artificial ADC variations, still yielded an unexplained variation of 3% of the mean ADC. Together with the strong correlation of measured ADC variations with incremental shear strain, this observation points to an underlying effect responsible for increased ADC variation. It is conceivable that additional mixing or stirring of the interstitial fluid or perivascular spaces driven by tissue deformation adds to an additional variation in ADC.

In conclusion, the developed slice-selective DENSE sequence is capable of simultaneously measuring ADC and strain variations of brain tissue. By combining these results with a single DTI dataset, we were able to successfully estimate the artificial ADC variations induced by tissue deformation. Measured ADC variations were up to 3 times larger than these artificial variations, which is probably explained by a physiological effect. Here, future research is welcome to propose physiological effects that are responsible for the observed differences. We hypothesize that mixing or stirring of the interstitial fluid or perivascular spaces driven by tissue deformation. Although further investigation is required to substantiate this hypothesis, it is conceivable that this additional mixing adds to an additional increased ADC variation over the cardiac cycle. The novel method provides a tool to study this effect and holds the potential to serve for detecting abnormalities in ADC variations in disease.

ACKNOWLEDGEMENTS

The authors thank Miha Fuderer for fruitful discussions and valuable comments on the formulation of the theoretical material.

SUPPLEMENTARY MATERIAL

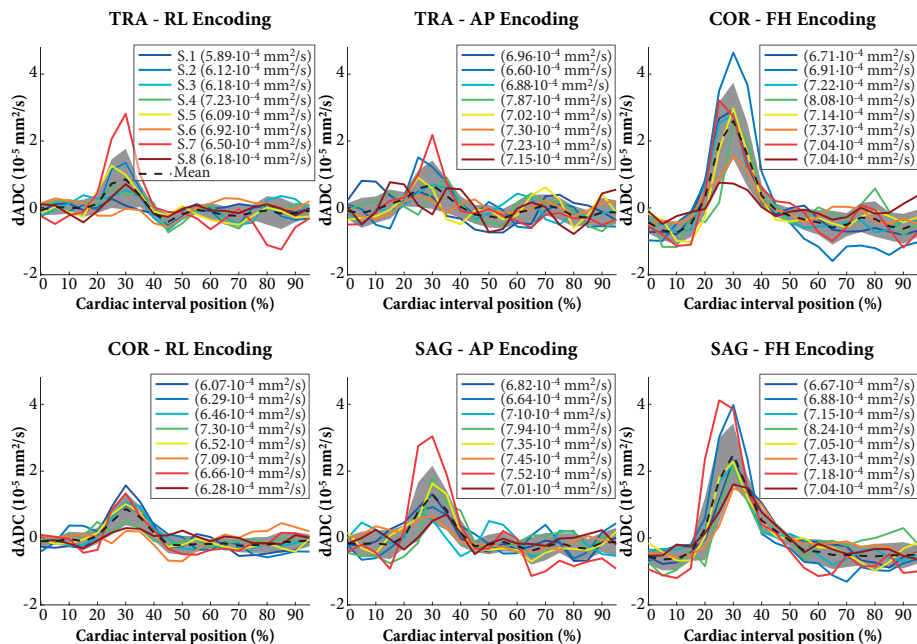
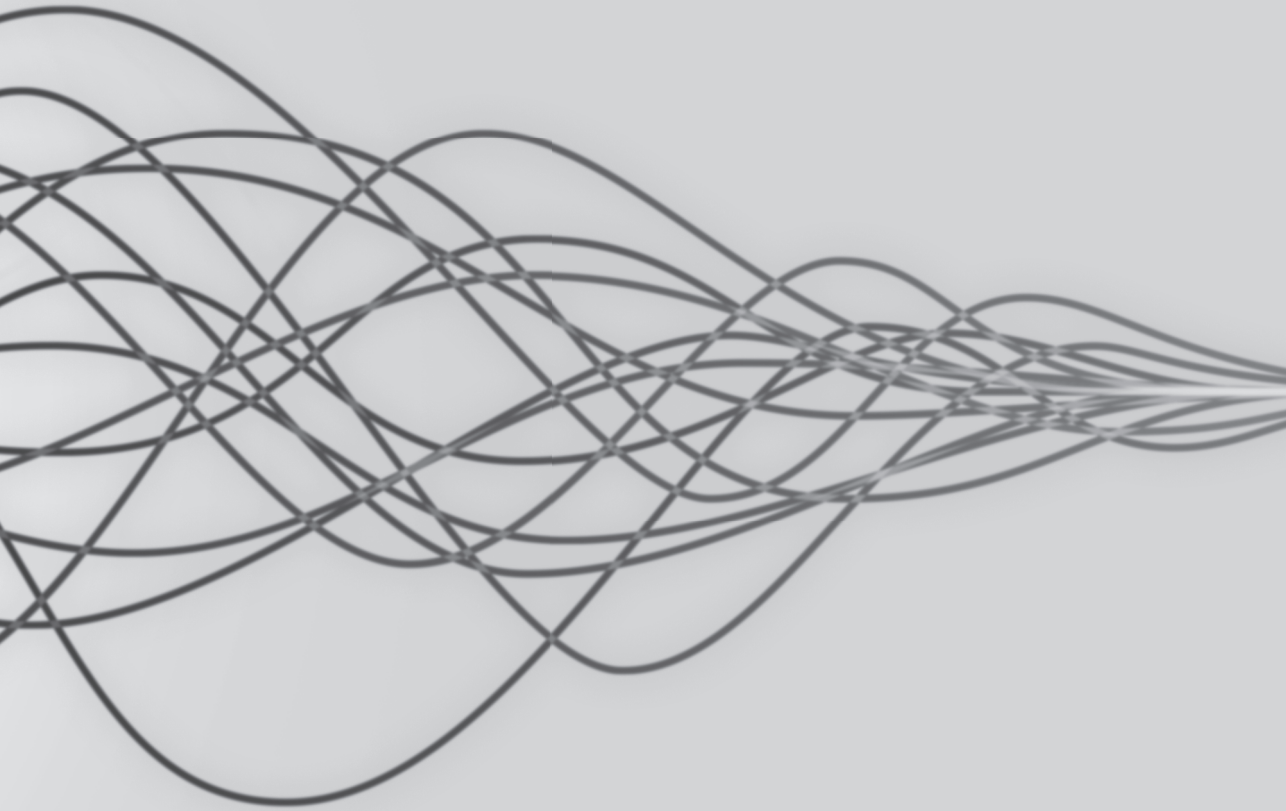


Figure 6-S1 Measured $dADC$ curves over the cardiac cycle separately shown per acquisition orientation and encoding direction. Curves over the cardiac cycle were obtained by averaging over the conservative white matter mask, avoiding blood and CSF signals. Mean ADC values over the cardiac cycle per subject, obtained for the associated acquisition orientation and encoding direction are indicated in the legend. Curves between subjects were synchronized such that peak incremental shear strain occurred at 30% of the cardiac interval. The dotted black line represents the mean $dADC$ over all subjects whereas the gray shaded area indicates the standard deviation. The largest $dADC$ was observed in the Feet-to-Head direction.



7

Summary and general discussion



SUMMARY

The objective of the work presented in this thesis was to develop non-invasive imaging techniques of brain pulsations in response to the beating heart and respiration, in order to pave the way to non-invasive, *in-vivo* assessment of the impact of disease and physiological stressors on the properties of the brain tissue and microvasculature. Physiological brain tissue deformation is driven, among others, by variations in blood pressure induced by cardiac and respiratory cycles. As the arterial pressure wave reaches the microvasculature, the cerebral tissue expands inwards towards the ventricles, and the related tissue motion shows a funnel shaped pattern directed towards the foramen magnum [58]. At the same time, cerebral spinal fluid (CSF) is squeezed out of the skull to compensate for the additional blood volume change. The pulsations of brain tissue form a valuable source of information. The tissue deformation is not only driven by variations in blood volume from the microvasculature, but also reflects differences in tissue properties like stiffness.

Tissue deformation is physically described by strain, which is derived from motion field maps. In this work, we started from two MRI motion mapping methods that provide these motion field maps. These MRI methods, phase-contrast MRI (PC-MRI) and displacement encoding using stimulated echoes (DENSE), deploy the MRI phase signal to encode the respective velocity or displacement into the MRI signal. High signal to noise ratio (SNR) in the motion field maps is crucial for strain computations, as these strain computations involve the use of spatial derivatives, which amplify the noise present in the motion field maps. In **Chapter 2** we compared the performance of PC-MRI with DENSE through computer simulations and found that DENSE outperforms PC-MRI for small deformations in the human brain tissue, such as induced by the heartbeat. The difference between DENSE and PC-MRI becomes even more pronounced when, besides the cardiac cycle, pervasive animators with lower frequency, such as respiration, are targeted. Consequently, we specifically focused on the DENSE sequence and validated simulations with phantom measurements. Simulations compared well to the phantom measurements. We used these validated simulations to optimize the DENSE settings and tested these settings in a healthy volunteer. We achieved a factor of 1.6 SNR increase *in-vivo* compared to the motion encoding sensitivity as reported in previous experiments [1; 140]. Two key aspects played a role here. First, the single-shot approach of the DENSE sequence avoids increased artifacts that plagued the 3D approach, as the motion sensitivity increases. Second, the assumption of small tissue strains allows for resolving additional phase wraps in the displacement maps. While optimizing the DENSE sequence, it is important to take into account the additional diffusion weighting that large encoding gradients induce on the magnitude signal. Shorter mixing-times between encoding and decoding will allow for stronger encoding gradients, while maintaining reasonable diffusion weighting. It depends on the frequencies of the targeted animators what mixing times may be desirable. Low frequency animators such as vasomotion or respiration

require extended mixing times compared to higher frequencies such as the cardiac cycle [162]. Once these boundary settings have been determined, optimal encoding sensitivities can always be computed unambiguously.

Cardiac and respiration-induced contributions to brain tissue deformation were disentangled in **Chapter 3**. The implementation of the DENSE sequence was modified to include an additional cardiac cycle between encoding and decoding, for increased sensitivity to tissue deformations induced by respiration. Furthermore, we modeled the snapshot images as a linear combination of both cardiac and respiratory contributions and introduced a linear model that utilized the physiological data to disentangle these contributions. The single-shot approach of the acquisition was crucial in this regard, not only for achieving optimal motion sensitivity, but also to capture the unique physiological ‘states’ (i.e. mixture of respiration and heartbeat related contributions to motion) of each acquired image. Yet, the single-shot approach limited the acquired volume to 2D images only. We acquired two orthogonal slices and performed a 3D analysis of tissue strain along the intersection line. Here we observed, for the first time, the Poisson effect reflected in the tissue deformation, where longitudinal tissue stretch was accompanied by transverse shrinkage of tissue. Furthermore, the results showed that cardiac-induced tissue deformation is dominating respiration contributions by approximately a factor of five.

As the cardiac cycle proved to be the dominant factor in driving pulsatile brain tissue deformation, we focused the remainder of our work on cardiac-induced tissue deformations. In **Chapter 4**, we extended the single-shot DENSE method by combining the approach with a simultaneous multi-slice (SMS) acquisition. In addition, we implemented slice-shuffling to acquire all slices covering the entire brain at different locations in the cardiac cycle. Because the focus was on cardiac-induced contributions only, we reduced the time between encoding and decoding substantially which led to a new optimal encoding sensitivity. The work was the first to report the full cardiac-induced strain tensor of brain tissue deformation with complete brain coverage, for which we found well-defined strain patterns that are consistent between subjects. We called this novel approach Strain Tensor Imaging (STI). STI provided a method to visualize and quantify tissue dynamics that reflect fundamental aspects of the interaction between tissue and blood. The method may be able to detect abnormalities in disease.

The potential of the STI technique to detect abnormalities in disease, was explored in a case study patient that was treated with a craniectomy. At the time of the MRI acquisitions, the cranial opening – 12 cm in diameter – had not yet been closed by a reconstructed skull part. The case study therefore has an analogy with the first recordings of the brain ever, which was developed and carried out at the time by Angelo Mosso (1846-1910). We compared the strain maps from the patient with the strain maps obtained in healthy subjects, and showed distinct differences between these maps in **Chapter 5**. This ‘Angelo Mosso experiment in modern days’ shows that the

MRI technique is sensitive enough to detect abnormalities in brain tissue deformation. Although the loss of skull is an evident alteration in boundary conditions, the technique may hold potential in detecting more subtle abnormalities as well, such as from vascular disease.

The motion sensitizing gradients of the DENSE sequence induce diffusion weighting in the magnitude images that need to be accounted for in optimizing the DENSE settings for application in the brain. Consequently, the unique situation arises that the DENSE sequence can simultaneously provide both strain data and diffusion data in the brain. We used this property in **Chapter 6** to investigate to what extent observed ADC variations in the brain over the cardiac cycle can be explained by measurement errors induced by variations in tissue strain. We found that observed ADC variations are at least a factor of 2 larger than could be explained by variations in the tissue strain. Particularly in the Feet-to-Head direction, the observed ADC variations were much larger compared to the simulated 'artificial' ADC variations, as predicted based on the observed tissue strain. ADC variations in the brain thus likely reflect physiological processes such as mixing or stirring of the interstitial fluids.

DISCUSSION

We thus developed non-invasive MRI techniques that quantitatively map brain tissue deformations induced by physiological animators such as heartbeat and respiration. We found that cardiac-induced tissue deformations are dominant over respiration contributions by approximately a factor of five. We extended the MRI technique to obtain these cardiac-induced tissue deformations with whole-brain coverage and observed abnormal deformations after a craniectomy on an individual level. The technique was also able to simultaneously quantify ADC variations over the cardiac cycle, which were at least a factor of 2 larger than the artificial ADC variation from deformation-induced measurement errors. Hence, these variations likely reflect mixing or stirring of the interstitial fluids. In this section, I would like to place the developed technique in a broader perspective of alternative methods that aim to assess blood volume pulsations and the condition of the microvasculature. I continue with an contemplation on how brain tissue deformation carries an intrinsic complexity, as the observations are related to the interplay between the microvasculature, blood volume pulsations, and tissue properties, such as stiffness. In separate sections that follow, we discuss the strengths and limitations of the technique, and address its implications and future steps.

Considerations regarding measurements of brain tissue deformation

From whole brain approaches to voxel-wise measures

The methods proposed in this thesis provide complementary information to data obtained by conventional MRI ‘mass-balance’ approaches. The main difference between both approaches is their spatial localization. Mass-balance approaches employ established techniques such as PC-MRI to study the overall mass balance of blood- and CSF flows at the spinal [15; 41; 165]. Although these approaches have provided valuable insight in the flow dynamics to the brain, they reflect effects from the entire brain, including from the larger arteries and veins that reside in the intracranial CSF space surrounding the brain. The methods presented in this thesis provide information on local blood volume pulsations from vessels embedded in the tissue, which can help to unravel relative contributions from vessels in the tissue and the larger vessels in the intracranial CSF. This is an important advancement, especially in disease, because these relative contributions could change with disease, while the overall mass-balance remains unchanged. Conventional mass-balance approaches would not be able to detect such a change, while the technique described in this thesis is indeed sensitive to a change in blood volume pulsations from the microvasculature embedded in the tissue. Moreover, now that we have a tool to distinguish between relative contributions in blood volume pulsations from the microvasculature and the larger vessels that surround the brain, we can also advance our understanding of basic brain physiology. For instance, the close similarity between CSF volume flows and brain tissue volume pulsations as observed in Chapter 4, imply that the large vessels surrounding the brain exhibit limited volume pulsations. The limited contribution from the larger vessels in overall volume pulsation (reflected by CSF volume flows) may be explained by simultaneous compression of the cortical veins and the cavernous sinus, thereby compensating for increased blood volume [2]. However, a caveat to this interpretation is the validity of Monro-Kellie doctrine, which assumes constant intracranial volume over the cardiac cycle [58; 103], which is still debated [6; 14; 157].

Indeed, there is evidence that the skull does not behave like a truly rigid box, but slightly varies in volume over the cardiac cycle. Variations in skull diameter were observed by Ueno et al., who used cranial sonography (US) to measure variations in skull diameter over the cardiac cycle [160; 161]. He provided additional evidence that the skull diameter pulsates with the heartbeat by performing separate measurements in which he applied variable external counter pressure, which was found to reduce the observed skull diameter pulsations. US transmits sound waves in the brain and records the reflections, from which the image is reconstructed. The technique has high temporal resolution (up to several kHz), but suffers from a limited field of view (FOV) [38; 152]. Generally, the transducer is placed at the temporal bone window, as it has reduced skull thickness. This allows the sound waves to penetrate the skull better, but at the same time reduces the FOV even further. Although speed, cost and convenience are some evident advantages of US [61], the full brain coverage of the MRI technique proposed in this thesis is advantageous,

especially in a research setting. The DENSE sequence shows potential to measure the displacement of the fatty bone marrow in the skull, that is required to assess potential pulsations of the skull. If we could show with DENSE that skull layers facing each other are found to move apart over the cardiac cycle, this could help to negate the Monro-Kellie doctrine. Thus, the DENSE sequence shows potential to validate the Monro-Kellie doctrine and provide a more complete picture of the skull pulsations than US.

The eye as a window to the brain

Optical coherence tomography (OCT) is an imaging technique that can assess the condition of the vessels and retinal nerve fibers in the eye. The technique typically uses near-infrared light to study the microvessels of the eye with up to sub-micrometer spatial resolution, depending on the light source [151]. These microvessels originate from the brain directly and are therefore considered as a surrogate for the condition of the brain's microvasculature. Nerve fiber and retinal thinning in the eye were found to be associated with both neurodegeneration (gray matter loss of occipital and temporal lobe) [115] and increased risk of dementia [109]. Compared to MRI, the technique is more convenient and has lower cost, showing potential to be applied in large cohorts. However, the question remains whether the central retinal blood vessels and nerve fibers in the eye are affected prior to the brain damage, or whether damage in the brain occurs first, after which alterations in the eye are observed. The methods described in this thesis provide a window to the brain's microvasculature, that is crucial to gain more insight in the order in which neurodegeneration occurs in both the eye and in the brain.

The complexity of brain tissue deformation

As brain tissue deformation result from the interplay between the microvascular network and tissue, it carries an intrinsic complexity that makes direct interpretation difficult. The interweaving of tissue properties and microvasculature is best reflected in the volumetric strain, which describes the net expansion or compression of each voxel of tissue and thereby reflects both blood volume increase and tissue stiffness. Previous studies have found that gray matter exhibits larger volumetric strain variations over the cardiac cycle compared to white matter [1; 2; 70]. Since white matter could be stiffer [80] and has reduced blood-volume to tissue ratio compared to gray matter [9; 30; 164], both blood volume and tissue properties could contribute to this effect. Here, it is important to note that volumetric strain serves as a lower bound estimation of the underlying blood volume pulsation, as any simultaneously compression of the interstitial space would reduce the amount of observable volumetric tissue strain [91; 92]. This compression may occur only if the interstitial fluid is squeezed out of the tissue and drained into the veins or CSF. Thus, as we target the microvasculature with the developed methods, we seem to hit the intricate tissue-blood vessel interaction at a level where vascular contributions are difficult to distinguish from tissue contributions. This merger between vascular and tissue contributions in the DENSE measurements reflects the complexity not only of brain tissue deformation, but also of research

on neurodegenerative diseases in general, as the question remains to what extent these diseases are primarily driven by vascular or neuronal disease [35; 133; 158].

The interaction between tissue and vascular properties that constitute the measured tissue deformation may well be disentangled using extensive computer modeling and reconstructions on elastography [68; 150]. So far, results on these reconstructions have not always been as unambiguous, which may also be explained by the use of different measurements methods [31]. For instance, MR elastography (MRE) uses external vibrating devices to induce propagating shear waves in the tissue, from which the properties can be inferred. Yet, as the brain can be considered a porous medium (cells and interstitial fluid) [57], the brain tissue requires time to adapt to variations in (external) conditions. Shear waves that propagate through the brain thereby experience different resistance depending on their frequency, similar to a boat that can experience considerable increase in drag with just a small reduction in speed. Consequently, the use of different vibration frequencies leads to considerably different outcomes, which reflect the complexity of the mechanical properties of the brain [29; 34]. Methods described in this thesis provide tools to obtain data from ‘intrinsic’ activation [169]. This ‘intrinsic’ activation arises from cardiac frequencies, that are lower compared to the shear wave frequencies and better resemble in-vivo brain dynamics.

Technical considerations

A clear strength of the STI technique is that it can provide tissue strain maps with full brain coverage. In its current form, the technique provides sufficient SNR for these maps to be assessed on a voxel-wise basis. Moreover, the technique is capable to detect abnormalities in brain tissue deformation on an individual subject level in a reasonable scan time. Furthermore, the single-shot technique acquires 2D slices in 50 ms and is therefore less sensitive to subject motion. This is particularly an advantage when applied in patients, because patients are more prone to (involuntary) movement as compared to healthy (young) subjects.

The main limitation of the STI technique is that we could assess the strain maps only with a rather coarse resolution (3mm isotropic). Consequently, the derived strain maps suffer from partial volume effects, which are particularly seen at CSF-tissue boundaries. The effective resolution of strain maps was even further reduced by the use of spatial derivatives, which uses the displacement information from two neighboring voxels to compute the strain. If one of these voxels is located in a CSF region, the results are not reliable. We mitigated these effects by using a stringent mask that eliminates all voxels near CSF by adding an additional erosion step. This hampered us in our analysis, especially in regions near free moving water like sulci, and in structures below the current resolution, like the cerebral cortex. Increasing the resolution is not only limited by the limited sample time of the single-shot acquisition, but also requires sufficiently increased SNR. Each factor of resolution increase requires that same factor to the power of 4 in additional

SNR: 3 for the reduction in volume and an additional term for the spatial derivative. We suspect that increasing the SNR will require improved hardware, such as coil arrays with more elements, faster gradients or even higher field strengths [67]. Placing receive arrays close to the head could already help to obtain sufficient SNR to study the cerebral cortex in more detail, albeit at the cost of reduced brain coverage. Still, even with sufficient SNR, methodological improvements will be required to translate the increased SNR into higher spatial resolution. For instance, the simultaneous multi-slice approach is limited by the multi-band excitation pulse, which is prolonged significantly for thinner slices (higher resolution). Chunk encoding could potentially circumvent this effect, as it acquires thicker slabs [27]. By sampling these slabs with advanced sampling methods like compressed sensing, higher spatial resolution may be obtained in still reasonable sampling time [54; 95]. Additionally, computing the derivative on the complex signal through the Fourier transform could possibly avoid reducing the effective resolution through the spatial derivative, albeit at the cost of SNR [89].

In assessing the strain maps, it is important to note that both the principle strains and shear strain maps have higher intrinsic SNR as compared to volumetric strain maps. This is also evident from the repeated measurements reported in Chapter 4 and is due to the fact that volumetric strain is derived from the summation over the three principle strains. Because these principle strains consist of both positive and negative values – of which the first and third principle strain largely cancel each other – the result converges to a value close to zero while the noise increases by a factor of $\sqrt{3}$. Diseases that result in different shear strains rather than volumetric strains are therefore expected to be detected more easily. It is therefore important to study how changed conditions of brain tissue affect volumetric strain and shear strain. Volumetric strain and shear strain are not correlated, and only show a weak relation in the temporal behavior. This suggests that volumetric increase of tissue does not (necessarily) cause tissue shear strains (Poisson effect). The two quantities thereby likely reflect different aspects of both local and overall mechanical behavior of the tissue. In Chapter 5 we saw that a skull defect significantly impacted principle strains and shear strains. Although this was a major change in boundary condition, it is conceivable that STI may therefore have much wider potential applications in the evaluation of conditions with aberrant brain deformation or tissue compliance, such as hydrocephalus or brain tumors. On the other hand, volumetric strain predominantly reflects blood volume change. Although vascular diseases may affect shear strain, we expect that these diseases are predominantly reflected by changes in volumetric strain. Whether the technique holds also direct potential in assessing more subtle diseases such as vascular diseases and dementia – especially when they appear to be mainly reflected by changes in the volumetric strain – remains for future studies.

Future steps to apply strain tensor imaging in studies of brain health and disease

Now that the techniques are developed, the territory of tissue deformation in the brain can be explored further, in particular in patients with diseases like cerebral small vessel disease (cSVD) and dementia, but possibly also in other conditions such as brain tumors or people with aberrant CSF circulation (e.g. normal pressure hydrocephalus). Patient studies are more convenient to perform on 3T clinical scanners, yet SNR constraints probably will complicate the translation. Even in its current form, we do not think the developed method can tolerate a 3/7 factor reduction in SNR resulting from a translation to these scanners without compensating this SNR loss. The 4th-power relationship between SNR and voxel-size now is advantageous for compensating the SNR reduction, and a full compensation would still yield an isotropic resolution of only 3.7 mm.

The strain maps indicate that the STI technique has potential to study abnormal tissue deformations in disease. Given the random orientation of the microvasculature, we initially expected a more isotropic deformation pattern as a result of the non-oriented swelling of the microvascular bed. However, in Chapter 3 we observed, for the first time, interesting details of the tissue deformation including positive and negative principle strains consistent with the Poisson effect. The coronal slice showed large tissue deformation around the ventricles, which coincides with the area where white matter hyperintensities (WMH) often form in patients with vascular diseases [84; 167; 168]. Considering the brain as a porous medium [57], we hypothesized that large tissue deformations could potentially ‘choke’ the tissue locally by systolic compression of the (venous) microvasculature leading to this tissue damage [171]. However, the limited coverage of the 2D slices did not provide the full pattern of strain. In Chapter 4, we were able to acquire tissue strains with full brain coverage and obtained maps with regional normal differences of the octahedral shear strain, which reflects the Poisson effect. Yet, the mean spatial pattern of the shear strain does not seem to match with previously reported probability maps of WMH occurrence derived from patients with various degrees of ageing related degenerative and vascular pathologies [84]. Instead, shear strain patterns roughly followed the distribution of deep medullary veins that support venous drainage from the brain (see Figure 7-1) [60; 85; 108; 174]. Here, it must be acknowledged that we obtained our data in a rather young population, which is not representative for studying these types of diseases. As deformation patterns may alter in disease, future studies can use the STI technique to assess whether change in shear strain is related to macroscopic (mostly irreversible) tissue damage, such as observed in cSVD.

Future steps to measure brain waste clearance

Brain tissue deformations propel CSF around the brain and may deform the interstitial space, which in turn causes mixing or stirring of the interstitial fluid (ISF) [10; 12; 100; 153]. Since CSF and ISF flows are considered to clear metabolic waste products from the brain, brain tissue

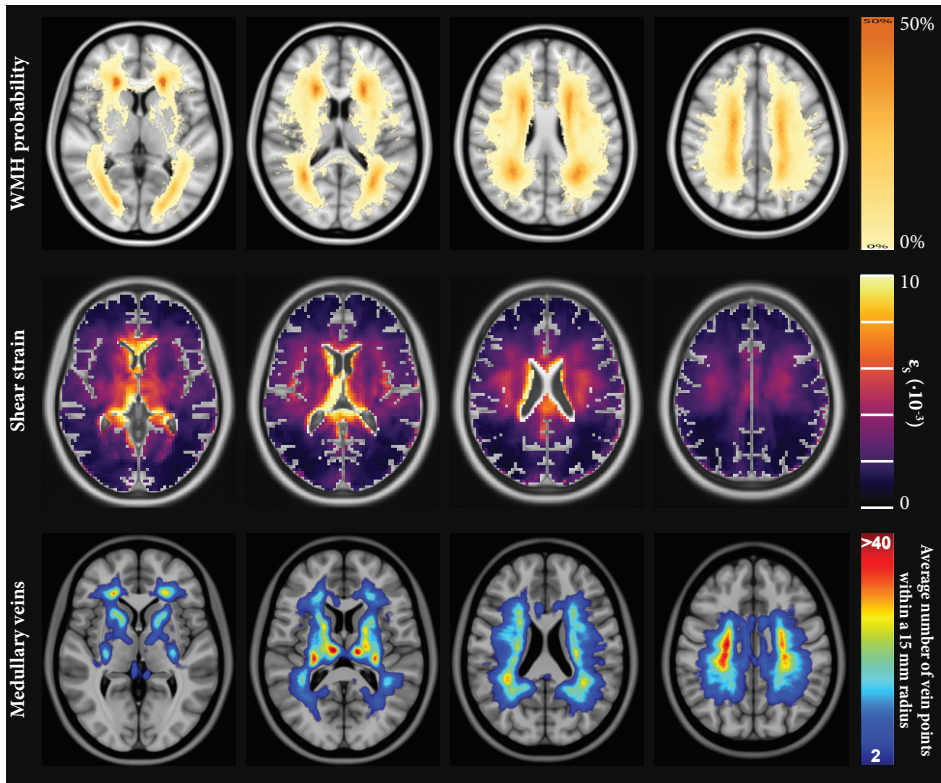


Figure 7-1 Tissue shear strain maps (middle row) compared with WMH probability maps (top row) and density of deep medullary veins (bottom row). Per column, the location of the slices corresponds as much as possible. Shear strain maps were obtained in a young population (age 30 ± 4 years), while the WMH maps and deep medullary vein maps were originated from data acquired in an older population (mean age 70 years). The maps therefore do not originate from representative groups to be compared directly, as deformation patterns may alter with age and disease. The results merely indicate that Strain Tensor Imaging has potential to study abnormal tissue deformations in disease. WMH probability maps were reproduced with permission from Kuijf et al., *IEEE Trans. Med. Imaging*, 2019 [84]. Deep medullary vein maps were reproduced with permission from Kuijf et al., *Eur. Radiol.*, 2016 [85].

deformation as such may be one of the main drivers of the brain's waste clearance system [77; 100]. Alterations in the microvasculature due to aging or disease may alter brain tissue deformation, which may have profound downstream effects on the brain's waste clearance. The exact mechanisms of the brain's clearance system are still under debate, but they are important to advance our understanding of, for instance, the clearance of amyloid beta, which is recognized as a primary process in Alzheimer disease [153]. It is currently believed that CSF-ISF exchange in perivascular spaces (PVS) facilitates the drainage of waste products from neuronal cells [76; 125]. Non-invasive imaging techniques, however, remain vital to further substantiate the hypotheses, especially in humans. Increasing efforts to develop such methods generally propose high spatial

resolution MRI diffusion sequences to assess ISF pulsations in PVS, including those along large vessels such as the circle of Willis [65; 71; 72]. In Chapter 6, we proposed a multimodal approach, which links both diffusion and tissue strain. These methods show interesting variations of the apparent diffusion coefficient (ADC) over the cardiac cycle, but lack information on the direction of transport. Rather, these methods focus on the clearance process through dispersion, which is a combined effect of mixing and diffusion [10]. However, DENSE offers the opportunity to provide information on both coherent (displacement) as incoherent (ADC) motion. To make DENSE fluid specific, a T2-preparation sequence can be incorporated between the motion sensitizing gradients. As the signal then only originates from water, it is no longer confounded by tissue motion and the spatial resolution will become less of an obstacle as a result. Once coherent motion – for example in PVS – can be observed, the question then becomes what animators drive this net transport.

The wavelength of the cardiac related pulsations appears to be too long to induce significant spatial gradients that are needed for transport [4]. Instead, pervasive animators at lower frequency such as vasomotion may be more important drivers in clearance, [4; 162]. Vasomotion are spontaneous fluctuations of the arterial diameter initiated by vascular smooth muscle cells that occurs at approximately 0.1 Hz and have much shorter wavelengths [63]. Vasomotion is currently investigated in invasive preclinical studies. In humans, low-frequency fluctuations of CSF in the spinal canal have been observed in sleep, which correlated with both EEG and blood originated level dependent (BOLD) MRI [51]. Especially the CSF fluctuations indicate that brain tissue deformations are also involved here. It is yet unclear whether vasomotion is sufficiently spatially coherent to lead to measureable tissue strains, and whether our method would be sensitive enough to detect those low frequencies. The duration between motion encoding and decoding is limited by the T1 tissue relaxation time, which is less than 2 seconds in the human brain at 7T. Still, we detected respiration related effects, which have a frequency of approximately 0.25 Hz, not too far from the vasomotion frequency. A key difference, however, is the availability of physiological traces. While we modeled the observed tissue strain directly from these traces, vasomotion experiments rely on frequency spectrum data obtained from systematic acquisitions. The temporal resolution determines which frequencies can be analyzed. While lower temporal resolutions allow for larger tissue strains to accumulate over time, they cause physiological animators with higher frequencies to alias back as low frequencies into the spectrum. A possible remedy would be to first correct for the physiological frequencies from heartbeat and respiration by using the traces, before transforming the residuals to the frequency domain. It remains for future investigations to assess the potential of our methods in targeting vasomotion.

Strain tensor imaging as covariate measure

MRI measurements are sometimes corrupted by unintended secondary factors like blood volume pulsations and inflow effects. When these secondary effects are not carefully considered, they can

lead to misinterpretation of the results. In Chapter 6, we discussed studies that incorporated data with low diffusion weighting (low b-values) in the experimental setup to assess ADC variation over the cardiac cycle [111; 114]. These low b-values are, however, known to be affected by blood volume pulsations [23; 24]. As blood flows into the brain with every heartbeat, it is therefore not surprising that these studies reported large ADC variations. Consequently, dispersion effects in tissue over the cardiac cycle were overestimated, as increased ADC variations due to perfusion were attributed to ADC variations in the tissue. Similarly, blood oxygen level dependent (BOLD) MRI signal fluctuations in the brain have been studied as a measure for physiological fluctuations due to the heartbeat and respiratory cycles [81]. BOLD MRI, however, depends on T2* weighted signals, which are not specific and depend on blood oxygenation levels that vary with neuronal activity related changes in venous oxygenation, perfusion, CSF flow into the slice and tissue motion. For the methods described in this thesis, we used TE's ranging from 24 to 48 ms in combination with high b-values from the motion sensitizing gradients to ensure suppression of the signal from blood flow, while inflow effects were spoiled by the decoding gradient. Our measurements therefore show potential to provide covariate measures for MRI techniques that – like BOLD MRI – are inherently sensitive to blood volume pulsations. Resting state (RS) functional MRI (fMRI) also relies on BOLD MRI and is used to evaluate regional interactions between brain regions that occur in resting-state [25; 69]. Apart from very low observed frequencies, the support for a neuronal basis of these RS-fMRI signals mainly comes from its correlation with EEG activity as covariate measure [32; 44; 99]. Although the temporal resolution of EEG is high, the spatial resolution remains low and is typically around 10 cm³. Our methods – especially when capable to target vasomotion – could provide tissue strains as an additional covariate measure in these cases. Especially as RS-fMRI is increasingly applied in patients, these covariate measures become more necessary. For instance, cerebral amyloid angiopathy (CAA) has shown to affect the neurovascular response [116], which directly affects RS-fMRI measurements [78]. Altered brain connectivity has been reported in patients multiple-sclerosis (MS) [149], which is a demyelinating disease that degrades the insulating covers of nerve cells. Yet, these altered connectivity findings should be interpreted cautiously, as RS-fMRI observations in this patient group may also result – at least partly – from downstream effects of the underlying inflammation process on tissue integrity and the microvasculature [97; 149]. Here, the techniques proposed in this thesis may help to unravel the different physiological vascular and neuronal aspects that constitute the RS-fMRI signal.

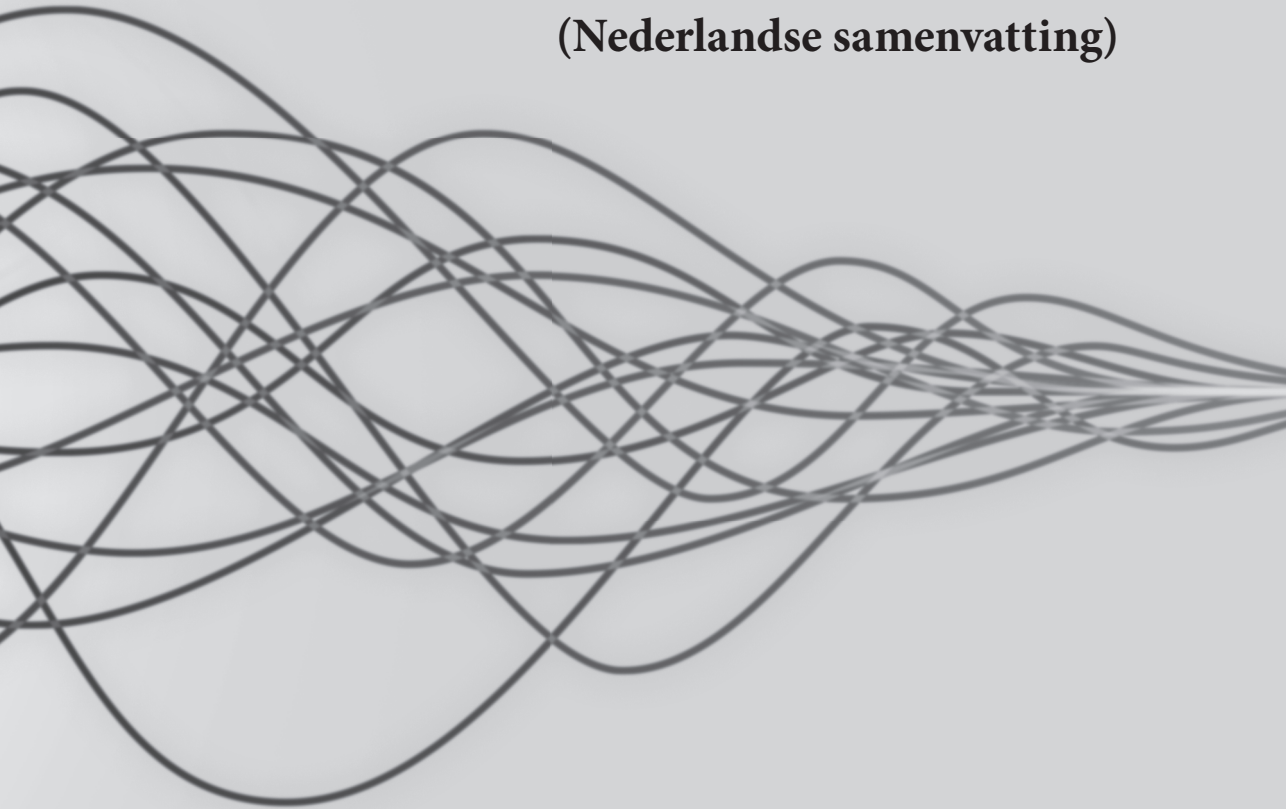
In conclusion, the developed MRI methods described in this thesis enable to non-invasively quantify brain tissue deformation. Brain tissue deformation forms an important link in the complex relationship between blood volume pulsations and CSF flow, which are considered to play a role in maintaining brain homeostasis. Now that the techniques are available, the tissue territory in the brain can be explored further, in particular in patients with diseases like cSVD and dementia. Open questions remain whether and how brain tissue deformation is associated

with these diseases. Tissue deformation carries information on both tissue properties and microvessels, and thereby captures the complex mechanisms of brain dynamics. Hence, being able to assess brain tissue deformation may play an important role in advancing our understanding of the (mechanical) interaction between brain tissue, blood vessels and CSF, both in healthy subjects and disease.



8

**Summary in Dutch
(Nederlandse samenvatting)**



ACHTERGROND

Variaties in bloeddruk, gedreven door onder meer hartslag en ademhaling, veroorzaken subtiële vervormingen van het hersenweefsel. Bij iedere hartslag reist de arteriële drukgolf door de vaatboom en bereikt het zo het niveau van de microvasculatuur – de kleine bloedvaten – in de hersenen. Als gevolg van het toegenomen bloedvolume zwelt het microvasculaire vaatbed op en wordt het omliggende weefsel vervormd, wat resulteert in een pulserend brein. Wanneer de microvasculatuur nu als onderdeel van het weefsel beschouwd wordt, kan men zeggen dat het weefsel opzwellt door het toegenomen bloedvolume als gevolg van het samentrekken van de hartspier. Omdat de hersenen zich in de schedel bevinden, die geen ruimte biedt aan extra volume, wordt ter compensatie voor de bloedvolume toename tegelijkertijd een even groot volume aan hersenvocht (CSF) uit de schedel geperst, richting het spinale kanaal in de wervelkolom. Als het hart zich weer ontspant en het bloed het brein verlaat, keert het CSF weer terug.

Deze pulsatiele vervorming van weefsel in het brein kan informatie geven over de bloedtoevoer, maar ook over de microvaten en het weefsel zelf. Zo is in eerder onderzoek al een kleinere weefselexpansie waargenomen in witte stof vergeleken met grijze stof, wat waarschijnlijk zowel door een lager bloedvolume als door een grotere weefselstijfheid van de witte stof wordt verklaard. Veranderingen in conditie van de kleine vaten of het weefsel worden in verband gebracht met belangrijke hersenziekten zoals beroerten of vasculaire dementie. Deze ziekten, bekend onder de Engelse term *Cerebral small vessel disease*, kunnen op dit moment enkel worden gedetecteerd wanneer macroscopische, meestal onomkeerbare schade is ontstaan. Het kunnen vaststellen van veranderingen in de eigenschappen van het weefsel en microvasculatuur die wellicht aan zulke schade vooraf gaat, zou inzicht kunnen bieden in de veranderde fysiologische omstandigheden die aan deze ziekten ten grondslag liggen.

Daarnaast kunnen hersenweefselvervormingen ook van belang zijn voor hun mogelijke rol in fysiologische processen. De mechanische pulsaties van het hersenweefsel wekken mechano-transductieve reacties op – als een spier die sterker wordt wanneer men deze traint – in endotheelcellen, die de bloed-brein barrière vormen. Tevens zorgen de pulsaties ervoor dat CSF rond de hersen beweegt, wat weer een rol speelt bij de afvoer van afvalstoffen uit de hersenen. Vervorming van hersenweefsel kan daarom worden beschouwd als een belangrijke drijvende kracht van dit afvoersysteem.

DOELSTELLING

Het onderzoek zoals dat in dit proefschrift is beschreven, had als doel om non-invasieve meetmethoden voor MRI te ontwikkelen waarmee de vervorming van hersenweefsel in relatie

tot hartslag en ademhaling kan worden gekwantificeerd. Hiermee wordt beoogd de weg vrij te maken naar non-invasieve manieren om *in-vivo* de impact van ziekte en fysiologische stressoren op de eigenschappen van hersenweefsel en de microvasculatuur te kunnen bestuderen.

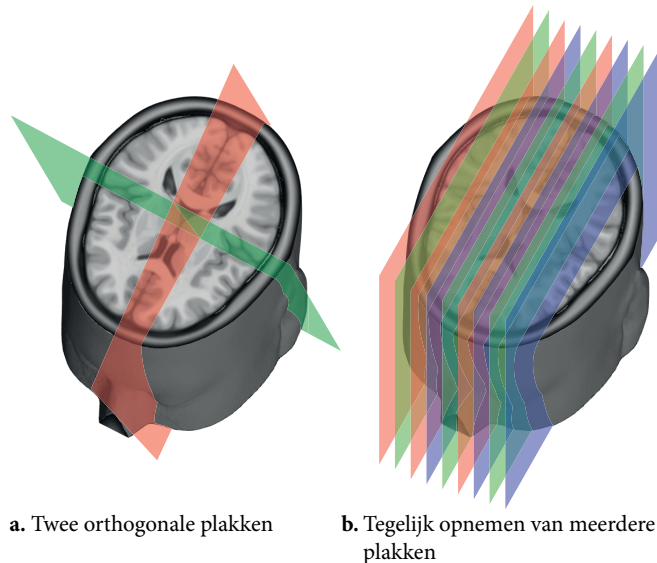
De mechanische vervorming van de hersenen wordt beschreven in termen van de relatieve verplaatsing van de pixels in de afbeelding van de hersenen. Om de vervorming van de hersenen te kunnen berekenen, meten we die verplaatsing met *Magnetic Resonance Imaging* (MRI). MRI heeft de mogelijkheid om op een unieke niet-invasieve wijze de verplaatsing van het hersenweefsel te meten. Tijdens de meting legt de MRI scanner daarvoor twee bewegingsgevoelige gradiënten in het magneetveld aan. Daarmee wordt het MRI-fasesignaal zodanig gecodeerd, dat hieruit de beweging van het hersenweefsel kan worden afgeleid. In de uiteindelijke afbeelding die de MRI scanner van de hersenen maakt, heeft elk voxel (3D pixel) een getal gekregen waaruit blijkt hoeveel het hersenweefsel op die plek verplaatst is.

BEVINDINGEN

In dit werk zijn we uitgegaan van twee MRI sequenties – een sequentie is een serie tijdelijke magneetvelden die in een bepaalde volgorde worden ‘afgespeeld’ – die de beweging van hersenweefsel kunnen meten. Deze twee MRI sequenties worden *fasecontrast MRI* (PC-MRI) en *verplaatsingscodering met behulp van gestimuleerde echo's* (DENSE) genoemd. Beide sequenties coderen het MRI-fasesignaal zodanig dat deze evenredig wordt met respectievelijk de snelheid of de verplaatsing van het weefsel. Voor de berekening van vervorming uit het verplaatsingsveld is het belangrijk om een hoge signaal-ruis verhouding (SNR) te behalen, omdat de berekening gebruik maakt van plaats-afgeleiden, wat de ruis in de verplaatsingsvelden versterkt. **Hoofdstuk 2** vergelijkt de SNR in verplaatsingsvelden die met PC-MRI en DENSE verkregen kunnen worden. Dit wordt gedaan door middel van computersimulaties, waaruit blijkt dat DENSE beter presteert dan PC-MRI voor het meten van hartslag-gerelateerde pulsaties. Wanneer de focus verschuift van de hartslag naar de ademhaling als drijvende kracht van de vervorming, neemt de prestatie van DENSE in verhouding tot PC-MRI nog verder toe. Dit komt omdat DENSE beter geschikt is om de bewegingsgevoelige gradiënten in het magneetveld verder uit elkaar te plaatsen in de tijd, wat gunstiger is om ademhaling te bestuderen vanwege de lagere frequentie. Daarom hebben we ons verder uitsluitend gericht op de DENSE sequentie en de simulaties van deze sequentie gevalideerd met metingen in een fantoom. De simulaties kwamen goed overeen met deze metingen. Daardoor waren we in staat om van tevoren de optimale instellingen te kiezen en bereikten we een factor van 1,6 in SNR toename *in-vivo*, vergeleken met de instellingen die tot dan toe gebruikt werden. Hierbij speelden de aanpak om DENSE te combineren met een MRI-momentopnamen, en de aanname van zeer kleine vervormingen een cruciale rol.

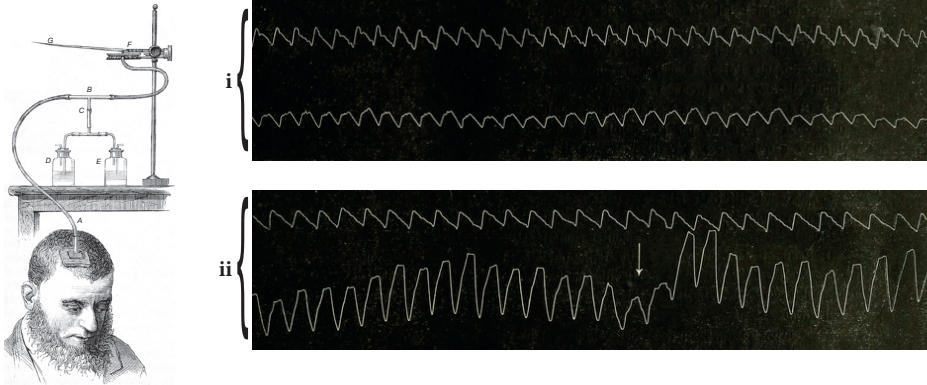
Zowel hartslag als ademhaling dragen bij aan vervorming van hersenweefsel. In **Hoofdstuk 3** wordt de afzonderlijke bijdrage van beide ontrafeld. Daartoe werd de DENSE sequentie zodanig aangepast dat er een extra hartslagcyclus tussen de twee bewegingsgevoelige gradiënten zat. De gevoeligheid voor weefselvervormingen als gevolg van ademhaling werd daardoor groter. Bovendien werd de sequentie zodanig aangepast dat deze momentopnames kon maken (korte MRI opnames met een duur van slechts 50 ms). De momentopnames van de vervorming konden we vervolgens modelleren als een lineaire combinatie van zowel een hartslag- als ademhalingscomponent, waarbij de relatieve bijdragen van deze componenten werd bepaald door de fysiologische gegevens die we tijdens de experimenten hadden opgenomen. Hoewel de MRI-momentopname in dit geval nodig was om de fysiologische 'toestand' van elke afzonderlijke afbeelding vast te leggen, beperkte deze aanpak ons tot het verkrijgen van enkel 2D-afbeeldingen. We hebben data opgenomen van twee orthogonale (haaks op elkaar staande) MRI plakken in negen gezonde proefpersonen en een 3D analyse van de vervorming uitgevoerd langs de snijlijn van de plakken. Een illustratie van deze plakken is weergegeven in Figuur 8-1a. Met de resultaten konden we voor het eerst non-invasief een bekend fysisch fenomeen in hersenweefsel waarnemen, dat het Poisson-effect wordt genoemd. Dit effect houdt in dat rek van het weefsel in een bepaalde richting gepaard gaat met weefselkrimp in een richting die hier haaks op staat. Daarnaast lieten de resultaten zien dat de hartslag een factor vijf meer bijdraagt aan weefselvervorming dan de ademhaling.

Uit hoofdstuk 3 blijkt dat van hartslag en ademhaling, de hartslag de dominante factor is bij vervorming van hersenweefsel. Daarom hebben we ons in de rest van het werk uitsluitend gericht op deze hartslagcomponent. **Hoofdstuk 4** beschrijft de verdere uitbreiding van de DENSE momentopnamen naar het gelijktijdig opnemen van meerdere plakken, zoals geïllustreerd in Figuur 8-1b. Deze plakken rouleerden we in de tijd, zodanig dat alle plakken op verschillende locaties in de hartslag werden opgenomen. Omdat dit hoofdstuk is gericht op de bijdrage van alleen de hartslag, hebben we de tijd tussen de bewegingsgevoelige gradiënten aanzienlijk verkort, wat leidde tot een verder geoptimaliseerde gevoeligheid van de DENSE sequentie. Met deze aanpak is het gelukt om voor het eerst de vervorming van hersenweefsel als gevolg van de hartslag op elke plek in het brein 3D in beeld te brengen (wiskundig aangeduid met de vervormingstensor). Met deze techniek kunnen we kenmerken meten als mate van vervorming, maar ook de richting van rek en krimp. Deze metingen kunnen als input dienen voor elastografische analyses die per voxel de stijfheid en eventueel porositeit (ofwel het lokale bloedvolume) van het weefsel bepalen. De weefselstijfheid is onder meer van belang omdat het een maat is voor de vitaliteit van het weefsel, die verandert bij ouderdom en ziekte.

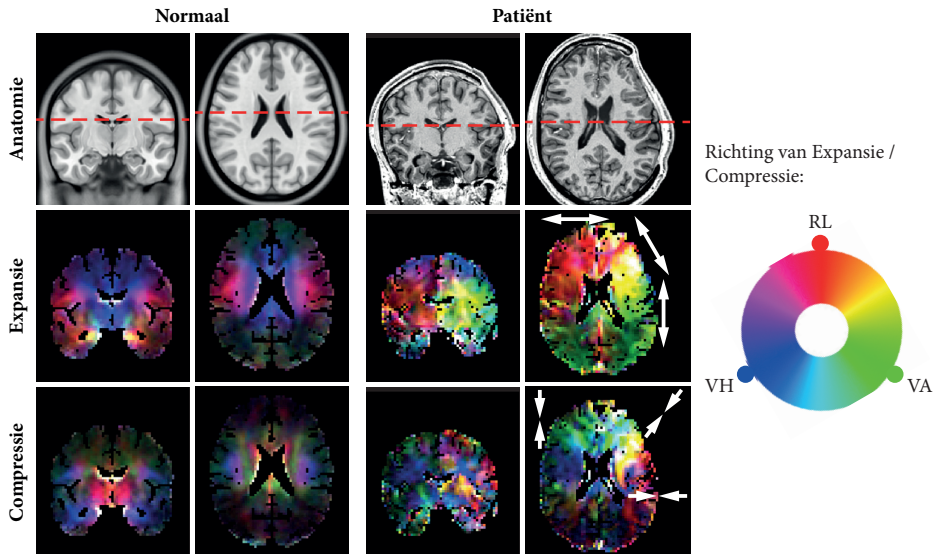


Figuur 8-1 Illustratie van 2D afbeeldingen gemaakt van plakken op verschillende locaties in de hersenen. De locatie van de plakken is aangegeven met kleur en zijn in het geval van onze techniek 3mm dik. Figuur (a) geeft twee orthogonale (haaks op elkaar staande) plakken weer op de locaties die we in hoofdstuk 3 gebruikten om bijdragen van hartslag en ademhaling op weefselvervorming te kunnen meten. Figuur (b) laat zien hoe we in hoofdstuk 4 een methode ontwikkelden waarmee meerdere plakken tegelijk opgenomen kunnen worden, zodat het hele brein wordt omvat. In dit geval namen we 3 plakken tegelijk op (aangegeven met dezelfde kleur), waarna we direct de volgende 3 plakken opnamen. Dit proces moest worden herhaald zodat elke plak op verschillende tijdstippen in de hartslag werd opgenomen. Uit die data kon vervolgens voor elke plak een tijdscurve over de hartslag worden gereconstrueerd.

De mogelijkheid om afwijkingen op te sporen bij ziekte met behulp van de weefselvervormingssensor wordt in **Hoofdstuk 5** verder onderzocht bij een patiënt die eerder werd behandeld met een schedeloperatie waarbij een deel van de schedel tijdelijk werd verwijderd om hoge hersendruk na een ongeval te behandelen. Ten tijde van ons onderzoek met de MRI, was het stuk schedel – 12 cm in doorsnede – nog niet terug geplaatst. In het hoofdstuk vergelijken we de vervorming van hersenweefsel bij deze patiënt met de vervorming van hersenweefsel bij gezonde proefpersoenen, waarvan de resultaten in Figuur 8-2 zijn weergegeven. Dit onderzoek heeft daarmee een analogie met het eerste beeldvormende onderzoek naar de hersenen ooit (zie Figuur 8-2), destijds ontwikkeld en uitgevoerd door Angelo Mosso (1846 – 1910). Het onderzoek zoals in hoofdstuk 5 beschreven, beschouwen we dan ook als het Angelo-Mosso-experiment in de huidige tijd. Het onderzoek laat zien dat de ontwikkelde MRI-techniek gevoelig genoeg is om afwijkingen in vervorming van hersenweefsel te detecteren op het individuele niveau van de patiënt. Echter is het weghalen van een deel van de schedel een grote wijziging van de omstandigheden en zal de toekomst moeten uitwijzen of de techniek ook gevoelig genoeg is om meer subtiele afwijkingen – zoals vaatziekten – te detecteren.



a. Experiment van Angelo Mosso



b. Resultaten van patiënt met schedelopening

Figuur 8-2 Figuur (a) geeft het experiment van Angelo Mosso (1846 – 1910) weer. Angelo Mosso ontwikkelde de 'volumemeter', waarmee hij variaties in het volume van de hersenen kon waarnemen. De volumemeter werd aangesloten bij een persoon die door een ongeval een gat in zijn hoofd had opgelopen, waardoor het volume van de hersenen over de tijd kon worden waargenomen. Twee van deze waarnemingen zijn weergegeven in het figuur, waarbij iedere waarneming het bovenste spoor de referentie gemeten bij de voorarm is, terwijl het onderste spoor de pulsaties van de hersenen is. Daarmee is deze volumemeter de eerste beeldvormingstechniek voor het brein, ooit. Figuur (b) toont de resultaten van de patiënt die ik heb onderzocht en een deel van de schedel miste, analoog aan de situatie bij Angelo Mosso's proefpersoon, hoewel nu een veel groter deel van de schedel was verwijderd. De kleuren geven de richting van de weefsel expansie/compressie aan: rood is de rechts-links (RL) richting, groen de voor-achter (VA) richting and blauw de voet-hoofd (VH) richting. De resultaten laten duidelijke verschillen zien met de referentie (de referentie is het gemiddelde resultaat over 9 gezonde proefpersonen). Terwijl het weefsel bij gezonde personen uitrekt naar het centrum van het brein, rekt het weefsel bij de patiënt voornamelijk op parallel aan de schedelopening. Dit is het beste te vergelijken met een uitpuilende fietsband, waarbij er rek optreedt parallel aan de opening en krimp haaks op de opening (aangegeven met de witte pijlen in de afbeelding).

De bewegingsgevoelige gradiënten van de DENSE sequentie induceren tegelijkertijd een diffusieweging. Diffusie is een proces ten gevolge van de willekeurige beweging van deeltjes, wat er voor zorgt dat een druppel inkt zich in een glas water gelijkmatig verspreid. Hoe sneller de inkt zich verspreidt ('diffundeert'; bijvoorbeeld door hogere temperatuur, of wanneer de vloeistof wordt geroerd), hoe hoger de diffusiecoëfficiënt is. De mate van diffusie komt tot uitdrukking in de magnitudebeelden van het MRI signaal. Met dit effect dient rekening te worden gehouden tijdens het berekenen van de optimale gevoeligheid van de sequentie. Wanneer de DENSE sequentie dus in de hersenen wordt toegepast, doet zich de unieke situatie voor dat de sequentie tegelijkertijd zowel informatie over weefselvorming (in het MRI-fase signaal) als diffusie (in het MRI-magnitude signaal) kan geven. Deze eigenschap hebben we in **Hoofdstuk 6** gebruikt om te onderzoeken in hoeverre waargenomen variaties van de kennelijke diffusiecoëfficiënt (ADC) over de hartslag verklaard kunnen worden door variaties in vervorming van weefsel. Variaties in weefselvorming beïnvloeden namelijk de magnitude van het MRI-signaal, waardoor het lijkt alsof er ADC variaties optreden, terwijl dit in werkelijkheid niet zo hoeft te zijn. We ontdekten dat waargenomen ADC variaties minstens een factor 2 groter zijn dan de variaties die door weefselvorming konden worden verklaard. Dat houdt in dat er na correctie weldegelijk ADC variaties over de hartslag optraden. Vooral in de voet-hoofd richting waren de waargenomen ADC variaties veel groter in vergelijking met de gesimuleerde 'kunstmatige' ADC variaties, zoals verwacht op basis van de waargenomen weefselvorming. ADC variatie in de hersenen weerspiegelen dus waarschijnlijk ook fysiologische processen zoals het 'mixen' of 'roeren' van de interstitiële vloeistof.

Concluderend vormt de vervorming van hersenweefsel een belangrijke schakel in de complexe relatie tussen bloedvolume pulsaties en CSF stroming, waarvan wordt aangenomen dat ze een cruciale rol spelen bij de ontwikkeling van neurodegeneratieve ziekten. De ontwikkelde MRI methoden zoals beschreven in dit proefschrift, stellen ons in staat om deze vervorming van hersenweefsel non-invasief te kunnen kwantificeren. Nu de technieken beschikbaar zijn, kunnen de hersenen op het gebied van weefselvorming verder worden bestudeerd, met name bij patiënten met ziekten als *cerebral small vessel disease* en dementie. Weefselvorming weerspiegelt de complexe fysiologische mechanismen die zich in de hersenen afspelen, hoewel de vervorming van hersenweefsel van verschillende factoren afhangt. Dit bemoeilijkt mogelijk de interpretatie van veranderingen in weefselvorming. Niettemin kan het bestuderen van de vervorming van hersenweefsel helpen om beter te begrijpen welke (mechanische) interactie bestaat tussen bloedvaten en het hersenweefsel, zowel bij gezonde als zieke mensen.





A

List of publications

Acknowledgements (Dankwoord)

References

Curriculum Vitae

LIST OF PUBLICATIONS

Peer-reviewed publications

Sloots JJ, Biessels GJ & Zwanenburg JJM. Cardiac and respiration-induced brain deformations in humans quantified with high-field MRI. *Neuroimage* 210: 116581 (2020).

Sloots JJ, Biessels GJ, de Luca A & Zwanenburg JJM. Strain Tensor Imaging: Cardiac-induced brain tissue deformation in humans quantified with high-field MRI. *Neuroimage* 236: 118078 (2021).

Submitted manuscript

Sloots JJ, Froeling M, Biessels GJ & Zwanenburg JJM. Dynamic brain ADC variations over the cardiac cycle and its relation to tissue strain assessed with DENSE at high-field MRI.

In preparation

Sloots JJ, Biessels GJ, Amelink GJ & Zwanenburg JJM. Strain Tensor Imaging: abnormalities in cardiac-induced brain tissue deformation detected on an individual subject level.

Conference proceedings

Sloots JJ, Adams AL, Luijten PR, Biessels GJ & Zwanenburg JJM. Unraveling cardiac and respiratory contributions to brain tissue motion using single shot 2D DENSE at 7T MRI. *Proc. Int. Soc. Magn. Reson. Med.* 26: 0368 (2018). **Summa Cum Laude ISMRM merit award.**

Sloots JJ, Luijten PR, Biessels GJ & Zwanenburg JJM. Optimizing the DENSE Sequence for Accurate Brain Tissue Strain Measurements at 7T MRI. *Proc. Int. Soc. Magn. Reson. Med.* 27: 2800 (2019).

Sloots JJ, Luijten PR, Biessels GJ & Zwanenburg JJM. Cardiac and Respiratory induced 3D Brain Tissue Strain as Marker of Physiological Blood Volume Dynamics at 7T MRI. *Proc. Int. Soc. Magn. Reson. Med.* 27: 2799 (2019). **Magna Cum Laude ISMRM merit award.**

Sloots JJ, Luijten PR, Biessels GJ & Zwanenburg JJM. Mapping whole brain cardiac and respiratory induced tissue motion using a single-shot multi-slice acquisition with at 7T MRI. *Magn. Reson. Mater. Physics, Biol. Med.* 2020 32: S07.08 (2020).

Sloots JJ, De Luca A, Biessels GJ & Zwanenburg JJM. Strain Tensor Imaging (STI): Voxelwise assessment of cardiac-induced brain tissue strain at 7T MRI. *Proc. Int. Soc. Magn. Reson. Med.* 28: 0536 (2020)

Slouts JJ, Froeling M, Biessels GJ & Zwanenburg JJM. Dynamic Changes in Brain Tissue Strain and ADC over the Cardiac Cycle quantified at 7T MRI. *Proc. Int. Soc. Magn. Reson. Med.* 29: 0648 (2021)

ACKNOWLEDGEMENTS (DANKWOORD)

Onderzoek is nooit af. Ook het schrijven van de laatste hoofdstukken van dit proefschrift leidde dikwijls tot nieuwe ideeën en inspiratie. Echter markeert dit proefschrift wel degelijk een einde van een bijzondere tijd. Graag wil ik iedereen bedanken zonder wiens steun en aanmoediging dit proefschrift nooit tot stand was gekomen. Hieronder richt ik mij tot een aantal mensen in het bijzonder.

Allereest prof. dr. G.J. Biessels, beste Geert Jan, bedankt voor al je adviezen en nieuwe inzichten die onze besprekingen brachten. Iedere keer als we een bespreking hadden gehad was ik verast door de uitkomst en had ik de kern van het onderzoek weer helder op mijn netvlies. Ik bewonder je manier waarop je de tijd neemt om tot de essentie van de techniek door te dringen en mij daarbij uitdaagt om helder te formuleren. Met argumenten als ‘omdat het kan’ nam je geen genoegen. Ik wil je bedanken voor het vertrouwen dat je mij gaf om het onderzoek naar eigen inzicht in te vullen. Vooral de steun en de snelheid waarmee we de techniek uiteindelijk bij een patiënt konden testen, hebben mij enorm gemotiveerd om dit alles tot een goed einde te brengen.

Prof. dr. P.R. Luijten, beste Peter, bedankt dat ik in de stimulerende omgeving van de 7T groep mijn onderzoek mocht doen. De goede sfeer en samenwerking tussen de verschillende subgroepen zorgde ervoor dat ik mij snel thuis voelde op de afdeling. Je betrokkenheid bij het traject heb ik erg gewaardeerd, zeker in de afrondende fase en bij het schrijven van de inleiding en discussie.

Dr. ir. J.J.M. Zwanenburg, beste Jaco, ik had mij geen betere co-promotor kunnen wensen. Je bent zowel een bevlogen wetenschapper als een persoonlijk betrokken begeleider. Bedankt voor de kans die je mij bood om na mijn stage bij de 7T groep terug te komen als promovendus. Als dagelijkse begeleider was je altijd wel even beschikbaar als ik langs liep om een idee te bespreken. Meestal ontaarde dat in een kleine brainstormsessie die nieuwe ideeën en inspiratie opleverde om mee aan de slag te gaan. Je gedrevenheid zorgde ervoor dat ik doorzette (en het abstract voor de ISMRM toch maar schreef, ook al was voor mijn idee nog niet alles af en kon het nog nét allemaal wat beter). De historische context met Angelo Mosso's experimenten en de overeenkomsten met onze studies was er zonder jouw historisch onderzoek waarschijnlijk niet gekomen. Ik wil je bedanken voor de afgelopen jaren.

Zonder de bijdrage van alle co-auteurs was dit proefschrift nooit geweest wat het nu is. Dr. A. de Luca, beste Alberto, dank voor de hulp bij het visualiseren van de strain tensor in DECKleurencodering. Prof. dr. G.J. Amelink, beste Hans, dank voor je enthousiasme en medewerking bij het valideren van de MRI techniek bij een patiënt. Ik vind het resultaat een hele mooie toevoeging aan het proefschrift. Dr. M. Froeling, beste Martijn, dank voor je bijdrage aan het ADC verhaal. Je kijk op en uitleg bij het onderwerp vanuit cardiale diffusie hebben ervoor gezorgd dat

de fysische principes voor mij helder werden. Deze bijdragen waren daarmee bepalend voor de invalshoek van het stuk.

Graag wil ik de beoordelingscommissie bedanken die de tijd en moeite hebben genomen om dit proefschrift te lezen: prof. dr. Rick Dijkhuizen, prof. dr. Birgitta Velthuis, prof. dr. Nick Ramsey, prof. dr. Thijs van Osch en prof. dr. John Weaver.

De afgelopen vier jaar heb ik onderzoek mogen doen in de high-field groep. Graag wil ik iedereen van deze groep en het coil-lab bedanken voor de collegialiteit, hulp en goede sfeer. Kees, Anneloes, Sander, Edwin, Evita, Tine, Jeanine, Zahra, Sarah, Peter, Carlo, Lieke, Ayhan, Rick, Seb en Kyung-Min: zonder jullie was er geen koffietrein geweest. Het dagelijkse koffiemoment (meestal met bijbehorende wandeling) was altijd iets om naar uit te kijken. Even achter het beeldscherm vandaan om even bij te praten over (niet) werk-gerelateerde zaken.

Daarnaast kan de wetenschap nooit zijn wat het nu is, zonder de structuur van het secretariaat. Sylvia, dank voor alles wat je voor de 7T groep betekent. Ook Angela, dank voor de planning van alle afspraken tijdens mijn PhD traject.

Ook wil ik iedereen van de VCI groep bedanken. Het was altijd leerzaam om mijn verhaal te kunnen spiegelen aan jullie medische blik. Nick, bedankt voor de interesse in het onderzoek. Hilde, het was gezellig om je zo nu en dan bij de 7T tegen het lijf te lopen en je later te helpen bij het scannen van je patiëntenpopulatie. Laurien, mijn eerste mini-congres in Berlijn was een stuk leuker met jou als partner-in-crime.

Lieve vrienden, bedankt voor alle mooie momenten. Jullie hebben de afgelopen jaren onvergetelijk gemaakt. Martijn, ik wil je bedanken voor de koffie-momenten waarin we het werk bespraken, maar nog meer de zin en onzin van het leven. Club Priem, bedankt voor alle activiteiten buiten het werk om. Vooral de Utrecht Clan (Hendrik, Bert en Tobias), omdat die nu eenmaal dichtbij wonen en het daardoor logistiek makkelijker is om een koffietje te doen. Maar ook De Kandidaten (Duco, Adriaan en Dirk) wil ik bedanken voor al het lief en leed omtrent onderzoek doen. De zin en onzin van het PhD leven is nu eenmaal het beste te delen met hen die hetzelfde doormaken. Naast sommigen van jullie die als vrijwilliger hebben gefungeerd, wil ik bij dezen ook alle andere vrijwilligers bedanken die mijn onderzoek mogelijk hebben gemaakt. Zonder hun medewerking en geduld waren de beschreven MRI technieken nooit geworden wat zij nu zijn.

Lieve familie Kestens, dank voor jullie interesse in mijn promotieonderzoek de afgelopen jaren, maar ook de gezellige momenten waarop ik even niet aan mijn onderzoek hoefde te denken.

Lieve familie, heel erg bedankt voor alle steun. Jullie betekenen veel voor mij. Pap en mam, altijd staan jullie klaar voor mij. De onvoorwaardelijke liefde en solide basis hebben mij gebracht waar ik nu ben. Bram en Rosanne, als grote broer baande ik vaak de paden (of het gras voor jullie voeten weg, het is maar net hoe je het bekijkt). Ik ben trots op jullie hoe jullie ieder je eigen weg hebben gekozen. Bram, ik vindt het heel mooi dat jij mijn paranimf bent.

Lieve Matthijs, jouw ontdekkingstocht is de afgelopen twee jaar de mooiste geweest van allemaal. Je pret-ogen en grote lach laten alle dagelijkse beslommeringen als sneeuw voor de zon verdwijnen. Vooral het uitje naar het spoorwegmuseum is zowel voor jou als voor mij onvergetelijk geweest.

Lieve Christine, ik had dit onderzoek nooit zonder jouw steun en liefde kunnen volbrengen. Jij bent er altijd voor me geweest en je haalt het beste in mij naar boven. Je bracht me bij het onderzoek altijd weer op het juiste pad als ik dreigde te verzanden in randzaken. Ik heb genoten van al onze avonturen, zowel met, maar de laatste tijd veel vaker zonder benzinebrandertje. Zeker in de laatste fase was er steeds minder ruimte in mijn hoofd om nieuwe plannen te maken. Jij zorgde ervoor dat ze er toch kwamen (en ik alleen nog even de auto hoefde in te pakken). Ik kijk uit naar alle nieuwe avonturen. Dat ik die met jou mag beleven is het beste wat mij ooit is overkomen.

REFERENCES

1. **Adams AL, Kuijf HJ, Viergever MA, Luijten PR & Zwanenburg JJM.** Quantifying cardiac-induced brain tissue expansion using DENSE. *NMR Biomed.* 32: e4050 (2019).
2. **Adams AL, Viergever MA, Luijten PR & Zwanenburg JJM.** Validating faster DENSE measurements of cardiac-induced brain tissue expansion as a potential tool for investigating cerebral microvascular pulsations. *Neuroimage* 208: 116466 (2020).
3. **Ahn S & Lee SK.** Diffusion tensor imaging: Exploring the motor networks and clinical applications. *Korean J. Radiol.* 12: 251–261 (2011).
4. **Aldea R, Weller RO, Wilcock DM, Carare RO & Richardson G.** Cerebrovascular Smooth Muscle Cells as the Drivers of Intramural Periarterial Drainage of the Brain Roxana. *Front. Aging Neurosci.* 11: 1 (2019).
5. **Aletras AH, Ding S, Balaban RS & Wen H.** DENSE: Displacement Encoding with Stimulated Echoes in Cardiac Functional MRI. *J. Magn. Reson.* 137: 247–252 (1999).
6. **Alperin N, Lee SH, Sivaramakrishnan A & Hushek SG.** Quantifying the effect of posture on intracranial physiology in humans by MRI flow studies. *J. Magn. Reson. Imaging* 22: 591–596 (2005).
7. **Alperin NJ, Lee SH, Loth F, Raksin PB & Lichtor T.** MR-Intracranial Pressure (ICP): A Method to Measure Intracranial Elastance and Pressure Noninvasively by Means of MR Imaging: Baboon and Human Study. *Radiology* 217: 877–885 (2000).
8. **Andersson JLR, Skare S & Ashburner J.** How to correct susceptibility distortions in spin-echo echo-planar images: Application to diffusion tensor imaging. *Neuroimage* 20: 870–888 (2003).
9. **Artzi M, Liberman G, Nadav G, Vitinshtein F, Blumenthal DT, Bokstein F, Aizenstein O & Bashat DB.** Human cerebral blood volume measurements using dynamic contrast enhancement in comparison to dynamic susceptibility contrast MRI. *Neuroradiology* 57: 671–678 (2015).
10. **Asgari M, de Zélicourt D & Kurtcuoglu V.** Glymphatic solute transport does not require bulk flow. *Sci. Rep.* 6: 38635 (2016).
11. **Axel L & Dougherty L.** MR imaging of motion with spatial modulation of magnetization. *Radiology* 171: 841–845 (1989).
12. **Bakker ENTPTP, Bacskai BJ, Arbel-Ornath M, Aldea R, Bedussi B, Morris AWJJ, Weller RO & Carare RO.** Lymphatic Clearance of the Brain: Perivascular, Paravascular and Significance for Neurodegenerative Diseases. *Cell. Mol. Neurobiol.* 36: 181–194 (2016).
13. **Balédent O.** Imaging of the cerebrospinal fluid circulation. In: *Adult Hydrocephalus* pp. 121–138 (Cambridge University Press, 2014).
14. **Balédent O, Fin L, Khuoy L, Ambarki K, Gauvin AC, Gondry-Jouet C & Meyer ME.** Brain hydrodynamics study by phase-contrast magnetic resonance imaging transcranial color Doppler. *J. Magn. Reson. Imaging* 24: 995–1004 (2006).
15. **Balédent O, Gondry-Jouet C, Meyer ME, De Marco G, Le Gars D, Henry-Feugeas MC & Idy-Peretti I.** Relationship between cerebrospinal fluid and blood dynamics in healthy volunteers and patients with communicating hydrocephalus. *Invest. Radiol.* 39: 45–55 (2004).
16. **Bammer R.** Basic principles of diffusion-weighted imaging. *Eur. J. Radiol.* 45: 169–84 (2003).
17. **Barth M, Breuer F, Koopmans PJ, Norris DG & Poser BA.** Simultaneous multislice (SMS) imaging techniques. *Magn. Reson. Med.* 75: 63–81 (2016).

18. **Basser PJ, Mattiello J & LeBihan D.** MR diffusion tensor spectroscopy and imaging. *Biophys. J.* 66: 259–267 (1994).
19. **Becker AS, Boss A, Klarhoefer M, Finkenstaedt T, Wurnig MC & Rossi C.** Investigation of the pulsatility of cerebrospinal fluid using cardiac-gated Intravoxel Incoherent Motion imaging. *Neuroimage* 169: 126–133 (2018).
20. **Bernstein MA, King KF & Zhou XJ.** *Handbook of MRI Pulse Sequences.* Elsevier Academic Press (2004).
21. **Bianciardi M, Fukunaga M, van Gelderen P, Horovitz SG, de Zwart JA, Shmueli K & Duyn JH.** Sources of functional magnetic resonance imaging signal fluctuations in the human brain at rest: a 7 T study. *Magn. Reson. Imaging* 27: 1019–1029 (2009).
22. **Le Bihan D.** What can we see with IVIM MRI? *Neuroimage* 187: 56–67 (2019).
23. **Le Bihan D, Breton E, Lallemand D, Aubin ML, Vignaud J & Laval-Jeantet M.** Separation of diffusion and perfusion in intravoxel incoherent motion MR imaging. *Radiology* 168: 497–505 (1988).
24. **Le Bihan D, Breton E, Lallemand D, Grenier P, Cabanis E & Laval-Jeantet M.** MR imaging of intravoxel incoherent motions: application to diffusion and perfusion in neurologic disorders. *Radiology* 161: 401–7 (1986).
25. **Biswal BB.** Resting state fMRI: A personal history. *NeuroImage* 62: 938–944 (2012).
26. **Blanco PJ, Müller LO & Spence JD.** Blood pressure gradients in cerebral arteries: a clue to pathogenesis of cerebral small vessel disease. *Stroke Vasc. Neurol.* 2: 108–117 (2017).
27. **Blatter DD, Parker DL & Robison RO.** Cerebral MR angiography with multiple overlapping thin slab acquisition: Part I. Quantitative analysis of vessel visibility. *Radiology* 179: 805–811 (1991).
28. **Bryant DJ, Payne JA, Firmin DN & Longmore DB.** Measurement of flow with nmr imaging using a gradient pulse and phase difference technique. *J. Comput. Assist. Tomogr.* 8: 588–593 (1984).
29. **Budday S, Ovaert TC, Holzapfel GA, Steinmann P & Kuhl E.** Fifty Shades of Brain: A Review on the Mechanical Testing and Modeling of Brain Tissue. *Arch. Comput. Methods Eng.* 27: 1187–1230 (2019).
30. **Bulte D, Chiarelli P, Wise R & Jezzard P.** Measurement of cerebral blood volume in humans using hyperoxic MRI contrast. *J. Magn. Reson. Imaging* 26: 894–899 (2007).
31. **Bunevicius A, Schregel K, Sinkus R, Golby A & Patz S.** REVIEW: MR elastography of brain tumors. *NeuroImage. Clinical* 25: 102109 (2020).
32. **Burle B, Spieser L, Roger C, Casini L, Hasbroucq T & Vidal F.** Spatial and temporal resolutions of EEG: Is it really black and white? A scalp current density view. *Int. J. Psychophysiol.* 97: 210–220 (2015).
33. **Chistiakov DA, Orekhov AN & Bobryshev Y V.** Effects of shear stress on endothelial cells: go with the flow. *Acta Physiologica* 219: 382–408 (2017).
34. **Clayton EH, Garbow JR & Bayly P V.** Frequency-dependent viscoelastic parameters of mouse brain tissue estimated by MR elastography. *Phys. Med. Biol.* 56: 2391–2406 (2011).
35. **Dai G, Kaazempur-Mofrad MR, Kamm RD, Zhang Y, Vaughn S, Garcia-Cardena G & Gimbrone MA.** Distinct Endothelial Phenotypes Evoked By Arterial Waveforms Derived From Atherosclerosis-Prone and Atherosclerosis-Protected Regions of the Human Vasculature. *Cardiovasc. Pathol.* 13: 26 (2004).

36. **Daouk J, Bouzerar R & Balédent O.** Heart rate and respiration influence on macroscopic blood and CSF flows. *Acta radiol.* 58: 977–982 (2017).
37. **Davies PF, Civelek M, Fang Y & Fleming I.** The atherosusceptible endothelium: Endothelial phenotypes in complex haemodynamic shear stress regions in vivo. *Cardiovascular Research* 99: 315–327 (2013).
38. **Deffieux T, Demené C & Tanter M.** Functional Ultrasound Imaging: A New Imaging Modality for Neuroscience. *Neuroscience* (2021).
39. **Dreha-Kulaczewski S, Joseph AA, Merboldt K-D, Ludwig H-C, Gartner J & Frahm J.** Inspiration Is the Major Regulator of Human CSF Flow. *J. Neurosci.* 35: 2485–2491 (2015).
40. **Dreha-Kulaczewski S, Joseph AA, Merboldt K-DD, Ludwig H-CC, Gärtner J & Frahm J.** Identification of the Upward Movement of Human CSF *In Vivo* and its Relation to the Brain Venous System. *J. Neurosci.* 37: 2395–2402 (2017).
41. **Enzmann DR & Pelc NJ.** Cerebrospinal Fluid Flow Measured by Phase-Contrast Cine MR. *Am. J. Neuroradiol.* 14: 1301–1307 (1993).
42. **Federau C, Hagmann P, Maeder P, Müller M, Meuli R, Stuber M & O'Brien K.** Dependence of Brain Intravoxel Incoherent Motion Perfusion Parameters on the Cardiac Cycle. *PLoS One* 8: 1–7 (2013).
43. **Feinberg DA & Mark AS.** Human brain motion and cerebrospinal fluid circulation demonstrated with MR velocity imaging. *Radiology* 163: 793–799 (1987).
44. **Ferree TC, Clay MT & Tucker DM.** The spatial resolution of scalp EEG. *Neurocomputing* 38–40: 1209–1216 (2001).
45. **Fischer SE, McKinnon GC, Maier SE & Boesiger P.** Improved myocardial tagging contrast. *Magn. Reson. Med.* 30: 191–200 (1993).
46. **Fonov V, Evans A, McKinstry R, Almlí C & Collins D.** Unbiased nonlinear average age-appropriate brain templates from birth to adulthood. *Neuroimage* 47: S102 (2009).
47. **Fonov V, Evans AC, Botteron K, Almlí CR, McKinstry RC & Collins DL.** Unbiased average age-appropriate atlases for pediatric studies. *Neuroimage* 54: 313–327 (2011).
48. **Forouhandehpour R, Bernier M, Gilbert G, Butler R, Whittingstall K & Van Houten E.** Cerebral stiffness changes during visual stimulation: Differential physiological mechanisms characterized by opposing mechanical effects. *Neuroimage: Reports* 1: 100014 (2021).
49. **Frahm J, Merboldt KD, Hänicke W & Haase A.** Stimulated echo imaging. *J. Magn. Reson.* 64: 81–93 (1985).
50. **Fuchs VR & Sox HC.** Physicians' views of the relative importance of thirty medical innovations. *Health Aff.* 20: 30–42 (2001).
51. **Fultz NE, Bonmassar G, Setsompop K, Stickgold RA, Rosen BR, Polimeni JR & Lewis LD.** Coupled electrophysiological, hemodynamic, and cerebrospinal fluid oscillations in human sleep. *Science (80-)*. 366: 628–631 (2019).
52. **Fung YC (Yuan-cheng).** *A first course in continuum mechanics : for physical and biological engineers and scientists.* (Prentice Hall, 1994).
53. **Gallichan D, Andersson JLR, Jenkinson M, Robson MD & Miller KL.** Reducing distortions in diffusion-weighted echo planar imaging with a dual-echo blip-reversed sequence. *Magn. Reson. Med.* 64: 382–390 (2010).

54. **Geethanath S, Reddy R, Konar AS, Imam S, Sundaresan R, Ramesh Babu DR & Venkatesan R.** Compressed sensing MRI: A review. *Critical Reviews in Biomedical Engineering* 41: 183–204 (2013).
55. **Van Gelderen P, De Zwart JA, Starewicz P, Hinks RS & Duyn JH.** Real-time shimming to compensate for respiration-induced B0 fluctuations. *Magn. Reson. Med.* 57: 362–368 (2007).
56. **Gordon-Wylie SW, Solamen LM, McGarry MDJ, Zeng W, VanHouten E, Gilbert G, Weaver JB & Paulsen KD.** MR elastography at 1 Hz of gelatin phantoms using 3D or 4D acquisition. *J. Magn. Reson.* 296: 112–120 (2018).
57. **Goriely A et al.** Mechanics of the brain: perspectives, challenges, and opportunities. *Biomech. Model. Mechanobiol.* 14: 931–965 (2015).
58. **Greitz D, Wirestam R, Franck A, Nordell B, Thomsen C & Ståhlberg F.** Pulsatile brain movement and associated hydrodynamics studied by magnetic resonance phase imaging. The Monro-Kellie doctrine revisited. *Neuroradiology* 34: 370–380 (1992).
59. **Groot Koerkamp MAM, Snoep G, Muijtjens AMM & Kemerink GJ.** Improving contrast and tracking of tags in cardiac magnetic resonance images. *Magn. Reson. Med.* 41: 973–982 (1999).
60. **De Guio F, Vignaud A, Ropele S, Duering M, Duchesnay E, Chabriat H & Jouvent E.** Loss of venous integrity in cerebral small vessel disease: A 7-T MRI study in cerebral autosomal-dominant arteriopathy with subcortical infarcts and leukoencephalopathy (CADASIL). *Stroke* 45: 2124–2126 (2014).
61. **Gupta P, Sodhi KS, Saxena AK, Khandelwal N & Singhi P.** Neonatal cranial sonography: A concise review for clinicians. *Journal of Pediatric Neurosciences* 11: 7–13 (2016).
62. **Haddar H, Li JR & Schiavi S.** Understanding the time-dependent effective diffusion coefficient measured by diffusion mri: The intracellular case*. *SIAM J. Appl. Math.* 78: 774–800 (2018).
63. **Haddock RE & Hill CE.** Rhythmicity in arterial smooth muscle. *Journal of Physiology* 566: 645–656 (2005).
64. **Hahn M, Klyszcz T & Jünger M.** Synchronous measurements of blood pressure and red blood cell velocity in capillaries of human skin. *J. Invest. Dermatol.* 106: 1256–1259 (1996).
65. **Harrison IF et al.** Non-invasive imaging of CSF-mediated brain clearance pathways via assessment of perivascular fluid movement with diffusion tensor MRI. *Elife* 7: (2018).
66. **Helenius J, Soine L, Perko J, Salonen O, Kangasmaki A, Kaste M, Carano RA, Aronen HJ & Tatlisumak T.** Diffusion-weighted MR imaging in normal human brains in various age groups. *AJNR Am J Neuroradiol* 23: 194–199 (2002).
67. **Hennig J, Kiviniemi V, Riemenschneider B, Barghoorn A, Akin B, Wang F & LeVan P.** 15 Years MR-encephalography. *Magnetic Resonance Materials in Physics, Biology and Medicine* 34: 85–108 (2021).
68. **Hetzer S, Birr P, Fehlner A, Hirsch S, Dittmann F, Barnhill E, Braun J & Sack I.** Perfusion alters stiffness of deep gray matter. *J. Cereb. Blood Flow Metab.* 38: 116–125 (2018).
69. **van den Heuvel MP & Hulshoff Pol HE.** Exploring the brain network: A review on resting-state fMRI functional connectivity. *European Neuropsychopharmacology* 20: 519–534 (2010).
70. **Hirsch S, Klatt D, Freimann F, Scheel M, Braun J & Sack I.** In vivo measurement of volumetric strain in the human brain induced by arterial pulsation and harmonic waves. *Magn. Reson. Med.* 70: 671–682 (2013).

71. **Hirschler L, Aldea R, Petitsclerc L, Ronen IA, De Koning PJ, Van Buchem MA & Van Osch MJP.** High resolution T2-prepared MRI enables non-invasive assessment of CSF flow in perivascular spaces of the human brain Lydiane. *Proc. Intl. Soc. Mag. Reson. Med.* 27: 746 (2019).
72. **Hirschler L, Runderkamp BA, Franklin S, Harten T van, Nederveen A, Caan MW & Osch MJ van.** The driving force of glymphatics: influence of the cardiac cycle on CSF-mobility in perivascular spaces in humans. *Proc. Intl. Soc. Mag. Reson. Med.* 28: 0643 (2018).
73. **Holdsworth SJ, Rahimi MS, Ni WW, Zaharchuk G & Moseley ME.** Amplified magnetic resonance imaging (aMRI). *Magn. Reson. Med.* 75: 2245–2254 (2016).
74. **Hutchinson JMS, Sutherland RJ & Mallard JR.** NMR imaging: Image recovery under magnetic fields with large non-uniformities. *J. Phys. E.* 11: 217–221 (1978).
75. **Ibrahim ESH.** Myocardial tagging by cardiovascular magnetic resonance: evolution of techniques-- pulse sequences, analysis algorithms, and applications. *Journal of cardiovascular magnetic resonance : official journal of the Society for Cardiovascular Magnetic Resonance* 13: 36 (2011).
76. **Iliff JJ et al.** A paravascular pathway facilitates CSF flow through the brain parenchyma and the clearance of interstitial solutes, including amyloid β . *Sci. Transl. Med.* 4: 147ra111-147ra111 (2012).
77. **Iliff JJ, Wang M, Zeppenfeld DM, Venkataraman A, Plog BA, Liao Y, Deane R & Nedergaard M.** Cerebral arterial pulsation drives paravascular CSF-Interstitial fluid exchange in the murine brain. *J. Neurosci.* 33: 18190–18199 (2013).
78. **Jahanian H, Christen T, Moseley ME, Pajewski NM, Wright CB, Tamura MK & Zaharchuk G.** Measuring vascular reactivity with resting-state blood oxygenation level-dependent (BOLD) signal fluctuations: A potential alternative to the breath-holding challenge? *J. Cereb. Blood Flow Metab.* 37: 2526–2538 (2017).
79. **Jezzard P & Balaban RS.** Correction for geometric distortion in echo planar images from B0 field variations. *Magn. Reson. Med.* 34: 65–73 (1995).
80. **Jin X, Zhu F, Mao H, Shen M & Yang KH.** A comprehensive experimental study on material properties of human brain tissue. *J. Biomech.* 46: 2795–2801 (2013).
81. **Kiviniemi V et al.** Ultra-fast magnetic resonance encephalography of physiological brain activity – Glymphatic pulsation mechanisms? *J. Cereb. Blood Flow Metab.* 36: 1033–1045 (2016).
82. **Klein S, Staring M, Murphy K, Viergever MA & Pluim JPW.** Elastix: A toolbox for intensity-based medical image registration. *IEEE Trans. Med. Imaging* (2010).
83. **Kuijjer JPA, Hofman MBM, Zwanenburg JJM, Marcus JT, Van Rossum AC & Heethaar RM.** DENSE and HARP: Two views on the same technique of phase-based strain imaging. *J. Magn. Reson. Imaging* 24: 1432–1438 (2006).
84. **Kuijff HJ et al.** Standardized Assessment of Automatic Segmentation of White Matter Hyperintensities and Results of the WMH Segmentation Challenge. *IEEE Trans. Med. Imaging* 38: 2556–2568 (2019).
85. **Kuijff HJ, Bouvy WH, Zwanenburg JJM, Razoux Schultz TB, Viergever MA, Vincken KL & Biesels GJ.** Quantification of deep medullary veins at 7 T brain MRI. *Eur. Radiol.* 26: 3412–3418 (2016).
86. **Lai M, Krempl E & Rubin D.** *Introduction to Continuum Mechanics. Journal of Chemical Information and Modeling* 53: (Elsevier Inc., 2010).
87. **Leemans A, Jeurissen B, Sijbers J & Jones DK.** ExploreDTI: a graphical toolbox for processing, analyzing, and visualizing diffusion MR data. *Proc. Int. Soc. Magn. Reson. Med.* 17: 3537 (2009).

88. **Leemans A & Jones DK.** The B-matrix must be rotated when correcting for subject motion in DTI data. *Magn. Reson. Med.* 61: 1336–1349 (2009).
89. **De Leeuw H & Bakker CJG.** Correction of gradient echo images for first and second order macroscopic signal dephasing using phase derivative mapping. *Neuroimage* 60: 818–829 (2012).
90. **Linninger AA, Tangen K, Hsu C-Y & Frim D.** Cerebrospinal Fluid Mechanics and Its Coupling to Cerebrovascular Dynamics. *Annu. Rev. Fluid Mech.* 48: 219–257 (2016).
91. **Linninger AA, Tsakiris C, Zhu DC, Xenos M, Roycewicz P, Danziger Z & Penn R.** Pulsatile cerebrospinal fluid dynamics in the human brain. *IEEE Trans. Biomed. Eng.* 52: 557–565 (2005).
92. **Linninger AA, Xenos M, Sweetman B, Ponskshe S, Guo X & Penn R.** A mathematical model of blood, cerebrospinal fluid and brain dynamics. *J. Math. Biol.* 59: 729–759 (2009).
93. **Lorenz R, Bock J, Snyder J, Korvink JG, Jung BA & Markl M.** Influence of eddy current, Maxwell and gradient field corrections on 3D flow visualization of 3D CINE PC-MRI data. *Magnetic Resonance in Medicine* 72: 33–40 (2014).
94. **De Luca A, Franklin S, Lucci C, Hendrikse J, Froeling M & Leemans A.** Investigation of the dependence of free water and pseudo-diffusion MRI estimates on the cardiac cycle. *Proc. Int. Soc. Magn. Reson. Med.* 0344 (2019).
95. **Lustig M, Donoho D & Pauly JM.** Sparse MRI: The application of compressed sensing for rapid MR imaging. *Magn. Reson. Med.* 58: 1182–1195 (2007).
96. **MacDonald ME, Forkert ND, Pike GB & Frayne R.** Phase Error Correction in Time-Averaged 3D Phase Contrast Magnetic Resonance Imaging of the Cerebral Vasculature. *PLoS One* 11: e0149930 (2016).
97. **Matthews PM.** Chronic inflammation in multiple sclerosis — seeing what was always there. *Nature Reviews Neurology* 15: 582–593 (2019).
98. **McGarry MDJJ et al.** An octahedral shear strain-based measure of SNR for 3D MR elastography. *Phys. Med. Biol.* 56: N153–64 (2011).
99. **Mele G, Cavaliere C, Alfano V, Orsini M, Salvatore M & Aiello M.** Simultaneous EEG-fMRI for functional neurological assessment. *Frontiers in Neurology* 10: 848 (2019).
100. **Mestre H et al.** Flow of cerebrospinal fluid is driven by arterial pulsations and is reduced in hypertension. *Nat. Commun.* 9: 4878 (2018).
101. **Mestre H, Kostrikov S, Mehta RI & Nedergaard M.** Perivascular spaces, glymphatic dysfunction, and small vessel disease. *Clin. Sci.* 131: 2257–2274 (2017).
102. **Moghari MH, Barthur A, Amaral ME, Geva T & Powell AJ.** Free-breathing whole-heart 3D cine magnetic resonance imaging with prospective respiratory motion compensation. *Magn. Reson. Med.* 80: 181–189 (2018).
103. **Mokri B.** The Monro-Kellie hypothesis: applications in CSF volume depletion. *Neurology* 56: 1746–8 (2001).
104. **Moran PR.** A flow velocity zeugmatographic interlace for NMR imaging in humans. *Magn. Reson. Imaging* 1: 197–203 (1982).
105. **Moran PR, Moran RA & Karstaedt N.** Verification and evaluation of internal flow and motion. True magnetic resonance imaging by the phase gradient modulation method. *Radiology* 154: 433–441 (1985).

106. **Mori S, Crain BJ, Chacko VP & Zijl PCM Van.** Three-dimensional tracking of axonal projections in the brain by magnetic resonance imaging. *Ann. Neurol.* 45: 265–269 (1999).
107. **Mosso A.** Sulla circolazione del cervello dell'uomo. *Atti della R. Accad. dei Lincei* 5: 237–358 (1880).
108. **Mucke J et al.** Asymmetry of deep medullary veins on susceptibility weighted MRI in patients with acute MCA stroke is associated with poor outcome. *PLoS One* 10: (2015).
109. **Mutlu U et al.** Association of Retinal Neurodegeneration on Optical Coherence Tomography with Dementia: A Population-Based Study. *JAMA Neurol.* 75: 1256–1263 (2018).
110. **Nagy Z & Weiskopf N.** Efficient fat suppression by slice-selection gradient reversal in twice-refocused diffusion encoding. *Magn. Reson. Med.* 60: 1256–1260 (2008).
111. **Nakamura T et al.** Bulk motion-independent analyses of water diffusion changes in the brain during the cardiac cycle. *Radiol. Phys. Technol.* 2: 133–137 (2009).
112. **Nayak KS et al.** Cardiovascular magnetic resonance phase contrast imaging. *J. Cardiovasc. Magn. Reson.* 17: 71 (2015).
113. **Nolte UG, Finsterbusch J & Frahm J.** Rapid isotropic diffusion mapping without susceptibility artifacts: Whole brain studies using diffusion-weighted single-shot STEAM MR imaging. *Magn. Reson. Med.* 44: 731–736 (2000).
114. **Ohno N et al.** Idiopathic Normal-Pressure Hydrocephalus: Temporal Changes in ADC during Cardiac Cycle. *Radiology* 261: 560–565 (2011).
115. **Ong YT et al.** Retinal neurodegeneration on optical coherence tomography and cerebral atrophy. *Neurosci. Lett.* 584: 12–16 (2015).
116. **van Opstal AM et al.** Cerebrovascular function in presymptomatic and symptomatic individuals with hereditary cerebral amyloid angiopathy: a case-control study. *Lancet Neurol.* 16: 115–122 (2017).
117. **Osawa T et al.** Changes in Apparent Diffusion Coefficient (ADC) during Cardiac Cycle of the Brain in Idiopathic Normal Pressure Hydrocephalus Before and After Cerebrospinal Fluid Drainage. *J. Magn. Reson. Imaging* 53: 1200–1207 (2021).
118. **Osman NF, Kerwin WS, McVeigh ER & Prince JL.** Cardiac motion tracking using CINE harmonic phase (HARP) magnetic resonance imaging. *Magn. Reson. Med.* 42: 1048–1060 (1999).
119. **Pahlavian SH, Oshinski J, Zhong X, Loth F & Amini R.** Regional Quantification of Brain Tissue Strain Using Displacement-Encoding With Stimulated Echoes Magnetic Resonance Imaging. *J. Biomech. Eng.* 140: 081010 (2018).
120. **Pajevic S & Pierpaoli C.** Color schemes to represent the orientation of anisotropic tissues from diffusion tensor data: Application to white matter fiber tract mapping in the human brain. *Magn. Reson. Med.* 42: 526–540 (1999).
121. **Pantoni L.** Cerebral small vessel disease: from pathogenesis and clinical characteristics to therapeutic challenges. *Lancet Neurol.* 9: 689–701 (2010).
122. **Polimeni JR, Wald LL, Bhat H, Evans KC, Boas DA, Bianciardi M, Keil B, Toschi N & Rosen BR.** The pulsatility volume index: an indicator of cerebrovascular compliance based on fast magnetic resonance imaging of cardiac and respiratory pulsatility. *Philos. Trans. R. Soc. A Math. Phys. Eng. Sci.* 374: 20150184 (2016).
123. **Poustchi-Amin M, Mirowitz SA, Brown JJ, McKinstry RC & Li T.** Principles and applications of echo-planar imaging: a review for the general radiologist. *Radiographics: a review publication of the Radiological Society of North America, Inc* 21: 767–779 (2001).

124. **Raichle ME, Shepherd GM & Fabbri CN.** *Angelo Mosso's Circulation of blood in the human brain.* (2014).
125. **Rasmussen MK, Mestre H & Nedergaard M.** Rapid Review The glymphatic pathway in neurological disorders. 17: (2018).
126. **Reese TG, Feinberg DA, Dou J & Wedeen VJ.** Phase contrast MRI of myocardial 3D strain by encoding contiguous slices in a single shot. *Magn. Reson. Med.* 47: 665–676 (2002).
127. **Reese TG, Van Wedeen J & Weisskoff RM.** Measuring diffusion in the presence of material strain. *J. Magn. Reson. - Ser. B* 112: 253–258 (1996).
128. **Reese TG, Weisskoff RM, Smith RN, Rosen BR, Dinsmore RE & Wedeen VJ.** Imaging myocardial fiber architecture in vivo with magnetic resonance. *Magn. Reson. Med.* 34: 786–791 (1995).
129. **Rivera-Rivera LA, Johnson KM, Turski PA, Wieben O & Schubert T.** Measurement of microvascular cerebral blood volume changes over the cardiac cycle with ferumoxytol-enhanced T 2* MRI. *Magn. Reson. Med.* (2019).
130. **Rooney WD, Johnson G, Li X, Cohen ER, Kim SG, Ugurbil K & Springer CS.** Magnetic field and tissue dependencies of human brain longitudinal 1H2O relaxation in vivo. *Magn. Reson. Med.* 57: 308–318 (2007).
131. **Rzedzian R, Mansfield P, Doyle M, Guilfoyle D, Chapman B, Coupland RE, Chrispin A & Small P.** Real-time nuclear magnetic resonance clinical imaging in paediatrics. *Lancet* 322: 1281–1282 (1983).
132. **Sack I, Beierbach B, Wuerfel J, Klatt D, Hamhaber U, Papazoglou S, Martus P & Braun J.** The impact of aging and gender on brain viscoelasticity. *Neuroimage* 46: 652–657 (2009).
133. **Sack I, Streitberger K-JJ, Krefting D, Paul F & Braun J.** The influence of physiological aging and atrophy on brain viscoelastic properties in humans. *PLoS One* 6: e23451 (2011).
134. **Shore AC, Sandeman DD & Tooke JE.** Capillary pressure, pulse pressure amplitude, and pressure waveform in healthy volunteers. *Am. J. Physiol. - Hear. Circ. Physiol.* 268: (1995).
135. **DE Simone R, Ranieri A & Bonavita V.** Starling resistors, autoregulation of cerebral perfusion and the pathogenesis of idiopathic intracranial hypertension. *Panminerva Med.* 59: 76–89 (2017).
136. **Sloots JJ, Biessels GJ, de Luca A & Zwanenburg JJM.** Strain Tensor Imaging: Cardiac-induced brain tissue deformation in humans quantified with high-field MRI. *Neuroimage* 236: 118078 (2021).
137. **Sloots JJ, Biessels GJ & Zwanenburg JJM.** Cardiac and respiration-induced brain deformations in humans quantified with high-field MRI. *Neuroimage* 210: 116581 (2020).
138. **Sloots JJ, Luijten PR, Biessels GJ & Zwanenburg JJM.** Cardiac and Respiratory induced 3D Brain Tissue Strain as Marker of Physiological Blood Volume Dynamics at 7T MRI . *Proc. Int. Soc. Magn. Reson. Med.* 27: 2799 (2019).
139. **Sloots JJ, Luijten PR, Biessels GJ & Zwanenburg JJM.** Optimizing the DENSE Sequence for Accurate Brain Tissue Strain Measurements at 7T MRI . *Proc. Int. Soc. Magn. Reson. Med.* 27: 2800 (2019).
140. **Soellinger M, Rutz AK, Kozerke S & Boesiger P.** 3D cine displacement-encoded MRI of pulsatile brain motion. *Magn. Reson. Med.* 61: 153–162 (2009).
141. **Spector R, Robert Snodgrass S & Johanson CE.** A balanced view of the cerebrospinal fluid composition and functions: Focus on adult humans. *Exp. Neurol.* 273: 57–68 (2015).

142. **Spottiswoode BS, Zhong X, Hess AT, Kramer CM, Meintjes EM, Mayosi BM & Epstein FH.** Tracking myocardial motion from cine DENSE images using spatiotemporal phase unwrapping and temporal fitting. *IEEE Trans. Med. Imaging* 26: 15–30 (2007).
143. **Ståhlberg F *et al.*** A method for MR quantification of flow velocities in blood and CSF using interleaved gradient-echo pulse sequences. *Magn. Reson. Imaging* 7: 655–667 (1989).
144. **Ståhlberg F, Henriksen O, Thomsen C, Stubgaard M & Persson B.** Determination of flow velocities from magnetic resonance multiple spin-echo images: A phantom study. *Acta radiol.* 28: 643–648 (1987).
145. **Stehling MK, Turner R & Mansfield P.** Echo-planar imaging: Magnetic resonance imaging in a fraction of a second. *Science* 254: 43–50 (1991).
146. **Stejskal EO & Tanner JE.** Spin diffusion measurements: Spin echoes in the presence of a time-dependent field gradient. *J. Chem. Phys.* 42: 288–292 (1965).
147. **Stoeck CT *et al.*** Dual-phase cardiac diffusion tensor imaging with strain correction. *PLoS One* 9: 1–12 (2014).
148. **Strik C, Klose U, Erb M, Strik H & Grodd W.** Intracranial oscillations of cerebrospinal fluid and blood flows: Analysis with magnetic resonance imaging. *J. Magn. Reson. Imaging* 15: 251–258 (2002).
149. **Tahedi M, Levine SM, Greenlee MW, Weissert R & Schwarzbach J V.** Functional connectivity in multiple sclerosis: Recent findings and future directions. *Frontiers in Neurology* 9: 828 (2018).
150. **Tan L, McGarry MDJ, Van Houten EEW, Ji M, Solamen L, Zeng W, Weaver JB & Paulsen KD.** A numerical framework for interstitial fluid pressure imaging in poroelastic MRE. *PLoS One* 12: e0178521 (2017).
151. **Tan TE *et al.*** Global Assessment of Retinal Arteriolar, Venular and Capillary Microcirculations Using Fundus Photographs and Optical Coherence Tomography Angiography in Diabetic Retinopathy. *Sci. Rep.* 9: 1–9 (2019).
152. **Tanter M & Fink M.** Ultrafast imaging in biomedical ultrasound. *IEEE Trans. Ultrason. Ferroelectr. Freq. Control* 61: 102–119 (2014).
153. **Tarasoff-Conway JM *et al.*** Clearance systems in the brain - Implications for Alzheimer disease. *Nat. Rev. Neurol.* 11: 457–470 (2015).
154. **Tarbell JM, Simon SI & Curry F-RE.** Mechanosensing at the Vascular Interface. *Annu. Rev. Biomed. Eng.* 16: 505–532 (2014).
155. **Tecelão SRR, Zwanenburg JJM, Kuijper JPA & Marcus JT.** Extended harmonic phase tracking of myocardial motion: Improved coverage of myocardium and its effect on strain results. *J. Magn. Reson. Imaging* 23: 682–690 (2006).
156. **Terem I, Ni WW, Goubran M, Rahimi MS, Zaharchuk G, Yeom KW, Moseley ME, Kurt M & Holdsworth SJ.** Revealing sub-voxel motions of brain tissue using phase-based amplified MRI (aMRI). *Magn. Reson. Med.* 80: 2549–2559 (2018).
157. **Tsai YH *et al.*** Noninvasive assessment of intracranial elastance and pressure in spontaneous intracranial hypotension by MRI. *J. Magn. Reson. Imaging* 48: 1255–1263 (2018).
158. **Tsao CW *et al.*** Relations of arterial stiffness and endothelial function to brain aging in the community. *Neurology* (2013).
159. **Tseng W-YI, Reese TG, Weisskoff RM & Wedeen VJ.** Cardiac diffusion tensor MRI in vivo without strain correction. *Magn. Reson. Med.* 42: 393–403 (1999).

160. **Ueno T, Ballard RE, Macias BR, Yost WT & Hargens AR.** Cranial diameter pulsations measured by non-invasive ultrasound decrease with tilt. *Aviat. Sp. Environ. Med.* 74: 882–885 (2003).
161. **Ueno T, Ballard RE, Shuer LM, Cantrell JH, Yost WT & Hargens AR.** Noninvasive Measurement of Pulsatile Intracranial Pressure Using Ultrasound. *Acta Neurochir. Suppl.* 1998: 66–69 (1998).
162. **van Veluw SJ, Hou SS, Calvo-Rodriguez M, Arbel-Ornath M, Snyder AC, Frosch MP, Greenberg SM & Bacsikai BJ.** Vasomotion as a Driving Force for Paravascular Clearance in the Awake Mouse Brain. *Neuron* 105: 549–561
163. **Viessmann O, Möller HE & Jezzard P.** Cardiac cycle-induced EPI time series fluctuations in the brain: Their temporal shifts, inflow effects and T2* fluctuations. *Neuroimage* 162: 93–105 (2017).
164. **Vonken EJPA, Van Osch MJP, Bakker CJG & Viergever MA.** Measurement of cerebral perfusion with dual-echo multi-slice quantitative dynamic susceptibility contrast MRI. *J. Magn. Reson. Imaging* 10: 109–117 (1999).
165. **Wählin A, Ambarki K, Hauksson J, Birgander R, Malm J & Eklund A.** Phase contrast MRI Quantification of pulsatile volumes of brain arteries, veins, and cerebrospinal fluids compartments: Repeatability and physiological interactions. *J. Magn. Reson. Imaging* 35: 1055–1062 (2012).
166. **Wardlaw JM *et al.*** Neuroimaging standards for research into small vessel disease and its contribution to ageing and neurodegeneration. *Lancet Neurol.* 12: 822–838 (2013).
167. **Wardlaw JM, Smith C & Dichgans M.** Mechanisms of sporadic cerebral small vessel disease: Insights from neuroimaging. *Lancet Neurol.* 12: 483–497 (2013).
168. **Wardlaw JM, Smith C & Dichgans M.** Small vessel disease: mechanisms and clinical implications. *Lancet Neurol.* 18: 684–696 (2019).
169. **Weaver JB, Pattison AJ, McGarry MD, Perreard IM, Swienckowski JG, Eskey CJ, Lollis SS & Paulsen KD.** Brain mechanical property measurement using MRE with intrinsic activation. *Phys. Med. Biol.* 57: 7275–7287 (2012).
170. **Wedeen VJ, Weisskoff RM & Poncelet BP.** MRI signal void due to in-plane motion is all-or-none. *Magn. Reson. Med.* 32: 116–120 (1994).
171. **Wirth B, Sobey I & Eisentrager A.** Conditions for choking in a poroelastic flow model. *IMA J. Appl. Math.* 79: 254–273 (2014).
172. **Yamada S *et al.*** Influence of respiration on cerebrospinal fluid movement using magnetic resonance spin labeling. *Fluids Barriers CNS* 10: 36 (2013).
173. **Yamamori R, Miyati T, Ohno N, Hiramatsu Y, Kurita T, Miki S, Sekiya A, Hoshina Y & Gabata T.** Dynamic ADC Change during Cardiac Cycle in Human Brain in Sleep State. *Proc. Int. Soc. Magn. Reson. Med.* 2419 (2017).
174. **Yan S, Wan J, Zhang X, Tong L, Zhao S, Sun J, Lin Y, Shen C & Lou M.** Increased Visibility of Deep Medullary Veins in Leukoaraiosis: A 3-T MRI Study. *Front. Aging Neurosci.* 6: 144 (2014).
175. **Yildiz S, Thyagaraj S, Jin N, Zhong X, Heidari Pahlavian S, Martin BA, Loth F, Oshinski J & Sabra KG.** Quantifying the influence of respiration and cardiac pulsations on cerebrospinal fluid dynamics using real-time phase-contrast MRI. *J. Magn. Reson. Imaging* 46: 431–439 (2017).
176. **Yin Z, Kearney SP, Magin RL & Klatt D.** Concurrent 3D acquisition of diffusion tensor imaging and magnetic resonance elastography displacement data (DTI-MRE): Theory and in vivo application. *Magn. Reson. Med.* 77: 273–284 (2017).

177. **Young AA, Axel L, Dougherty L, Bogen DK & Parenteau CS.** Validation of tagging with MR imaging to estimate material deformation. *Radiology* 188: 101–108 (1993).
178. **Zago S, Ferrucci R, Marceglia S & Priori A.** The Mosso method for recording brain pulsation: The forerunner of functional neuroimaging. *Neuroimage* 48: 652–656 (2009).
179. **Zeng LL, Wang D, Fox MD, Sabuncu M, Hu D, Ge M, Buckner RL & Liu H.** Neurobiological basis of head motion in brain imaging. *Proc. Natl. Acad. Sci. U. S. A.* 111: 6058–6062 (2014).
180. **Zhong X *et al.*** Tracking brain motion during the cardiac cycle using spiral cine-DENSE MRI. *Med. Phys.* 36: 3413–3419 (2009).
181. **Zorgani A, Souchon R, Dinh AH, Chapelon JY, Ménager JM, Lounis S, Rouvière O & Catheline S.** Brain palpation from physiological vibrations using MRI. *Proc. Natl. Acad. Sci. U. S. A.* 112: 12917–12921 (2015).

CURRICULUM VITAE

Jacob-Jan Sloots was born on June 2nd, 1989 in Zeist, the Netherlands. After completing his secondary education in 2009 at the Stichtse Vrije School in Zeist, he obtained his bachelor's degree in Applied Physics in 2014 at the Technical University Delft. A minor in Biomedical Engineering to Delft sparked his interest in the cutting edge of technology and medicine, which led him to continue with a master in Biomedical Engineering (track Medical Physics) at the Technical University Delft. During his master's he fulfilled an internship on extracting T2 relaxation properties of interstitial fluids in the human brain at the Radiology department of the University Medical Center Utrecht. He then returned to Delft where he finished his master thesis, focusing on MR scanner invariant feature representation of MRI images. He obtained his master's degree in 2016.

After his master's degree, he was invited back to the University Medical Center Utrecht as a PhD candidate. His research focused on the development of MRI techniques to quantify physiological brain tissue deformation in humans under the supervision of prof. dr. Geert Jan Biessels, prof. dr. Peter Luijten and dr. ir. Jaco Zwanenburg. The results of this research are presented in this thesis.

Jacob-Jan is currently working as system test engineer at Philips.

